KARAGANDA
BUKETOV
UNIVERSITY
Est.1938

EURASIAN PHYSICAL TECHNICAL JOURNAL

Eurasian Physical Technical Journal, 2024, Vol. 21, No. 2(48)

CONTENTS

Dear authors and readers!
Dear colleagues!

In the preface, we traditionally inform authors and readers about the most important achievements of the Eurasian Physical Technical Journal at the moment.

In 2024, it was 20 years since the publication of the 1st issue of the Eurasian Physical Technical Journal, which is published on the basis of Karaganda University named after E. A. Buketov and is a peer-reviewed open access scientific journal for the publication of original scientific works on current fundamental and applied problems of physics and technology. On June 7, 2024, an online meeting of the journal's editorial board was held to mark this date. The meeting was organized to analyze the results of the work of the editorial board of the Eurasian Physical Technical Journal over 20 years and discuss development prospects for promoting the journal at the international level. The main indicators include the following:

✓ The journal is included in the List of publications recommended by the Committee for Quality Assurance in Science and Higher Education of the Ministry of Science and Higher Education of the Republic of Kazakhstan for the publication of the main results of scientific activities in the areas of Physical Sciences, Materials Science, Energy;

✓ The editorial board includes 23 leading scientists from research-educational centers of 11 countries.

✓ Since 2019, the journal has been indexed in the Scopus database in the following areas: Energy; Engineering; Materials Science; Physics and Astronomy. As of June 5, 2024, digital metrics have increased across the board: CiteScoreTracker score is 1.1 with a maximum percentile of 27% for Engineering);

✓ According to the analytical platform Scimago Journal & Country Rank (SJR), based on the results of 2023, H-index 7 and the journal is included in the Q3 quartile in the field of Engineering.

✓ Open Access status is ensured by free access to published materials in PDF format on the journal's website and websites of electronic scientific libraries, including the US Santa Barbara Library, USA.

✓ An interactive journal website like OJS allows you to carry out all stages of preparing articles for publication online. The site contains basic information in 3 languages about the journal's performance, detailed instructions for authors on how to correctly enter materials, news is regularly updated, https://phtj.buketov.edu.kz/index.php/EPTJ/index

✓ Since 2004, 614 articles by authors from more than 30 countries have been published, of which 225 articles by foreign authors, 207 articles by authors from various universities in Kazakhstan, and 185 articles prepared by employees of our university.

At the meeting, one of the founders of the journal, winner of the al Farabi gold medal, who since 2004 has been continuously the member of the editorial board of the journal, professor of al Farabi Kazakh National University, Zhanabev Z.Zh. emphasized the special role of the first editor-in-chief in the journal creation. "Being the Rector at that time, professor Akylbaev Zh.S. with the support of the International Academy of Higher Schools, invited authoritative scientists from leading scientific centers not only in Kazakhstan and Russia, but also in Belarus, Ukraine, France, Germany, Taiwan, Uzbekistan, South Korea, etc. to the editorial board. The international collaboration of scientists has improved the quality of scientific research and publications in various areas of technical physics, in particular nonlinear physics". To comply with modern trends in world science, professor Zhanabaev Z.Zh. recommended to intensify the publication of articles on Physics and Astronomy, in particular, on Astrophysics.

Among the first to join the meeting was Dr. Jiun-Jih Miau, a professor at the Department of Aeronautics and Astronautics at National Cheng Kung University, Tainan, Taiwan. Dr. Jiun-Jih Miau has served on the editorial board since 2004. Along with congratulations to the journal on its 20th anniversary and wishes for further success, he noted that due to the quality of publications, the journal has been indexed in the SCOPUS database for 5 years. Professor Jiun-Jih Miau expressed his readiness to inform fellow experts from Taiwan, both readers and potential authors.

The laureate of the Academician V.A. Koptyug, awarded by the National Academy of Sciences of Belarus and the Siberian Branch of the Russian Academy of Sciences, member of the editorial board from Minsk, chief researcher at the Laboratory of Nanostructured and Superhard Materials of the Joint Institute of Mechanical Engineering of the National Academy of Sciences of Belarus, Dr. Senyut V.T. approved the proposal to prepare special thematic issues based on materials from conferences or dedicated to anniversaries of leading scientists or research centers.

The head of the laboratory of multi-physical processes at the Institute of Numerical Modeling of the University of Latvia, Riga, Latvia, scientific director of a number of scientific projects, Professor Andris Jakovich noted that the journal consistently maintains its position as an indexed international publication. He emphasized that "continuous work on optimizing the website and online services for editing and preparing articles for publication can be an example for other magazines."

Director of the Center for Laser and Information Biophysics at Orenburg State University, Orenburg, Russia, Professor Kucherenko expressed words of approval and support to the editors in implementing methods to improve editorial processes. He suggested introducing a request for authors to suggest possible reviewers when uploading an article, which is a well-known practice of many leading journals and will expand the base of reviewers.

Professor Saulebekov A.O. (Kazakh branch of Moscow State University named after M.V. Lomonosov, Astana), professor Baktybekov K.S. ("Kazakhstan Gharysh Sapary", Nur-Sultan), professor Zeinidenov A.K. (Dean of the Faculty of Physics and Technology) were joined the discussion.

The meeting participants discussed effective ways and methods to improve the journal's performance, and adopted a number of proposals that could contribute to the growth of citations of the Eurasian Physical Technical Journal and further strengthening of the ranking at the international level.

This issue presents readers with 11 articles devoted to solving pressing problems of modern technical physics. The section "Materials Science" presents new original results on the study of the properties of various materials. In particular, "the results of a study of the resistance of neodymium zirconate doped with MgO and Y_2O_5 to radiation damage caused by radiation destruction by ions comparable to fission fragments of nuclear fuel." Researchers from Indonesia studied "the effect of low-density polymer grade on the temperature transition and charge behavior of wax as a solid-liquid thermal accumulator."

In the "Energy" section, readers are offered two articles that discuss the environmental aspects of energy. The article by Almaty colleagues presents the results of numerical experiments "on the atomization of liquid fuel and the distribution of its droplets in a turbulent reacting flow." The second article proposes an experimental model of a wind turbine with blades combined with a special device in the form of rotating cylinders.

The "Engineering" section offers ways to solve pressing problems of automation of modern technologies and management and control systems. In an article by authors from Tomsk, Russia and Egypt, a method for measuring contact resistance directly in the process of monitoring thermoEMF» is proposed. The Almaty authors conducted "a study of the effectiveness of methods for increasing the productivity of uranium mining through preliminary forecasting." The article by the Baku authors "describes an on-board control and measuring system designed to record the main technical parameters of the engines of a micro-unmanned aerial vehicle of the tiltrotor type in various flight modes." A rather unique method for evaluating "routing algorithms in various wireless network topologies using the NS-3 simulator" was developed by researchers from al-Farabi University. The last article in the section presents the results of "simulating the localization of noise sources on a construction site using an array of radial microphones at the intersection of the directions of the largest signal."

As a result of the joint work of authors from Kazakhstan, Italy and the USA, "the distribution of dark matter in four spiral galaxies with low surface brightness is studied using two models of scalar dark matter field theory, an alternative to the cold dark matter paradigm." Also, in the "Physics and Astronomy" section, articles by scientists from Nigeria are shown the results of a study of "cyclical properties of solar geomagnetic activity and global surface temperature using trend, frequency and time-frequency analysis."

We hope that the presented research results will be of interest to scientists, teachers, researchers, doctoral students and undergraduates. I would especially like to express my deep gratitude to our reviewers for their objective and qualified examination of the materials, which contributed to ensuring the quality of the articles.

We will be glad to see you among our readers and authors of the next issues.

Best regards,
Editor-in-chief, professor Saule E. Sakipova
June, 2024

STUDY OF THE EFFECT OF THE FORMATION OF TWO-PHASE CERAMICS BASED ON NEODYMIUM ZIRCONATE DUE TO DOPING WITH MGO AND Y₂O₅ ON THE STABILITY OF STRENGTH AND THERMOPHYSICAL PARAMETERS UNDER IRRADIATION

Kozlovskiy A.L.[1,2], Kabiyev M.B.[2], Shlimas D.I.[1,2], Uglov V.V.[3]

[1] Engineering Profile Laboratory, L.N. Gumilyov Eurasian National University, Astana, Kazakhstan
[2] Laboratory of Solid-State Physics, The Institute of Nuclear Physics, Almaty, Kazakhstan
[3] Belarusian State University, Minsk,Belarus
*Corresponding author: kozlovskiy.a@inp.kz

Abstract. The work presents the study results of the determination of the resistance of neodymium zirconate doped with MgO and Y₂O₅ to radiation damage stemming from irradiation with heavy ions akin to nuclear fuel fission fragments. The attraction towards this type of ceramics stems from its potential to raise the operational temperatures within the core of next-generation nuclear reactors. This is owed to its superior thermal conductivity when compared to zirconium dioxide, coupled with the heightened strength parameters that signify the ceramics' resistance against external factors. The main results of this study are to determine the influence of the formation of substitution or interstitial phases when adding magnesium and yttrium oxides to the composition, on increasing the stability of the strength and thermophysical parameters of neodymium zirconate to the radiation defects accumulation in the damaged surface layer. During the studies, it was found that the formation of impurity phases in the form of MgO inclusions (when it is added to the composition) and a substitution phase of the Y₂Zr₂O₇ type (with the addition of Y₂O₅) results in an elevation in the hardness and crack resistance stability of neodymium zirconate ceramics, which indicates the positive effect of doping linked to the formation of additional interphase boundaries that prevent strain embrittlement of the damaged layer under high-dose irradiation. During determination of the thermophysical parameters of the studied neodymium zirconate ceramics, it was observed that the formation of interphase boundaries during doping not only enhances thermal conductivity but also mitigates the decline in the thermal conductivity coefficient during irradiation for two-phase ceramics in comparison with undoped neodymium zirconate ceramics.

Keywords: neodymium zirconate, doping, increasing stability, radiation defects, hardening, thermophysical parameters.

1. Introduction

The main problems in the energy sector today are the need to transition from hydrocarbon raw materials to alternative energy sources, in order to reduce not only harmful emissions from the combustion of hydrocarbons, but also to reduce the production of deposits, leading to the depletion of natural resources [1,2]. Recently, there has been significant focus on advancing nuclear and thermonuclear energy technologies to bolster their contribution to energy production from alternative sources. Specifically, efforts

have been directed towards exploring new technological solutions aimed at enhancing the efficiency of nuclear power plants and increasing the burnup rate of nuclear fuel, thereby potentially reducing fuel consumption [3,4]. Simultaneously, a considerable portion of research in this realm is dedicated to devising technological solutions associated with the potential utilization of weapons-grade plutonium as a fissile nuclear material, as well as creation of new fuel elements, which are dispersed ceramic materials, which are assemblies of inert material with fissile nuclear material placed in it [5,6]. The focus on this type of fuel materials (with a dispersed matrix) primarily stems from the potential for containing high neutron densities, which are planned to be used in new types of nuclear reactors (Gen IV generation) [7,8], as well as the possibility of operating this fuel at elevated temperatures (about 700 – 1000 °C). Also, one of the advantages of the transition from the traditional type of fuel rods to dispersed materials is the possibility of creating fuel rods of various shapes and configurations (in the shapes of cylinders, balls, plates, rings, etc.). Also, an unimportant factor when choosing materials for creating inert matrices of dispersed nuclear fuel is the indicator of resistance to radiation damage, in particular, the ability to contain the decay products and fission of fissile nuclear material, which is a necessary condition for increased operating life of nuclear reactors [9]. In most cases, when opting for inert matrices for dispersed nuclear fuel, preference is given to refractory oxide materials [10-12]. The amalgamation of their structural, strength, and thermophysical attributes enables the development of high-strength, radiation-resistant materials capable of withstanding elevated temperatures and substantial radiation doses. Particular attention in this area of research is paid to zirconium-containing materials or zirconates [13-15], the use of which is attributed to high strength characteristics, and low thermal expansion values, which makes it possible to increase the stability of materials during their operation at high temperatures.

The use of ceramics based on zirconates of the $Ln_xZr_2O_7$ type (Ln is a rare earth element) as structural materials in nuclear energy stems from the potential to utilize them as thermal barrier materials, inert matrices of dispersed nuclear fuel, as well as to create containers for disposal and long-term storage of nuclear waste [16-20]. Moreover, the main advantages of these ceramic types (meaning zirconates containing rare earth elements) are high strength indicators (hardness, crack resistance, resistance to mechanical stress), and thermophysical parameters (higher thermal conductivity compared to zirconium dioxide-based ceramics) [15-17]. One of the ways to increase the stability of zirconate-based ceramics is to use methods of alloying or doping with stabilizing additives in the form of oxides of magnesium, cerium or yttrium, the addition of which in certain proportions allows the formation of substitution or interstitial phases in the structure of the ceramics, which in turn results in the appearance of interphase boundaries and an increase in dislocation density. This method of increasing the stability of materials relies on the possibility of creating additional boundary effects linked with the formation of interstitial phases (in the form of simple oxides) or substitution phases (when the main elements are replaced by dopants, resulting in the formation of inclusions in the form of new phases). In this case, the presence of interphase boundaries results in the creation of additional barriers, thereby augmenting resistance to radiation embrittlement, due to the inability of some of the resulting defects to agglomerate into larger inclusions within the damaged layer. These effects of interphase boundaries, along with dimensional factors that determine changes in dislocation density, are one of the most effective ways to increase the radiation damage resistance of ceramics, alongside to increase the service life and stability of strength and thermophysical parameters under high-dose irradiation. However, in most cases, the use of different concentrations of dopants can lead to both positive effects associated with strengthening and increasing the stability of ceramics due to interphase boundaries and dislocation strengthening, and negative effects due to the acceleration of polymorphic or phase transformation processes because of external factors. In this connection, the use of this modification method requires a detailed study and determination of the strengthening mechanisms linked to alterations in ceramic properties during doping. Given the foregoing, the primary objective of this investigation is to examine the impact of adding magnesium and yttrium oxides to the composition of neodymium zirconate ($Nd_2Zr_2O_7$) ceramics to enhance the stability of strength and thermophysical parameters under high-dose irradiation with heavy Xe^{23+} ions, commensurate in energy to fission fragments of nuclear fuel.

2. Materials and research methods

For the synthesis of ceramics, Nd_2O_3, ZrO_2, MgO, Y_2O_5 oxides, acquired from Sigma Aldrich (Sigma, USA) were used. The chemical purity of the oxides used was about 99.95%. The synthesis of $Nd_2Zr_2O_7$ ceramics was carried out using the method of mechanical activation (mechanical grinding), by mixing the

initial oxides in a given stoichiometric molar ratio of 1:1 Nd_2O_3 and ZrO_2 oxides. Mechanical activation was carried out using a planetary mill PULVERISETTE 6 (Fritsch, Berlin, Germany) under the following grinding conditions - 250 rpm for 30 minutes. The choice of these conditions was used to obtain powders that were homogeneous in composition, which were subsequently subjected to heat treatment at a temperature of 1200 °C. Doping with oxides of magnesium (MgO) and yttrium (Y_2O_3) was carried out by adding them in a molar ratio of 0.15 M from the total volume of the resulting components Nd_2O_3 and ZrO_2 when mixing them for mechanical activation.

Determination of the effect of variation in the type of dopant on the alteration in the phase composition of the studied $Nd_2Zr_2O_7$ ceramics was conducted using the X-ray phase analysis method, the results in the form of a set of X-ray diffraction patterns of which are presented in Figure 1. The data were obtained using a D8 ADVANCE ECO X-ray diffractometer (Bruker, Karlsruhe, Germany). Diffraction patterns were recorded in the Bragg – Brentano mode in the angular range from 20 to 80°, with a step of 0.03°. The phase composition with variations in the dopant (in the case of magnesium and yttrium oxides) was determined by comparing the positions of the diffraction reflections of experimentally obtained diffraction patterns with the data of reference values from the PDF-2(2016) database. According to X-ray phase analysis of ceramic samples, it was found that the dominant phase in the composition of ceramics is the cubic phase $Nd_2Zr_2O_7$ (PDF-01-074-8769) with a pyrochlore-type structure and crystal lattice parameters a=10.5702 Å. Moreover, the position of the diffraction lines and their intensity indicate the absence of any clearly expressed textural effects that are uncharacteristic of structural alterations linked to phase transformations during high-temperature sintering.
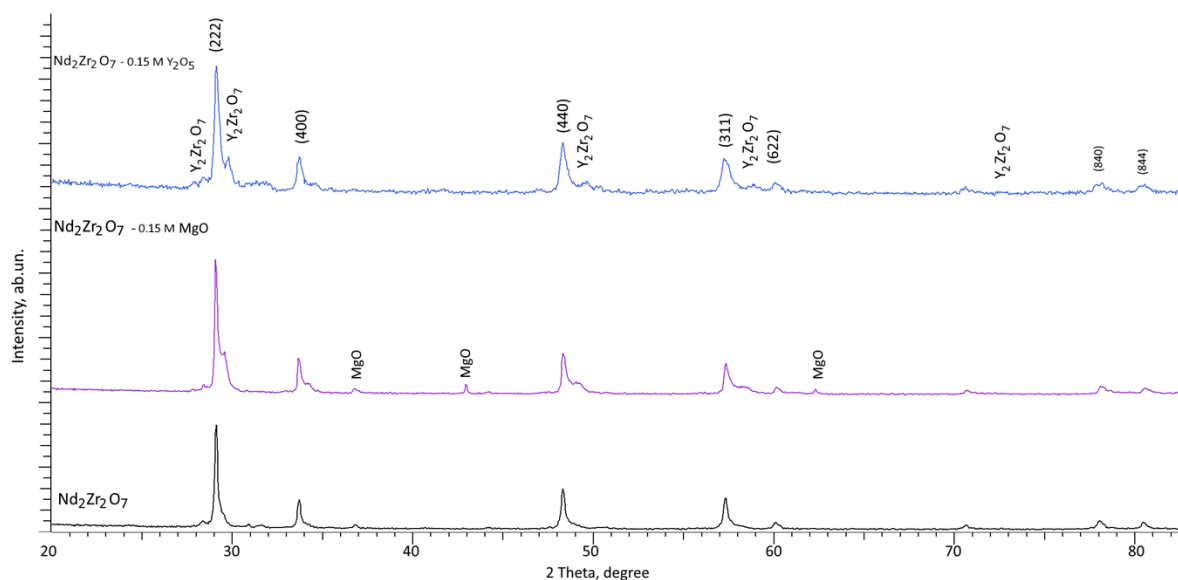
Fig.1. X-ray phase analysis results of the studied $Nd_2Zr_2O_7$ ceramics in the initial state and doped with magnesium and yttrium oxides

In the case of adding MgO to the $Nd_2Zr_2O_7$ ceramics composition in a molar ratio of 0.15 M, according to the obtained X-ray diffraction patterns, the appearance of low-intensity diffraction reflections characteristic of the hexagonal MgO phase (PDF-01-080-4185) with crystal lattice parameters a=3.4785 Å, c=4.2082 Å is observed, the content of which in the ceramic composition is no more than 15 wt. %. Also, an assessment of the structural parameters of the main (dominant) phase of $Nd_2Zr_2O_7$, which amounted to a = 10.6157 Å, indicates an increase in parameters, which is associated with the effects of replacing neodymium or zirconium ions with magnesium ions in the cubic lattice of the main phase. In turn, the formation of the MgO impurity phase causes the effect of strengthening and structural ordering (the crystallinity degree grows approximately by 2 – 3 % for doped ceramics). For samples of $Nd_2Zr_2O_7$ ceramics doped with Y_2O_5, according to X-ray diffraction analysis data, in addition to the main reflection characteristic of the cubic Y_2O_3 phase, the formation of reflections characteristic of the cubic substitution phase $Y_2Zr_2O_7$ is observed, the weight contribution of which is about 12.5 wt. %. The crystal lattice parameters for the $Nd_2Zr_2O_7$ phase were a=10.6604 Å, for the $Y_2Zr_2O_7$ phase a=5.2162 Å.

Determination of the effect of modification of $Nd_2Zr_2O_7$ ceramics by doping them with magnesium and yttrium oxides on resistance to radiation damage was carried out by irradiating the ceramic samples under study with heavy Xe^{23+} ions with an energy of 230 MeV (1.75 MeV/nucleon). Irradiation was carried out at the DC-60 heavy ion accelerator (Institute of Nuclear Physics, Astana Branch, Astana, Kazakhstan). Irradiation fluences with Xe^{23+} ions ranged from 10^{11} ion/cm^2 to 5×10^{14} ion/cm^2, the choice of which was determined by the possibility of simulation of the radiation damage accumulation processes, both in the case of the formation of isolated defective areas at low irradiation fluences, and the effects of overlapping defective areas during high-dose irradiation, in which case the effect of the appearance of highly deformed areas with locally altered electron density occurs.

Figure 2 demonstrates the simulation results of the ionization losses of incident Xe^{23+} ions in a near-surface layer with a thickness of about 15 μm of $Nd_2Zr_2O_7$ ceramics, alongside the dependence of the variation in the atomic displacement values (dpa) along the trajectory of ion movement into the ceramics with varying irradiation fluence. The dependence of the change in the values of ionization losses during interaction with electron shells ($dE/dx_{electron}$) and nuclei ($dE/dx_{nuclear}$) reflects the influence of the processes of interaction of incident particles and energy losses along the ion motion trajectory. Based on the provided data, at a depth of 0 to 9 – 10 μm, the dominant role in interaction processes is played by ionization processes during collisions with electrons due to electron–phonon interactions, and as a consequence, the emergence of energy dissipation effects through thermal heating of locally isolated regions along the ion trajectory. Moreover, these processes in the case of dielectric ceramics can compete with the processes of formation of defects, their thermal relaxation and ionization, which subsequently initiates the so-called athermal effects associated with thermally induced deformation processes.

Simultaneously, within a penetration depth of ions ranging from 9 to 15 μm, the primary influence stems from the processes of elastic interaction between ions and nuclei. These interactions result in the generation of atomic displacement effects (dpa), the accumulation of which contributes to amplified deformation distortions within the damaged layer (refer to Figure 2b). Moreover, the obtained relationships depicting alterations in the values of $dE/dx_{electron}$ and $dE/dx_{nuclear}$ closely align with the findings of [21,22], according to which, during irradiation with heavy ions, the main role in changing the properties of materials is played by the interactions of ions with electrons, for which the value of ionization electron losses is an order of magnitude greater than nuclear losses.

a)   b)
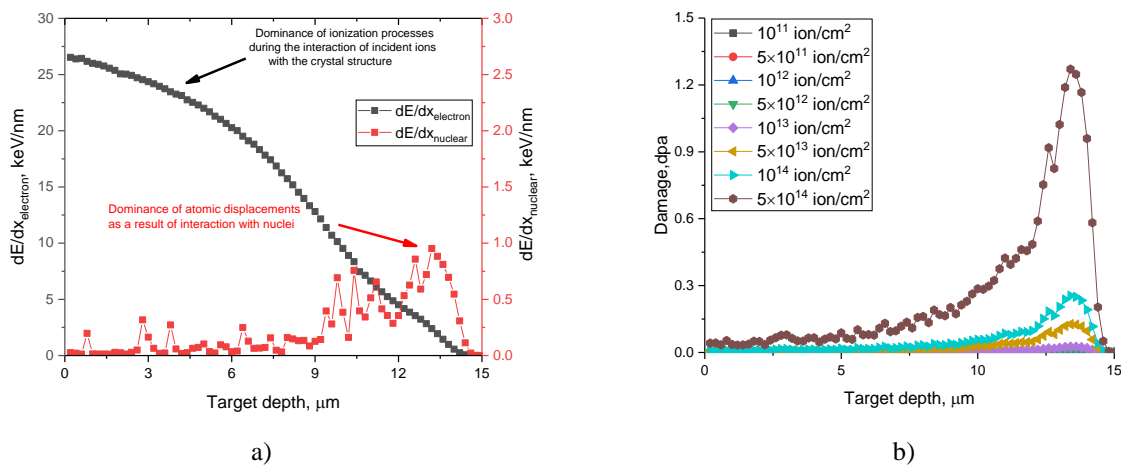
Fig.2. a) Simulation results of ionization losses along the ion movement trajectory in $Nd_2Zr_2O_7$ ceramics;
b) Distribution profile data of atomic displacement values (dpa) along the trajectory of ions in ceramics

The obtained results of changes in the values of atomic displacements (in particular, the maximum values of dpa values), presented in Figure 2b, were subsequently used in assessing the influence of variations in irradiation fluence on changes in strength and thermophysical parameters.

To determine the strength characteristics, the indentation method was used, implemented on a Duroline M1 microhardness tester (Metkon, Bursa, Turkey). The measurements were carried out using a tetrahedral Vickers pyramid with an angle of 136° between opposite faces, by loading the indenter with 100 N for 15 seconds, after which the indent sizes were estimated and the hardness values were determined. Determination of softening factors was carried out by comparative analysis of hardness values in the initial

state and after irradiation. The average hardness value was determined by measuring about 10 - 15 surface indentations, followed by determining the hardness values and standard deviation.

Determination of changes in thermophysical parameters depending on the modification type (with doping with magnesium and yttrium oxides), as well as upon irradiation of ceramics with heavy ions, was conducted using the longitudinal heat flow method, which consists in establishing the temperature difference on both sides of the sample when it is heated. The measurements were carried out using a thermal conductivity meter KIT-800 (KB Teplofon, Russia). The stability of thermophysical parameters to radiation damage during irradiation with heavy ions was assessed by comparing data on the thermal conductivity coefficient in the initial state and after irradiation. Moreover, the obtained dependences of heat losses on the atomic displacement values during irradiation were used to describe the mechanisms for reducing the thermophysical parameters of ceramics, alongside to determine the effect of doping with magnesium and yttrium oxides on increasing stability and resistance to radiation degradation.

3. Results and discussion

In the case of choosing materials for creating inert matrices of dispersed nuclear fuel, much attention, as a rule, is paid to the study of their strength and thermophysical parameters, which are one of the key criteria in the selection of materials used in extreme conditions. In this case, a variation in the concentration of accumulated defects during irradiation, especially during high-dose irradiation, can have a significant impact on the change in strength parameters due to softening effects linked to the accumulation of deformation distortions and local defective inclusions. In this case, knowledge of the mechanisms of changes in strength and thermophysical parameters depending on the structural disorder degree or the atomic displacement value is necessary when determining the potential for using new types of ceramics as materials of inert matrices. Thus, Figure 3a demonstrates the results of alterations in the ceramics' surface layer hardness, measured contingent upon the value of atomic displacements caused by irradiation with heavy ions. Also shown in Figure 3b are the comparative analysis results of the alteration in the softening value (ΔHV), which characterizes the decrease in hardness contingent upon the degree of accumulation of atomic displacements.

Based on the evaluation data of the strength parameters of the studied $Nd_2Zr_2O_7$ ceramics, in the case of the original ceramics the hardness value is 563 ± 12 HV, for $Nd_2Zr_2O_7$ ceramics doped with MgO it is 824 ± 15 HV, for $Nd_2Zr_2O_7$ ceramics doped with Y_2O_5 it is 846 ± 11 HV. The strengthening factor for $Nd_2Zr_2O_7$ doped ceramics was about $46 - 50$ % compared to undoped ceramics, which indicates a positive effect of the formation of interphase boundaries on increasing the stability and strength of ceramics.

a)   b)
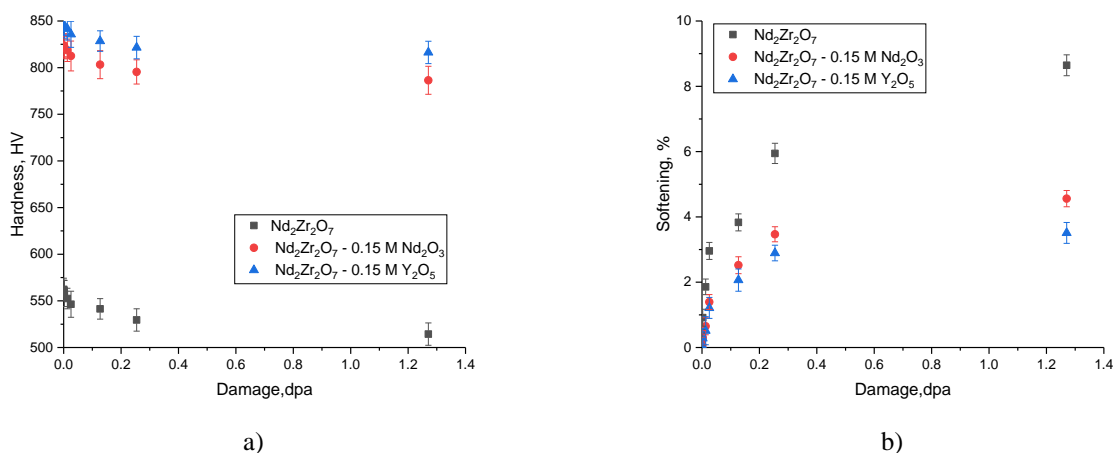
Fig.3. a) Results of alterations in ceramic hardness values contingent upon the atomic displacement values; b) Results of alterations in the softening degree

The overall trend observed in the alterations of hardness, contingent on the atomic displacement value, suggests the detrimental effect of accumulated structural changes induced by irradiation on the strength characteristics of the examined $Nd_2Zr_2O_7$ ceramics. Moreover, significant changes in hardness (about 1-2 %) for unmodified $Nd_2Zr_2O_7$ ceramics are observed at irradiation fluences of the order of 5×10^{12} ion/cm^2, while for modified $Nd_2Zr_2O_7$ ceramics similar changes are observed at fluences above 10^{13} ion/cm^2. Such

differences in hardness reduction trends are primarily due to the presence of interphase boundaries in $Nd_2Zr_2O_7$ modified ceramics, the presence of which results in an increase not only in the initial hardness values by more than 1.5 times, but also a rise in resistance to embrittlement processes during the accumulation of structurally deformed inclusions in the near-surface damaged layer. In the case of an increase in irradiation fluence above 10^{13} ion/cm^2 for unmodified $Nd_2Zr_2O_7$ ceramics, the reduction in hardness, and as a consequence, the amount of softening is about 6-8.5%, while for modified $Nd_2Zr_2O_7$ ceramics, the maximum decrease in hardness is less than 5 %. It is worth mentioning that the formation of two-phase ceramics of the $Y_2Zr_2O_7/Nd_2Zr_2O_7$ type results in an enhanced resistance to softening in comparison with $MgO/Nd_2Zr_2O_7$ ceramics (the value of the softening factor in this case at the maximum irradiation fluence is about 3.5 %).

The observed effects of strengthening, as well as increasing resistance to embrittlement and softening under high-dose irradiation in the case of modified ceramics, reflect the positive effect of the use of dopants in the form of magnesium and yttrium oxides on increasing resistance to radiation-stimulated softening. Figure 4 demonstrates the results of changes in the thermophysical parameters of the studied $Nd_2Zr_2O_7$ ceramics (in the original state and doped with magnesium and yttrium oxides), reflecting the effect of irradiation on a decrease in thermal conductivity with the accumulation of structural damage (with an irradiation fluence growth). In the case of the initial samples, it is clearly seen that modification of $Nd_2Zr_2O_7$ ceramics by adding dopants in the form of MgO or Y_2O_5 results in the thermal conductivity coefficient growth from 2.15 W/(m×K) to 3.8 – 3.9 W/(m×K), which indicates the positive effect of modification of $Nd_2Zr_2O_7$ ceramics, which was also proven when assessing changes in strength parameters.

According to the presented data on changes in the value of the thermal conductivity coefficient depending on the magnitude of atomic displacements, it can be concluded that the most pronounced changes associated with a decrease in thermophysical parameters appear at irradiation fluences above 10^{13} ion/cm^2, which, according to the data of [23, 24], are characterized by the presence of effects associated with the overlap of local structurally deformed areas, leading to a destructive change in the damaged layer. At lower irradiation fluences (for which the dpa value is less than 0.1), alterations in the thermal conductivity coefficient are less than 0.6 – 0.7 %. Moreover, the most pronounced alterations in the thermal conductivity coefficient are observed for samples of undoped $Nd_2Zr_2O_7$ ceramics, for which the maximum decrease in the thermal conductivity coefficient is about 4.9 – 5.0 %, which is more than 1.5 – 2 times greater than similar changes for doped $Nd_2Zr_2O_7$ ceramics (refer to Figure 4b). It is also worth to note that the most pronounced changes observed with an irradiation fluence growth above 10^{13} ion/cm^2 have a clear trend of accelerating the degradation of thermophysical parameters at large degrees of accumulated atomic displacements, which indicates that the decrease in thermophysical parameters has a clear dependence on the concentration of structurally deformed inclusions in the surface layer.

a)   b)
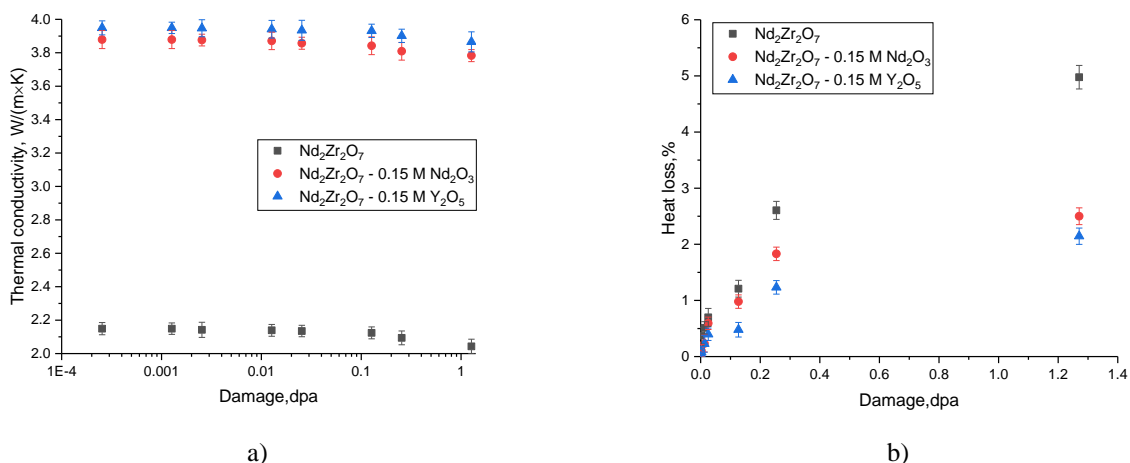
Fig.4. a) Results of a decrease in the thermal conductivity of ceramics contingent upon the irradiation fluence; b) Assessment results of heat loss in samples during the accumulation of structural damage

This change is primarily associated with phonon mechanisms of heat transfer in ceramics, the change of which is influenced by the number of scattering factors linked to the accumulation of deformed regions, leading to an elevation in phonon scattering and thereby reducing the rate of heat transfer. At the same time,

analysis of the obtained data on changes in thermophysical parameters indicates that when interphase boundaries associated with impurity inclusions are formed in $Nd_2Zr_2O_7$ ceramics, the observed decrease in thermal conductivity due to increased heat losses is significantly less than in undoped $Nd_2Zr_2O_7$ ceramics. This change in the trend of decreasing thermophysical parameters for modified ceramics can be explained by effects linked to a rise in structural ordering during the formation of interphase boundaries, which leads to heightened resistance to softening and degradation of thermophysical parameters. When using this type of ceramics as inert matrices of dispersed nuclear fuel, the obtained dependences of changes in thermophysical parameters depending on the irradiation dose make it possible to predict the critical service life, as well as the necessary adjustments when using them. Moreover, the data acquired regarding the impact of dopants, specifically magnesium and yttrium oxides, in enhancing resistance against deterioration in thermophysical and strength parameters in irradiated samples, can be valuable for selecting this type of ceramics as inert matrices with high radiation resistance. This is attributed to the presence of interphase boundaries. However, when considering the possibility of using this type of ceramics as materials for creating thermal insulating barriers during the storage of spent nuclear fuel, the observed thermal conductivity reduction patterns of irradiated ceramics allow us to consider these materials as one of the promising thermal insulators for long-term storage of spent fuel. In this case, the spontaneous decay of fissile material of spent fuel during long-term storage is accompanied by the formation of radiation defects, alongside heating of the container material, which in the case of ceramics with low thermal conductivity (which also decreases with the radiation damage accumulation in the irradiated material) allows one to avoid the effect of internal heating of the containers.

4. Conclusion

Analyzing the obtained experimental data related to determining the effect of irradiation with heavy Xe^{23+} ions on the decrease in strength and thermophysical parameters, the following conclusions can be drawn. During the studies, it was observed that for $Nd_2Zr_2O_7$ ceramics, the maximum value of the hardness reduction at fluences over 5×10^{13} ion/cm^2 is more than $6 - 8$ %, which in turn indicates that the absence of interphase boundaries characteristic of $Nd_2Zr_2O_7$ doped ceramics results in a more pronounced deterioration in strength properties. In the case of ceramics doped with $Nd_2Zr_2O_7$, the presence of interphase boundaries leads to strengthening by more than $1.5 - 2$ times at maximum irradiation fluence, which indicates the softening rate reduction and higher stability of modified $Nd_2Zr_2O_7$ ceramics due to doping. During assessment of changes in the thermophysical parameters of the studied $Nd_2Zr_2O_7$ ceramics depending on the type of modifier used, a decrease in the deterioration trend in the thermal conductivity coefficient under high-dose irradiation was established, which is associated with increased resistance to structural disorder of the modified ceramics.

References

1   Davies A., Simmons M. D. (2021) Demand for 'advantaged'hydrocarbons during the 21st century energy transition. *Energy Reports*. 7, 4483-4497. DOI: 10.1016/j.egyr.2021.07.013.
2   Stančin H., Mikulčić H., Wang X., Duić N. (2020) A review on alternative fuels in future energy system. *Renewable and sustainable energy reviews*. 128, 09927. DOI: 10.1016/j.rser.2020.109927.

3   Lorusso P., Bassini S., Del Nevo A., Di Piazza I., Giannetti F., Tarantino M., Utili M. (2018) GEN-IV LFR development: status & perspectives. *Progress in Nuclear Energy*. 105, 318-331. DOI: 10.1016/j.pnucene. 2018.02.005.

4   Yan X.L. (2023). Very High Temperature Reactor. In *Handbook of Generation IV Nuclear Reactors*. *Woodhead Publishing*. 133-165. DOI:10.1016/B978-0-12-820588-4.00009-8.

5   Restani R., Martin M., Kivel N., Gavillet D. (2009) Analytical investigations of irradiated inert matrix fuel. *Journal of nuclear materials*, *385*(2), 435-442. DOI: 10.1016/j.jnucmat.2008.12.030.

6   Lombardi C., Luzzi L., Padovani E., Vettraino F. (2008) Thoria and inert matrix fuels for a sustainable nuclear power. *Progress in Nuclear Energy*. 50 (8), 944-953. DOI: 10.1016/j.pnucene. 2008.03.006.

7   Kelly J.E. (2014) Generation IV International Forum: A decade of progress through international cooperation. *Progress in Nuclear Energy*. 77, 240-246. DOI: 10.1016/j.pnucene.2014.02.010.

8   Zohuri B. (2020) Generation IV nuclear reactors. Nuclear reactor technology development and utilization. *Woodhead Publishing*. 213-246. DOI: 10.1016/B978-0-12-818483-7.00006-8.

9   Hellwig C., Streit M., Blair P., Tverberg T., Klaassen F.C., Schram R.P.C., Yamashita T. (2006) Inert matrix fuel behaviour in test irradiations. *Journal of nuclear materials*. 352 (1-3), 291-299. DOI:10.1016/j.jnucmat. 2006.02.065.

10   Restani R., Martin M., Kivel N., Gavillet D. (2009) Analytical investigations of irradiated inert matrix fuel. *Journal of nuclear materials*. 385 (2), 435-442. DOI:10.1016/j.jnucmat. 2008.12.030.

11   Frieß F., Liebert W. (2022) Inert-matrix fuel for transmutation: Selected mid-and long-term effects on reprocessing, fuel fabrication and inventory sent to final disposal. *Progress in Nuclear Energy*. 145, 104106. DOI:10.1016/j.pnucene.2021.104106.

12   Ledergerber G., Degueldre C., Heimgartner P., Pouchon M. A., Kasemeyer U. (2001) Inert matrix fuel for the utilisation of plutonium. *Progress in Nuclear Energy*. 38 (3-4), 301-308. DOI:10.1016/S0149-1970(00)00122-0.

13   Nuritdinov I., Tashmetov M.Yu, Khodzhaev U.O., Umarov S.Kh., Khallokov F.K. (2024). Influence of electron irradiation on the crystal structure, surface microrelief and bandganp width of the triple crystals of iron doped monoselinide of thallium and indium. *Eurasian Physical Technical Journal*, *20*(4(46), 23–32. DOI:10.31489/2023No4/23-32.

14   Degueldre C., Pouchon M., Döbeli M., Sickafus K., Hojou K., Ledergerber G., Abolhassani-Dadras S.(2001) Behaviour of implanted xenon in yttria-stabilised zirconia as inert matrix of a nuclear fuel. *Journal of nuclear materials*. 289 (1-2), 115-121. DOI:10.1016/S0022-3115(00)00690-5.

15   Arima T., Yamasaki S., Torikai S., Idemitsu K., Inagaki Y., Degueldre C. (2005) Molecular dynamics simulation of zirconia-based inert matrix fuel. *Journal of alloys and compounds*. 398 (1-2), 296-303. DOI:10.1016/j.jallcom.2005.02.041.

16   Pan W., Xu Q., Qi L.H., Wang J.D., Miao H.Z., Mori K., Torigoe T. (2004) Novel low thermal conductivity ceramic materials for thermal barrier coatings. *Key Engineering Materials*. 280, 1497-1500. DOI:10.4028/www.scientific.net/KEM.280-283.1497.

17   Popov V.V., Menushenkov A.P., Ivanov A.A., Gaynanov B.R., Yastrebtsev A.A., d'Acapito F., Ponkratov K.V. (2019) Comparative analysis of long-and short-range structures features in titanates $Ln_2Ti_2O_7$ and zirconates $Ln_2Zr_2O_7$ (Ln= Gd, Tb, Dy) upon the crystallization process. *Journal of Physics and Chemistry of Solids*. 130, 144-153. DOI:10.1016/j.jpcs.2019.02.019.

18   Shlyakhtina A.V., Belov D.A., Knotko A.V., Kolbanev I.V., Streletskii A.N., Karyagina O.K., Shcherbakova L.G. (2014) Oxygen interstitial and vacancy conduction in symmetric Ln $2\pm x$ Zr $2\pm x$ O $7\pm x/2$ (Ln= Nd, Sm) solid solutions. *Inorganic Materials*. 50, 1035-1049. DOI:10.1134/S002016851410015X.

19   Moudir D., Kamel Z., Ait-Amar H. (2013) Synthesis and characterization of a neodymium zirconate pyrochlore doped with ytterbium:(YbxNd1-x) 2Zr2O7 (x=0.1, 0.25 and 0.4). *Journal of Materials Science and Engineering. B*. 3 (1B), 1-10. DOI: 55b84d5aac700.

20   Park S., Tracy C.L., Zhang F., Park C., Trautmann C., Tkachev S.N., Ewing R.C. (2018) Radiation-induced disorder in compressed lanthanide zirconates. *Physical Chemistry Chemical Physics*. 20(9), 6187-6197. DOI:10.1039/C7CP08664D.

21   Weber W.J., Duffy D.M., Thomé L., Zhang Y. (2015) The role of electronic energy loss in ion beam modification of materials. *Current Opinion in Solid State and Materials* Science. 19(1), 1-11. DOI:10.1016/j.cossms.2014.09.003.

22   Zhang Y., Egami T., Weber W.J. (2019) Dissipation of radiation energy in concentrated solid-solution alloys: Unique defect properties and microstructural evolution. *Mrs Bulletin*. 44 (10), 798-811. DOI:10.1557/mrs.2019.233.

23   Van Vuuren A.J., Ibrayeva A.D., O'Connell J.H., Skuratov V.A., Mutali A., Zdorovets M.V. (2020) Latent ion tracks in amorphous and radiation amorphized silicon nitride. *Nuclear Instruments and Methods in Physics Research Section B: Beam Interactions with Materials and Atoms*. 473, 16-23. DOI:10.1016/j.nimb.2020.04.009.

24   Van Vuuren A.J., Ibrayeva A., Rymzhanov R.A., Zhalmagambetova A., O'connell J.H., Skuratov V.A., Zdorovets M. (2020) Latent tracks of swift Bi ions in Si3N4. *Materials Research Express*. 7(2), 025512. DOI:10.1088/2053-1591/ab72d3.

AUTHORS' INFORMATION

Kozlovskiy, Artem Leonidovich – PhD (Phys.), Associate Professor, Head of the Laboratory of Solid-State Physics, Astana branch of the Institute of Nuclear Physics; Ministry of Energy of the Republic of Kazakhstan, Astana; Scopus Author ID: 55632118900; ORCID iD: 0000-0001-8832-7443; kozlovskiy.a@inp.kz

Kabiev, Mussa Bolatovich – PhD student, Department of Nuclear Physics, New Materials and Technologies, L.N. Gumilyov Eurasian National University, Astana, Kazakhstan; ORCID iD: 009-0007-9734-844X; kabiyevmussa@gmail.com

Shlimas, Dmitriy Igorevich – PhD, Teacher-researcher, Associate Professor, Department of Nuclear Physics, New Materials and Technologies, L.N. Gumilyov Eurasian National University, Astana, Kazakhstan; Scopus ID 5789516212, ORCID iD: 0000-0003-2454-7177; shlimas@mail.ru

Uglov, Vladimir Vasilevich – Doctor of Physical and Mathematical Sciences, Professor, Head of the Department of Solid State Physics and Nanotechnologies of the Belarusian State University, Minsk, Belarus; Scopus Author ID: 7005653968; ORCID iD: 0000-0003-1929-4996; uglov@bsu.by

.

UDC: 536.4

STUDY ON THE INFLUENCE OF RATING CHARGE ON TEMPERATURE AND PHASE BEHAVIOR OF STABILIZED MATRIX WAX-BASED THERMAL STORAGE

Rahman R.A.[1,2], Sulistyo[1]*, Utomo M.S.K.T.S.[1], Febriansyah I.[2]

[1] Department of Mechanical Engineering, Universitas Diponegoro, Semarang, Indonesia
[2] Department of Mechanical Engineering, Faculty of Engineering, Universitas Pancasila, DKI Jakarta, Indonesia
*Corresponding author: sulistyo@lecturer.undip.ac.id

Abstract. The rating charge characteristic is crucial for the heat energy storage, particularly for low-temperature system which uses paraffin wax. The influence of different rating charge causes severe temperature fluctuation, which is undesirable for the heat system. It is affected by unstable phase transformation, reducing the heat distribution and makes the average rating charge insufficient. In this work, the fluctuation can be minimized by adding polyethylene plastic as phase stabilizer for the wax. The polyethylene is added by ratio of weight of 15% from the total mass of 134 grams. Each material is mixed in the liquid state, stirred and molded into the apparatus. The phase transition evaluation is performed, showing the mixture indicates an additional transition peak after the principal phase transformation, ranging between 15.26 °C – 19.34 °C (melting) and 11.98 °C – 9.45 °C (freezing). The steady operation makes the lowest rating variation is only 0.3 °C/min, which is obtained by the mixture of wax and polyethylene. In the same rating charge, the wax has rating variation of 2.9 °C/min, signifying the effect of unsteady melting transition. It clearly demonstrates the addition of polyethylene for the mixture promotes a better phase transformation under various rating charge, maintaining the effective temperature distribution for the heat storage.

Keywords: decomposition, rating charge, hydrocarbon, melting, solidification, polymer.

1. Introduction

The provision of clean and sustainable energy is a global topic due to the urgency of mitigating the energy crisis. A short mitigation effort is done through reutilization of the old oil well [1]. At the same effort, various concepts of harvesting energy from different sources are developed extensively. For example, the utilization of waste is proven as a reliable solution to obtain alternative fuel and also reducing the waste issue in society [2]. The development is also supported in the technological aspect, including the research in the burner system to provide alternative thermal energy through the combustion of the alternative fuel. Thermal load is taken as one of the highest global energy consumptions. It can be solved through the utilization of solar thermal system [3]. The system is supported by heat storage device (HSD) [4], making it possible to store the excess energy production in the daytime and released it when required in the nighttime [5].

The HSD is considered as a cost-effective energy storage, since the energy can be discharged directly to thermal load [6]. It reduces significantly the need for electric energy for heating systems. The HSD works by storing the heat through the material within the system, preferably solid-liquid storage material (SLSM), which has a higher storage density [7]. One good example of solar thermal utilization is solar drying.

Alkahdery L.A. [8], studied improvement of the solar drying system which used additional heat source, implying a better drying mechanism and higher temperature within the chamber. The system can be supported using HSD to promote a continuous drying in the nighttime. It makes the improvement of alternative energy can be maximized, since it combines several power sources to drive the energy exchange within the system [9]. Thus, HSD is potentially applied in various solar thermal system, which is expected to accelerate the energy mix from solar source.

One crucial problem related with the SLSM in an HSD is poor heat exchange rate due to low conductivity. S.A. Abtahi Mehrjardi et al. [10], optimizes the HSD system using fins for accelerating the average heat transfer within the system. It shows the suitable configuration of fin spacing and angle which allows to improve the conduction and convection heat transfer within the system. W. Cui et al. [11], utilize nanoparticles and ultrasonic fields to improve the average time processing within the system. The result demonstrates a notable achievement for the time reduction of the system up to 46.5%. B. Brahma et al. [12], proposed a combined air heater system with HSD. The proposed method utilizes SLSM from paraffin wax (Pw) which has the highest solar absorption rate of about 36.56 kW. The optimization provides a better heat exchange rate for the HSD system. The high heat exchange rate leads to an acceleration of rating charge (RC) within the system. H. Hosseininaveh et al. [13], analyzed the charge/discharge cycle for Pw-based HSD using intermediate boiling fluid, indicating the melting transition was followed by various temperature increment within the system. Z. Zhang et al. [14], performed an analysis of SLSM for building, showing the high temperature fluctuation in the charge process which highly affected by the rating convective heat transfer rate from air. D.S. Mehta et al. [15], demonstrated the uneven distribution of the temperature of the finned-HSD, showing each measured zone indicates different temperature rating during charge operation. The uneven temperature distribution is unsatisfactory which causes partial energy exchange [16], difficulty for determining the charge level [17], leading to extensive measurement for setting the charge controller [18].

The variation on the temperature of SLSM in an HSD is related with the molecular movement during energy exchange. Y. Du et al. [19], highlighted this aspect for thermal-conductivity enriched SLSM material, indicating the conduction path plays critical role in the energy transfer within the high rating charge system. To promote a steady temperature distribution, using an additional binder to the SLSM is suitable [20]. The proposed method also has a better safety factor which related to the mechanical strength of the modified SLSM [21]. M. He et al. [22], developed graphene aerogel (GA) as the matrix for Pw, indicating a good affirmation of the produced modified-Pw/GA. M. Zarrinjooy Alvar et al. [23], introduces monomer for Pw through impregnation and combined with graphite powder, allowing for a reliable performance both in stability and conductivity of the produced modified-Pw.

The additional matrix for the Pw can be obtained from various material, while polyethylene (PE) comes as the most suitable candidate considering its availability and cost [24]. The PE-based matrix is favorable for SLSM which promotes a steady phase-transformation of the SLSM. T. Al-Gunaid et al. [25], employed PE-low density (LD) with Pw for phase stabilization, demonstrating an excellent mechanical strength with an excellent ratio of stored/released energy. Another PE-class (high-density/HD) was also utilized for stabilization with nano-additives, showing a satisfactory mechanical and phase behavior [26]. However, characterization is generally concentrated for mechanical evaluation, with minimum evaluation on the effect of rating charge in the temperature profile. Thus, further work is required to address the effect of rating charge on the phase-transformation behavior and charge profile of the stabilized-SLSM.

The novelty from this work is a detailed temperature profile of the stabilized-SLSM under different RC. It aims to promote a better understanding on the effect RC on phase transformation of the stabilized-SLSM. Moreover, this study employs PE-LD and linear-LD (LLD) as phase stabilizer, which considered as one major component in plastic waste [27]. Thus, the finding is expected to improve the capability of HSD and offer additional consideration for waste reutilization. The assessment is focused through evaluation using low RC (LRC), medium RC (MRC) and high RC (HRC), providing a detailed result which can be used for developing suitable RC of an HSD.

2. Materials and Method

This work used Pw as the SLSM, while the matrix comes from polymer PE-LD and PE-LLD. The all-raw materials were obtained from local supplier, where the Pw has an average melting temperature of 60 °C. The polymers were used sheet-based structure in order to maximizing the mixing process. The preparation of

the sample was performed without causing any polymerization, which is the advantage of forming PE-based stabilized-SLSM (sSLSM). The sSLSM was produced following the direct melting method [28] to accommodate the solid-liquid transition between the SLSM and binders. The ratio of SLSM was 85% of its weight while the binder was set only 15%. It is aimed to maintain the total storage capacity of the mixture as recommended here [29]. Each component was melted at different temperature (80 °C for SLSM and 160 °C for LD and LLD). The molten binder was poured to the liquid SLSM, continuously stirred at the elevated temperature (140 °C) to ensure the homogeneity. A small portion of SLSM, sSLSM$_1$ (Pw/LD) and sSLSM$_2$ (Pw/LLD) were taken for thermal analyzing through calorimetry and thermogravimetric method. Then, the liquid was moved to the charge container for evaluating the temperature change under various RC (Fig. 1).
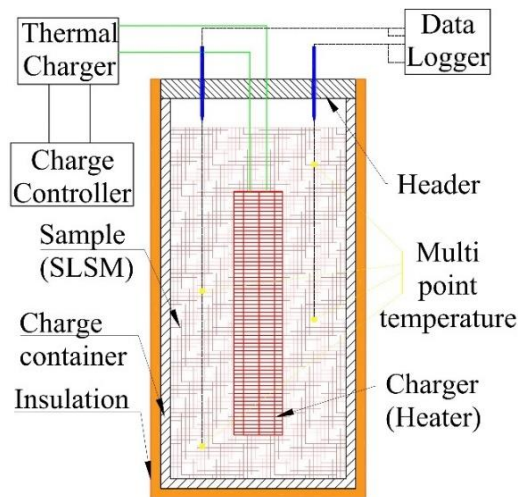
Fig.1. Charge evaluation for the SLSM and sSLSM

Fig. 1 shows the schematic of charge evaluation, which was adopted using temperature-history and temperature-energy method for a detailed assessment [30–32]. In this scenario, the liquid sample was placed within the charge container and four temperature sensors (K thermocouple) were located at the upper, middle (two sensor) and lower zone. The mass of sample was 134 grams, while direct contact heater (surface area of 673 mm^2 and diameter 9.5 mm) was placed and set precisely at the center point of the container. The charge controller was used to adjust the heating rate with three different powers: 30 Watts (LRC), 60 Watts (MRC) and 100 Watts (HRC). The charge profile then taken to determine the charge behavior for each sample.

3. Results and Discussions

The initial observation was taken for mapping the surface morphology using scanning electron microscope (SEM) of the SLSM to support the justification of unsteady phase behavior. The presented profile in Fig. 2a clearly signifies the effect of slow nucleation, causing wavy structure (yellow circle) where most of the solid interface stacked each other. The feature is caused by unfavorable crystallization rate which occurs in the liquid-solid transformation as the heat liberated from the SLSM [33]. It also potentially leads to void formation which causes unsuitable distribution of the solid SLSM within the tank. It can be seen notably in the Fig. 2b where some part of the surface is agglomerated (red square).

The direct decomposition is observed for the SLSM under thermogravimetric evaluation (Fig. 3). The curve indicates the evaporation of the compound occurs as a single process, which is started at temperature 220 °C until 365 °C. Contrary to that, the both sSLSM has two curves. The first curve corresponds to the decomposition of the SLSM, while the latter curve belongs to the matrix PE (LD and LLD). It indicates the sSLSM is formed as non-eutectic system, since the phase separation occurred at different temperature [34]. The higher decomposition temperature for the matrix PE makes the sSLSM more favorable in term of thermal stability, which is suitable for a higher temperature operation in HSD.

The impact of the matrix-PE within the sSLSM is observed distinctively since the temperature at this transition varies compared to the SLSM. Moreover, the melt transition for the sSLSM exhibit a longer temperature range, which is higher around 5.38 °C and 2.14 °C for sSLSM$_1$ and sSLSM$_2$, respectively. It seems the thermal behavior of PE-LD causes a longer melting transition.

a)   b)

Fig.2. Surface profile of the SLSM at magnification (a) 100 and (b) 500
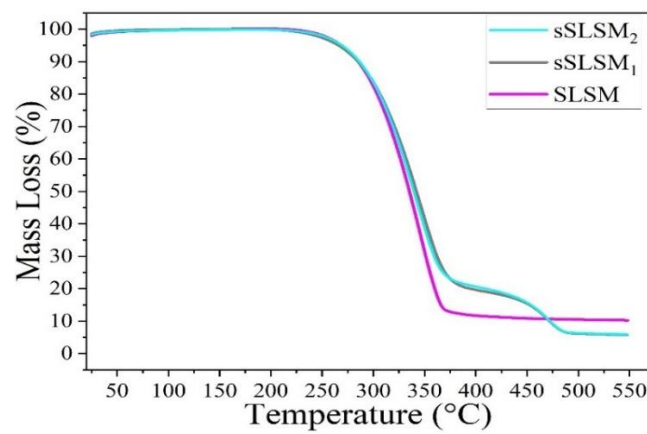
Fig.3. The mass loss behavior under thermal decomposition evaluation

There is one additional solid–liquid transition for the sSLSM. It occurs at temperature above 100 °C. Therefore, the physical characteristic for the sSLSM is immiscible. It makes the correspond substance melt separately. The change in thermal properties between SLSM and sSLSM can be analyzed in detail according to the its temperature transition. As seen in Fig. 4a, the SLSM has one significant characteristic which experiences solid-solid transition prior to melt. The process takes at higher temperature span, around 10.4 °C.

a)   b)

Fig.4. The detailed temperature transition for each sample during heating (a) and cooling (b) cycle

The impact of the matrix-PE within the sSLSM is observed distinctively since the temperature at this transition varies compared to the SLSM. Moreover, the melt transition for the sSLSM exhibit a longer temperature range, which is higher around 5.38 °C and 2.14 °C for sSLSM$_1$ and sSLSM$_2$, respectively. It seems the thermal behavior of PE-LD causes a longer melting transit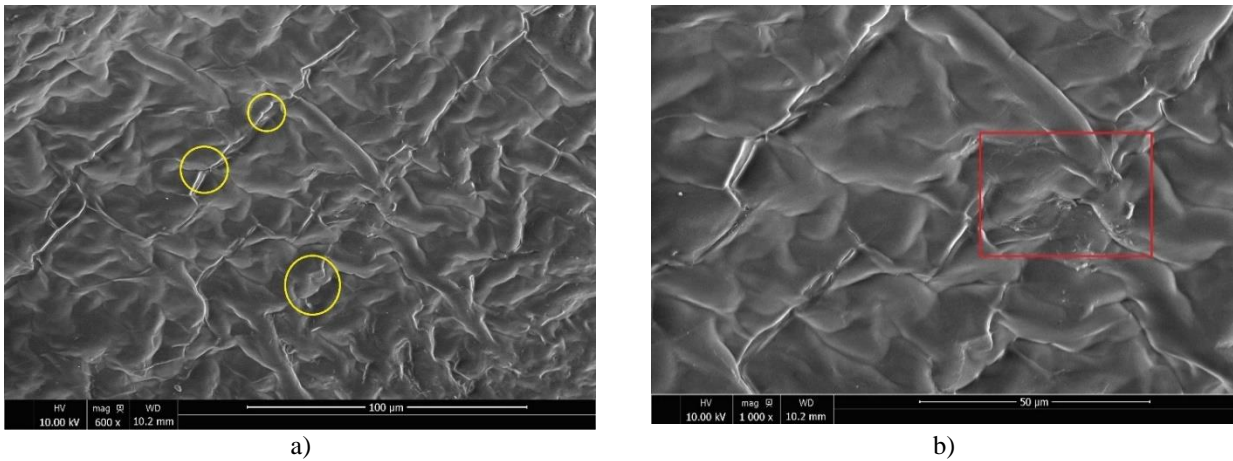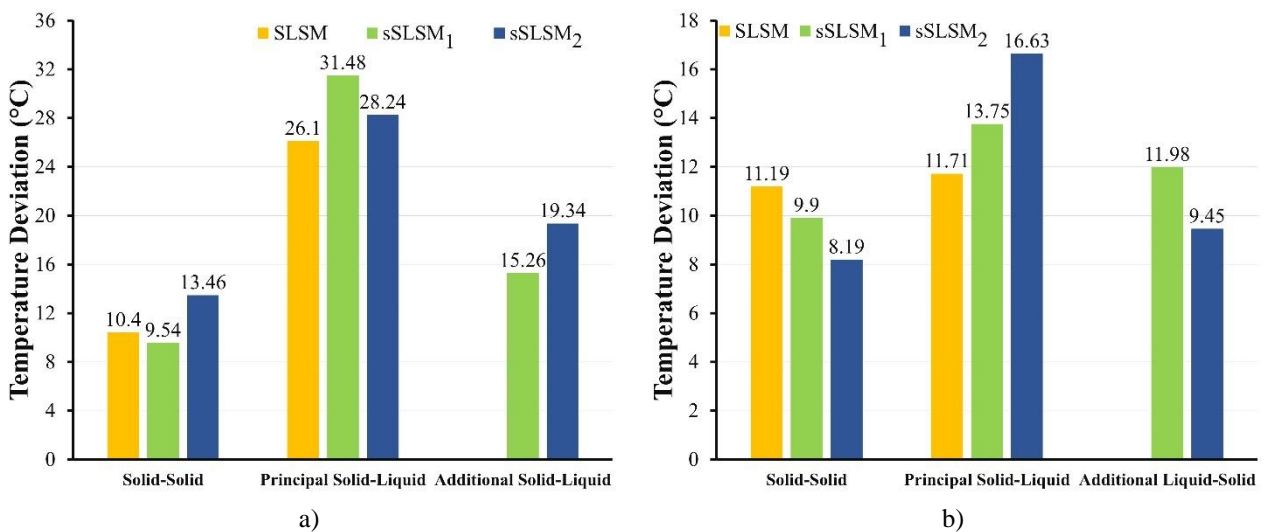ion. There is one additional solid–liquid transition for the sSLSM. It occurs at temperature above 100 °C. Therefore, the physical characteristic for the sSLSM is immiscible. It makes the correspond substance melt separately.

The freezing behavior for the SLSM is quite different (Fig. 4b). The main finding is shown as a shorter freezing transition. For example, the principal transition for SLSM is decreased by 55.1%. It makes the solidification occur at relatively shorter temperature range. It is also observed for the all sSLSM which indicates a shorter temperature transition during solidification. Interestingly, the solid–solid transition for SLSM and sSLSM$_1$ is increased around 0.8 °C and 0.4 °C, respectively. In contrast, the sSLSM$_2$ experiences a significant decrement for the transition which reduced about 39.2%. Each matrix has an identic pattern for the additional peak, where the temperature span reduces around 3.28 °C and 9.89 °C, respectively. Thus, the major change is caused by the interaction between the correspond matrix and SLSM (Pw).

Charge behavior is extremely important for the HSD. It indicates the ability of the storage material to absorb heat, which is critical to determine the performance of the system. The effect of charge rate causes significant change on the temperature profile. For example, charge rate of 30 Watts for SLSM (Fig. 5a) causes two step melt transition which starts at the identic temperature (around 70 °C).

The increment in charge rate makes the melt step becomes shorter at the identic temperature region. It indicates the melt transition for SLSM is delayed at higher temperature compared to its melt transition which is observed at 62.8 °C. It is the major issue for SLSM because the delayed transition reduces the heat absorption rate. Moreover, the pattern demonstrates the transition occurs as a non-isothermal behavior.
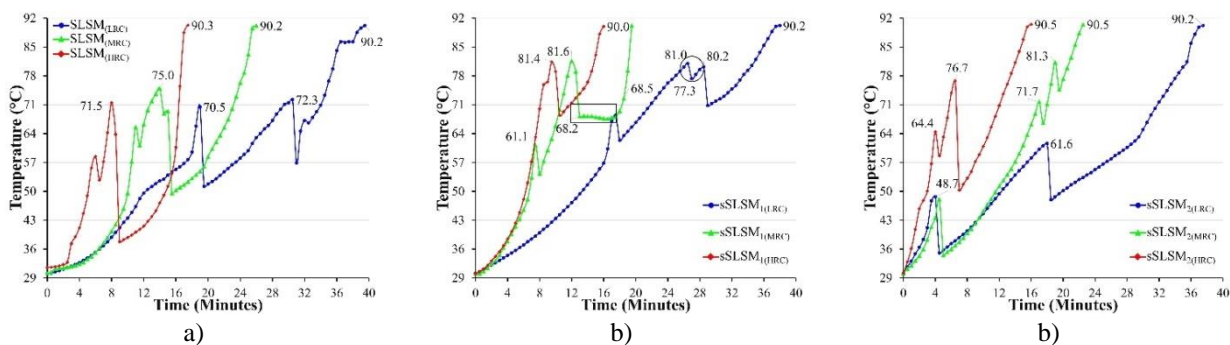
Fig.5. The effect of RC on the temperature evolution for (a) SLSM, (b) sSLSM$_1$, and (c) sSLSM$_2$

Positive influence is observed for the all sSLSM. For sSLSM$_1$ (Fig. 5b), the melt transition still observed under 70 °C. It indicates the melting process is stabilized sufficiently. The mixture also indicates a short isothermal transition at temperature 68.2 °C (rectangular in Fig. 5b) which is highly desirable for the actual HSD. Despite the advantages, thermal disruption is observed (circle in Fig. 5b). It can be taken as the second stage transition of the composite due to low charge rate. The peak transition at higher charge rate (100 Watts) is shown at 81.4 °C, which is close to the thermal disruption temperature as occurred in low charge rate. Thus, determining a suitable charge rate is highly important to ensure a stable charge process for the HSD.

One unique charge behavior is observed for sSLSM$_2$ (Fig. 5c). It is the only sample which experiences three stages transition. Considering the temperature transition (Fig. 4), the three stages is highly related with each transition [35]. It makes the sSLSM$_2$ takes the longest duration to achieve the final temperature compared to SLSM and sSLSM$_1$. The positive influence for sSLSM$_2$ is observed at higher rate (60 Watts and 100 Watts) with a significant charge acceleration compared to SLSM. It allows the material to achieve the final temperature faster around 3.5 minutes (60 Watts) and 1.5 minutes (100 Watts). It can be assumed that sSLSM$_2$ is suitable for high charge rate system to achieve the advantages of adding matrix within the SLSM.

The detailed effect of matrix as stabilizer is shown in Fig. 6. The pure SLSM is the only sample which experiences decrement in the temperature rate between the upper and lower zone under LRC. It confirms the insufficient phase transformation of the material. Increasing the RC level leads to a higher deviation between the upper and lower zone. The highest deviation is obtained under HRC, with variation of 6.59 °C/min. As a result, the system unable estimate the precise value of the charge level due to high variation between each zone.
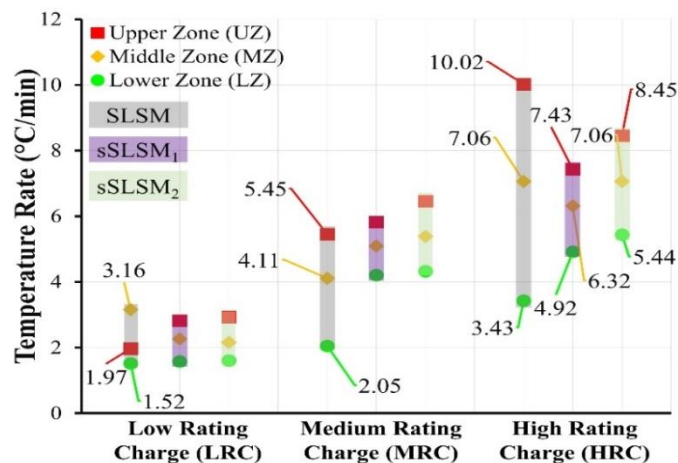
Fig.6. The changes in temperature rate for each zone under different RC

The effect of matrix demonstrates a better temperature rating between each zone. It has maximum temperature rate deviation of 1.24 °C/min (LRC), 2.13 °C/min, and 3.01 °C/min (HRC). It clearly demonstrates a steady phase transformation, particularly for the HRC operation. It corresponds to the plastic behavior of the matrix which maintain a suitable distribution of the liquid phase in the charge stage. Thus, the heat can be distributed effectively with minimum deviation, making the charge fluctuation can be decreased sufficiently and promoting a better estimation of charge indicator.

4. Conclusion

Utilization of polyethylene as matrix for SLSM (Pw) successfully promotes a steady phase transformation of the sSLSM in HSD. The matrix reduces the effect of temperature fluctuation in all RC scenario. The temperature rate deviation can be decreased up to 52.71% and 61.9% under medium and high RC. It is a direct impact on the presence of plastic behavior which increases the phase transformation characteristic of SLSM. The proposed method allows to accelerate the average temperature rate with the highest rating of 6.98 °C/min, which only deviates 3.01 °C/min between the upper and lower zone.

The surface observation of the SLSM clearly indicates the effect of insufficient phase transformation behavior. It contributes to the high deviation between each zone of the storage tank, which is disadvantageous for the operation of HSD, especially for large tank. The presence of additional matrix comes from polyethylene group is proven to reduce the drawback, minimize the temperature rate deviation, including the possibility to operate the system under high rating charge operation. Therefore, the proposed solution is suitable for developing a reliable HSD system with suitable phase transformation of the storage material.

References

1   Ismail I., Mulyanto A.T., Rahman R.A. (2022) Development of free water knock-out tank by using internal heat exchanger for heavy crude oil. *EUREKA: Physics and Engineering*, 4, 77–85. DOI: 10.21303/2461-4262.2022.002502.

2   Firman L.O.M., Adji R.B., Ismail, Rahman R.A. (2023) Increasing the feasibility and storage property of cellulose-based biomass by forming shape-stabilized briquette with hydrophobic compound. *Case Studies in Chemical and Environmental Engineering*, 8(April), 100443. DOI:10.1016/j.cscee.2023.100443.

3   Suyitno B.M., Rahman R.A., Sukma H., Rahmalina D. (2022) The assessment of reflector material durability for concentrated solar power based on environment exposure and accelerated aging test. *Eastern-European Journal of Enterprise Technologies*, 6(12–120), 22–29. DOI:10.15587/1729-4061.2022.265678.

4   Khademi A., Abtahi Mehrjardi S.A., Tiari S., Mazaheri K., Shafii M.B. (2022) Thermal efficiency improvement of brayton cycle in the presence of phase change material. *International Conference on Fluid Flow, Heat and Mass Transfer*, 135, 1–9. DOI:10.11159/ffhmt22.135.

5   Khademi A., Darbandi M., Behshad Shafii M., Schneider G.E. (2019) Numerical simulation of thermal energy storage process benefiting from the phase change materials concept. *AIAA Propulsion and Energy Forum and Exposition*, 2019, August, 1–9. DOI:10.2514/6.2019-4225.

6   Khademi A., Mehrjardi S.A.A., Said Z., Chamkha A.J. (2023) Heat transfer improvement in a thermal energy storage system using auxiliary fluid instead of nano-PCM in an inclined enclosure: a comparative study. *Journal of Applied and Computational Mechanics*, 9(2), 475-486. DOI:10.22055/jacm.2022.41867.3829.

7   Khademi A., Darbandi M., Schneider G.E. (2020) Numerical study to optimize the melting process of phase change material coupled with extra fluid. *AIAA Scitech 2020 Forum*, 1 Part F, 1–6. DOI:10.2514/6.2020-1932.

8   Alkahdery L.A., Yurchenko A.V., Mohammed J.A.K., Mekhtiyev A.D., Neshina Y.G. (2023) Performance improvement of solar dryer using an auxiliary heat source under different values of airflow rates. *Eurasian Physical Technical Journal*, 20(1–43), 42–50. DOI:10.31489/2023No1/42-50.

9   Usenkov R.A., Kokhanova S.Y., Trushin M.V. (2023) The use of alternative energy sources for the operation of engineering systems of detached consumers. *Eurasian Physical Technical Journal*, 20(2–44), 46–56. DOI:10.31489/2023No2/46-56.

10   Ali S., Mehrjardi A., Khademi A., Fazli M. (2024) Optimization of a thermal energy storage system enhanced with fins using generative adversarial networks method. *Thermal Science and Engineering Progress*, 49(February), 102471. DOI:10.1016/j.tsep.2024.102471.

11   Cui W., Li X., Li X., Lu L., Ma T., Wang Q. (2022) Combined effects of nanoparticles and ultrasonic field on thermal energy storage performance of phase change materials with metal foam. *Applied Energy*, 309(August 2021), 118465. DOI:10.1016/j.apenergy.2021.118465.

12   Palacio M., Ramírez C., Carmona M., Cortés C. (2022) Effect of phase-change materials in the performance of a solar air heater. *Solar Energy,* 247(April), 385–396. DOI:10.1016/j.solener.2022.10.046.

13   Hosseininaveh H., Mohammadi O., Faghiri S., Shafii M.B. (2021) A comprehensive study on the complete charging-discharging cycle of a phase change material using intermediate boiling fluid to control energy flow. *Journal of Energy Storage,* 35, 102235. DOI:10.1016/j.est.2021.102235.

14   Zhang Z., Zhang N., Yuan Y., Phelan P.E., Attia S. (2023) Thermal performance analysis of an existing building heating based on a novel active phase change heater. *Energy and Buildings*, 278, 112646. DOI:10.1016/j.enbuild.2022.112646.

15   Mehta D.S., Vaghela B., Rathod M.K., Banerjee J. (2020) Thermal performance augmentation in latent heat storage unit using spiral fin: An experimental analysis. *Journal of Energy Storage*, 31(April), 101776. DOI:10.1016/j.est.2020.101776.

16   Hashem Zadeh S.M., Ghodrat M., Ayoubi Ayoubloo K., Sedaghatizadeh N., Taylor R.A. (2022) Partial charging/discharging of bio-based latent heat energy storage enhanced with metal foam sheets. *International Communications in Heat and Mass Transfer*, 130(November 2021), 105757. DOI:10.1016/j.icheatmasstransfer.2021.105757.

17   Bastida H., De la Cruz-Loredo I., Ugalde-Loo C.E. (2023) Effective estimation of the state-of-charge of latent heat thermal energy storage for heating and cooling systems using non-linear state observers. *Applied Energy*, 331(August 2022), 120448. DOI:10.1016/j.apenergy.2022.120448.

18   Beyne W., Couvreur K., T'Jollyn I., Lecompte S., De Paepe M. (2022) Estimating the state of charge in a latent thermal energy storage heat exchanger based on inlet/outlet and surface measurements. *Applied Thermal Engineering*, 201(PB), 117806. DOI:10.1016/j.applthermaleng.2021.117806.

19   Du Y., Zhou T., Zhao C., Ding Y. (2022) Molecular dynamics simulation on thermal enhancement for carbon nano tubes (CNTs) based phase change materials (PCMs). *International Journal of Heat and Mass Transfer*, 182, 122017. DOI:10.1016/j.ijheatmasstransfer.2021.122017.

20   Gandhi M., Kumar A., Elangovan R., Meena C.S., Kulkarni K.S., Kumar A., Bhanot G., Kapoor N.R. (2020) A review on shape-stabilized phase change materials for latent energy storage in buildings. *Sustainability* (Switzerland), 12(22), 1–17. DOI:10.3390/su12229481.

21   Weng J., Huang Q., Li X., Zhang G., Ouyang D., Chen M., Yuen A.C.Y., Li A., Lee E.W.M., Yang W., Wang J., Yang X. (2022) Safety issue on PCM-based battery thermal management: Material thermal stability and system hazard mitigation. *Energy Storage Materials*, 53(September), 580–612. DOI:10.1016/j.ensm.2022.09.007.

22   He M., Xie D., Yin L., Gong K., Zhou K. (2023) Influences of reduction temperature on energy storage performance of paraffin wax/graphene aerogel composite phase change materials. *Materials Today Communications*, 34(October 2022), 105288. DOI:10.1016/j.mtcomm.2022.105288.

23   Zarrinjooy Alvar M., Abdeali G., Bahramian A.R. (2022) Influence of graphite nano powder on ethylene propylene diene monomer/paraffin wax phase change material composite: Shape stability and thermal applications. *Journal of Energy Storage*, 52(PC), 105065. DOI:10.1016/j.est.2022.105065.

24   Suyitno B.M., Anggrainy R., Plamonia N., Rahman R.A. (2023) Preliminary characterization and thermal evaluation of a direct contact cascaded immiscible inorganic salt/high-density polyethylene as moderate temperature heat storage material. *Results in Materials*, 19, 100443. DOI:10.1016/j.rinma.2023.100443.

25   Al-Gunaid T., Sobolčiak P., Chriaa I., Karkri M., Mrlik M., Ilčíková M., Sedláček T., Popelka A., Krupa I. (2023) Phase change materials designed from Tetra Pak waste and paraffin wax as unique thermal energy storage systems. *Journal of Energy Storage*, 64(October 2022). DOI:10.1016/j.est.2023.107173.

26   Mu M., McNally T. (2022) The effect of multi-walled carbon nanotubes on the thermo-physical properties of shape stabilised phase change materials for buildings based on high density polyethylene and paraffin wax. *Journal of Energy Storage*, 55(PC), 105601. DOI:10.1016/j.est.2022.105601.

27   Al-Haydari I.S., Al-Haidari H.S., Khudhur H.M.N., Jummah N.W., Al-Hamza M.A. (2021) Durability and aging characteristics of sustainable paving mixture. *International Journal of Engineering, Transactions B: Applications*, 34(8), 1865–1873. DOI:10.5829/ije.2021.34.08b.07.

28   Liu C., Xiao T., Zhao J., Liu Q., Sun W., Guo C., Ali H.M., Chen X., Rao Z., Gu Y. (2023) Polymer engineering in phase change thermal storage materials. *Renewable and Sustainable Energy Reviews*, 188, 113814. DOI:10.1016/j.rser.2023.113814.

29   Rahmalina D., Zada A.R., Soefihandini H., Ismail I., Suyitno B.M. (2023) Analysis of the thermal characteristics of the paraffin wax/high-density polyethylene (HDPE) composite as a form-stable phase change material (FSPCM) for thermal energy storage. *Eastern-European Journal of Enterprise Technologies*, 1(6 (121)), 6–13. DOI:10.15587/1729-4061.2023.273437.

30   Rolka P., Kwidzinski R., Przybylinski T., Tomaszewski A. (2021) Thermal characterization of medium-temperature phase change materials (Pcms) for thermal energy storage using the t-history method. *Materials*, 14(23). DOI:10.3390/ma14237371.

31   Firman L.O.M., Rahmalina D., Rahman R.A. (2023) Hybrid energy-temperature method (HETM): A low-cost apparatus and reliable method for estimating the thermal capacity of solid – liquid phase change material for heat storage system. *HardwareX*, 16, e00496. DOI:10.1016/j.ohx.2023.e00496.

32   Brütting M., Vidi S., Hemberger F., Ebert H.P. (2019) Dynamic T-History method - A dynamic thermal resistance for the evaluation of the enthalpy-temperature curve of phase change materials. *Thermochimica Acta*, 671(September 2018), 161–169. DOI:10.1016/j.tca.2018.10.030.

33   Yang B., Raza A., Bai F., Zhang T., Wang Z. (2019) Microstructural evolution within mushy zone during paraffin's melting and solidification. *International Journal of Heat and Mass Transfer*, 141, 769–778. DOI:10.1016/j.ijheatmasstransfer.2019.07.019.

34   Tang Y., Su D., Huang X., Alva G., Liu L., Fang G. (2016) Synthesis and thermal properties of the MA/HDPE composites with nano-additives as form-stable PCM with improved thermal conductivity. *Applied Energy*, 180, 116–129. DOI:10.1016/j.apenergy.2016.07.106.

35   Janghel D., Karagadde S., Saha S.K. (2023) Measurement of shrinkage void and identification of solid-liquid phases in phase change materials: Ultrasound-based approach and simulated predictions. *Applied Thermal Engineering*, 223(December 2022), 120048. DOI:10.1016/j.applthermaleng.2023.120048.

_____

AUTHORS' INFORMATION

Rahman, Reza Abdu – PhD Student, Universitas Diponegoro, Semarang, Indonesia; Master (Eng.), Lecturer, Department of Mechanical Engineering, Universitas Pancasila, Jakarta, Indonesia. Scopus Author ID: 57218544155; https://orcid.org/0000-0002-8047-6716; reza.a@univpancasila.ac.id

Sulistyo, - PhD, Doctor of Engineering, Associate Professor, Universitas Diponegoro, Semarang, Indonesia Scopus Author ID: 35184175000; https://orcid.org/0000-0002-3232-7871; sulistyo@lecturer.undip.ac.id

Utomo, Mohamad Said Kartono Tony Suryo – PhD, Doctor of Engineering, Assistant Professor, Universitas Diponegoro, Semarang, Indonesia Scopus AuthorI D: 57567230600; https://orcid.org/0000-0002-6857-0857; tonysuryoutomo@lecturer.undip.ac.id

Febriansyah, Ilham - Master (Eng.), Department of Mechanical Engineering, Universitas Pancasila, Jakarta, Indonesia; https://orcid.org/0009-0006-0412-5013; 5322220007@univpancasila.ac.id

.

UDC 532.517.4

SIMULATION OF LIQUID FUEL SPRAY FORMATION AND DISTRIBUTION IN A REACTING TURBULENT FLOW

Bolegenova S.A., Askarova A.S., Ospanova Sh.S., Makanova A.B., Zhumagaliyeva S.A., Nurmukhanova A.Z., Adilbayev N.A., Shalkar A.

Al-Farabi Kazakh National University, Almaty, Kazakhstan
Corresponding author: Shynar.Ospanova@kaznu.edu.kz

Abstract. *The paper presents the computational experiments of the liquid fuels spray and its droplets distribution in a turbulent reacting flow. Primary and secondary atomization of two types of liquid fuel droplets (isooctane and dodecane) in the presence of combustion was described by the equations of continuity, momentum, internal energy, concentration of components of reacting substances and a two-parameter model for calculating turbulent flow. The study results of the spray, dispersion and combustion of droplets of hydrocarbon liquid fuels in a model combustion chamber when changing the injector injection angle were obtained. The injection angle values varied from 2 to 10 degrees. Based on the computational experiment temperature profiles and concentration characteristics of combustion products and gas in the combustion chamber at various times were obtained. Numerical calculations of the droplets' Sauter mean diameter distributions have the same dispersion pattern for dodecane. This suggests that the accuracy and adequacy of developed complex model of the formation and distribution of spray in a reacting flow has been confirmed by its strong correlation and good agreement of the modeling results with experimental data from other researchers. This kind of modeling methods and the obtained computational experiments results from them are widely used not only in traditional thermal power engineering, but also in the study of technological processes in the new generation engines chambers, combustion of alternative types of fuels and optimization of their combustion.*

Keywords: fossil fuel, spray, simulation, combustion, injection angle, emissions.

1. Introduction

The increase in harmful emissions of combustion products into the environment is a consequence of the extended consumption of hydrocarbon fuels in the energy, industry and transport sectors. According to long-term monitoring, the volume of environmentally hazardous chemical compounds, wastes and substances emitted into the atmosphere as a result of fuel combustion doubles every 12-14 years. Thus, one of the major environmental problems of the modern world is environmental pollution due to anthropogenic impact. The quality and type of liquid fuel burned, the conditions for organizing its combustion and the technical condition of internal combustion engines affect the toxicity of gas emissions and soot into the surrounding atmosphere. Although the use of low-quality fuels reduces the costs spent on its purchase, it also increases the concentration of environmentally harmful substances that enter the air [1].

The internal combustion engines exhaust gases emitted into the air contain more than 70% carbon oxides, about 52% nitrogen oxides, up to 5.5% soot and water. A complex combination of physical and chemical, kinetic, thermodynamic and heat exchange processes influence the environmentally hazardous

pollutants formation dynamics during the various types of fuels combustion. However, despite the existing significant amount of research in this area, the mechanisms of such harmful substances' formation are still not fully understood [2, 3]. By actively influencing the harmful emissions formation, it is possible to reduce thermal and gas pollution of the air, which is the most promising way to eliminate them. Improvement of the technological cycle of fuel processing and supply, methods of modernization and updating of injection devices contributes to changing the conditions for the harmful pollutants' formation in the environment. At the current stage of energy development, environmental problems are becoming a priority. Since carbon dioxide is the most common indicator of harmful substances, reducing its production into the atmosphere and using up to 80% of renewable energy sources by 2050 is a long-term goal set for all countries by the International Energy Agency. In this regard, it becomes imperative to improve and increase the efficiency of devices and systems for supplying and burning various types of fuel, as well as minimizing harmful gaseous emissions into the atmosphere. Figure 1 shows the main specific pollutant emissions dynamics for 2019-2023 in Kazakhstan [4].
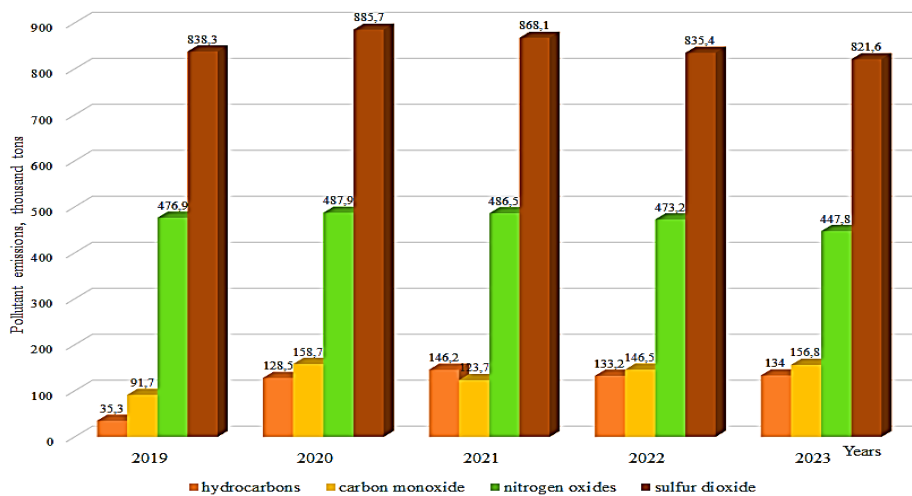
Fig.1. Emissions of main pollutants in Kazakhstan, thousand tons

In this paper, the study of thermophysical processes in heat engines is carried out, considering the geometry of the combustion chamber, methods of fuel supply, design parameters, and location of injection devices, and also identified effective technological mechanisms of the injection, allowing for rational fuel combustion optimization with minimal gaseous waste emissions.

2. Mathematical model of the problem and computational grid

During two-phase reacting flow modeling, the continuity, momentum, internal energy and reaction components concentration equations are solved by using numerical methods, taking into account chemical transformations, medium high turbulence, interphase heat and mass transfer and interfacial interaction [5-8].

The reacting components mass conservation in a two-phase flow is described by the continuity equation taking into account the atomized dispersed phase contribution:

$$\frac{\partial \rho}{\partial t} + \mathrm{div}(\rho \mathbf{u}) = S_{mass},$$ (1)

where u is the fluid phase velocity, S_{mass} is source term describing the change in gas phase density as a result of liquid fuel droplets evaporation.

The particles movement in a two-phase reacting flow is determined by the gas phase momentum conservation equation:

$$\rho \frac{\partial \mathbf{u}}{\partial t} + \rho(\mathrm{grad}\,\mathbf{u})\mathbf{u} = \mathrm{div}\boldsymbol{\xi} + \rho\mathbf{g} + S_{mom},$$ (2)

where S_{mom} is source term describing the moving drops contribution to the gas phase momentum velocity change.

The two-phase reacting flow internal energy conservation with dispersed particles is as follows:

$$\rho\frac{\partial E}{\partial t} = \mathbf{\tau}\mathbf{:}\mathbf{D} - \rho\,\mathrm{div}\mathbf{u} - \mathrm{div}\mathbf{q} + S_{energy}\,, \tag{3}$$

where $\mathbf{q}$ is isolated heat flow according to Fourier's law, S_{energy} is contribution to the change in the system's internal energy coming from atomized dispersed phase droplets.

The system's mass density is determined by the conservation equation for the component m:

$$\frac{\partial(\rho c_m)}{\partial t} = -\frac{\partial(\rho c_m u_i)}{\partial x_i} + \frac{\partial}{\partial x_i}\left(\rho D_{c_m}\frac{\partial c_m}{\partial x_i}\right) + S_{mass}\,, \tag{4}$$

where ρ_m is the m component mass density, ρ is the total mass density.

During the complex turbulent flows simulation, according to the turbulent kinetic energy cascade transfer law the high turbulence of the reacting two-phase flow was taken into account by two main parameters: the kinetic energy of turbulence k and its dissipation degree ε, which was expressed by an empirical turbulence model included in the mathematical model of the problem [9, 10]:

$$\rho\frac{\partial k}{\partial t} + \rho\frac{\partial\overline{u}_j k}{\partial x_j} = \frac{\partial}{\partial x_j}\left[\left(\mu + \frac{\mu_t}{\sigma_k}\right)\frac{\partial k}{\partial x_j}\right]\frac{\partial\overline{u}_i}{\partial x_j} + G - \frac{2}{3}\rho k\delta_{ij}\frac{\partial\overline{u}_i}{\partial x_j} - \rho\varepsilon\,, \tag{5}$$

$$\rho\frac{\partial\varepsilon}{\partial t} + \rho\frac{\partial\overline{u}_j\varepsilon}{\partial x_j} - \frac{\partial}{\partial x_j}\left[\left(\mu + \frac{\mu_t}{\sigma_\varepsilon}\right)\frac{\partial\varepsilon}{\partial x_j}\right] = c_{\varepsilon_1}\frac{\varepsilon}{k}G - \left[\left(\frac{2}{3}c_{\varepsilon_2} - c_{\varepsilon_3}\right)\rho\varepsilon\delta_{ij}\frac{\partial\overline{u}_i}{\partial x_j}\right] - c_{\varepsilon_2}\rho\frac{\varepsilon^2}{k}\,. \tag{6}$$

The constants c_{ε_1}, c_{ε_2}, c_{ε_3}, σ_k, σ_ε, used in the empirical turbulence model above are determined from experiment [11, 12].

Aircraft and rocket engines inject a liquid jet with a high-velocity co-current gas flow. When interacting with a co-current gas flow, the liquid jet breaks up into fragments, which is called primary atomization. When modeling the formation and evolution dynamics of liquid injections, the main attention was paid to the air-blast atomization process, which is most common in highly reactive jets. The air-blast atomization process configuration is shown in Figure 2 [13-15]. In such injection systems, a stream of liquid fuel is injected into thin liquid fragmentary sheets at low pressure. High-speed liquid jets surrounded by a co-current gas jet make a large contribution to the kinetic energy of the entire flow. Due to the presence of the jet-to-jet interaction phenomenon and intense interaction with co-current gas stream, liquid's layered sheets are torn on both sides into ligaments. Further downstream, these liquid ligaments break up into various size droplets. This phenomenon is called secondary atomization.

a)   b)
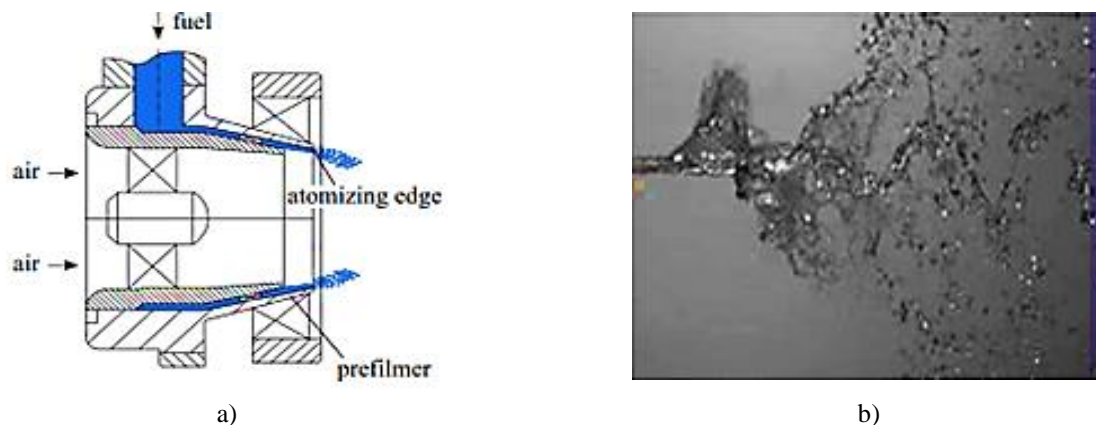
Fig.2. Premixed air-blast atomizing scheme [13-15]

Using a calculation program, a cylindrical combustion chamber virtual prototype with a height of 15 cm and a diameter of 4 cm was built. Liquid fuel is sprayed throughout the entire volume of the chamber through a nozzle located in its lower part. Before the experiment, the fuel droplets had a temperature of 900 K. Two types of liquid fuels (isooctane and dodecane) injected droplets' mean radius was 25 μm. The optimal initial injection mass and pressure for isooctane were 6 mg and 100 bar, for dodecane were 7 mg and 80 bar. These optimal parameters for the combustion process of these fuels were obtained in previous studies by the authors [16, 17].

The combustion chamber general view and generated computational mesh template are presented in Figure 3. The computational domain is centered on a Cartesian coordinate 3D structured grid with various node configurations. The computational grid is divided into blocks of cells across the entire logical space.

a) model chamber　　　　　　　　　　　　b) computational mesh
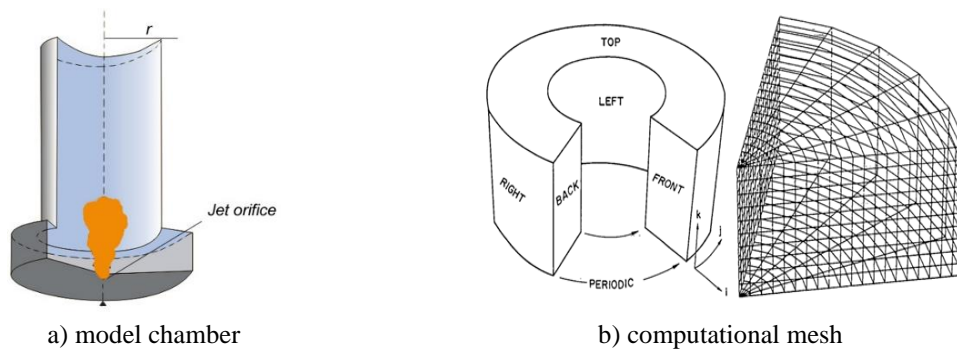
Fig.3. a) Model camera general view; b) Pseudo-polar grid and perspective view of the sector grid outline

Using the initial and boundary conditions of the problem, a three-dimensional mesh is formed from pseudo-polar blocks of cells. Although the program's functions cover broader areas of its application, our main goal was its targeted application for modeling thermal processes in reacting flows. Using an automatic mesh generator built into the SETUP subroutine, a three-dimensional cylindrical mesh was created to describe the different types of injectors and nozzles of gasoline and diesel thermal engines [6, 18].

3. Simulation results and analysis

Influence of the injection angle on the two types of liquid fuel (isooctane and dodecane) spray formation, droplets distribution, and combustion in a turbulent reacting flow in the cylindrical chamber was investigated. The values of the injection angle varied from 2 to 10 degrees. Figures below show the graphs for determining the fuels optimal combustion regime depending on the injector injection angle value.

The distribution of the maximum combustion temperature of the reacting mixture throughout the entire volume of the combustion chamber when the injection angle changes is shown in Figure 4 (a). As a result of a detailed analysis of the curves in the Figure 4 (a), it was found that the maximum combustion temperature of isooctane is 2690 K at 4 and 8 degrees of injection angle. Because diesel fuels have high surface tension, the interface between the two phases remains stable for a long time. In this regard, during the ignition and combustion of dodecane droplets, the highest temperature value of 2707 K is observed at 8 degrees of injection angle. Therefore, we can say with confidence that the greater the droplet spray angle, the more intense the fuel burns, the heat exchange between the two phases increases and the temperature rises to 3000 K.

a) combustion temperature　　　　　　　　　　　b) CO_2 concentration
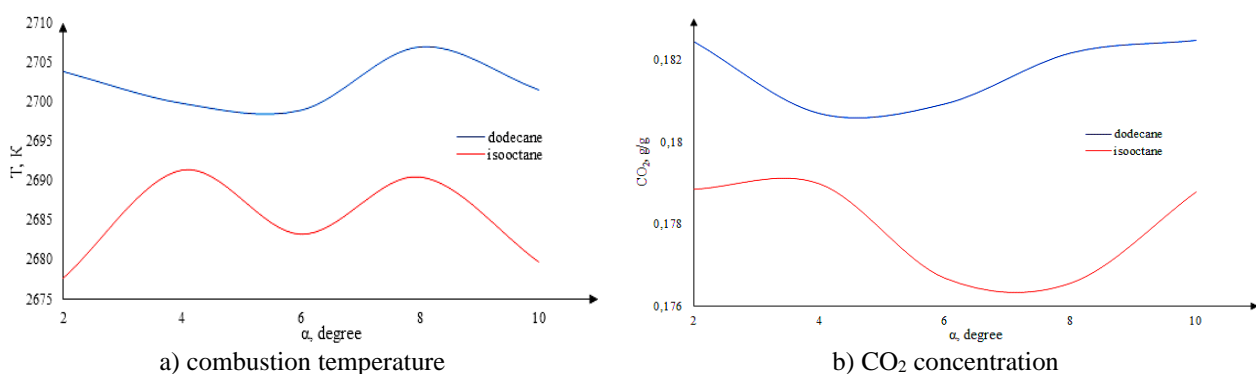
Fig.4. Dependences of the maximum combustion temperature and carbon dioxide concentration on the injection angle during the combustion of isooctane and dodecane

The influence of two types of fuels (isooctane and dodecane) droplets injection angle on the distribution of the carbon dioxide maximum concentration was investigated. As is known, CO_2 is the main component of greenhouse gases. The amount of carbon dioxide produced during the combustion of dodecane exceeds the

concentration of CO_2 released during the isooctane droplets combustion. The volume of carbon dioxide formed during the dodecane combustion varies between 0.180-0.182 g/g at injection angles of 4-10 degrees. The distribution of carbon dioxide concentration during combustion of isooctane is very different from that of dodecane, since its decrease is observed with increasing injection angle. For this reason, within 6-8 degrees, the volume of CO_2 released is 0.176 g/g, which is much less compared to dodecane. This difference in the behavior of fuels can be explained as follows: isooctane is a reference fuel with high octane number and lower concentration of impurities.

According to the distribution of temperature and CO_2 concentration in Figure 4, it was found that for the two types of liquid fuels most often used in internal combustion engines and included in gasoline and diesel, the effective injection angle is 8 degrees. With an effective injection angle, due to intensive mixing of the fuel jet with the co-current gas flow, the temperature in the combustion chamber increases, and the amount of carbon dioxide in the combustion products does not exceed environmental standards requirements.

Three-dimensional graphs of the temperature and concentration characteristics of the reacting flow of two types of liquid fuels (isooctane and dodecane) were obtained through a numerical CFD modeling experiment taking into account an effective injection angle of 8 degrees (Figures 5-7). Liquid fuel combustion is a heterogeneous process, since the interaction products are in the condensed phase due to phase separation and high temperatures of more than 2000 K, the role of plasma processes increases. The same picture of the formation of areas with high temperatures and its distribution over the entire combustion chamber height is observed during the combustion of solid fossil fuels in high-temperature energy, thermophysical and technological facilities [19]. At different times and combustion zones, isooctane and dodecane have similar temperature profiles with a monotonic spreading gradient (Figure 5).
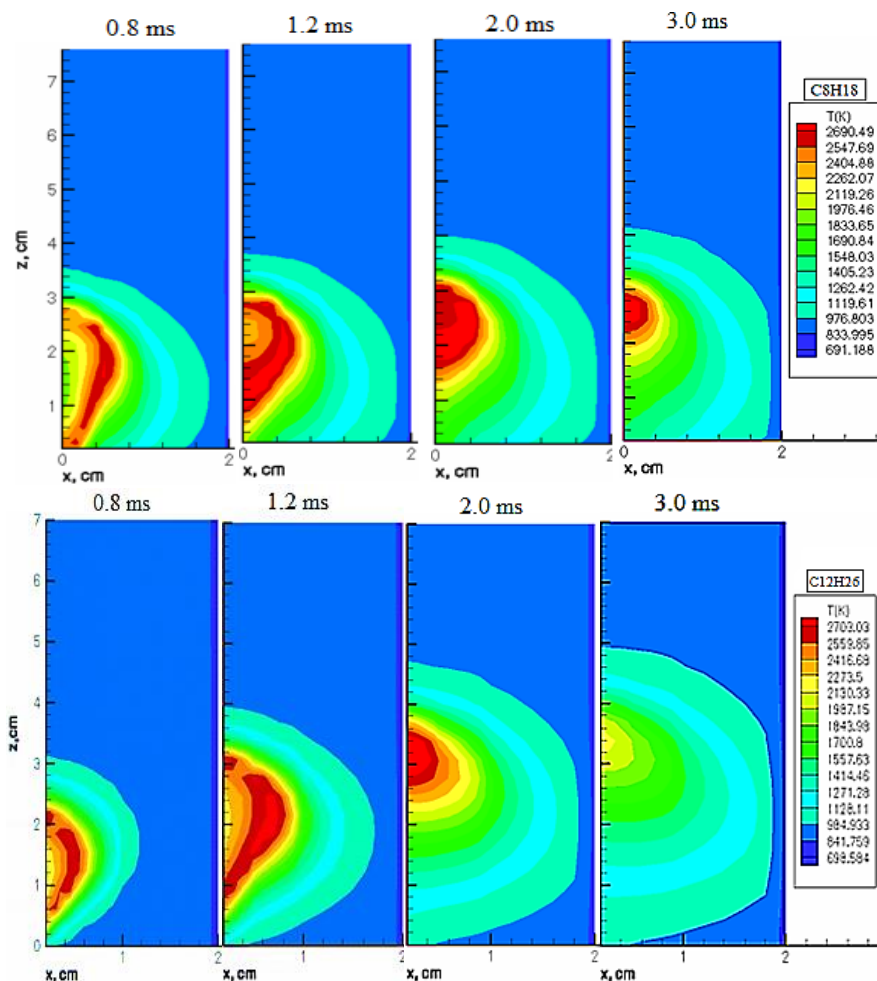
Fig.5. Temperature profiles during isooctane and dodecane combustion at different time moments in the combustion chamber

Due to the temperature gradient, intense heat exchange and mixing with the oxidizer, a high-temperature flame spreads throughout the entire volume from the central part of the combustion chamber. Spray areas remote from the flame core heat up to 975-985 K during combustion of both types of fuels. The core of the flame when burning isooctane occupies 3 cm in height, and 0.8 cm in width, and the temperature reaches 2690 K, for dodecane, it is much larger than 3.6 cm by 0.5 cm, respectively, but the maximum temperature is 2703 K. The concentration fields of consumed oxygen and carbon dioxide at an effective injection angle at a time of 3 ms are shown in Figures 6 and 7.

Oxygen consumption in various parts of the combustion chamber and its distribution across combustion zones for two types of fuels is shown in Figure 6. Since the fuel droplets intensive combustion process occurs in the flame core, the highest oxygen consumption is observed in the central part of the chamber. And in other parts of the combustion chamber, a high concentration of oxidizer remains for both isooctane and dodecane.

The amount of oxygen that has not reacted with the fuel for isooctane and dodecane is 0.22 g/g. The unconsumed oxidizer concentration located in the flame core was 0.015 g/g for both types of fuel. An intense reaction of isooctane with oxygen occurs in the area of 2.9-4.8 cm along the model combustion chamber height. When dodecane is burned, O2 consumption begins from a chamber height of 3.8 cm, which is an indicator of the high mobility and reactivity of its droplets. Since the region of high temperatures for dodecane begins at this height of the chamber, we can confidently say that oxygen molecules are focused in the plume core. This statement can be observed in Figure 6.

Numerical data on the concentration profiles of carbon dioxide formation during the combustion of isooctane and dodecane, depending on the effective injection angle, are presented in Figure 7. On the axis of the combustion chamber, where the temperature flame is formed and the highest fuel consumption, the maximum amount of carbon dioxide is produced, which confirms the fulfillment of the laws of chemical kinetics.
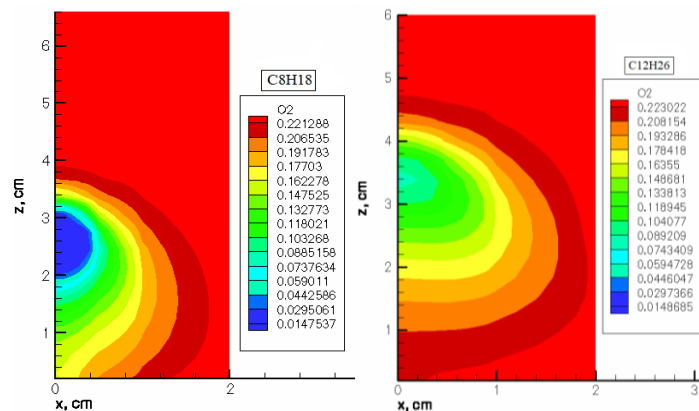
Fig.6. The oxidizer O_2 concentration profiles in a model combustion chamber at t=3 ms
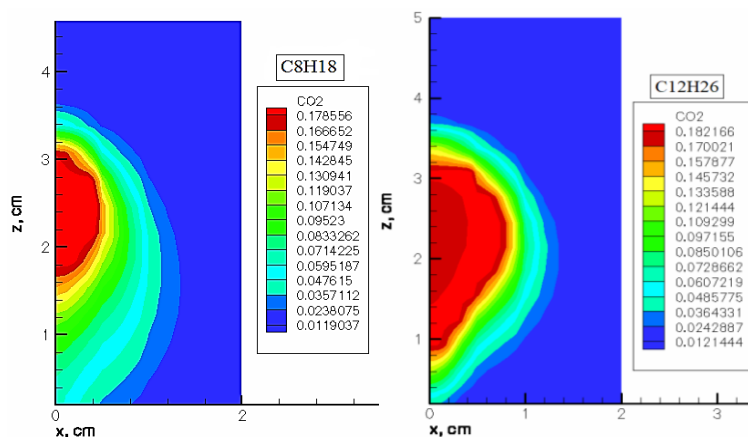
Fig.7. The carbon dioxide concentration properties in the combustion chamber at t=3 ms

The maximum concentration of CO_2 formed in the central part of the model chamber was 0.18 g/g for both isooctane and dodecane. At the combustion chamber exit, the amount of CO_2 gradually decreases, thereby at the final moment of fuel combustion it takes on minimum values for the two types of fuels. This phenomenon shows that the formation and distribution of greenhouse gases during the combustion of liquid hydrocarbon fuels is identical. At an effective injection angle of 8 degrees, the concentration of released carbon dioxide is 0.012 g/g. The efficiency of the combustion process of liquid fuel droplets in internal combustion engines directly depends on their spraying from the nozzle and breakup into small secondary droplets, including their size distribution. The isooctane and dodecane droplets' Sauter mean diameters (SMD) were measured at different distances from the injector nozzle edge at various times (Figure 8). Since the Sauter mean diameter is a volume-surface unit of droplets, this value is a parameter of the particle size distribution and is involved in the secondary atomization of liquid fragments. To verify the computer simulation data, a comparative analysis was carried out with experimental data taken from [20]. According to a thorough analysis of the calculated and experimental indicators presented in Figure 8, it was found that model calculations for the size distribution of dodecane droplets are similar to the experimental data.

In the experiment the dispersion of the droplets' Sauter mean diameter was measured at distances from 10 to 60 mm from the nozzle at various times [20].
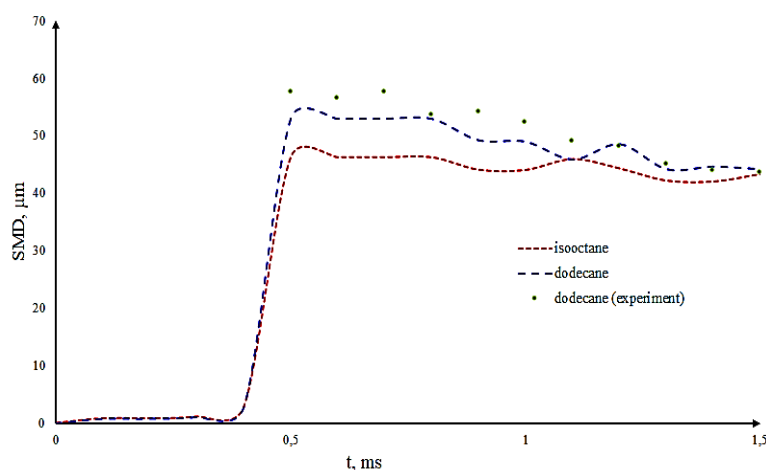
Fig.8. The isooctane and dodecane droplets Sauter mean diameter (SMD) dispersion
at a distance of x=40 mm from the injector nozzle

Identical researches of the isooctane and dodecane droplets' Sauter mean diameter dispersion at various times were carried out in simulation at a distance of 40 mm from the injector nozzle. When comparing the relative data in Figure 8, it is established that the measured results of the numerical experiment are in good agreement with the experimental measurements belonging to the authors of [20]. Relying on this agreement between the numerical results and the experiment, we can state that the complex CFD model of the distribution, atomization and combustion of liquid fuel droplets in a cylindrical combustion chamber proposed in our work is adequate and can be applied to real processes and phenomena occurring in thermal power and thermophysical facilities with built-in injection systems.

4. Conclusion

The processes of distribution and atomization of two types of fossil fuels (isooctane and dodecane) in a highly turbulent flow in the presence of combustion were studied using a set of complex methods for modeling technological structural systems. The effective injection angle influence on the liquid fuels' droplets atomization and distribution in the presence of combustion was determined by simulation methods based on computational experiments in order to organize rational combustion of fuels with the least negative impact on the environment. From the analysis of computer experiments, it was found that for isooctane and dodecane, the optimal injection angle of the injector is 8 degrees. At this effective value of the injection angle, the fuel quickly reacts with the oxidizer, due to high temperatures, intermediate products of the chemical reaction are released in a minimal volume, and the concentration of carbon dioxide produced does not exceed environmentally acceptable standards.

The proposed numerical data in the work have practical significance and will serve as a background for their use in the design of various heat engines with injection devices and optimal structural parameters. The results obtained in the work will contribute to solving the problems of rational and efficient combustion of various types of fossil fuels with subsequent optimization of these processes and reducing the carbon footprint from their anthropogenic impact.

References

1 Bolegenova S., Askarova A., Slavinskaya N., Ospanova Sh., Maxutkhanova A., Aldiyarova A., Yerbosynov D. (2022) Statistical modeling of spray formation, combustion, and evaporation of liquid fuel droplets, *Phys. Sci. Technol.* 9 (2), 69-82. DOI:10.26577/phst.2022.v9.i2.09.

2 Gallen L., Riber E., Cuenot B. (2023) Investigation of soot formation in turbulent spray flame burning real fuel. *Combust. Flame.* 258, 112621. DOI:10.1016/j.combustflame.2023.112621.

3 Hinrichs J., Schweitzer-De Bortoli S., Pitsch H. (2021) 3D modeling framework and investigation of pollutant formation in a condensing gas boiler. *Fuel.* 300, 120916. DOI:10.1016/j.fuel.2021.120916.

4 Report from the Bureau of National Statistics on air protection in the Republic of Kazakhstan (2022). [in Russian]. Available at: https://stat.gov.kz/ru/industries/business-statistics/stat-inno-/publications/68178/

5 Amsden A.A. (1993) *KIVA-3: A KIVA Program with Block-Structured Mesh for Complex Geometries*. Los Alamos, 95. Available at: https://www.lanl.gov/projects/feynman-center/deploying-innovation/intellectual-property/software-tools/ kiva/_assets/docs/KIVA3man.pdf

6 Amsden A.A. (1999) *KIVA-3V, RELEASE 2, IMPROVEMENTS TO KIVA-3V*. Los Alamos, 34. Available at: https://www.lanl.gov/projects/feynman-center/deploying-innovation/intellectual-property/software-tools/kiva_assets/docs/KIVA3V.pdf

7 Gorokhovski M., Hermann M. (2008) Modeling primary atomization. *Annu. Rev. Fluid Mech.* 40, 343-366. DOI:10.1146/annurev.fluid.40.111406.102200.

8 Askarova A.S., Bolegenova S.A., Ospanova Sh.S., Rakhimzhanova L.A., Nurmukhanova A.Z., Adilbayev N.A. (2024) Optimization of fuel droplet sputtering and combustion at high turbulence flows. *Russ. Phys. J.*, 67, 2, 167-170. DOI:10.1007/s11182-024-03104-5.

9 Li Y., Huang Y., Luo K., Liang M., Lei B. (2021) Development and validation of an improved atomization model for GDI spray simulations: Coupling effects of nozzle-generated turbulence and aerodynamic force. *Fuel.* 299, 120871. DOI:10.1016/j.fuel.2021.120871.

10 Berezovskaya I.E., Tasmukhanova A.A., Ryspaeva M.Zh., Ospanova Sh.S. (2023) Investigation of the influence of liquid fuel injection rate on the combustion process using KIVA-II software. *Eurasian Physical Technical Journal*, 20, 3(45), 43–51. DOI:10.31489/2023No3/43-51.

11 Amsden A.A., O'Rourke P.J., Butler T.D. (1989) *KIVA-II: A computer program for chemically reactive flows with sprays*. Los Alamos, 160. Available at: https://www.lanl.gov/projects/feynman-center/deploying-innovation/intellectual -property/software-tools/kiva/_assets/docs/KIVA2.pdf

12 Gorokhovski M., Zamansky R. (2018) Modeling the effects of small turbulent scales on the drag force for particles below and above the Kolmogorov scale. *Phys. Rev. Fluids.* 3, 034602. DOI:10.1103/PhysRevFluids.3.034602.

13 Liao Y., Jeng S.M., Jog M.A., Benjamin M.A. (2001) Advanced submodel for airblast atomizers. *J. Propul. Power.* 17, 2, 411–417. DOI:10.2514/2.5757.

14 Gorokhovski M.A., Oruganti S.K. (2022) Stochastic models for the droplet motion and evaporation in under-resolved turbulent flows at a large Reynolds number. *J. Fluid Mech.* 932, 18. DOI:10.1017/jfm.2021.916.

.

15 Shen L., Fang G., Wang S., Xing F., Chan Sh. (2022) Numerical study of the secondary atomization characteristics and droplet distribution of pressure swirl atomizers. *Fuel*. 324, Part B, 124643. DOI:10.1016/ j.fuel.2022.124643.

16 Askarova A.S., Bolegenova S.A., Maximov V.Yu., Bolegenova S.A., Ospanova Sh.S., Beketayeva M.T., Nugymanova A.O., Pilipenko N.V., Shortanbayeva Zh.K., Baktybekov K.S., Syzdykov A.B. (2018) Investigation of the different Reynolds numbers influence on the atomization and combustion processes of liquid fuel. *Bulg. Chem. Commun*. 50, 68-77. Available at: http://www.bcc.bas.bg/bcc_volumes/Volume_50_Special_G_2018/50G_PD_68-77.66.pdf

17 Askarova A., Bolegenova S., Ospanova Sh., Slavinskaya N., Aldiyarova A., Ungarova N. (2021) Simulation of non-isothermal liquid sprays under large-scale turbulence. *Phys. Sci. Technol*. 8, 28-40. DOI:10.26577/phst.2021.v8.i2.04.

18 Choi M., Lee S., Park S. (2023) Numerical and experimental study of gaseous fuel injection for CNG direct injection. *Fuel*. 140, 693-700. DOI:10.1016/j.fuel.2014.10.018.

19 Chen L., Sun D., Yang K., Song P., Wang Sh., Zeng W. (2023) Experimental study on the effect of plasma excitation on the atomization characteristics of aviation kerosene transverse jet. *Fuel*. 332, Part 2, 126210. DOI:10.1016/j.fuel.2022.126210.

20 Arcoumanis C., Gavaises M. (1998) Linking nozzle flow with spray characteristics in a diesel fuel injection systems. *Atom. Sprays*. 8, 307–347. DOI:10.1615/AtomizSpr.v8.i3.50.

_____

AUTHORS' INFORMATION

Bolegenova, Saltanat Alikhanovna - Doctor of Phys. and Math. Sciences, Professor, Head of the Department of Thermophysics and Technical Physics, al-Farabi Kazakh National University, Almaty, Kazakhstan; SCOPUS Author ID: 57192917040; ORCID iD: 0000-0001-5001-7773; Saltanat.Bolegenova@kaznu.edu.kz

Askarova, Aliya Sandybayevna – Doctor of Phys. and Math. Sciences, Professor, Department of Thermophysics and Technical Physics, al-Farabi Kazakh National University, Almaty, Kazakhstan; SCOPUS Author ID: 6603209318; ORCID: iD: 0000-0003-1797-1463; Aliya.Askarova@kaznu.edu.kz

Ospanova, Shynar Sabitovna - PhD, Senior Lecturer, Department of Thermophysics and Technical Physics, al-Farabi Kazakh National University Almaty, Kazakhstan; Scopus Author ID: 55988678700; ORCID ID: 0000-0001-6902-7154; Shynar.Ospanova@kaznu.edu.kz

Makanova, Ayaulym Bolatkanovna – Master's student, Department of Thermophysics and Technical Physics, al-Farabi Kazakh National University Almaty, Kazakhstan; ORCID iD: 0009-0005-1721-3090; aiko.20.20@mail.ru

Zhumagaliyeva, Sabina Audanbaikyzy - Master's student, al-Farabi Kazakh National University, Almaty, Kazakhstan; ORCID iD: 0009-0001-7975-1135; zhumasabina@icloud.com

Nurmukhanova, Alfiya Zeinullovna – Candidate of Techn. Sciences, Senior Lecturer, Department of Thermophysics and Technical Physics, al-Farabi Kazakh National University, Almaty, Kazakhstan; SCOPUS Author ID: 57217224044; ORCID iD: 0000-0002-0289-3610; alfiya.nurmukhanova777@gmail.com

Adilbayev, Nurken Amidollayevich – Doctoral student, al-Farabi Kazakh National University Almaty, Kazakhstan; SCOPUS Author ID: 58906640200; ORCID iD: ORCID iD: 0000-0002-8622-8588; adilbayev_nurken2@live.kaznu.kz

Shalkar, Akzhol – Master's student, al-Farabi Kazakh National University, Almaty, Kazakhstan; ORCID iD: 0009-0001-0485-0358; Shalkar.akzhol@gmail.com

EXPERIMENTAL STUDIES OF THE PERFORMANCE EFFICIENCY OF A WIND TURBINE WITH COMBINED BLADES

Tleubergenova A.Zh.[1,2], Dyusembayeva A.N.[1], Tanasheva N.K.[1,2], Bakhtybekova A.R. [1,2], Kutumova Zh.B.[1], Mukhamedrakhim A.R. [1,2]

[1] E.A. Buketov Karaganda University, Karaganda, Kazakhstan
[2] Scientific Research Center "Alternative Energy", Karaganda, Kazakhstan
*Corresponding author: akmaral.tzh7@mail.ru

Abstract. *This article studies the aerodynamic characteristics of a wind turbine at different streamline parameters. For this purpose, an experimental sample of the plant with combined power elements in rotating cylinders form with fixed blades was fabricated. The airflow velocity was varied, ranging from 3 to 12 m/s. The results of the experiment to study the variation of the angle α of the fixed blade position relative to the cylinder from the air flow velocity were analyzed. The changes in aerodynamic forces from the air flow velocity are graphically presented. It was found that at the optimal angle α = 0 ° of the fixed blade relative to the cylinder, the maximum values of aerodynamic forces were obtained. Graphs of the dependence of aerodynamic coefficients on the Reynolds number are also constructed, in which it is established that, at α= 0º, the minimum value of the lift coefficient is 0.012 N and the maximum value of the drag coefficient is 10.07 N at $Re = 1 \cdot 10^5$. The presented results show the effectiveness of the combined use of the and the fixed blade. The experimental results obtained on the aerodynamic parameters of a wind turbine can be used in the development of prototypes of installations designed for low wind speeds.*

Keywords: wind turbine, combined blades, wind tunnel T-1-M, flow velocity, drag force, lift force, Reynolds number.

1. Introduction

Wind energy is a promising project in the power generation sector due to its clean energy production and extensive wind resources around the world. Wind turbines can be installed at any scale to reduce the increasing energy demand [1]. Today, wind energy in many countries has become an independent branch of the economy and no longer requires additional subsidies. The wind energy development, a non-conventional source of energy, along with the energy problem in the country, helps to solve many economic as well as environmental issues. In particular, in the field of alternative energy, less money is spent each year with the work done. As a result, fossil fuel reserves are limited and do not have a negative impact on global climate change [2].

Kazakhstan has also voluntarily committed to reducing harmful carbon dioxide emissions to zero by 2050. Kazakhstan has renewable energy sources, including hydropower, wind and solar energy. The number of implemented renewable energy projects is growing every year [3]. Kazakhstan has the ability to build

wind turbines. Because the climate is favorable and there are enough areas for wind turbines to have a wind speed of more than 5 m/s.

Wind turbines serve in energyfield, which deals with the development of theoretical foundations, methods and technical means of converting wind energy into mechanical, thermal or electrical energy.The existing types of wind turbines differ in the design of installations, in power, as well as in the speed of rotation and location of the wind wheel. According to the axis of rotation of the wind wheel, there are two types: with a horizontal (HAWT) and vertical axis of rotation(VAWT) [4].

For vertical installations, i.e., the axis of rotation is located vertically relative to the earth, for horizontal installations, the axis of rotation is directed parallel to the axis of the earth. In practice, wind turbines are increasingly used with a horizontal axis of rotation[5]. In addition, there are other ways to convert wind energy. For example, the Savonia Rotor wind turbines [6] Bernoulli wind turbine utilizes the dynamic pressure effect and the Horizontal Flow Rotor [7] utilizes the momentum exchange effect.

This research paper presents a Magnus HAWT. A distinctive feature from other installationsis that the power elements are in the form of combined blades consisting of a rotating cylinder and a fixed blade.

2. Materials and research method

The aim of the work is to analyze the aerodynamic characteristics of a three-bladed wind turbine containing combined power elements. Experiments were conducted in a wind tunnel (Figure 1), which are channels in which an artificial airflow is created using a fan [8]. A wind tunnel is an apparatus that investigates the phenomena accompanying the rotation of bodies by creating a flow of air or gas for an experiment. The process when the movement of a body relative to air (or liquid) can be replaced by the movement of air flowing into a stationary body is the basis of the principle of reversibility of the process, which is the basis for conducting experiments in a wind tunnel.

To carry out the research work, a model of a wind turbine with combined blades has been developed. Combined blade operating mechanism - electric motors connected to the cylinders drive the cylindrical blades into rotational motion under the action of airflow, they rotate the wind wheel along with the fixed blades. To eliminate physical phenomena such as flow deformation behind the form cylinders of swirling flow, a fixed blade was added. Figure 1 shows a schematic diagram and an image of the experimental setup arrangement on the working part of the wind tunnel, where the fixed blade is located at different angles with respect to the cylinder axis rotation.

a)   b)

Fig. 1. A scheme (a) and a photo from the side of the wind turbine model (b) with combined blades:
1-generator, 2-cylinder, 3 - instantaneous blade, 4-mast.

The installation operation principle is based on the creation of a lifting force due to the difference in pressure on the blades. When a rotating cylinder is streamlined transversely, a reduced pressure is created on one side of the blade and an increased pressure on the opposite side, resulting in a lift force.

The new wind turbine design has the ability to increase lift by combining two force effects - rotation of a cylindrical element using the Magnus effect and a fixed blade (Figure 2). The wind wheel has cylinders that are activated by electric motors and begin to rotate around their axis. When the cylinder rotates, an additional force arises due to the Magnus effect, which interacts with the fixed blades and causes the entire

wind wheel to rotate. During the circular motion in the airflow in the upper part of the cylinder, the air flow velocity and the cylinder surface velocity are equal and add up, which leads to an acceleration of the flow and an increase in its velocity.
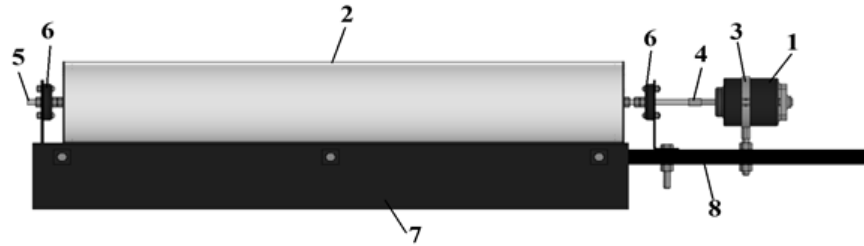
Fig. 2. The design of the combined blade: 1 - electric motor; 2 - cylinder; 3 - electric motor mount; 4 - coupling; 5 - connection between cylinder and engine; 6 - bearings; 7 - fixed blade; 8 - blade base.

The process of operation of this device can be explained as follows:

When voltage is applied to the electric motor (1), rotation is transmitted through the coupling (4) to the axis of rotation (5) and the cylinder (2) mounted on bearings (6). Bearings (6), a fixed blade (7) and an electric motor mount (3) are fixed to the base (8).

The geometric dimensions of the wind turbine layout are shown in Table 1.

Table 1. Geometric dimensions of the wind turbine layout

Parameter	Value
Cylinder length	205 mm
Cylinder diameter	50 mm
The length of the fixed blade	225 mm
Width of the fixed blade	25 mm
Diameter of the wind wheel	450 mm
Mast length	420 mm

The measurement error of aerodynamic forces and their moments is (5-7)%.

3. Calculation of aerodynamic characteristics

The lightweight construction minimizes aerodynamic drag and provides higher wind energy efficiency. The device starts operating at wind speeds of 3-5 m/s and operates effectively at wind speeds of 8-12 m/s.

The lift coefficient is found by the next formula [9]:

$$C_y = \frac{\Delta F_y}{\rho \cdot \frac{u^2}{2} \cdot S} \text{ , or } C_y = \frac{2F_y}{\rho u^2 \cdot S} . \tag{1}$$

And the drag coefficient is determined by the following formula:

$$C_x = \frac{\Delta F_x}{\rho \cdot \frac{u^2}{2} \cdot S} \text{ , or } C_x = \frac{2F_x}{\rho u^2 \cdot S} . \tag{2}$$

Here ΔF_x – drag force, [N]; ΔF_y – lift force, [N]; ρ – air density, [kg/m^3]; u– air flow velocity, [m/s]; S – midsection area, [m^2].

As a similarity criterion, the ratio between the inertia force and the viscosity force used to determine is the Reynolds number:

$$\text{Re} = \frac{u \cdot d_c}{\nu} , \tag{3}$$

where dc – cylinder diameter, [m]; ν – kinematic viscosity of air, [m^2/s].

Constant values of density and viscosity were used in laboratory experiments: $\rho = 1{,}21$ kg/m³, $v = 1.49 \times 10^{-5}$ m²/s, accordingly.

4. Discussion of results

The maquette aerodynamic characteristics such as drag force and lift force of the wind turbine were determined at flow velocities ranging from 3 m/s to 12 m/s (Figures 3 and 4).
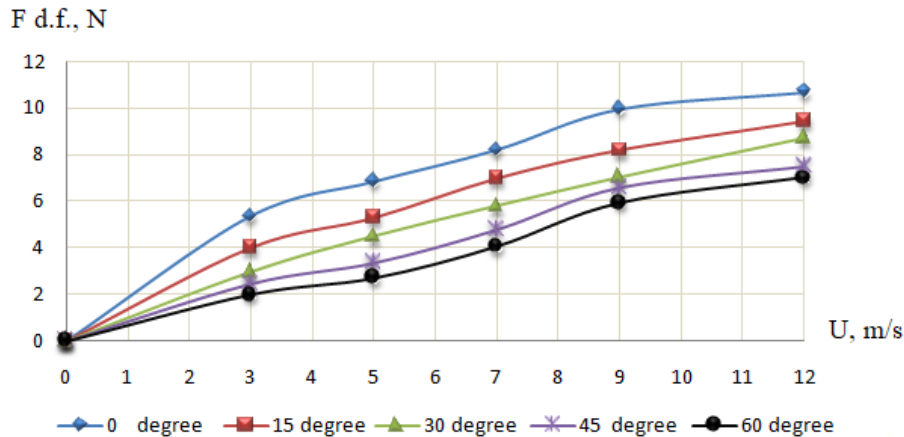
Fig. 3. Dependence of drag force on flow velocity

Figure 3 shows that the drag force also increases with increasing air flow velocity when the fixed blade is located at different distances relative to the cylinder axis rotation. The reason for the increase of drag force is that a flow travelling at a certain velocity action on the surface of a body that is exposed in its path. The magnitude of this force is directly proportional to the flow velocity. The drag force is inversely related to this action. As the flow velocity increases, the drag force of the investigated wind turbine under the pressure force also increases. Hence, the drag force increases with increasing airflow velocity. The drag force of the cylinder is also affected by the number of rotations.

Figure 4 below shows the change in the lifting force of the installation from the flow rate and angle. In Figure 3, we see an increase in lift force from 0.01-0.2 N to 0.41-1.07 N as the flow velocity increases from 3 m/s to 12 m/s. It can be seen on the graph that when the air flow rate increases, the lifting force decreases by almost 20-30% with increasing angle.
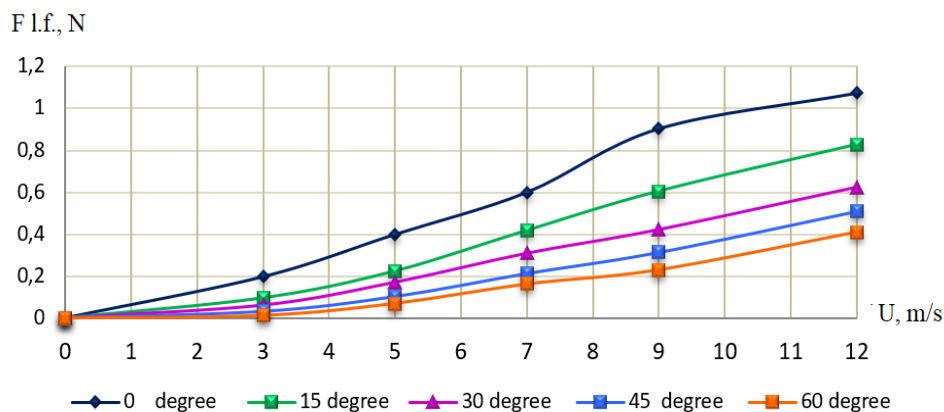
Fig. 4. Dependence of lift force on flow velocity

The explanation for this is the process of slowing down the flow at the back of the rotating cylinder [10]. The dependence shows that, at the maximum speed at 12 m/s the lift force is equal to 1.07 N, 0.83 N, 0.62 N, 0.51 N, 0.41 N, further the lift force stabilises, i.e. no increase is observed.

The nature of the growth of the lines of the obtained results of the dependencies of aerodynamic forces does not contradict the previous results [11,12]. Compared with the Magnus wind turbine [13], there are blades in the form of cylinders, the obtained values of the drag force are 1.5 times lower, but the lift values are 0.7-9 times higher.

The measurement uncertainty was analyzed [14] in order to find the true measurement value, and measurement errors were calculated (Tables 2).

Table 2. The results of calculating the uncertainty of the drag force.

U, m/s	Arithmetic mean	Uncertainty by type A	Uncertainty by type B	Total standard uncertainty	Standard deviation	Confidence interval	Error rate, %
3	5.5	±0.01	±0.02	±0.02	0.02	0.02	7.03
5	6.9	±0.01	±0.02	±0.02	0.02	0.02	7.13
7	8.2	±0.02	±0.03	±0.03	0.02	0.02	6.98
9	10.01	±0.01	±0.05	±0.05	0.03	0.03	7.10
12	10.5	±0.01	±0.06	±0.06	0.04	0.05	7.08

Table 3. Results of the calculation of the uncertainty of the lifting force.

U, m/s	Arithmetic mean	Uncertainty by type A	Uncertainty by type B	Total standard uncertainty	Standard deviation	Confidence interval	Error rate, %
3	0.2	±0.01	±0.01	±0.01	0.02	0.02	7.01
5	0.4	±0.01	±0.01	±0.01	0.03	0.03	7.04
7	0.6	±0.02	±0.03	±0.03	0.03	0.03	6.96
9	0.9	±0.02	±0.04	±0.04	0.02	0.02	7.07
12	1.05	±0.01	±0.06	±0.06	0.03	0.03	7.10
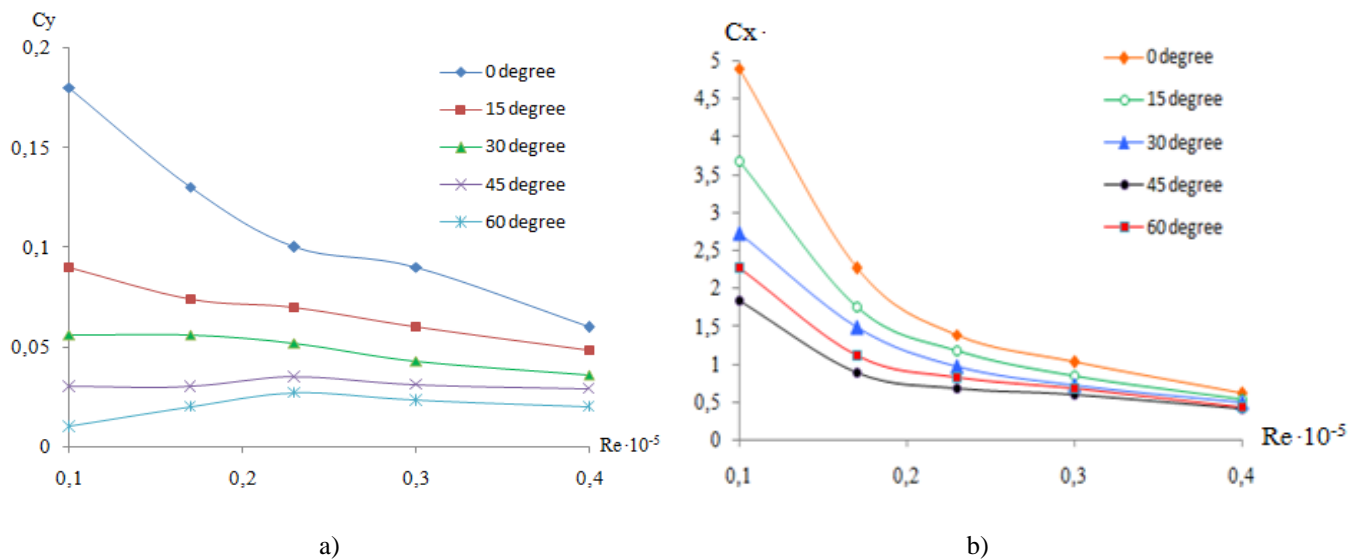
Fig. 4. Dependences of lift coefficient a) and drag force coefficient b) on Reynolds number

As shown in Figures 4a and 4b, when the fixed blade is positioned at an angle of 0 degrees relative to the cylinder, the optimum values of lift, and at Reynolds number $1 \cdot 10^{-5}$ are obtained drag force coefficients equal 0.18 and 4.9. Compared to the other three samples at 15°, 30°, and 45°, at 60°, the combined blade produces maximum drag force and minimum lift force. Under the influence of rotational movements of the cylinders, a vortex zone is formed behind the cylinders with a sufficient volume of reverse air flows, and their dimensions change at the flow rate.

5. Conclusion

In performing experimental studies to determine the efficiency of a wind turbine with combined blades:

-a wind turbine consisting of three combined blades with a rotating cylinder and a fixed blade was developed;

- the lift force and drag force dependence on the velocity when changing the degrees of the fixed blade has been determined;

-it is established, at the location of the fixed blade at 0 degrees relative to the cylinder Fd.f.= 10,7 N and Fl.f. = 1,074 N;

- it is established that the values of drag and lift force coefficients depending on the Reynolds number are optimal at α=0 degrees.

References

1 Tasneem Z., Noman A.A., Das S. K., Saha D. K., Islam R., Ali F., Badal F.R., Ahamed H., Moyeen S. I., Alam F. (2020) An analytical review on the evaluation of wind resource and wind turbine for urban application: Prospect and challenges. *Developments in the Built Environment*. 4, 100033. DOI:10.1016/j.dibe.2020.100033.

2 Boiko N. (2023) Winds of change in the economy of Kazakhstan's future. Available at: https://dknews.kz/ru/eksklyuziv-dk/293675-veter-peremen-v-ekonomike-budushchego-kazahstana. [in Russian]

3 Yershina A.K., Sakipova S.E. (2020) A method for increasing the efficiency of a wind turbine. *Eurasian Physical Technical Journal*. 17, 2(34), 73 – 77. DOI:10.31489/2020No2/73-77.

4 Mabrouk I.B., El Hami A. (2019). Effect of number of blades on the dynamic behavior of a Darrieus turbine geared transmission system. *Mechanical Systems and Signal Processing*, 121, 562-578. DOI:10.1016/j.ymssp.2018.11.048.

5 Kishinami K., Taniguchi H., Suzuki J., Ibano H., Kazunou T., Turuhami M. (2005). Theoretical and experimental study on the aerodynamic characteristics of a horizontal axis wind turbine. *Energy,* 30(11-12), 2089-2100. DOI:10.1016/j.energy.2004.08.015.

6 Fujisawa,N., Gotoh F. (1994) Experimental study on the aerodynamic performance of a Savonius rotor. DOI:10.1115/1.2930074.

7 Shigemitsu T., Fukutomi J., Toyohara M. (2016) Performance and flow condition of cross-flow wind turbine with a symmetrical casing having side boards. International Journal of Fluid Machinery and Systems, 9(2), 169-174. https://doi.org/10.5293/IJFMS.2016.9.2.169

8 Tanasheva, N.K., Tleubergenova, A.Zh., Shaimerdenova, K.M., Minkov, L.L. & Uzbergenova, S.Zh. (2021). Investigation of the aerodynamic forces of a triangular wind turbine blade for the low wind speeds. *Eurasian physical technical journal*, 18(4 (38), 59-64. DOI:10.31489/2021No4/59-64.

9 Tleubergenova A.Z., Dyusembayeva A.N., Tanasheva N.K., Kyzdarbekova S.S., Mukhamedrakhim A.R. (2023) Analysis of aerodynamic characteristics of a two-bladed wind power plant containing combined power elements. *Bulletin of the Karaganda University" Physics Series",* 111(3), 143-150. DOI:10.31489/2023ph3/143-150.

10 Battisti L., Benini E., Brighenti A., Dell'Anna S., Castelli M.R. (2018) Small wind turbine effectiveness in the urban environment. *Renewable energy,* 129, 102-113. DOI:10.1016/j.renene.2018.05.062.

11 Luo D., Huang D., Wu G. (2011) Analytical solution on Magnus wind turbine power performance based on the blade element momentum theory. *Journal of Renewable and Sustainable Energy*, 3(3). DOI:10.1063/1.3588039.

12 Lukin A., Demidova G.L., Lukichev D.V., Rassõlkin A., Kallaste A., Vaimann T., Belahcen A. (2020). Experimental prototype of high-efficiency wind turbine based on magnus effect. *27th International Workshop on Electric Drives: MPEI Department of Electric Drives 90th Anniversary (IWED)*. 1-6. DOI:10.1109/IWED48848.2020.9069565.

13 Tanasheva N.K., Bakhtybekova A.R., Shaimerdenova G.S., Sakipova S.E., Shuyushbaeva N. (2022) Modeling aerodynamic characteristics of a wind energy installation with rotating cylinder blades on the basis of the Ansys Suite. *Journal of Engineering Physics and Thermophysics*, 95(2), 457-463. DOI:10.1007/s10891-022-02500-3.

14 Tleubergenova A.Z., Tanasheva N.K., Shaimerdenova K. M., Kassymov S.S., Bakhtybekova A.R., Shuyushbayeva N.N., Ranova G.A. (2023) Mathematical modeling of the aerodynamic coefficients of a sail blade. *Advances in Aerodynamics,* 5(1), 14. DOI:10.1186/s42774-023-00140-6.

AUTHORS' INFORMATION

Tleubergenova, Akmaral Zharylkasynovna – PhD student, E.A. Buketov Karaganda University, Karaganda, Kazakhstan; ORCID iD: 0009-0009-5152-0050; akmaral.tzh7@mail.ru

Dyusembayeva, Ainur Nurtaevna – PhD, Postdoctoral fellow, E.A. Buketov Karaganda University, Karaganda, Kazakhstan; ORCID iD: 0000-0001-6627-7262; aikabesoba88@mail.ru

Tanasheva, Nazgul Kadyralievna – PhD, Associate Professor, E.A. Buketov Karaganda University, Karaganda, Kazakhstan; ORCID iD: 0000-0003-4273-0960; nazgulya_tans@mail.ru

Bakhtybekova, Asem Ravshanbekovna – PhD, Researcher, E.A. Buketov Karaganda University, Karaganda, Kazakhstan; ORCID ID: 0000-0002-2018-8966; asem.alibekova@inbox.ru

Kutumova, Zhibek Baysultanovna – Master (Sci.) Senior Lecture, E.A. Buketov Karaganda University, Karaganda, Kazakhstan; ORCID ID: 0009-0001-1392-6457; zhibek_kutumova@mail.ru

Mukhamedrakhim, Almat Ramazanuly – Student, E.A. Buketov Karaganda University, Karaganda, Kazakhstan; ORCID ID: 0009-0003-4242-6114; almatmuhamedrahim@gmail.com

.

UDC 537.322

DIRECT CONTACT RESISTANCE MEASUREMENT DURING THERMOELECTRIC TESTING

Soldatov A.I.[1], Soldatov A.A.[1], Abouellail A.A.[2], Kostina M.A.[1]

[1] National Research Tomsk Polytechnical University, Tomsk, Russia,
[2] Sphinx University, New Asyut, Egypt
*Corresponding author: mariyakostina91@mail.ru

Abstract. The article analyzes the influence of the contact resistance of the electrodes on the inspection result. It is shown that as the value of the measuring resistor increases, the permissible value of the contact resistance of the electrodes with the test sample increases. An indirect method for monitoring contact resistance has been proposed, which consists of passing a stable high-frequency current through the contact resistance and measuring the voltage across this resistance. The variation of relative voltage across the measuring resistor with respect to the total contact resistance has been graphed. The maximum allowable contact resistance has been determined to ensure that the measured thermoelectric EMF differs from the true value by no more than 10%. The proposed method allows to measure contact resistance directly in the process of monitoring thermoelectromotive force.

Keywords: thermoelectromotive force, hot electrode, cold electrode, contact resistance, current generator, filter, measuring resistor.

1. Introduction

The thermoelectric method is widely used for rapid testing of metals and alloys [1, 2]. It allows to define the size of the decarburized layer and the quality of heat treatment, to sort supplied rolled metal and sort finished products by steel grade, to determine the thickness of the steel carburization layer, and to determine the amount of plastic deformation [3-12]. The thermoelectric dependence of X5CrNi18-10 stainless steel on the magnitude of plastic deformation was studied in [13], and the thermoelectric characteristics of plastically deformed steels ST3, 08KP AND 12H18N10T were studied in [14].

At the beginning of the 21st century, the thermoelectric method began to be used to test the temperature of the weld in the friction stir welding process, based on measuring the temperature with a thermocouple formed by the tool-workpiece connection [15-19]. The thermoelectric method was also used to control the thermal resistance of the cooling radiator-body of a power semiconductor element system [20]. Another area of application of the thermoelectric method is the measurement of the Seebeck coefficient of materials and alloys [21-23]. The thermoelectric method has been successfully applied to inspect the thermal resistance of a thermal interface and assess the degree of hydrogenation of a titanium alloy [24-27].

To solve problems of thermoelectric testing, several types of thermoelectric testing devices are currently commercially produced. The ACTTR company from Taiwan produces SETARAM SeebeckPro for Seebeck coefficient measurement. Linseis Messgeraete GmbH from Germany produces a line-up of Seebeck coefficient and electrical resistance devices: SR-1, SR-3, etc. NETZSCH from Germany produces SBA 458

NEMESIS for measuring Seebeck coefficient. The Japanese ULVAC GmbH produces "ZEM-3" for measuring thermoelectromotive force (thermoEMF) and the Seebeck coefficient. Russian companies produce OMET, METEK and T-3SP devices.

The time consumed by the thermoelectric method does not exceed 3-5 seconds, which is an advantage of this method. The small dimensions of thermoelectric flaw detectors and the simple testing technique are additional advantages of this method [28].

One of the disadvantages of thermoelectric inspection devices is the presence of contact resistance at the points of connection of the electrodes with the test sample. The magnitude of the contact resistance will depend on the force of pressing the electrodes to the sample, the angle of inclination of the sensor, and the distribution of the load over the area of the electrodes [29-30]. This is especially evident during manual testing, in which it is impossible to ensure the same pressing force and the same deviation of the electrodes between the normal and the test sample. In addition, the contact resistance will depend on the quality of preparation of the surface of the electrodes and the tested product, on the presence of an oxide film, etc. In particular, in it is noted that upon the presence of an oil film on the surface of the electrodes or the test product, the contact resistance can increase to 100 Ω and higher. The influence of contact resistance on the thermoEMF value was studied in [31]. The authors proposed a way to reduce the contact resistance, which led to a decrease in the measurement error of thermoEMF. The only device that uses a contact quality monitoring system is the SBA 458 NEMESIS device from the German company NETZSCH. The authors also encountered complaints about the manufactured thermoelectric control device "TERMOTEST-1". Consumers noted low repeatability of results when taking multiple measurements of the same product. The analysis carried out by the authors showed that the low repeatability of the testing results was caused by high contact resistance with insufficient pressing force of the measuring electrodes to the test sample.

2. Problem statement

A thermoelectric monitoring device consists of an electronics unit and a sensor, which can be used for direct or differential measurement of thermoEMF. In the case of direct measurement of thermoEMF, the sensor consists of two electrodes: hot and cold (Fig. 1.a). For differential measurement of thermoEMF, the sensor must have two hot electrodes and two cold electrodes (Fig. 1.b).
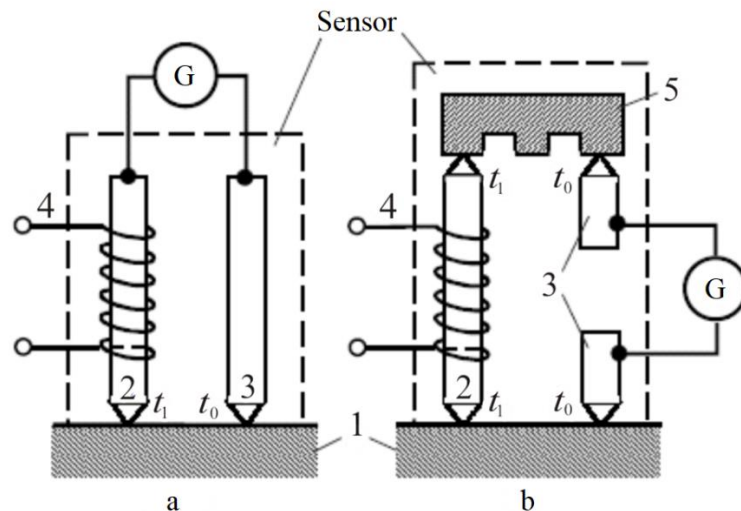
Fig.1. Sensor of a thermoelectric device, a – for direct measurement of thermoEMF, b – for differential measurement of thermoEMF, 1 – product under test; 2 – hot electrode; 3 – cold electrode; 4 – heater; 5 – standard sample (reference); G - galvanometer

The equivalent electrical circuit of the sensor for direct measurement of thermoEMF consists of contact thermoEMF E_1 and E_2, internal resistances of these thermoEMF R_1 and R_2, and contact resistances of each electrode R_3 and R_4 (Fig. 2). The current in the circuit (Fig. 2) will be determined by the internal resistance of the galvanometer, the internal resistances of the thermoEMF sources R_1 and R_2, and the contact resistances R_3 and R_4:

$$I = \frac{E_1 + E_2}{R_1 + R_2 + R_3 + R_4}.$$

The internal resistance of thermoEMF sources made of different materials can be in the range from 0.01 to 1 Ω. If the total contact resistance $R_c = R_3 + R_4$ changes from 0.01 to 100 Ω, then the thermoEMF source current will change by several orders. In practice, it is not the current that is measured, but the voltage; for this, instead of a galvanometer, a precision measuring resistor R_{ref} is used, on which the voltage resulting from the flow of current is measured. An equivalent circuit for this option is shown in Fig. 3, where E_1 – contact EMF of the hot electrode with an inspected sample, E_2 – contact EMF of the cold electrode with an inspected sample, R_1 – internal resistance of the contact EMF of the hot electrode with the inspected sample, R_2 – internal resistance of the contact EMF of the cold electrode with the inspected sample, R_3 – contact resistance of the hot electrode with the inspected sample, R_4 – contact resistance of the cold electrode with the inspected sample, G – galvanometer, R_c – total contact resistance, R_{ref} – measuring resistance.
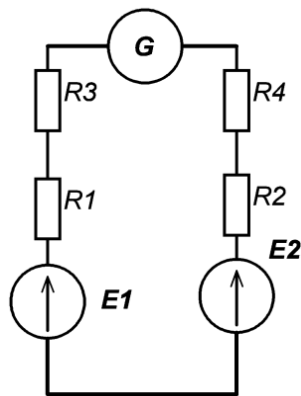
Fig.2. Equivalent electrical circuit of a thermoelectric sensor　　　**Fig.3**. ThermoEMF measurement circuit
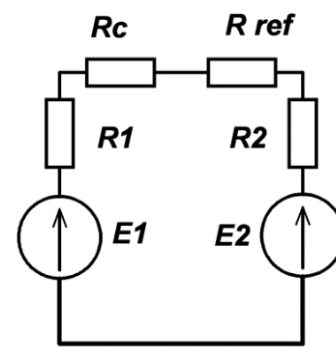
The voltage across the measuring resistor will be determined from the expression:

$$V = R_{ref} \frac{E_1 + E_2}{R_1 + R_2 + R_C + R_{ref}}.$$

The results of calculating the relative change in voltage across the measuring resistor when the total contact resistance R_c changes from 0.1 Ω to 10 kΩ for three resistances of the measuring resistor R_{ref} are shown in Fig.4. The internal resistance of the thermoEMF source was taken to be 0.1 Ω.
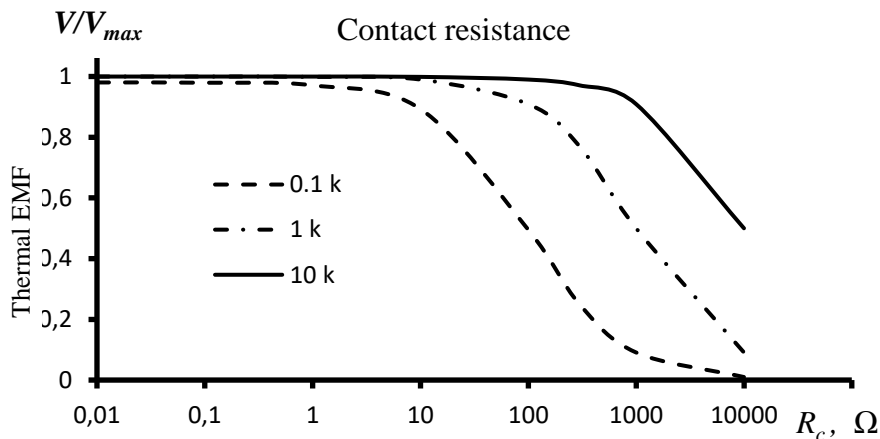
Fig.4. Dependence of the relative voltage across the measuring resistor on the total contact resistance for three measuring resistor values

From Fig. 4 it is clear that if a measuring resistor of 0.1 kΩ is used, the measured voltage will be 11% less than the true one with a 10 Ω contact resistance, and the measured voltage will be 50 % less than the true one with a 100 Ω contact resistance. If a 1 kΩ measuring resistor is used, then a 10 % decrease in measured voltage is observed for a 100 Ω contact resistance, and a 50 % decrease is observed for a 1 kΩ contact resistance. For a measuring resistance of 10 kΩ, a 10 % decrease in measured voltage is observed at a contact resistance of 1 kΩ. The permissible value of contact resistance, at which the measured thermoEMF value differs from the true value by no more than 10 %, should be no more than 9 Ω (measuring resistance 0.1 kΩ), 100 Ω (measuring resistance 1 kΩ) or 1 kΩ (measuring resistance 10 kΩ).

3. Method of Solution

Variations in contact resistance leads to variations in measurement results. To increase the reliability and repeatability of testing results, a contact resistance monitoring circuit is proposed. To do this, you can use an indirect method, which consists in measuring the voltage across the contact resistance thanks to the flow of a stable current. In order to find out the value of the total resistance of the contacts of the electrodes with the inspected product, a circuit shown in Fig. 5 was proposed.

The current from the generator flows through two circuits: through the measuring resistor R_{ref} and through series-connected resistors $R_c+R_1+R_2$. The equivalent load resistance for a stable current generator will be determined by the expression:

$$R_L = \frac{R_{ref} \cdot (R_C + R_1 + R_2)}{R_{ref} + R_C + R_1 + R_2}. \tag{1}$$

The results of the calculation using formula 1 of the dependence of the load resistance of the current generator on the contact resistance for three values of the measuring resistor are shown in Fig. 6. The following values were used in the calculation: $R_1+R_2 = 0.1$ Ω, $R_{ref} = 0.1$ kΩ; 1 kΩ; 10 kΩ.
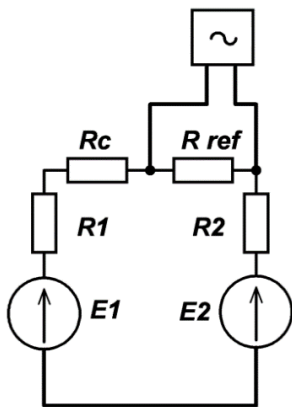
Fig.5. E Schematic diagram of the circuit used in the indirect measurement of the total contact resistance
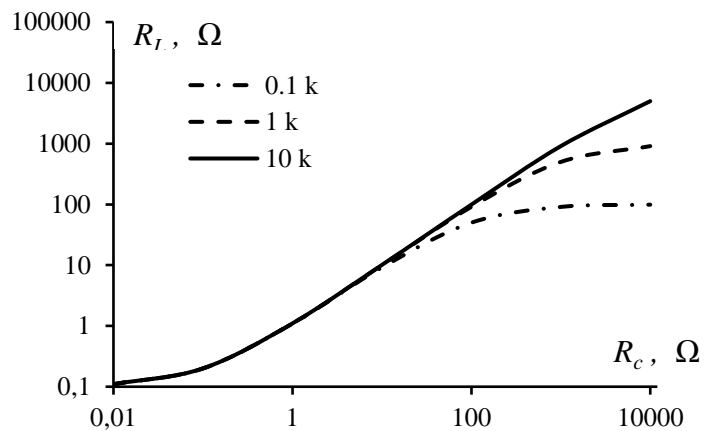
Fig.6. Dependence of the current generator load resistance on contact resistance

As can be seen from Fig. 6, with an increase in contact resistance, the load resistance of the stable current generator increases. At large values of contact resistance, it tends to the resistance of the measuring resistor. An increase in the load resistance of the current generator will lead to an increase in the voltage across the load, which will be determined by Ohm's law:

$$V_L = IR_L = I \frac{R_{ref} \cdot (R_C + R_1 + R_2)}{R_{ref} + R_C + R_1 + R_2}, \tag{2}$$

where I is the flowing generator current.

The modeling results of changes in the relative voltage across the load, performed in accordance with formula 2 for various values of the measuring resistance, are given in Table 1.

Table 1. Simulation results of relative voltage across the load

R_c, kΩ	$V_L / V_{L\,max}$		
	$R_{ref} = 0,1$ kΩ	$R_{ref} = 1$ kΩ	$R_{ref} = 10$ kΩ
0,01	0,00111	0,000121	2,19996E-05
0,1	0,002016	0,00022	3,9999E-05
1	0,010989	0,001209	0,000219975
10	0,092652	0,010999	0,002017952
100	0,505252	0,10009	0,019821487
1000	0,918189	0,550022	0,181833801
10000	1	1	1

The graphical dependence of the relative voltage across the current generator load on the contact resistance is shown in Fig. 7.
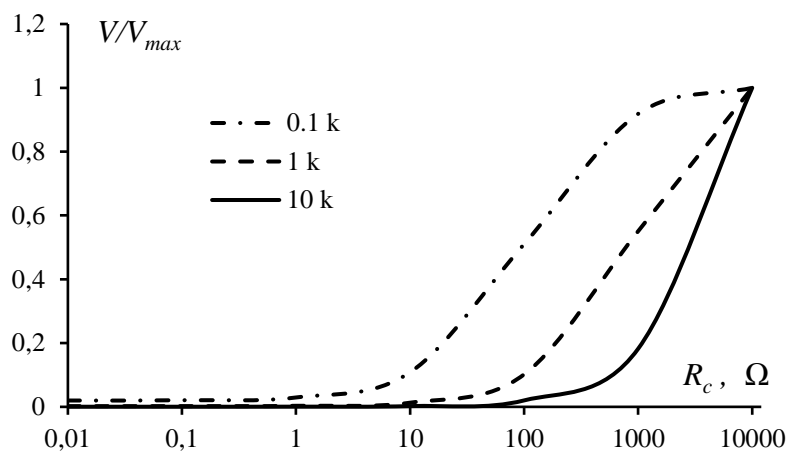
Fig.7. Dependence of the relative voltage on the load of the current generator on the contact resistance for three values of the measuring resistor

It is clear in Fig. 7 that if the contact resistance is less than 1 Ω, then the relative change in voltage across the load does not exceed 1% for a 0.1 kΩ measuring resistor and decreases by an order of magnitude for a 1 kΩ measuring resistor and by two orders of magnitude for a 10 kΩ measuring resistor. Taking into account the results presented in Fig. 4 for a contact resistance of 9 Ω (at R_{ref} = 0.1 kΩ), the relative change in voltage across the load of the current generator will be 10%, the same change will be for a contact resistance of 100 Ω (at R_{ref} = 1 kΩ) and 1 kΩ (at R_{ref} = 10 kΩ).

Connecting the current generator to the electrodes and determining the voltage at the contact resistance is explained in Fig.8. The current generator produces a sinusoidal current of constant amplitude I, independent of the load resistance. When this current flows through the measuring resistor, a voltage V_L appears. The same resistor is the load of the thermoEMF source and the voltage V_{EMF} is measured on it. Since V_{EMF} is a voltage with zero frequency, and V_L is a high-frequency voltage, then to separate these voltages, bandpass and band-stop filters with a resonant frequency equal to the frequency of the current generator are used.

From the output of the bandpass filter, the voltage is supplied to the amplifier, then to the rectifier, and to the analog-to-digital converter, from which the binary voltage code is sent to the microcontroller, which calculates the total contact resistance based on expression (4), after conversion of which we obtain

$$R_C = \frac{IR_{ref} \cdot (R_1 + R_2) - V_L(R_1 + R_2) - V_L R_{ref}}{V_L - IR_{ref}} \quad . \tag{3}$$

Taking into account the fact that $(R_1 + R_2) << R_{ref}$, expression 3 simplifies to the form:

$$R_C = \frac{V_L R_{ref}}{I R_{ref} - V_L} = R_{ref} \frac{1}{\dfrac{I R_{ref}}{V_L} - 1} . \tag{4}$$
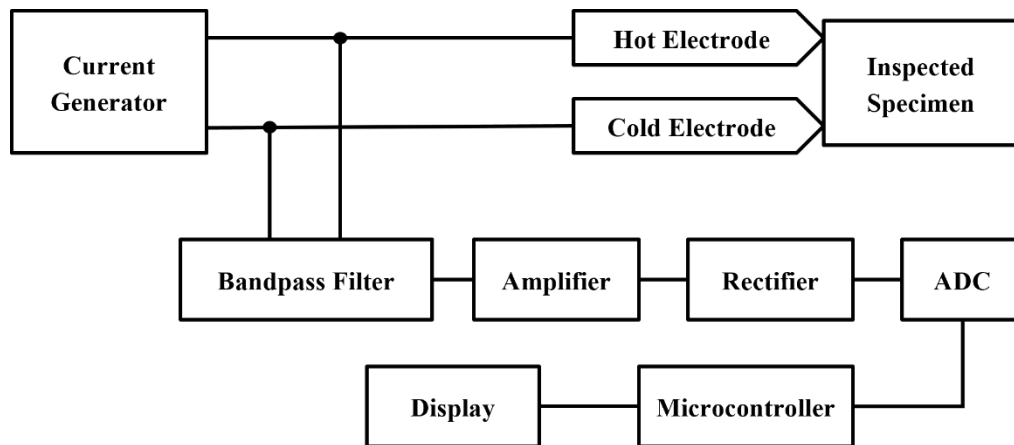
Fig.**8**. Block diagram of the control unit for the total contact resistance of the electrodes with the inspected product

The terms I and R_{ref} in expression (4) are constant quantities, therefore, to calculate the contact resistance it is necessary to measure only V_L. The proposed method allows you to check the value of the total contact resistance directly in the process of measuring thermoEMF.

4. Experimental Investigation

To conduct experimental studies, a stand was made containing an electronics module connected to a personal computer, a sensor and software that allows to display the value of thermoEMF and the total contact resistance (Fig. 9) [32]. The electronics module includes a system for heating and stabilizing the temperature of the hot electrode, a thermoEMF measurement system and a system for monitoring the total contact resistance. The measuring resistor in the experimental setup was 100 Ω with a tolerance of 1 %.

The hot electrode heating system and temperature stabilization system consist of Temperature Sensor 1, Temperature Sensor 2, heater, and microcontroller (Fig. 9). Information about the temperature of the hot electrode comes to the microcontroller from Temperature Sensor 1, and about the temperature of the cold electrode from Temperature Sensor 2. The microcontroller determines the temperature difference between the hot and cold electrodes and generates a control action for the heater to maintain the temperature difference between the hot and cold electrodes of 100 ºC.

The total contact resistance monitoring system consists of a high-frequency stable current generator, a bandpass filter, an amplifier, an AC voltage rectifier, an analog-to-digital converter (ADC2), and a microcontroller. A stable current generator produces an alternating current that flows through the contact resistance of the electrodes with the test sample. The voltage resulting from the flow of this current is isolated by a bandpass filter, amplified, rectified, and converted into a digital code that is sent to the microcontroller. The value of this voltage is used to determine the total contact resistance in accordance with formula (4).

The thermoEMF measurement system consists of a band-stop filter for suppressing the variable component, an amplifier, an analog-to-digital converter (ADC1) and a microcontroller. The voltage taken from the hot and cold electrodes, after suppressing the alternating component in the band-stop filter, is amplified, converted into a digital code and supplied to the microcontroller. The received information is transferred to a personal computer via the USB interface.

Fig.9. Structural diagram of the experimental installation

The computer software allows to display the obtained data in the form of a graphical dependence and save it in a separate file. The operator interface consists of two tabs (Fig. 10). The first tab is called "Charts" and allows to display data received continuously from the experimental setup. The second tab is called "Settings". This tab displays control data for the experimental setup (Fig. 11).

The "Charts" tab contains several windows. There is "Sum" at the top left of the window shown in Fig.10 displays the total thermoEMF value, and "Number of Values" displays the number of values involved in thermoEMF averaging, and "Average" displays the calculated average thermoEMF value. The next white box to the right shows the temperature of the hot electrode. The active tab shown in Fig. 10 contains two graphs. The top graph displays thermoEMF in green and contact resistance in red. Moreover, the scale of the axis for displaying contact resistance is reduced by 100 times, i.e. The displayed value must be increased by 100 times. The bottom graph displays thermoEMF in green and the temperature of the hot electrode in red, provided that the contact resistance is less than the set threshold value and the duration of this process is more than 1 second.

In order to explain the presented values in Fig. 10 and take them as an example, it is important to take into account that the x-axis of the top graph records time in 10 ms increments. The measurement process begins at a time corresponding to 2.2 s (count number 220). Until this time, the thermoEMF value is zero and the contact resistance is 4200 Ω, which corresponds to the maximum displayed value. In the reading interval 220…260, fluctuations in contact resistance up to 300 Ω are observed, the thermoEMF value is -20 μV. The calculated value is -18 μV. In the sampling interval of 280…300 and 320…340, the contact resistance is near zero, however, the measurement process was only 20 readings (200 ms), which is less than 1 second and therefore this data is not displayed in the lower graphic window. In the sampling interval 370…515, the contact resistance is about 10 Ω, the measurement process was 1.45 seconds. (515-370=145 counts), which is more than 1 second. and this interval is displayed in the lower window. From the bottom graph it can be seen that the temperature of the hot electrode is 132 ºC, and the thermoEMF is -69 μV. The graph shows a transient process that takes about 50 ms (counts from 0 to 5).

The "Settings" tab is used to control, manage and test the experimental setup (Fig. 11). The hot electrode heating system and temperature stabilization system consist of Temperature Sensor 1, Temperature Sensor 2, heater, and microcontroller (Fig. 9). Information about the temperature of the hot electrode comes to the microcontroller from Temperature Sensor 1, and about the temperature of the cold electrode from Temperature Sensor 2. The microcontroller determines the temperature difference between the hot and cold electrodes and generates a control action for the heater to maintain the temperature difference between the hot and cold electrodes of 100 ºC.

Fig.10. The developed computer software with the "Charts" tab on
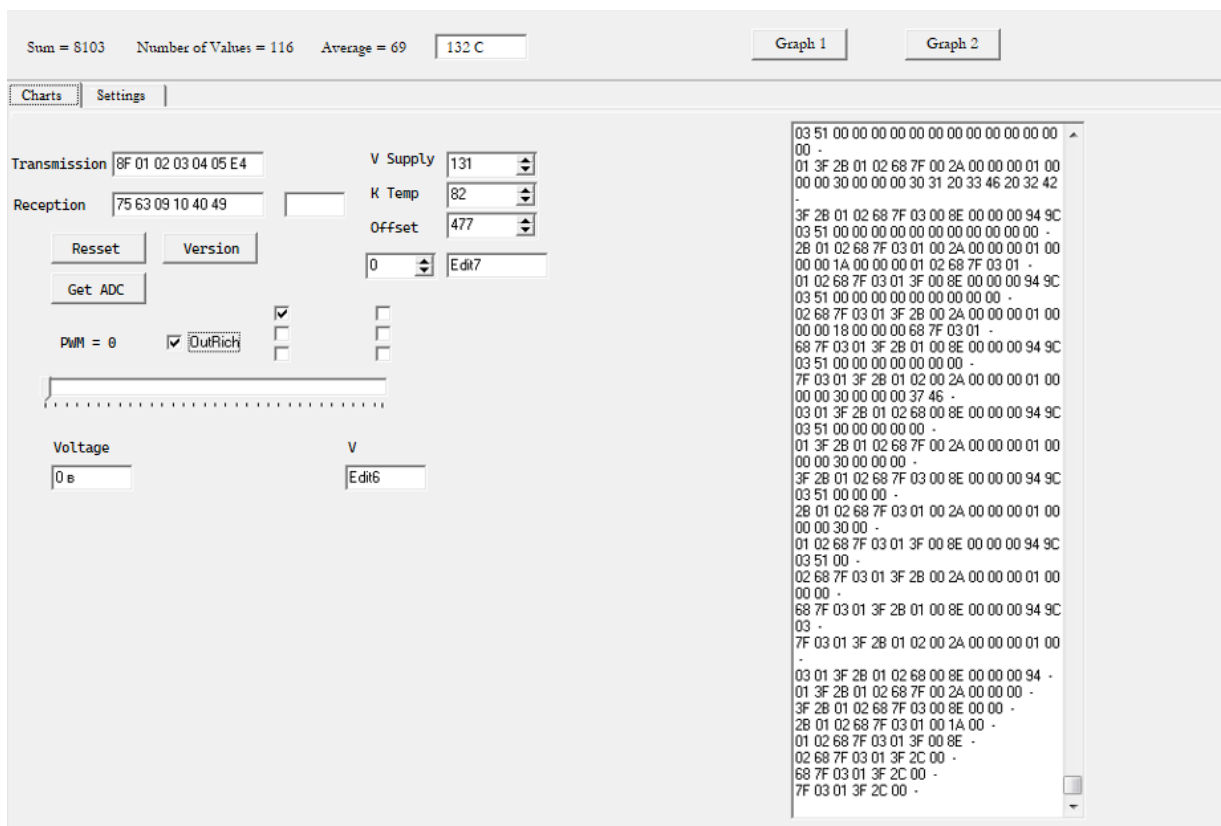
Fig.11. The developed computer software with the "Settings" tab on

The total contact resistance monitoring system consists of a high-frequency stable current generator, a bandpass filter, an amplifier, an AC voltage rectifier, an analog-to-digital converter (ADC2), and a microcontroller. A stable current generator produces an alternating current that flows through the contact resistance of the electrodes with the test sample. The voltage resulting from the flow of this current is isolated by a bandpass filter, amplified, rectified, and converted into a digital code that is sent to the microcontroller. The value of this voltage is used to determine the total contact resistance in accordance with formula (4).

The thermoEMF measurement system consists of a band-stop filter for suppressing the variable component, an amplifier, an analog-to-digital converter (ADC1) and a microcontroller. The voltage taken from the hot and cold electrodes, after suppressing the alternating component in the band-stop filter, is amplified, converted into a digital code and supplied to the microcontroller. The received information is transferred to a personal computer via the USB interface.
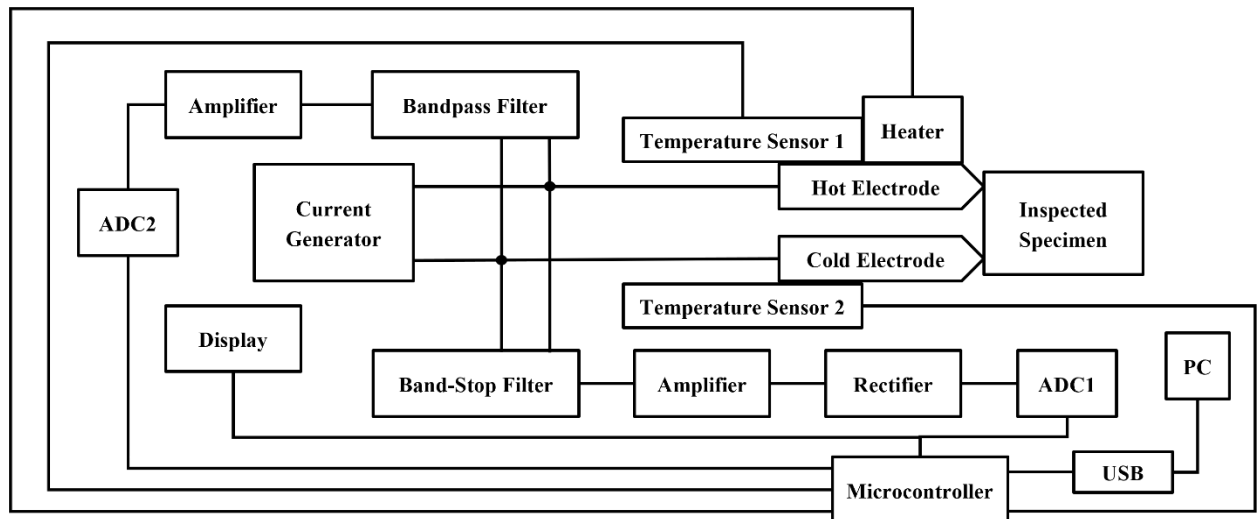
The "Reset" button allows to set the stand to its original state. The "Version" button allows you to display the name of the current version of the microcontroller program. The "Get ADC" button is used to check the operation of the analog-to-digital converter. The "V Supply" box displays supply voltage counts, whereas the "K temp" box shows a coefficient for calculating the temperature of the hot electrode. In the "Offset" window, you set the offset of the thermocouple characteristic for measuring the temperature of the hot electrode. The right window displays data coming from the test bench. The "Settings" tab is used during the initial setup of the experimental stand.

5. Conclusion

The conducted studies showed the influence of contact resistance on the result of inspection by the thermoelectric method. A method for monitoring contact resistance has been proposed and investigated, which consists of measuring the voltage across resistance when current flows from a high-frequency generator, which makes it possible to measure contact resistance directly in the process of monitoring thermoEMF.

The accuracy of measuring contact resistance depends on the accuracy of measuring the high-frequency voltage after rectification, which is determined by the ADC error and the quantization step. Modern microcontrollers have built-in ADCs, the quantization step of which is 2.5 mV, and the absolute error does not exceed 2 or 3 least significant digits of the ADC. In addition, the accuracy of the contact resistance measurement will be affected by the stability of the voltage and current of the high-frequency generator. In practical implementation, the total error in determining the contact resistance did not exceed 10%. The proposed method is advisable to use with manual testing devices when it is impossible to ensure the same pressing force of the sensor to the test sample during repeated measurements. In automated thermoEMF measurement systems, the clamping force is maintained the same in each measurement cycle and, in this manner, the potential for encountering this problem is eliminated. In the current case, the existing standards do not take into account the magnitude of contact resistance and are based on zero contact resistance. However, in the presence of contact resistance, the result of measuring thermoEMF will depend on the value of the contact resistance, which must be taken into account.

The proposed approach can provide a significant increase in the reliability of thermoelectric inspection results through the use of a contact resistance control unit and rejection of results with high contact resistance. The permissible value of contact resistance depends on the size of the measuring resistor and the internal resistance of the thermoEMF source. The larger the value of the measuring resistor, the greater the permissible value of contact resistance. The choice of acceptable value depends on the required accuracy of thermoEMF measurement. For a measuring resistor with a resistance of 1 kΩ, an internal resistance of the thermoEMF source of 0.1 Ω and an allowable value of contact resistance of 10 Ω, the thermoEMF measurement error caused by the contact resistance will not exceed 1%.

The proposed system for monitoring contact resistance was implemented in the thermoelectric testing device "TERMOTEST-2", where the problem of low repeatability of testing results disappeared. If the contact resistance is more than 1 Ohm, the measurement result is not displayed on the device indicator and it is necessary to re-measure. It should be noted that the system for measuring contact resistance can be made in the form of an autonomous unit, which can be equipped with thermoelectric control devices in operation and thereby increase the reliability of the measurement results.

Conflict of interest statement
The authors declare that they have no conflict of interest in relation to this research, whether financial, personal, authorship or otherwise, that could affect the research and its results presented in this paper.

CRediT author statement
Kostina M.A.: Formal analysis, Data Curation; Soldatov A.I.: Conceptualization, Methodology, Project administration; Soldatov A.A.: Investigation, Validation; Abouellail A.A.: Software.
The final manuscript was read and approved by all authors.

References

1 Carreon H. (2002) Thermoelectric Nondestructive Evaluation of Residual Stress in Shot-Peened Metals. *Research in Nondestructive Evaluation*. 14(2), 59 – 80. DOI: 10.1080/09349840209409705.

2 Nagy P.B. (2010) Non-destructive methods for materials' state awareness monitoring. *Insight: Non-Destructive Testing and Condition Monitoring*. 52(2), 61 – 71. DOI: 10.1784/insi.2010.52.2.61.

3 Li J.F., Liu W.S., Zhao L.D., Zhou M. (2010) High-performance nanostructured thermoelectric materials. *Npg Asia Mater*. 2(4), 152 – 158. DOI: 10.1038/asiamat.2010.138.

4 Kikuchi M. (2010) Dental alloy sorting by the thermoelectric method. *European Journal of Dentistry*. 4(1), 66 – 70. Available at: https://www.ncbi.nlm.nih.gov/pmc/articles/PMC2798792/

5 Stuart C. (1987) Thermoelectric Differences Used for Metal Sorting. *Journal of Testing and Evaluation*. 15(4), 224 – 230. DOI: 10.1520/JTE11013J. ISSN 0090-3973.

6 Dragunov V.K., Goncharov A.L. (2019) New approaches to the rational manufacturing of combined constructions by EBW. *Proceeding of the IOP Conference Series: Materials Science and Engineering*. 681, 012010. DOI:10.1088/1757-899X/681/1/012010.

7 Goncharov A., Sliva A., Kharitonov I., Chulkova A., Terentyev E. (2020). Research of thermoelectric effects and their influence on electron beam in the process of welding of dissimilar steels. *Proceeding of the IOP Conference Series: Materials Science and Engineering*. 759(1), 012008. DOI: 10.1088/1757-899X/759/1/012008

8 Kharitonov I.A., Rodyakina R.V., Goncharov A.L. (2020) Investigation of magnetic properties of various structural classes steels in weak magnetic fields characteristic for generation of thermoelectric currents in electron beam welding. *Solid State Phenomena*. 299, 1201–1207. DOI: 10.4028/www.scientific.net/SSP.299.1201.

9 Soldatov A.I., Soldatov A.A., Sorokin P.V., Abouellail A.A., Obach I.I., Bortalevich V.Y., Shinyakov Y.A., Sukhorukov M.P. (2017) An experimental setup for studying electric characteristics of thermocouples. *SIBCON 2017 – Proceedings*. 79985342017. DOI: 10.1109/SIBCON.2017.7998534.

10 Carreon H., Medina A. (2007) Nondestructive characterization of the level of plastic deformation by thermoelectric power measurements in cold-rolled Ti–6Al–4V samples. *Nondestructive Testing and Evaluation*. 22(4), 299-311. DOI: 10.1080/10589750701546960

11 Carreon H. (2013) Detection of fretting damage in aerospace materials by thermoelectric means. *Nondestructive Characterization for Composite Materials, Aerospace Engineering, Civil Infrastructure, and Homeland Security*. 8694. DOI: 10.1117/12.2009448.

12 Lakshminarayan B., Carreon H., Nagy P. (2003) Monitoring of the Level of Residual Stress in Surface Treated Specimens by a Noncontacting Thermoelectric Technique. *AIP Conference Procceding*. 657, 1523-1530. DOI:10.1063/1.1570311.

13 Milićević I., Popović M., Dučić N., Slavković R., Dragićević S., Maričić A. (2018) Experimental Identification of the Degree of Deformation of a Wire Subjected to Bending. *Science of Sintering*. 50(2), 183-191. DOI:10.2298/SOS1802183M.

14 Soldatov A.I., Soldatov A.A., Sorokin P.V., Abouellail A.A., Kostina M.A. (2018) Thermoelectric method of plastic deformation detection. *Materials Science Forum*. 938, 112-118. DOI: 10.4028/www.scientific.net/MSF.938.112.

15 Magalhães A., De Backer J., Bolmsjö G. (2019) Thermal Dissipation Effect on Temperature-controlled Friction Stir Welding. *Soldagem & Inspeção*. 24(3), 1-9. DOI: 10.1590/0104-9224/si24.28.

16 Silva Ana C.F., De Backer J., Bolmsjö G. (2015) TWT method for temperature measurement during FSW process. *The 4th international conference on scientific and technical advances on friction stir welding & processing*. 95-98. Available at: https://www.diva-portal.org/smash/record.jsf?pid=diva2%3A1290065&dswid=554.

17 De Backer J., Bolmsjö G., and Christiansson A.-K. (2014) Temperature control of robotic friction stir welding using the thermoelectric effect. *The International Journal of Advanced Manufacturing Technology*. 70, 375-383. DOI:10.1007/s00170-013-5279-0.

18 Silva Ana C. F., De Backer J., Bolmsjö G. (2015) Cooling rate effect on temperature controlled FSW process. *Proceeding of the VII Intern. Conf. "High-Strength Materials: Challenges and Applications"*. Available at: https://www.researchgate.net/publication/281450403_Cooling_rate_effect_on_temperature_controlled_FSW_process.

19 Silva Ana C.F., De Backer J., Bolmsjö G. 2016. Analysis of plunge and dwell parameters of robotic FSW using TWT temperature feedback control. *Proceeding of the 11ᵗʰ Intern. Symposium on FSW.* Available at: https://www.researchgate.net/publication/303389476_ANALYSIS_OF_PLUNGE_AND_DWELL_PARAMETERS.

20 Vasiliev I., Soldatov A., Abouellail A., Kostina M.A., Soldatov A.A., Soldatov D., Bortalevich S. (2021) Thermoelectric Quality Control of the Application of Heat-Conducting Compound. *Studies in Systems, Decision and Control.* 351, 59–68. DOI: 10.1007/978-3-030-68103-6_6.

21 Yang Zhou, Donghua Yang, Liangliang Li, Fu Li, and Jing-Feng Li. (2014) Fast Seebeck coefficient measurement based on dynamic method. *Review of Scientific Instruments.* 85, 054904. DOI: 10.1063/1.4876595.

22 Uchida K., Ota T., Adachi H., Xiao J., Nonaka T., Kajiwara Y., Bauer G.E.W., Maekawa S., Saitoh E. (2012) Thermal spin pumping and magnon-phonon-mediated spin-Seebeck effect. *Journal of Applied Physics.* 111(10), 103903. DOI:10.1063/1.4716012.

23 Uchida K., Takahashi S., Harii K., Ieda J., Koshibae W., Ando K., Maekawa S., Saitoh E. (2008) Observation of the spin Seebeck effect. *Nature.* 455, 778–781. DOI: 10.1038/nature07321.

24 Lider A.M., Larionov V.V., Syrtanov M.S. (2016) Hydrogen concentration measurements at titanium layers by means of thermo-EMF. *Key Engineering Materials.* 683, 199 – 202. DOI: 10.4028/www.scientific.net/KEM.683.199.

25 Iwanaga S., Toberer E.S., LaLonde A., Snyder G.J. (2011) A high temperature apparatus for measurement of the Seebeck coefficient. *Review of Scientific Instruments.* 82(6), 063905. DOI: 10.1063/1.3601358.

26 Sarath Kumar S.R., Kasiviswanathan S. (2008) A hot probe setup for the measurement of the Seebeck coefficient of thin wires and thin films using integral method. *Review of Scientific Instruments.* 79, 02432, DOI: 10.1063/1.2869039.

27 Abouellail A.A., Chang J., Soldatov A.I., Soldatov A.A., Kostina M.A., Vasiliev I.M. (2023) Thermoelectric Monitoring Of Thermal Resistance In Electronic Systems. *Eurasian Physical Technical Journal.* 20(3), 52-61. DOI: 10.31489/2023No3/52-61.

28 Soldatov A.I., Soldatov A.A., Sorokin P.V., Loginov E.L., Abouellail A.A., Kozhemyak O.A., Bortalevich S.I. (2016) Control system for device «thermotest». *International Siberian Conference on Control and Communications (SIBCON-2016).* 1-5. DOI: 10.1109/SIBCON.2016.7491869.

29 Hu J., Nagy P.B. (1998) On the role of interface imperfections in thermoelectric nondestructive materials characterization. *Applied Physics Letters.* 73, 467-469. DOI: http://dx.doi.org/10.1063/1.121902.

30 Abouellail A.A., Chang, J., Soldatov, A.I., Soldatov, A.A.,.Kostina, M.A., Bortalevich, S.I., Soldatov, D.A. (2022) Influence of Destabilizing Factors on Results of Thermoelectric Testing. *Russian Journal of Nondestructive Testing.* 58(7), 607–616. doi.org/10.1134/S1061830922070026.

31 Sergeev A.S., Tikhonova Z.S., Uvarova T.V. (2017) Method for measuring thermo-emf of a "tool-workpiece" natural thermocouple in chip forming machining. *MATEC Web of Conferences.* 129, 01044. DOI: 10.1051/matecconf/201712901044.

32 Abouellail1 A.A., Kostina M.A., Bortalevich S.I., Loginov E.L., Shinyakov Y.A., Sukhorukov M.P. (2018) Mathematical simulation of thermocouple characteristics. *Proceeding of the IOP Conference Series: Materials Science and Engineering.* 327(2), 022002. DOI: 10.1088/1757-899X/327/2/022002.

AUTHORS' INFORMATION

Soldatov, Andrey Alekseevich – Candidate of techn. sciences, Associate Professor, National Research Tomsk Polytechnical University, Tomsk, Russia; ORCID ID: 0000-0003-0696-716X; soldatov.88@bk.ru

Soldatov, Aleksey Ivanovich – Doctor of techn. sciences, Professor, National Research Tomsk Polytechnical University, Tomsk, Russia, Tomsk, Russia; ORCID iD: 0000-0003-1892-1644; asoldatof@mail.ru

Kostina, Maria Alekseevna – Candidate of techn. sciences, Associate Professor, National Research Tomsk Polytechnical University, Tomsk, Russia; ORCID ID: 0000-0003-2626-6002; mariyakostina91@mail.ru

Abouellail, Ahmed Ali – Candidate of techn. sciences, Lecturer, Sphinx University, New Asyut, Egypt; ORCID iD: 0000-0002-9357-6214; ahmed.abouellail@sphinx.edu.eg

UDC: 532.685; 546.791; 631.432.33

STUDY OF THE EFFECTIVENESS OF METHODS FOR INCREASING THE PRODUCTIVITY OF URANIUM THROUGH PRELIMINARY FORECASTING

Kachkinova A.K.[*], Turalina D.E., Nurmakhanov N.U.

al-Farabi Kazakh National University, Almaty, Kazakhstan
Corresponding author: kachkinova.aziza@gmail.com

Abstract. A study was conducted of the effectiveness of methods for increasing the productivity of uranium through preliminary forecasting. The objective of this study is to analyze and optimized the technological block currently in production. To analyze the performance of a block or cell different performance indexes are used: Tracer cut, Tracer in Place, Acid in place. Several scenarios of optimization have been tested using the HYTEC reactive transport program and modeling the uranium mining process. These scenarios involved new wells and the impact of "chemical well treatment" that increases the productivity of well. This work focused on improving the production of block. Three different scenarios were performed. Among the three scenarios, the third produced the highest amount of uranium 133 tons out of 154 tons of reserves. During optimization it is better to get the right efficiency value for each well's last trend in the cleaning action excel file. After chemical treatment of the well it was possible to increase the area where pH<1.85. This shows the importance of optimization and chemical treatment of the well.

Keywords: uranium mining, in-situ recovery, reactive transport, hytec, forecast, acid in place, tracer in place, tracer cut, chemical treatment of the well

1. Introduction

About 10% of the world's electricity is generated from uranium in nuclear reactors. This amounts to over 2500 TWh each year. France gets about 70% of its electricity from uranium [1]. About two-thirds of the world's production of uranium from mines is from Kazakhstan, Canada and Australia. An increasing amount of uranium, now over 60%, is produced by ISR (In situ recovery). In 2021, Kazakhstan produced the largest share of uranium from mines (45% of world supply) [2]. In situ recovery mining has been steadily increasing its share of the total, mainly due to Kazakhstan, and in 2021 accounted for over 60% of production (32088 tonnes U) [2]. In situ recovery uses a chemical technique to separate the uranium in the Earth's crust from the surrounding rock, making it a different mining approach from traditional ones. It is possible to employ the ISR approach without engaging in extensive rock mining. Additionally, ISR costs less and has less of an impact on the environment and health than the standard way. The movement of liquid as opposed to rock minimizes surface disturbance [3].

The KATCO mining company is a joint venture between Orano Mining (51%) and Kazakhstan national mining company Kazatomprom which are the Kazakh and French national nuclear fuel cycle companies, respectively. It specializes in the in-situ recovery of uranium, in roll-front type formations, with a 4.000 tons uranium yearly capacity. The mine, located in the Shu Saryssu Bassin - Kazakhstan, exploits the Tortkuduk

and Moiynkum deposits along a southwest-northeast axis over 40 km in length. It currently operates this large territory in an acidic way with processing plants connected to the deposit by a well field [4]. ISR requires modeling because it enables the forecasting of crucial variables and the reservoir's behavior during the recovery process. This is crucial for weighing the possible risks and rewards of various strategies as well as for making well-informed decisions concerning the design and implementation of ISR programs. Without modeling, there is a higher chance of unforeseen results and time and resource waste. Reactive transport models are built at the block scale using a mix of hydrogeochemical reservoir description and process identification [5].

2. Theoretical part

2.1 Chemical proccess

Uranium dissolution during acidic leaching is dominated by the oxidation of U(IV) minerals (e.g., uraninite UO_2, coffinite $USiO_4$) by Fe^{3+} in the bearing solution. The origin of ferric iron is multiple: local dissolution of gangue minerals (goethite, beidellite), recirculation of Fe^{3+} from the well field, or surface active regeneration of Fe^{3+} using peroxide or other oxidants. Low pH (typically < 2) is required to allow for ferric iron mobility [4].

Oxidizing conditions (under acidic conditions) are necessary to dissolved [4]:

$$UO_2 + 2H^+ + 0.5O_2(aq) \leftrightarrow UO_2{}^{2+} + H_2O \tag{1}$$

$$USiO_4 + 2H^+ + 0.5O_2(aq) \leftrightarrow UO_2{}^{2+} + SiO_2(aq) + H_2O \tag{2}$$
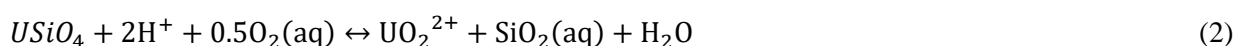
No dioxygen in the reservoir but Fe^{3+} reacts as a good oxidizer and is naturally present [4]:

$$UO_2 + 2Fe^{3+} \leftrightarrow UO_2{}^{2+} + 2Fe^{2+} \tag{3}$$

$$USiO_4 + 2Fe^{3+} \leftrightarrow UO_2{}^{2+} + SiO_2 + 2Fe^{2+} \tag{4}$$

Acid consumption: the reaction is controlled by the availability of ferric iron, solubility of uranium (in which complexation, notably with, $SO_4{}^{2-}$ can play an important role) and kinetics. Reactions with gangue minerals are also key, since they can control pH or local sources of ferric iron [6]:

$$CaCO_3 + H^+ \leftrightarrow Ca^{2+} + HCO_3{}^- \tag{5}$$

$$(Si_{3.67}Al_{0.47})(Al_{1.81}Fe^{3+}{}_{0.05}Mg_{0.165})O_{10}(OH)_2 + 7.32H^+$$
$$\leftrightarrow 0.165Mg^{2+} + 2.28Al^{3+} + 0.05Fe^{3+} + 3.67SiO_2(aq) + 4.66H_2O \tag{6}$$
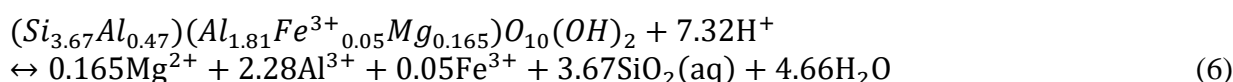
2.2 Porous media flow

The solution flow in porous media is governed by the basic law of underground hydrodynamics, Darcy's law:

$$Q = K_{cond}A\frac{\Delta h}{L} \tag{7}$$

Q is the flow rate; A is the cross-section area;; Δh is the pressure drop across length L; $K_{cond} = K\frac{\rho g}{\mu}$ is the permeability (hydraulic conductivity);

According to Darcy's equation, the physical properties of during the ISR process considerable changes to the TDS (total dissolved solids) take place. This is particularly true at the beginning of leaching when the pore water is replaced by the reactant (acid) solution. Therefore, the physical properties of fluid are variable [3].

Darcy velocity is written as follows:

$$u = \frac{Q}{A} = K_{cond}\frac{\Delta h}{L} = -K_{cond}\nabla h \tag{8}$$

Continuity equation for non-stationary flow:

$$\frac{\partial(\rho\omega)}{\partial t} + \nabla \cdot (\rho u) = 0 \tag{9}$$

Compressible-transient flow:

$$S_s \frac{\partial h}{\partial t} - \nabla \cdot (K_{cond}\nabla h) = q \tag{10}$$

Density-driven flow:

$$S_s \frac{\partial p}{\partial t} - \nabla \cdot \left(\frac{\rho}{\rho_0}K_{cond}\nabla(p + \rho gz)\right) = \rho gq \tag{11}$$

$S_s = \rho g\omega \left(\beta_l - \beta_s + \frac{\alpha}{\omega}\right)$ is the storage coefficient; ω is the porosity; β_l and β_s are water and matrix compressibilities; α is the elasticity; q is the source.

2.3 Reactive transport equation

Transport equation:

$$\frac{\partial \omega c}{\partial t} = \nabla \cdot (\mathbf{D}(\omega, D)\nabla c - cu) \tag{12}$$

The solute transport mechanisms considered in the formulation are:
- Advection (due to water phase movement): advection is the transfer of dissolved substances by the flow of a liquid. The actual filtration velocity is higher than the filtration velocity determined by Darcy's law.
- Molecular diffusion; in a porous medium, diffusion processes slow down, because the path of molecules and ions in the liquid phase increases as a result of their movement through tortuous pore channels, around individual particles. Molecular diffusion of a dissolved substance in water is described by Fick's law:
$$J = -D\nabla c \tag{13}$$

$$\frac{\partial c}{\partial t} = D\nabla^2 c \tag{14}$$

- Mechanical dispersion: dispersion is a mixture of two substances. Mechanical dispersion of a substance is explained by two effects. Molecules or ions of a dissolved substance in a porous medium follow path of different lengths, due to the structure of the pore space structure, local variability of the filtration velocity field. Molecular diffusion in the direction of decreasing concentration of the dissolved substance, branching of motion trajectories.
Diffusion-dispersion equation:

$$\mathbf{D}(\omega, D) = D_{diff} + \alpha_{L,T}\|\mathbf{u}\| \tag{15}$$

D is a diffusion coefficient; D_{diff} is a tensor with the diagonal coefficients α_L, α_T; α_L and α_T are longitudinal and transverse dispersivities, usually $\alpha_L > \alpha_T$.
The dispersion coefficients allow to quantify the phenomenon of dispersion. It is assumed that they are proportional to the actual speed of water, such that:
Longitudinal dispersion coefficient:

$$D_L[m^2/s] = \alpha_L[m] \cdot u[m/s] \tag{16}$$

Transverse dispersion coefficient:
$$D_T[m^2/s] = \alpha_T[m] \cdot u[m/s] \tag{17}$$

2.4 Geochemistry

2.4.1 Reactions at equilibrium. Thermodynamic equilibrium

In an in situ leaching operation, the recovery of uranium is determined by the often very complex interaction of the physico-chemical, hydro-geological and mineralogical characteristics of the mineralized level and the chemical kinetics of the leaching solutions used [7].

Chemical reactions are characterized by the global notion of chemical potential μ_A [9]:

$$\mu_A = \left(\frac{\partial G}{\partial n_a}\right)_{P,T,n_i} \tag{18}$$

$$\mu_A = \mu^0(p,T) + RT\ln(A) \tag{19}$$

$\mu^0(p,T)$ is the standart potential;
A is an activity.
pH is the main indicator for determining the oxidation state. (H^+) is the hydrogen ion activity [9]

$$pH = -\log_{10}(H^+) \tag{20}$$

Oxydation - loss of e^-:

$$U^{4+} \rightleftharpoons U^{6+} + 2e^- \tag{21}$$

Reduction - gain of e^-:

$$Fe^{3+} + 1e^- \rightleftharpoons Fe^{2+} \tag{22}$$

Mass action law (solubility product):

$$AB_2 \rightleftharpoons A^{2+} + 2B^-, \quad Ks = (A^{2+})(B^-)^2 \tag{23}$$

Saturation Index (SI) of a fluid in relation to a mineral:

$$SI = \log\left(\frac{(A^{2+})(B^-)^2}{Ks}\right) \tag{24}$$

Precipitation if $SI > 0$ and dissolution if $SI < 0$.

2.4.2. Kinetic control

Dissolution/precipitation of mineral M:

$$\frac{d[M]}{dt} = kA_v \prod_i (A_i)^{a_i}\left(\left(\frac{Q}{Ks}\right)^p - 1\right) \tag{25}$$

$A_v = A_s[M]$ is the specific surface, $[m^2/kg]$ and $\prod_i (A_i)^{a_i}, (A_i)$ is the catalyst if $a_i > 0$ or inhibitor if $a_i < 0$.

Arrhenius law [10]:

$$k = A\exp\left(\frac{-E_A}{RT}\right) \tag{26}$$

E_A is an apparent activation energy, [J/mol];

3. Method of research: Performance indicators

The indicator Tracer in Place (TIP) translates the process of invasion by the VR (leaching solution) fluid. The VR tracer is set-up to be non-reactive with the others elements and has a constant concentration. Once it is injected, the VR will propagate inside the reservoir and behave like a non-reactive tracer. By looking at the concentration of VR one can have an idea of where the injection fluid is going. The objective is that this VR invade all mineralization, in hope that the oxidizer will oxidize the uranium. A high TIP means a good invasion of the reservoir. This indicator TIP has its limits. Indeed, once the VR is injected it will replace the water in place from the aquifer. Once this water is removed and replaced by the VR, the TIP will remain high. The TIP is mainly useful during the acidification process and the first year of production. After, another indicator called Acid in Place (AIP) will be used. With the TIP you can quickly observe the problem of injectivity, balance and wrong screen position. The Tracer Cut (TC) is the percent of VR produced compared to what is injected. This indicator is showing the recovery of the VR fluid and is indicating whether the well is producing water from the aquifer or VR from the injector. This indicator is close to the pH but do not consider any geochemical process that may arise on its way.

The Acid in Place (AIP) can observe similar invasion as TIP, but considering the acidification process. Both injectivity problem and acidification problems can be observed with this indicator. The optimal condition for dissolution of uranium minerals is under acidic conditions (pH < 1.85). Initially, the pH of the reservoirs mostly more than 1.85 on block (red zone of the AIP evolution graphs Fig. 1(c), Fig. 3, Fig. 4(c), Fig. 6(c), Fig. 8). As the acid is injected in the reservoir, pH start decreasing. Over time, part of the reservoir with a pH less than 1.85 increases. This corresponds to the green zone of the AIP evolution graph. The yellow zone indicates the percentage of dissolved uranium (Fig. 1(c), Fig. 3, Fig. 4(c), Fig. 6(c), Fig. 8).

Thus, on the AIP evolution graph, the volume of uranium (in red) decreases as the uranium is dissolved, and the volume of this uranium itself is invaded by the acid (the pH<1.85 region in green of the graphs Fig. 1(c), Fig. 3, Fig. 4(c), Fig. 6(c), Fig. 8). The volume of uranium is interpreted as follows (red zone of the graphs Fig. 1(c), Fig. 3, Fig. 4(c), Fig. 6(c), Fig. 8):

$$\text{Mineralization pH} > 1.85 = \frac{(\text{Volume U>100ppm})_i \, [\text{m}^3]}{(\text{Volume U>100ppm})_{i=1} \, [\text{m}^3]}, \quad i = 1, 2, 3, \ldots \tag{28}$$

$(\text{Volume U} > 100\text{ppm})_i$ is the volume of uranium on i th day; $(\text{Volume U} > 100\text{ppm})_{i=1}$ is the initial volume of uranium on 1st day.

The volume of this uranium itself is invaded by the acid is interpreted as follows (green zone of the graph):

$$\text{Mineralization pH} < 1.85 = \frac{(\text{Invasion pH<1.85})_i \, [\text{m}^3]}{(\text{Volume U>100ppm})_{i=1} \, [\text{m}^3]}, \quad i = 1, 2, 3, \ldots \tag{29}$$

$(\text{Invasion pH} < 1.85)_i$ is the invasion of acid on i th day; The AIP is interpreted as follows (green curve of the graph):

$$\text{AIP} = \frac{\text{Value of green zone}}{\text{Value of red zone}} = \frac{(\text{Invasion pH<1.85})_i \, [\text{m}^3]}{(\text{Volume U>100ppm})_i \, [\text{m}^3]}, \quad i = 1, 2, 3, \ldots \tag{30}$$

4. Results and discussions

4.1 Scenario-1: Forecast with last trend

Forecast is long-term planning, one of the main applications of HYTEC [8]. The long-term production plan's objectives are to balance production by year and disperse production throughout the blocks. The sum of the active production blocks is used to determine global production. Each block includes a production curve for the amount of flow and acid. Flowrate options is creating flowrate for forecast by wells. The "last trend" for the flowrate option was chosen in this research work. Forecast scenario's data is given in the Table 1.

Table 1. Forecast scenarios information

Historical Data	15/03/22-27/06/23 (470 days)	837 days
Forecasting Data	28/06/23-28/06/24 (367 days)	

.

In the Fig.1. (a) shows a Tracer Cut plotted over time. A higher percentage indicates more solution is being recovered from the well, and lower indicates more solution is leaving the well through the aquifer. The historical data shows a steady TC around 79%. The forecast predicts the TC will slowly rise to 92.6% over time. This data suggests that the well is currently recovering about 79% of the leaching solution injected. Over time, the model predicts the well will recover more and more of the solution, reaching up to 92.6%.

a)

b)

c)
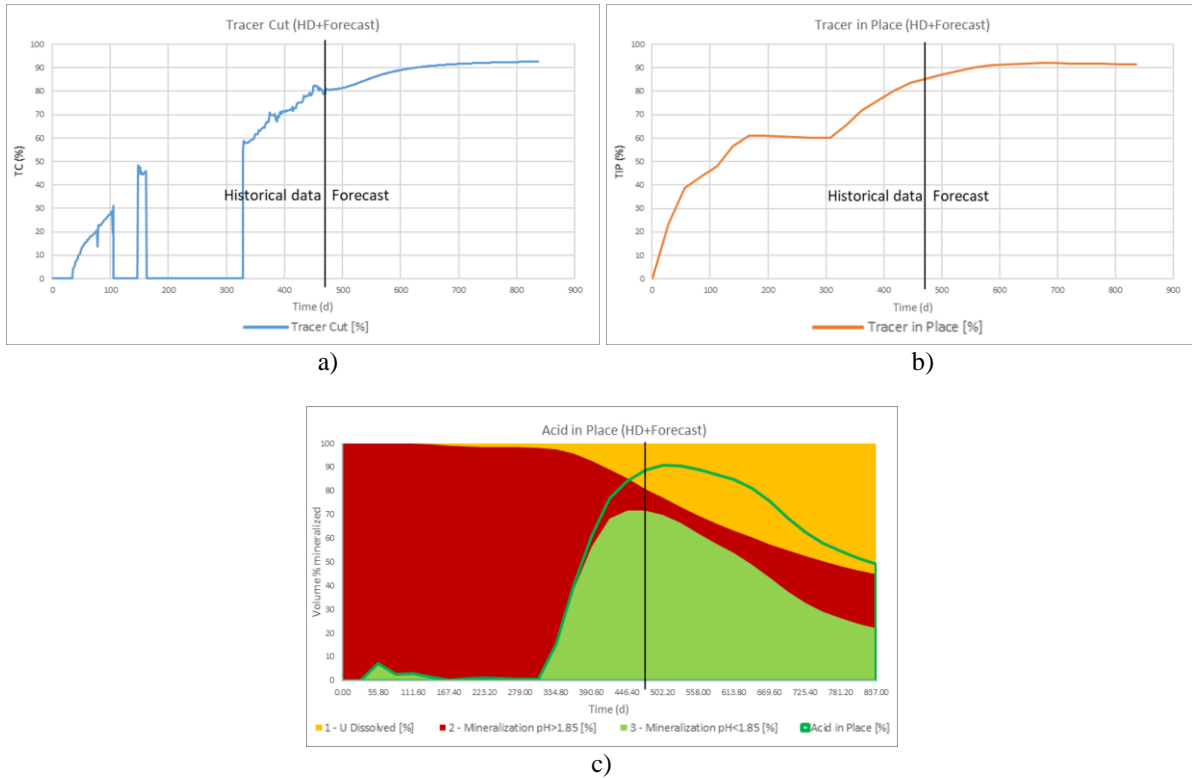
Fig.1. Forecast with last trend performance indicators

Fig.1. (b) shows Tracer in Place plotted over time. A higher TIP value means more of the reservoir has been reached by the solution. The historical data shows a TIP that steadily increases to about 85%. The forecast predicts the TIP will continue to increase to 91.4%. This data suggests that leaching solution has reached a large portion of the reservoir according to the model. Over time, the model predicts an even greater portion of the reservoir will be contacted by the solution. Fig.1. (c) shows AIP evolution.

AIP for the forecast of the block, the red part is 49%. And the green part, ready for production, is 27%. 105.5 tons (Fig.2 (a)) of uranium were produced in 837 days. This is equivalent to 68.5 percent of the 154 tons of initial uranium reserve (Fig.2 (b)).

a)

b)
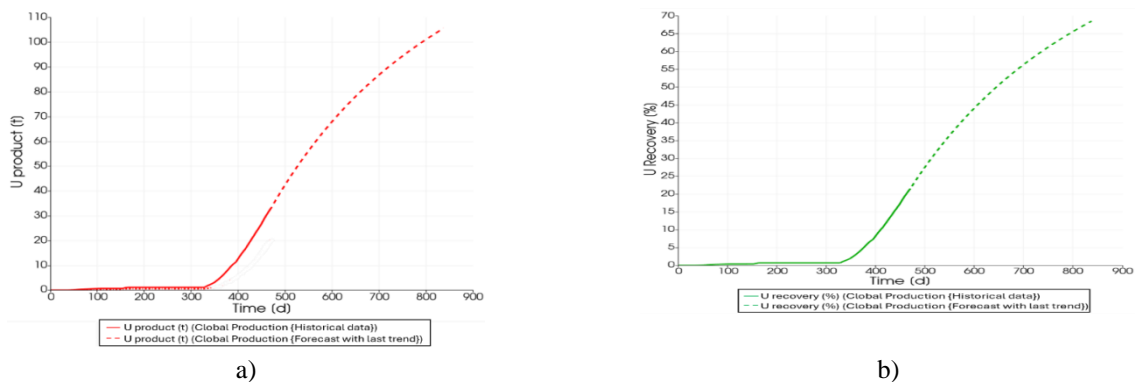
Fig.2. Forecast with last trend variables

5. Optimization

AIP considering the reaction of acid within the reservoir and the acidification process. Both injectivity problem and acidification problems can be observed with this indicator. The cells Cell_02, Cell _03, Cell _04, Cell _06, Cell _09, Cell _15, Cell _16, Cell _17 did not show a good AIP evolution.
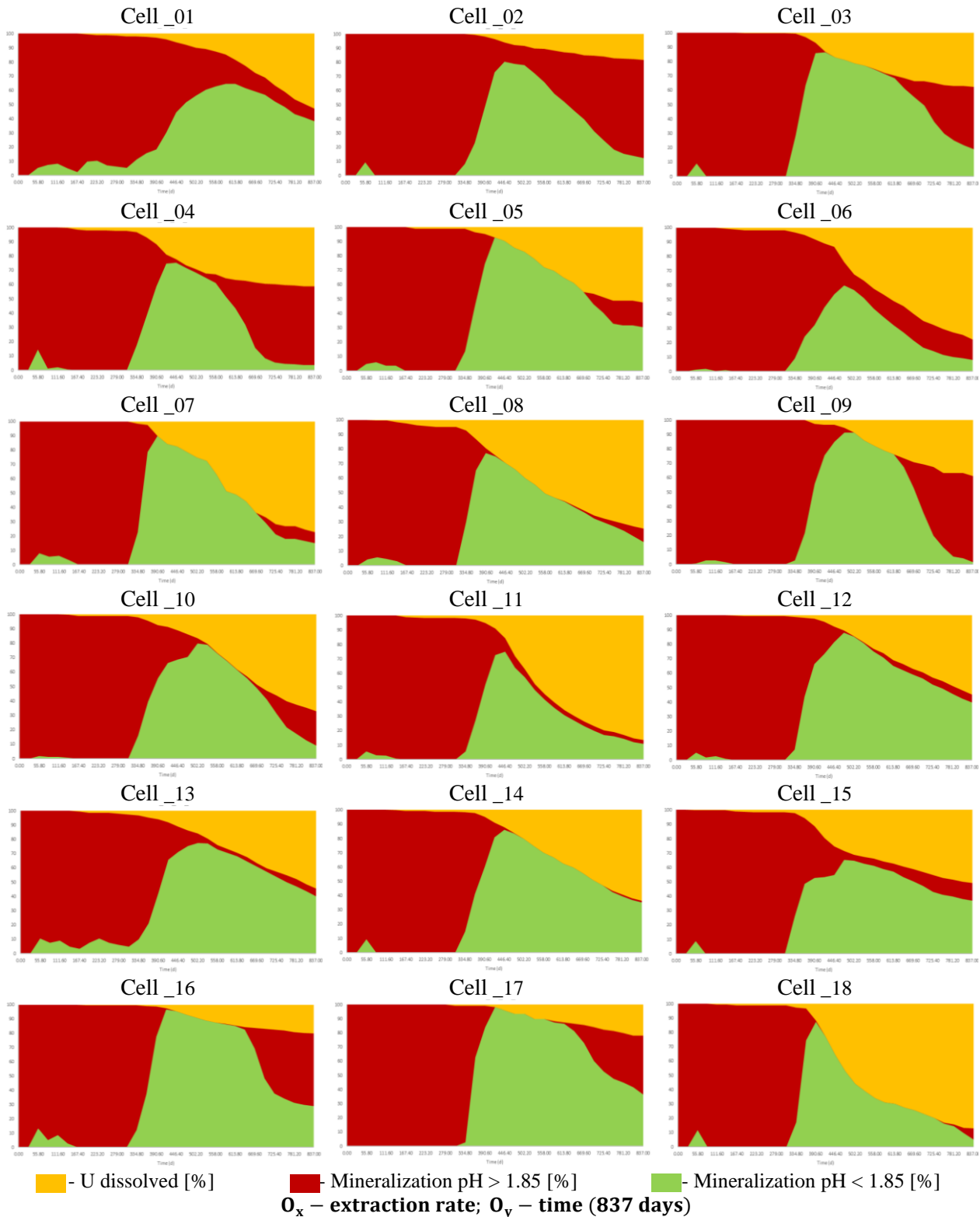
Fig.3. The AIP evolution of each cell

There's less green zone and that means less material we can mine (because the green zones have a good acidity level for mining, below 1.85 pH). If look at Fig. 1(c), you'll see a lot of red in the middle of the green and yellow zones. This red zone is uranium that hasn't been mined yet (because it's not acidic enough, with a pH higher than 1.85). So, to improve the mining process, we should focus on these zones with the most red. We need to improve well productivity by correcting flowrates and by cleaning actions on the well ABF. The list of cells with low performance and the necessary works to optimize these cells are shown in the Table 2.

Table 2. Table of cells problem cells and required works

Cells	Required works
Cell _02; Cell _03; Cell _04; Cell _06; Cell _09; Cell _15; Cell _16; Cell _17	- To increase flowrates for producer and injector wells; - ABF - Connect the well Producer Cell _15 to work.

5.1 Scenario-2: Forecast with ABF-1

Well filters get filled with clogging product this affects the performance of the well. The flowrate variation is able to the cleaning actions on the well. 3 types are possible: ABF (chemical treatment of the well); RVR (mechanical cleaning); Redrilling (additional wells). Every three months, the ABF procedure was carried out. At the end of the simulation the percentage the tracer cut rate following ABF is 91.6% (Fig.4 (a)). This is slightly lower than for the scenario-1 (92.6%). Fig.4 (b) shows that TIP reached after ABF 94% for forecast, 2.6% better than for the trend scenario-1. After ABF, AIP for the scenario-2 of the block, the red part is 43.2%. And the green part, ready for production, is 27% (Fig.4 (c)). For good results, the values of the red and green parts should be close to each other.

a)   b)

c)

Fig.4. Forecast with ABF-1 performance indicators

In 837 days, 110 tons (Fig.5) of uranium were mined. The outcomes are 5.5 tons better than before ABF. The first 154 tons of uranium reserve are comparable to 71.6 percent of this.

a)   b)
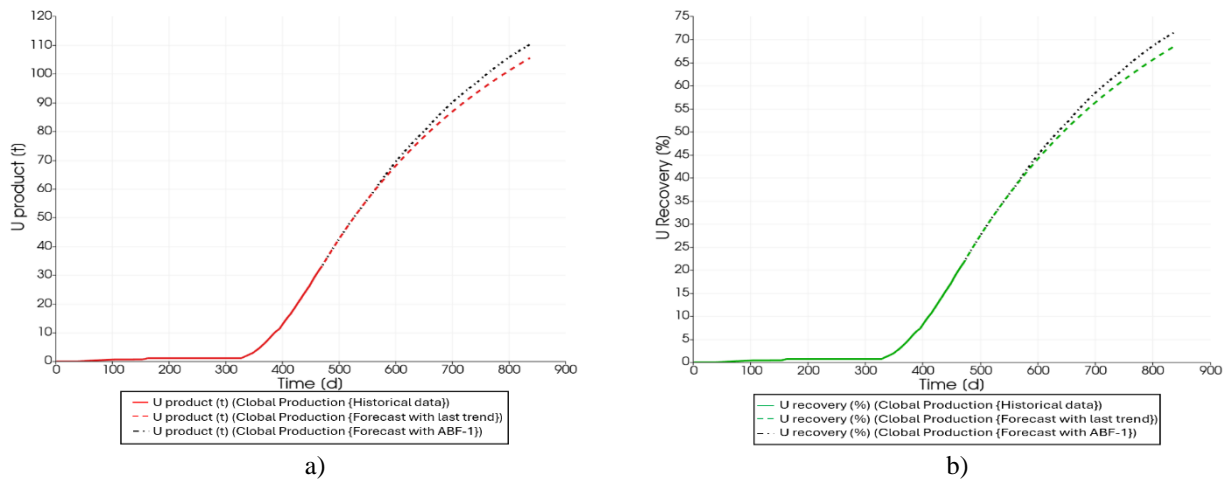
Fig.5. Forecast with ABF-1 variables

5.2 Scenario-3: Forecast with ABF-2

A chemical treatment of the well (ABF) was performed with other new data. For each cell, an efficiency value (flow rate) that closely matched the last trend line was chosen. The planning well Cell_15 was connected to the work. At the end of the simulation the percentage the tracer cut rate following ABF is 94% (Fig.6 (a)). Fig.6 (b) shows that TIP reached after ABF-2 94% for forecast. After ABF-2, AIP for the forecast of the block, the red part is 32%. And the green part, ready for production, is 29% (Fig.6 (c)).

a)   b)
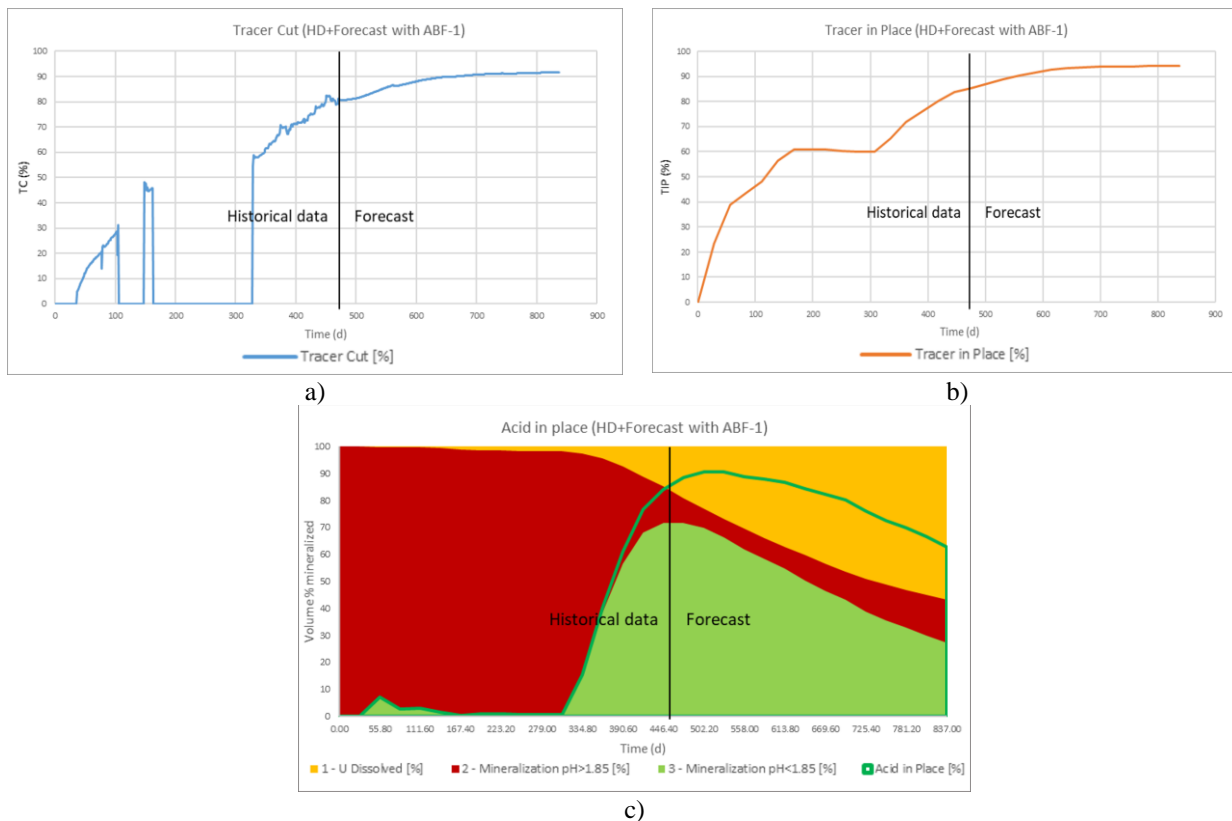

c)
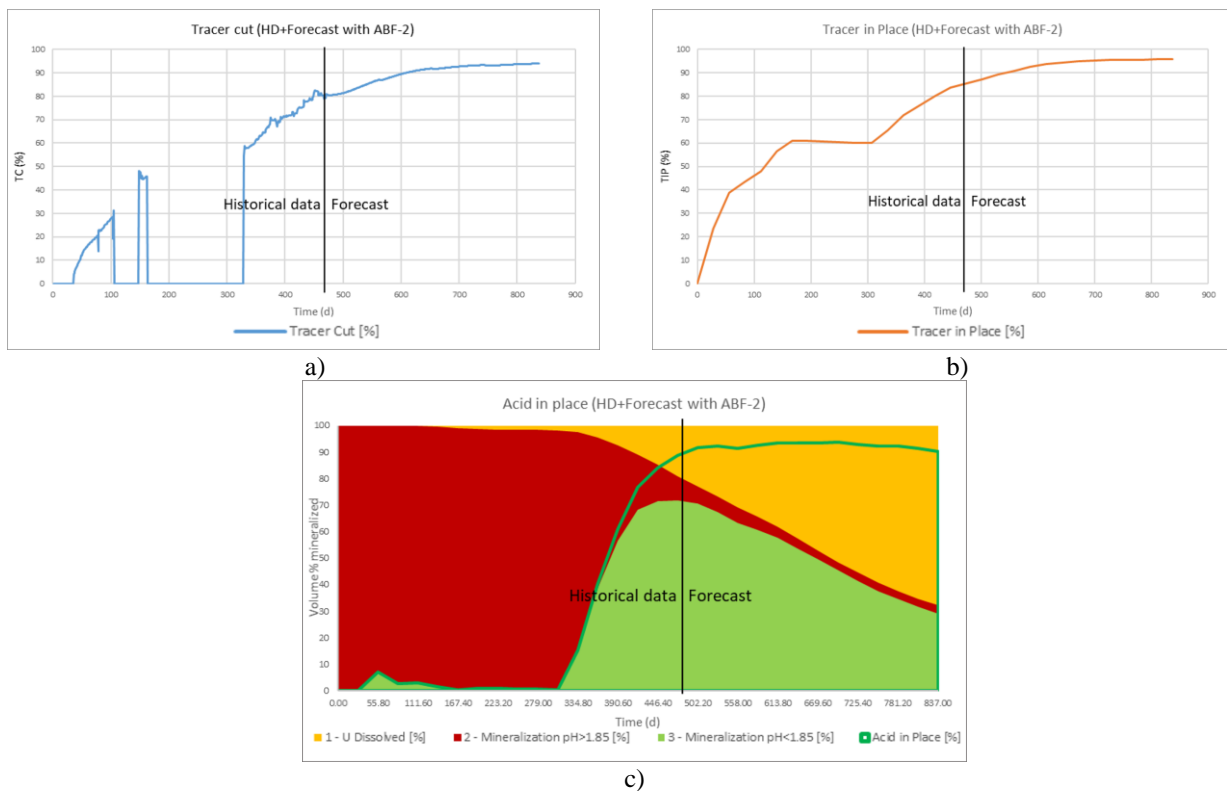
Fig.6. Forecast with ABF-1 performance indicators.

In 837 days, 133.3 tons (Fig.7 (a)) of uranium were mined. The result is 29 tons better than before ABF. By operating well Cell_15 and changing the efficiency of each well it was possible to increase production by 86.5% (Fig.7 (b)).

.

a)   b)
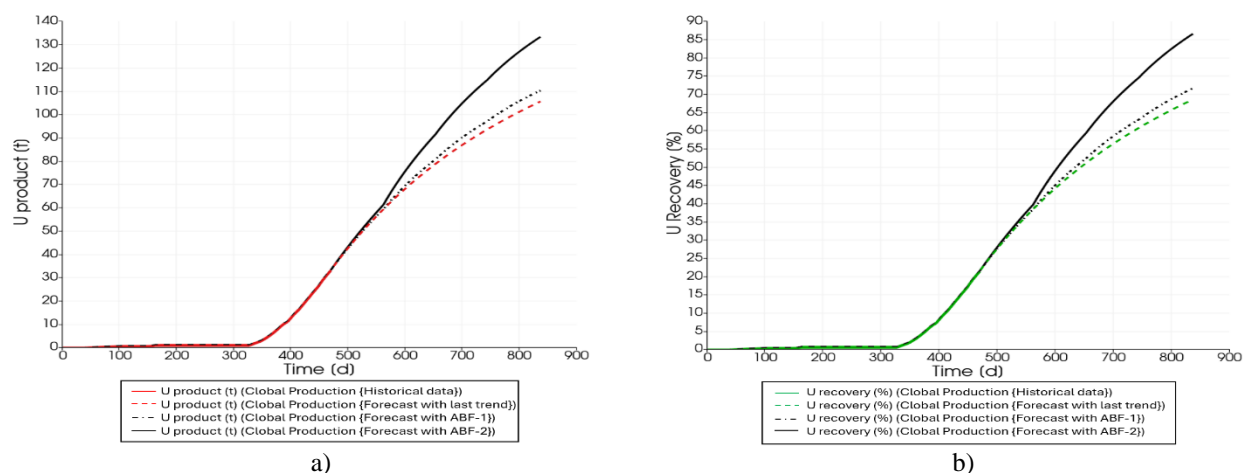
Fig.7. Forecast with ABF-2 variables

After chemical treatment of the well with ABF-2 it was possible to recover U from all the cells even those that were identified as problematic in the forecast scenario (Fig.A1, Appendix). This shows the importance of optimization. In long-term planning, flow rates forecasting is very important. When using build-in tools to forecast flowrate based on historical data, a manual verification has to be done to be sure that the results are in line with last trends. The volume of uranium production and the recovery percentage in the block of all three scenarios are shown in the Table 3. Among the three scenarios, the third produced the highest amount of uranium 133 tons out of 154 tons of reserves. During optimization it is better to get the right efficiency value for each well's last trend in the cleaning action excel file.

Table 3. Variables of three scenarios

	Historical data	Scenario-1	Scenario-2	Scenario-3
U_product, [t]	32.7 t	105.5 t	110 t	133.3 t
U_recovery, [%]	21%	68.5%	71.6%	86.5%

6. Conclusion

This study investigated methods to improve uranium production from block using in-situ recovery. Three forecast scenarios were evaluated. The results obtained will certainly be of value for future uranium mining in the technical block (Tortkuduk, KATCO). Thanks to the forecast, we can optimise production, plan a long-term strategy, reduce risks, and increase efficiency. Predicting potential problems, such as depletion or declining uranium quality, will help you take steps to minimise them in advance. By optimising production and planning, it is possible to improve the overall efficiency of uranium exploitation in the block. The long-term forecast provided in this paper will shorten the operating time of the block. Chemical treatment (ABF) is crucial for improving uranium recovery. Treatment significantly increased the area with a favorable pH level (below 1.85) in problematic wells. Flow rate forecasting requires careful consideration. While historical data provides a basis, manual verification is essential to ensure alignment with recent trends. Optimization is vital for maximizing production. Selecting the appropriate efficiency values for each well during cleaning actions significantly enhances uranium output. Overall, this study demonstrates that a combination of forecasting, well cleaning (ABF), and optimization can substantially increase uranium production in ISR mining.

Funding

References

1   Gospodarczyk M., Fisher M. Available at: https://www.world-nuclear.org/information-library/nuclear-fuel-cycle/introduction/what-is-uranium-how-does-it-work.aspx
2   World Nuclear Association. Available at: https://www.world-nuclear.org/information-library/nuclear-fuel-cycle/mining-of-uranium/world-uranium-mining-production.aspx
3   In-situ Leaching. Nuclear Power. Available at: https://www.nuclear-power.com/nuclear-power-plant/nuclear-fuel/nuclear-fuel-cycle/uranium-mining-uranium-mines/in-situ-leaching-in-situ-recovery/
4   Lagneau V., Regnault O., Descostes M. (2019) Industrial deployment of reactive transport simulation: an application to uranium in situ recovery. *Rev. Mineral. Geochem.* 85, 499–528. DOI: 10.2138/rmg.2019.85.16
5   Lagneau V., Van der Lee J. (2010) HYTEC results of the Mas reactive transport benchmark. *Comput. Geosci.* 14, 435–449. DOI: 10.1007/s10596-009- 9159-5.
6   Collet A, Regnault O, Ozhogin A, Imantayeva A, Garnier L. (2022) Three-dimensional reactive transport simulation of Uranium in situ recovery: Large-scale well field applications in Shu Saryssu Bassin, Tortkuduk deposit (Kazakhstan). *Hydrometallurgy*. 211, 105-873. DOI: 10.1016/j.hydromet.2022.105873.
7   Van der Lee J., De Windt L., Lagneau V., Goblet P. (2003) Module-oriented modeling of reactive transport with HYTEC. *Computers & Geosciences*. 29, 265–275. DOI:10.1016/S0098-3004(03)00004-9
8   Regnault O., Lagneau V., Fiet N. (2015) 3D Reactive Transport simulations of Uranium In Situ Leaching: Forecast and Process Optimization. *Uranium-Past and Future Challenges*. 7, 725-730. DOI:10.1007/978-3-319-11059-2_83
9   Sorenssen M.A. (2013) *Chemical potential and Gibbs Distribution.* October. Available at: https://www.uio.no/studier/emner/matnat/fys/FYS2160/h13/book/thermal-lecture-07.pdf
10   Kurmanseiit M.B., Tungatarova M.S., Kaltayev A., Royer J.-J. (2022) Reactive Transport Modeling during Uranium In Situ Leaching (ISL): The Effects of Ore Composition on Mining Recovery. *Minerals.* 2022, 12, 1340. DOI:10.3390/min12111340

_____

AUTHORS' INFORMATION

Kachkinova, Aziza Kenzhebaevna - Master (Sci.), Mechanics, al-Farabi Kazakh National University, Kazakhstan; ORCID ID: 0000-0002-1125-8491; kachkinova.aziza@gmail.com
Turalina, Dinara Eleusizovna - Candidate of phys.-math. sciences, Acting Associate Professor, Head of the Department of Mechanics, al-Farabi Kazakh National University, Kazakhstan; ORCID iD: 0000-0003-0762-2657; dinara.turalina@kaznu.kz
Nurmakhanov, Nurlybek Umirbekuly - Master (Eng.), Colorado School of Mines, Golden, Colorado, USA; ORCID iD: 0009-0002-8079-6506; nurlybek.nurmakhanov@orano.group

.

Appendix A
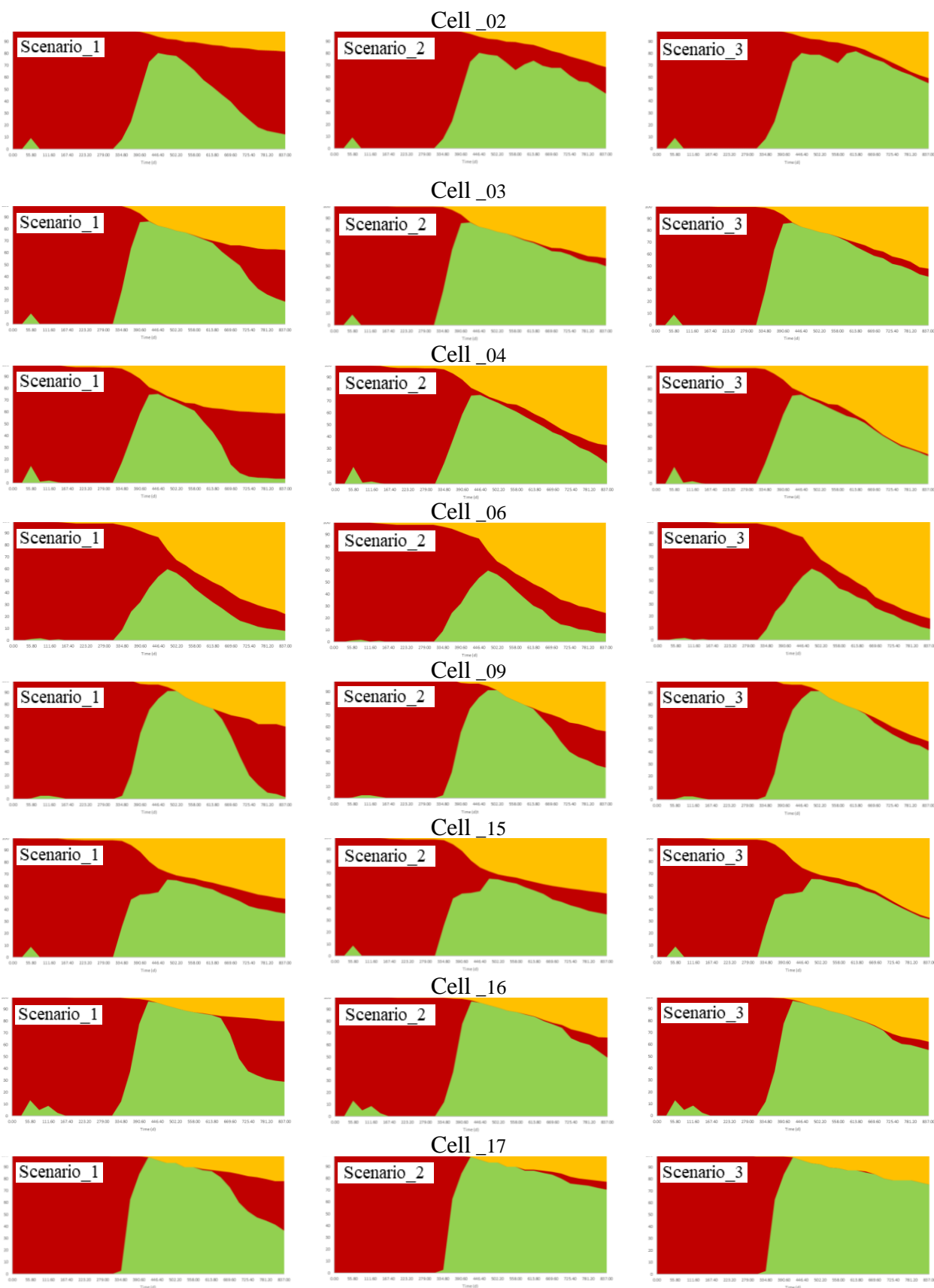
Fig.A1. Comparison of AIP evolutions of three different scenarios

ON-BOARD CONTROL-MEASUREMENT SYSTEM FOR MICRO CONVERTIPLANE-TYPE UNMANNED AERIAL VEHICLES

Nabiyev R.N., Abdullayev A.A.[*], Qarayev Q.I.

National Aviation Academy of the Azerbaijan, Baku, Azerbaijan
Corresponding author: anarcafarov09@mail.ru

Abstract. The article describes the on-board control-measurement system designed to record the main flight parameters of a micro-convertiplane type unmanned aerial vehicle and the element base used for this purpose. The methodology of conducting tests in stationary mode through the on-board control-measurement system was developed and tests were carried out. The engine's diagnostic check and condition assessment has been performed using the on-board control-measuring system. The possibility of on-ground check of the micro unmanned aerial vehicles power elements before and after the flight, as well as the possibility of monitoring the flight events that may occur in the air during the flight has been shown. The data on the power consumption and temperature of each engine in the stationary mode, the direction of the aircraft axes and the velocity vector have been recorded by mean of the developed on-board control-measurement system, as well as time dependence diagrams of the corresponding parameters have been built in comparative order based on the obtained values. A methodology has been developed for the diagnostics of the engine operation of the micro-unmanned aerial vehicle before and during the flight. It has been shown that the temperature, power consumption and number of revolutions of the engines included in the power system of the aircraft, as well as the aircraft axes and velocity vector direction data is recorded during the flight, by mean of the on-board control-measurement system designed to collect data on the flight-technical parameters of the convertiplane-type micro-unmanned aerial vehicles.

Keywords: convertiplane, unmanned aerial vehicles, on-board control-measurement system, accelerometer, gyroscope, diagnosis, thermometer

1. Introduction

Achievements obtained in aerodynamics, navigation systems, electronics, robotics, information technologies, etc. have allowed to raise the development of unmanned aerial vehicles (UAV) to a higher level [1]. The directions of development of UAVs are mainly military, law enforcement, environmental monitoring, mapping, aerial photography, cargo transportation, film and TV industry and academic research.

Currently, it is very relevant to solve the problems of recording flight, flight-technical and telemetric data during laboratory and practical flight studies of micro UAVs, as well as transmitting them to the ground in real time. Despite the implementation of large-scale works by scientific-research, project-constructor and specialized companies operating in this direction, no comprehensive solution to the issue in dynamic mode during flight has been presented.

In order to solve these problems in medium and large UAVs, the required number of sensors and a centralized on-board recording system (FDR - Flight data recorder) are easily placed on board. Data received from the aircraft's power, power distribution, inertial navigation and propulsion systems is synchronously recorded to the permanent memory of the onboard recording system via a central computer, and is used

during flight evaluation and post-flight diagnostics of aircraft equipment. Some telemetry data ($v_{horizontal}$, $v_{vertical}$, v_{wind}, H_{flight}, $T_{weather}$, $T_{flight\ duration}$, GPS_{number}, $D_{distance}$) is transmitted in real-time from on-board to the ground via a radio transmitter in micro UAVs. This information is received both at the ground control station and at the operator's display. However, in a convertiplane-type aircraft consisting of four lift engines, no research study has been found on the solution of a comprehensive approach to the works to be done in order to record the main flight, flight-technical parameters of each engine during the flight, flight evaluation and post-flight diagnostics of aircraft equipment, prevent the recurrence of the emergency situation in subsequent flights [2]. The following refers to flight-technical parameters:

- $\dot{I}_1...\dot{I}_5$ – current consumed by engines (A);
- $T_1...T_5$ – relevant temperatures of engines (^{o}S);
- $RPM_1...RPM_5$ – revolution per minute;
- $A_1...A_3$ – accelerometer indication;
- $G_1...G_3$ – gyroscope indication.

Most of the UAV flight performance characteristics can be determined in the laboratory in stationary mode, but some of them must be determined only in dynamic mode during flight.

Work objective. Conducting tests in real flight conditions by creating an on-board control-measurement system to systematically collect information about the flight-technical parameters of the convertiplane-type UAV in flight mode ("online").

The collected information serves to increase the reliability and efficiency of the UAV's work, as well as the safety of flights. Based on the obtained flight data about the power consumption and temperature of each engine, the direction of the aircraft axes and the velocity vector, it is possible to carry out diagnostics of technical devices, especially engines and other propulsion elements, to timely detect and control events that may occur on the UAV's board during flight.

2. Problem statement

Taking into account the arbitrary direction of the engine thrust vector, a method to increase the reliability of determining the flight characteristics of a UAV for a given aerodynamic configuration has been solved in the research work related to the field of experimental aerodynamics [3]. The method of determining the aerodynamic characteristics of the UAV is based on the measurement of the numerical value of the flight velocity using hardware and devices during the acceleration of the aircraft.

The parameters of electric drives and controlled movement of a tricopter-type UAV during vertical take-off and land are described in [4]. Taking into account the requirements of weight and dimensions, the calculation of the aerodynamic parameters of the UAV has been carried out using the "XFLR5" software. The lift and drag coefficients of the UAV were determined depending on the angle of attack based on the "vortex" method, and the influence of the wing profile on the calculated aerodynamic properties has been analyzed.

The design of an on-board data collection system to calculate the aerodynamic characteristics of the UAV, which is only possible during free flight, is described in [5]. A functional diagram and algorithm of operation of the flight parameters recording system are presented. The proposed solutions allow collecting a large amount of data and increasing the efficiency of the system due to selecting and compressing.

It has been noted that the collected data eliminates the need to test UAV models in wind tubes to determine their aerodynamic properties, and allows saving money and time spent on developing new models. It is shown that the frequency of polling-measuring devices is increased to speed up data transmission and increase the accuracy of measurements during data exchange between system elements. In order to calculate the aerodynamic characteristics of the UAV through the proposed method, it is noted that the parameters of the flight trajectory, as well as the linear accelerations and angular velocities that occur during the movement, are measured with high accuracy. The hardware version of the proposed system for UAVs has been reviewed in the article.

An on-board recording device for UAVs is described in [6]. The on-board telemetry data of the UAV is received, compressed, stored and transmitted to the ground unit via the device during normal operation. It has been noted that in emergency mode it is possible to control actuators, for example, the parachute release system, via the control interface.

The structural, aerodynamic, power and weight characteristics of an aircraft-type UAV were comprehensively studied in, and analytical methods for determining and calculating its aerodynamic

characteristics have been described [7]. It has noted that one of the important conditions for choosing the most efficient configuration of the glider is the determination of the aerodynamic characteristics of the UAV at the initial and design stage. In order to solve this problem, numerical evaluation methods of aerodynamics are widely used instead of expensive experimental research methods.

The power consumption and temperature of each engine in the aircraft, the direction of the aircraft axes and the velocity vector data are recorded during the flight via the developed on-board control-measurement system [8].

3. Experimental technique

Technical support of on-board control-measurement system:

The description of the on-board control-measurement system installed on the convertiplane-type UAV is described in Fig. 1. The list of modules and elements used in the recording device is given below: ESP32 controllers; 5×ACS758 current sensor; 5×FS-CPD02 sensor; 5×DS18B20 digital temperature sensor; IMU sensor; TTGO T-Display module; microSD card module; FS-i6 "Flysky" ground control console; 12 V to 5 V voltage converter; 3S LiPo type battery [9].

Fig. 1. Convertiplane-type UAV with installed on-board control and measurement system.

4. Results and discussion

4.1 Research in static mode

Necessary supplies and equipment: convertiplane type UAV; ground control console ("Futaba"); ground monitor; on-board control-measurement system (based on ESP-32 controller); ground control console of the on-board control-measurement system ("Flysky"); 3S or 4S type battery; 6S type battery; 3 SD memory cards; video camera or mobile phone; timing device (stopwatch or mobile phone).

Preparation for work

1. A reset memory card is inserted into both ground monitor and on-board control-measurement system.
2. The horizontal position of the UAV is ensured.
3. The position of the 4 lifting blades rotating clockwise and counter-clockwise is changed. At this time, the rotation of the lift blades presses the glider of the UAV to the ground (no lift is generated).
4. For safety reasons, no blade is attached to the thrust engine.
5. 5 current, 5 temperature, 5 RPM sensors, accelerometer and gyroscope are checked for both presence and tight fastening in the on-board control-measurement system.
6. The ground monitor is switched on.
7. 6S type battery is connected to the UAV. From this moment on, the telemetry data transmitted from the flight controller to the ground is displayed on the ground monitor and recorded to the memory card in the monitor. The following are the telemetry data: - voltage of the battery on board, GPS number, flight altitude, flight range, horizontal and vertical flight velocities.

.

8. First, 4 lift, then 1 thrust engine are activated by remote control.

9. A 3S or 4S type battery is connected to the on-board control-measurement system, from this moment the flight parameters are recorded to the memory card on it, information about the number of revolutions of each engine appears on the screen of the system's ground control console ("Flysky").

10. The information displayed on the screen of the on-board control-measurement system's ground control console is recorded in video format. A video camera or mobile phone is used for this purpose, then the engines are shut down.

11. The system is ready for research.

Research progress

1. The life engines are started and the starting time is recorded.

2. The information about the number of revolutions of the engines, which appears on the screen of the ground control panel ("Flysky") of the on-board control-measurement system, is recorded by a video camera.

3. Depending on the duration of the study, the engines are rotated at different speeds.

4. Accelerations on 3-axis coordinate systems are performed by moving the laboratory table with the aircraft attached on it, to the right-left and up-down.

5. The switching to glider mode is performed, and the 5th engine is started, from this moment the lifting engines are gradually getting shut down.

6. During the study, timelines were recorded sequentially by parameters, all recorded indicators were archived and studied.

Based on the received data, appropriate timelines were created using the "Excel 2016" program *(Figure 2)*. It is determined from the diagram that at the start of the engines, the temperature and current consumption of the 4 engines operating in multicopter mode start to increase proportionally to the number of revolutions (5-th engine does not work) *(Figure 2, a and b)*. At this time, the power consumption and temperature of each engine begin to vary proportionally to the received flight information about the direction of the aircraft axes and velocity vector. It is more obvious from the diagram where the indicators of the accelerometer and gyroscope change according to the turning moments of the aircraft in the right-left and up-down directions *(Figure 2, d and e)*.

As described in Figure 2, c - When the UAV switches from the "multicopter" flight mode to the "glider" flight mode, that is, from the moment the thrust engine is started, the number of revolutions, temperature and current consumption of the 5th engine begin to increase over time, and the temperature and current consumption indicators of the lifting engines decrease accordingly, and also the revolutions number of the engines has a "zero" indicator. At the same time, the accelerometer and gyroscope indicators change depending on the movement dynamics of the UAV.

The diagram describes that shortly before the end of the experiment, the aircraft switches to the "multicopter" flight mode, and the indicators for this mode are repeated, as at the beginning of the flight.

The diagram of engine revolutions' number versus time has been built on the basis of the data recorded from the screen of the ground control console of the on-board control-measurement system ("Flysky") via a video camera during the tests.

4.2 Diagnostics of engines

To diagnose the engine, parameters (S1...S4) and (RPM1...RPM4) have been used.

Here:

$S_1...S_4$ - is a control signal generated by the flight controller that controls the rotational speed of the four lift engines accordingly;

$RPM_1...RPM_4$ - is the number of real revolutions recorded at a given time for each engine.

The configurations obtained from the combinations of control signals applied to them while maintaining the location of the engines in the glider construction have been used for diagnostics (Figure 3). In all configurations (I-IV), the position of the inertial sensor (IMU) consisting of a three-axis accelerometer and a gyroscope and the value of the corresponding signals remained unchanged.

In configuration I described in Figure 3, for a given aircraft, the location of the engines on the glider and the sequence of distribution of the corresponding control signals in the flight controller is determined by the manufacturer (programmer).

The other three configurations (II-IV) have been used for diagnostic evaluation purposes. In configuration I, the rotation speed of the 1st front engine was higher than the 2nd one.

a)

b)

c)

d)

e)
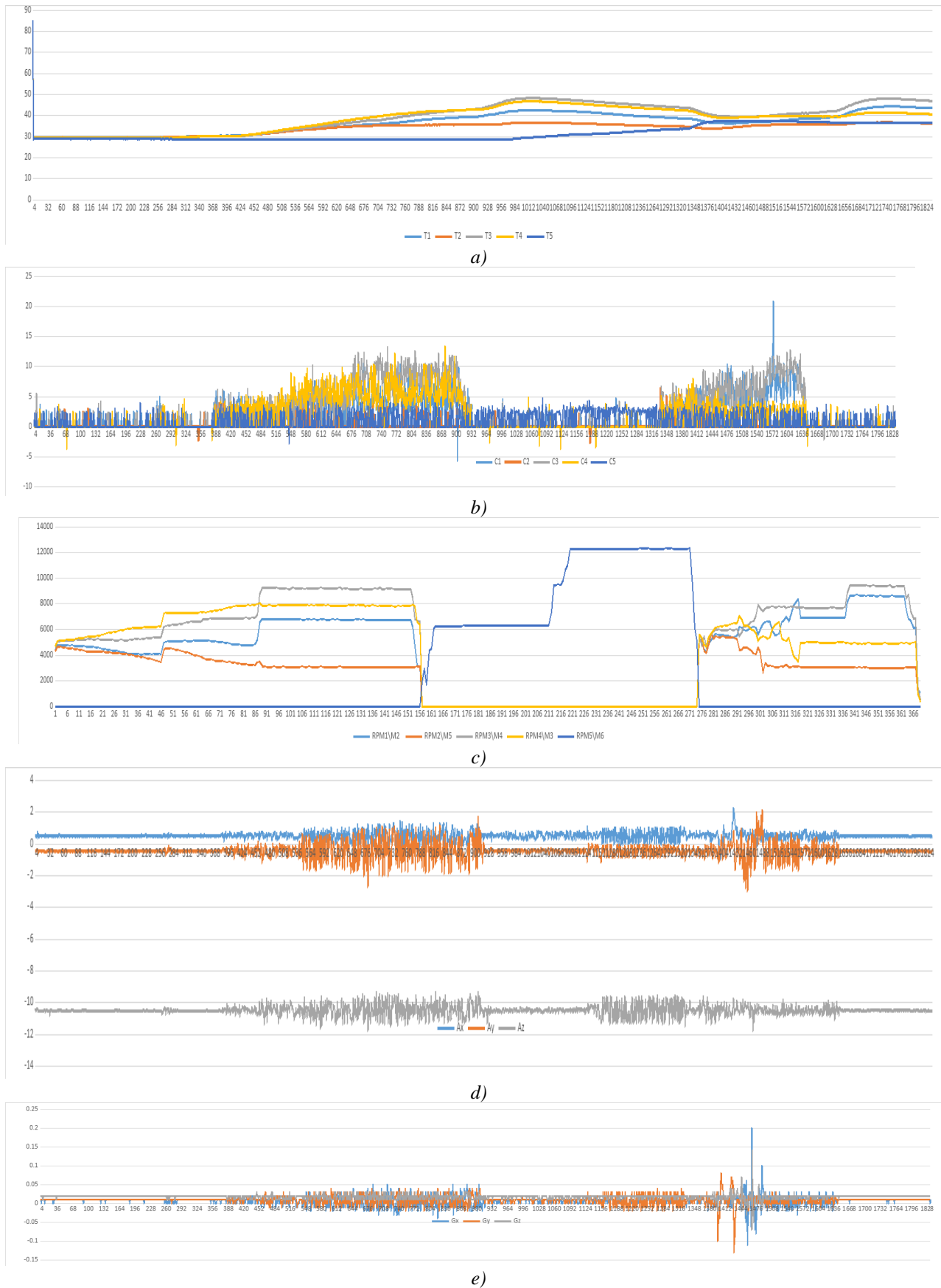
Fig. 2. Timelines built based on the indicators recorded by the on-board measurement system during the tests conducted in the stationary mode – temperature (ºS) a), current (A) b), number of revolutions of the engines (RPM) c), accelerometer d), gyroscope e) and "Excell 2016" software.
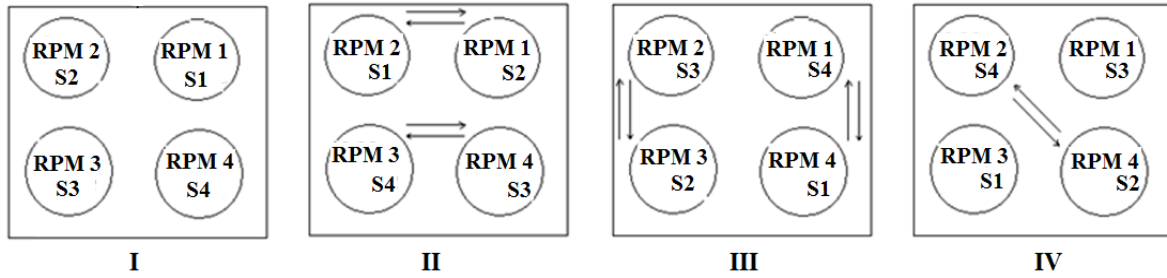
Fig. 3. Configurations corresponding to the possible displacement of the control signals of the lift motors in the flight controller.

a)

b)

c)

d)
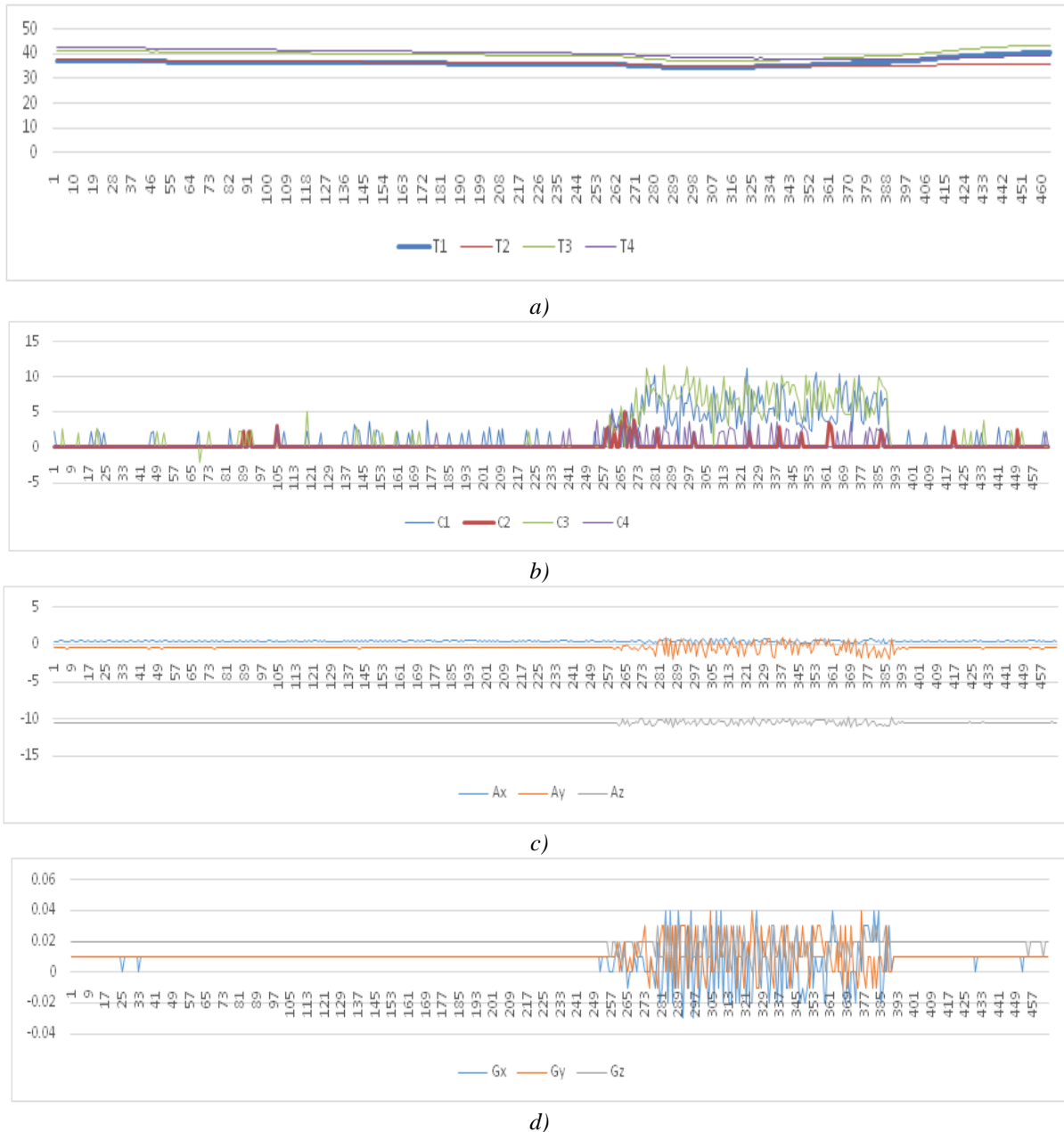
Fig. 4. Timelines of the revolutions during changes of control signals according to possible configurations:
a) temperature (ºS), b) current (a), c) accelerometer, and d) gyroscope.

However, when the signals from the flight controller to the engines were switched, the rotational speed of the 1st engine was less than that of the 2nd. In configuration I, the number of revolutions of the 4th engine was higher than in other cases (Figure 5, a). At the same time, it was observed that the current consumption (I1...I4) and temperature indicators (T1...T4), as well as the indicators of the accelerometer and gyroscope changed according to the number of engine revolutions. (Figure 4, a, b, c and d).
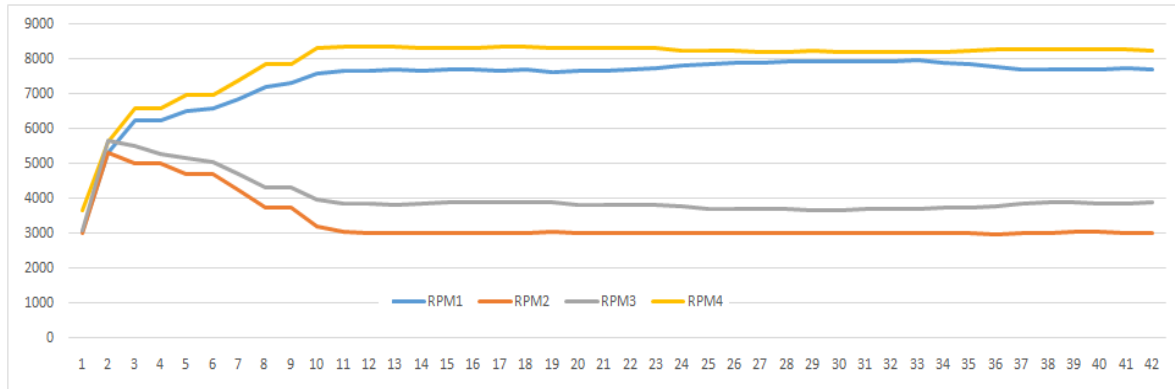
a)
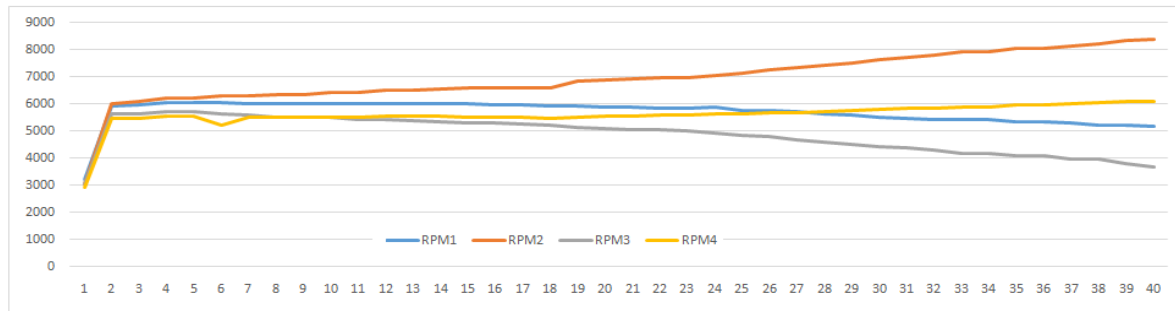
b)
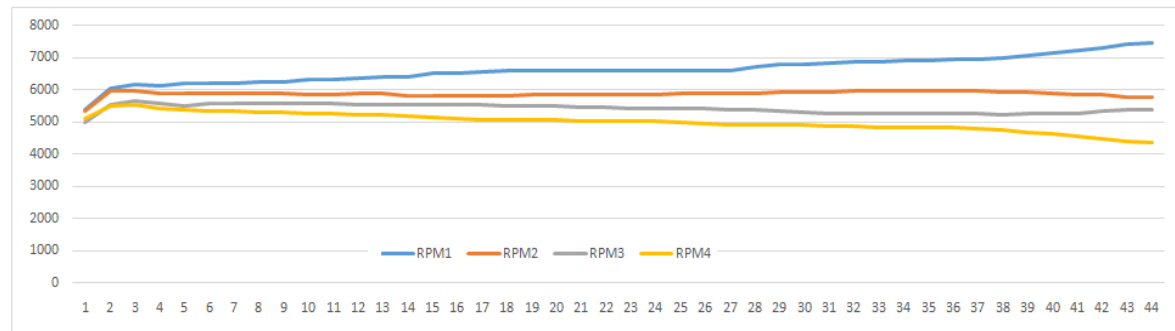
c)
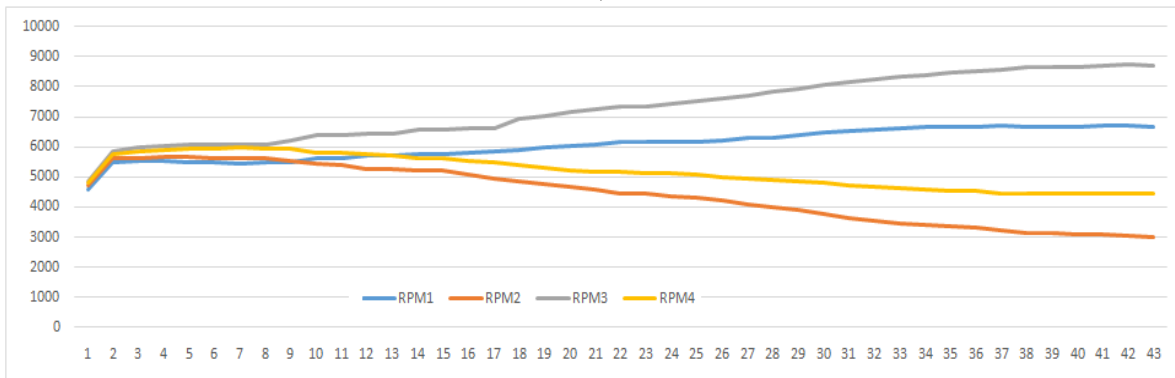
d)

Fig. 5. Timelines of the revolutions a), b), c), d) based on the indicators recorded in configuration I by mean of the on-board control-measurement system

Then the displacement corresponding to the 2nd, 3rd and 4th configurations was carried out (Figure 3). During the study, based on the recorded accelerometer and gyroscope indicators (Ax, Ay, Az and Gx, Gy, Gz) for each configuration, it was found that the horizontal position of the UAV is not ensured. Therefore, in the combination according to configuration I, the control signal of 4th engine corresponds to a relatively high number of revolutions.

Getting the corresponding engine to its highest rotational speed when applying this signal sequentially to the 2nd, 1st, and 3rd engines according to the 2nd, 3rd, and 4th configurations, confirmed once again the thesis that the horizontal position of the UAV is not ensured (Figure 5, b, c and d). Thus, it was determined that being different number of revolutions for a given case is not an indication of engine failure.

5. Conclusion

1. For the first time, an on-board control-measurement system has been created in order to comprehensively record the main flight-technical parameters (I1...I5, T1...T5, RPM1...RPM5, A1...A3, G1...G3) of the mcro convertiplane-type UAV.

2. Data on the power consumption and temperature of each engine, the direction of the aircraft axes and the velocity vector have been recorded in the stationary mode by mean of the developed on-board control-measurement system.

3. Based on the values obtained during the tests, the corresponding parameters versus time diagrams have been built in comparative order.

4. The on-board measurement system created for the micro-UAV allows for full monitoring of technical parameters online, which makes it possible to make operational decisions by noting changes in the situation that may occur on board during the flight.

5. A methodology has been developed for the diagnostics of the engine operation of the micro-unmanned aerial vehicle before and during the flight.

Conflict of interest statement
The authors declare that they have no conflict of interest in relation to this research, whether financial, personal, authorship or otherwise, that could affect the research and its results presented in this paper.

CRediT author statement
Nabiyev R.N.: Conceptualization, Methodology, Supervision, Data curation; **Abdullayev A.A.:** Writing- Original draft preparation, Visualization, Writing- Reviewing and Editing; **Qarayev Q.I.:** Software, Investigation, Validation.
The final manuscript was read and approved by all authors.

References

1   Nabiyev R.N., Abdullayev A.A., Qarayev Q.I., Abbasov V.A. (2022) Determination of the center of gravity of an unmanned aerial vehicle of a tiltrotor type. *Izvestiya SFedU. Engineering Sciences,* 229, 5, 258 – 268. [in Russian] DOI: 10.18522/2311-3103-2022-5-258-268.

2   Nabiyev R.N., Qarayev Q.I., Abdullayev A.A. (2020) Conceptual functional design of hybrid energy source of unmanned convertiplane. *Proceedings of the IOP Conference Series: Conference Scopus. Materials Science and Engineering.* 862, 022043. DOI: 10.1088/1757-899X/862/2/022043.

3   Mikhaylov S.A., Khamza M.A.K., Makhanko A.A. (2023) *Method for determınıng aırcraft aerodynamıc characterıstıcs based on flıght experıment results.* Patent – Invention, RU 2790358 C1. Federal servıce for ıntellectual property, Russian Federation. No.5, Publ.17.02.2023. Available at: https://patents.google.com/patent/RU2790358C1/ru

4   Emelyanova O.V., Kazaryan K.G., Martinez Leon A.S., Jatsun S.F. (2017) The synthesis of electric drives characteristics of the UAV of "convertiplane - tricopter" type. *Cloud of Science.* 4, 2, 249–263. [in Russian]. Available at: http://cloudofscience.ru

5   Khamza M.A.K. (2023) Designing a flight information collection system for calculating the aerodynamic charac-teristics of a UAV. *Ontology of Designing.* 13, 1, 93 – 98. DOI: 10.18287/2223-9537-2023-13-1-90-98.

6   Kleshnina S.A., Kleshnin V.YU., Boev N.M., Krilov E.D. (2018) *Device for recording and transmitting telemetric information of an unmanned aerial vehicle.* Patent RU 182090 C1, No. 22, Publ. 2018.08.03. Available at: https://patents.google.com/ patent/RU182090U1/ru

7 Kuat K.İ. (2022) Determination of aerodynamic characterisitcs of fixed-wing unmanned aerial vehicle by analytical techniques. *Tomsk State University Journal of Mathematics and Mechanics*, 78, 112 – 124. [in Russian]. DOI: 10.17223/1998821/78/9.

8 Nabiyev R.N., Abdullayev A.A., Garayev Q.I. (2024) Study of flıght-technıcal parameters of convertoplan-type unmanned mıcro aırcraft ın multıcopter mode. *Scientific Journal National Aviation Academy*. 26, 1, 17 – 29. [in Azerbaijani]. Available at: https://scientific-journals.naa.edu.az:8070/articles/get/62

9 Alkahdery L.A., Yurchenko A.V., Mohammed J.A.-K., Neshina Y.G. (2023) Automated temperatureand humidity control and monitoring system for improving the performance in drying system. *Eurasian Physical Technical Journal.* 20, 2(44), 32 – 40. DOI: 10.31489/2023No2/32-40

_____

AUTHORS' INFORMATION

Nabiyev, Rasim Nasib – Doctor of of Techn. Sciences, Professor; Head of Aviation Electronics Scientific Research Institute of Transport and Aviation Space Problems, National Aviation Academy of Azerbaijan, Baku, Azerbaijan; ORCID iD: 0000-0002-1727-0360; nabiyevrasim@gmail.com

Abdullayev, Anar Arif –- Candidate of Phys. and Math. Sciences, Doctorate of Aviation Electronics Scientific Research Institute of Transport and Aviation Space Problems, National Aviation Academy of Azerbaijan, Baku, Azerbaijan; ORCID iD: 0000-0001-7672-3940; anarcafarov09@mail.ru

Qarayev, Qadir Isaxan –- Candidate of Techn. Sciences, Scientific Researcher, Aviation Electronics Scientific Research Institute of Transport and Aviation Space Problems, National Aviation Academy of Azerbaijan, Baku, Azerbaijan; ORCID iD:: 0000-0001-7232-669X; qedir71@mail.ru

.

UDC 53.072

EVALUATING ROUTING ALGORITHMS ACROSS DIFFERENT WIRELESS MESH NETWORK TOPOLOGIES USING NS-3 SIMULATOR

Turlykozhayeva D.A. *, Akhtanov S.N., Baigaliyeva A.N., Temesheva S.A., Zhexebay D.M., Zaidyn M., Ussipov N.M., Skabylov A. A.

al-Farabi Kazakh National University, Almaty, Kazakhstan
*Corresponding author: turlykozhayeva.dana@kaznu.kz

Abstract. *Wireless Mesh Networks are gaining traction as a solution for delivering reliable connectivity without centralized infrastructure. They operate through wireless node interconnections, forming self-configuring networks ideal for scenarios where wired networks are impractical. Routing is crucial in Wireless Mesh Networks to ensure efficient communication among nodes. However, the suitability of routing algorithms for Wireless Mesh Network's topology requires further investigation. This paper proposes an investigation into the effectiveness of routing algorithms like AODV, DSDV, and OLSR across various Wireless Mesh Networks topologies using NS-3 simulation. It also aims to determine the optimal number of nodes and protocols to maximize throughput and minimize packet loss within a limited area. Through rigorous NS-3 simulations, the study demonstrates that AODV, DSDV, and OLSR exhibit differing effectiveness across random, mesh grid, and Fruchterman-Reingold topologies. These results emphasize the importance of considering topology-specific factors when selecting and optimizing routing protocols for Wireless Mesh Networks. In summary, Wireless Mesh Networks offer decentralized connectivity, but the effectiveness of routing algorithms in different topologies remains understudied. This investigation addresses this gap by evaluating routing algorithms across various topologies, shedding light on their suitability and performance in Wireless Mesh Networks.*

Keywords: Wireless Mesh Networks; Ad hoc On-Demand Distance Vector; Destination Sequenced Distance Vector; Optimized Link State Routing Protocol; Proactive Routing Protocols; NS-3.

1. Introduction

Wireless Mesh Networks (WMNs) have become a highly promising technology for providing robust and reliable connectivity in diverse environments, offering seamless coverage and efficient data transmission. This network type is distinguished by its self-organizing and self-configuring capabilities, requiring minimal initial investment for deployment. WMNs demonstrate versatile applicability by supporting a wide range of applications, including broadband home networks, education, healthcare, building automation, rescue operations, and military applications [1]. The architecture of a Wireless Mesh Network (WMN) is structured into three logically organized layers: Mesh Routers (MRs), Mesh Gateways (MGs), and Mesh Clients (MCs). Within this framework, Mesh Clients (MCs) encompass a variety of devices, including desktop computers, mobile devices, laptops, and Pocket-PCs, all establishing their connections to the internet through Mesh Routers (MRs). As intermediaries, Mesh Routers (MRs) are essential for transmitting network traffic to Mesh Gateways (MGs), which have direct connections to the internet infrastructure [2].

A crucial factor impacting WMN performance is the routing protocol used to forward data packets within the network. The dynamic and constantly shifting topology of client nodes significantly challenges the routing processes in WMNs. Effective data routing plays a key role in ensuring reliable communication between nodes, considering the specific features of the network topology. Despite the variety of routing algorithms available, their applicability in WMN topologies remains an under-researched area [3].

This article presents a study that assesses the performance of routing algorithms across various WMN topologies, using simulations conducted with the NS-3 modeling environment. Specifically, three routing protocols are evaluated: Ad hoc On-Demand Distance Vector (AODV), Destination Sequenced Distance Vector (DSDV), and Optimized Link State Routing Protocol (OLSR). To assess the effectiveness of these routing algorithms, a set of key routing metrics is considered, including throughput, jitter, time delay, and packet loss. These metrics play a crucial role for assessing the performance of routing protocols in WMN topologies. Additionally, this research aims to ascertain the optimal combination of nodes and protocols within a limited 1x1 km square area to achieve maximum throughput and minimize packet loss. The latest versions of routing protocols within NS-3.40 were utilized for this research.

The article is organized into five sections. Section II highlights related work on routing protocols, while Section III provides an overview of the selected routing protocols designed for WMNs, laying the groundwork for the comparative analysis presented in this study. Section IV is dedicated to different wireless mesh network topologies, such as random, mesh grid, and Fruchterman-Reingold. Section V showcases and discusses results, offering insights and interpretations based on the evaluation. Finally, a conclusion is presented to succinctly summarize the key features and findings of our study.

2. Related works

Rajeev Paulus and colleagues [4] conducted a comparison of the Ad hoc On-Demand Distance Vector (AODV), DSR, OLSR, and ZRP routing protocols. They utilized QualNet version 6.1 to evaluate the performance of these protocols based on metrics such as throughput, packet delivery ratio (PDR), average end-to-end delay, and average jitter. The findings indicated that ZRP exhibited slower speeds and lower packet delivery success rates compared to other protocols, particularly when encountering changes in pause time and maximum speed. AODV demonstrated superior performance across all criteria. While DSR outperformed OLSR and ZRP in terms of speed and packet delivery success, it exhibited the poorest performance in terms of average jitter and delay. OLSR exhibited the least favorable results for average jitter and delay, especially when pause times varied. These conclusions offer valuable insights for selecting the most suitable method when designing and utilizing computer networks.

Samba Sesay and colleagues [5] conducted a survey that examined the performance of DSDV, DSR, TORA, and AODV using an extended version of the UCB/LBNL network simulator ns-2. The simulation encompassed a virtual environment measuring 1200 by 300 meters and lasted 600 seconds. The study focused on several metrics, including throughput, average end-to-end latency, packet delivery ratio, route acquisition time, and routing overhead. Notably, DSR demonstrated superior performance with lower routing overhead across all scenarios. Conversely, DSDV showed suboptimal performance, particularly under conditions of high movement speeds and node density. TORA exhibited excellent performance, especially in larger networks characterized by high mobility rates and movement speeds. These findings offer valuable insights into the comparative strengths and weaknesses of these routing protocols in simulated settings.

Charles E. Perkins and colleagues [6] examined the performance of two prominent on-demand routing protocols, DSR and AODV, in ad hoc networks. Using the Ns-2 network simulator, the study evaluated various characteristics, including normalized routing load, normalized MAC load (reflecting efficient wireless medium utilization by data traffic), average end-to-end delay, and packet delivery ratio. The analysis revealed that DSR exhibited inadequate latency and throughput performance, primarily attributed to its aggressive caching technique and the absence of mechanisms for managing older routes or ensuring route freshness in scenarios with multiple choices. These findings contribute to the academic understanding of on-demand routing protocols in ad hoc networks [6].

Josh Broch and colleagues [7] investigated the performances of DSDV, TORA, DSR, and AODV using the ns network simulator. The study entailed comparing parameters such as packet delivery, routing overhead, path optimality, and node movement speed. Despite TORA being identified as the poorest performer in terms of routing packet overhead, it still succeeded in delivering over 90% of packets in

scenarios with 10 or 20 sources. AODV demonstrated nearly equivalent performance to DSR across various mobility rates and movement speeds, effectively achieving its goal of eliminating source routing overhead.

3. Routing protocols

The primary aim of routing in wireless mesh networks (WMNs) is to establish efficient paths for transmitting data packets between source and destination nodes within the network. Routing protocols in WMNs can be broadly categorized into three types: proactive, reactive, and hybrid, based on their approach to packet forwarding [8]. Proactive routing protocols, also known as table-driven methods, establish paths to all accessible destination nodes, regardless of whether they are currently required for data transmission. These protocols continuously compute routes to all reachable nodes, providing consistent and up-to-date routing information. The main advantage of proactive protocols lies in nodes quickly acquiring routing information, enabling rapid pathway establishment [9].

Reactive routing protocols, or on-demand methods, establish routes only when necessary. When a source node needs a route to a destination node, the route discovery process is initiated. This process continues until a route is found or until all potential routes are explored without success. In WMNs with minimal node mobility, reactive routing protocols offer superior scalability despite potential disruptions to active routes due to node mobility in mobile networks [10]. Hybrid Routing Protocols combine the strengths of proactive and reactive routing protocols while mitigating their weaknesses to identify optimal routes with minimal management overhead. This protocol type employs different routing protocols in various segments of the WMN infrastructure. Reactive protocols are used in the ad hoc network area, while proactive protocols are implemented in the wireless backbone, ensuring efficient and adaptive routing [11].

This study provides a comprehensive overview of three routing protocols: AODV, DSDV, and OLSR.

The Ad hoc On-Demand Distance Vector (AODV) algorithm facilitates the creation of dynamic, self-initiating, multihop routes among mobile nodes within an ad hoc network, and operates reactively by establishing routes only when needed in response to specific communication requests. AODV enables swift acquisition of routes to new destinations without necessitating the maintenance of routes to inactive destinations. Furthermore, it enables mobile nodes to promptly adapt to changes in network topology and respond to link failures [12].

AODV operates without loops, steering clear of the "counting to infinity" issue associated with the Bellman-Ford algorithm. This ensures rapid convergence in the face of changes in ad hoc network topology, especially when nodes relocate. In cases of link failures, AODV promptly notifies the affected nodes, allowing them to invalidate routes associated with the disconnected links [13].

A standout aspect of AODV is how it employs destination sequence numbers for each route entry. The destination itself generates this sequence number, which gets shared with requesting nodes along with route details. This clever use of destination sequence numbers guarantees loop-free routing and is easy to implement. When faced with two route options to a destination, a requesting node must opt for the one with the highest sequence number [14].

The AODV routing protocol is tailored for mobile ad hoc networks encompassing populations ranging from tens to thousands of mobile nodes. It can adeptly handle varying mobility rates, spanning from low to moderate and even relatively high, accommodating diverse levels of data traffic. AODV is specifically crafted for networks where mutual trust among nodes is established, either through preconfigured keys or a confirmed absence of malicious intruders [15]. The design of AODV prioritizes minimizing control traffic dissemination and cutting down on data traffic overhead, aiming to enhance scalability and overall performance.

The DSDV (Destination-Sequenced Distance Vector) is a proactive protocol that employs the Bellman-Ford algorithm to compute optimal paths in mobile ad hoc networks (MANETs). Its choice of hop count as the cost metric reflects the number of hops a packet must traverse to reach its intended destination. Unlike reactive protocols, DSDV is proactive and maintains a comprehensive routing table encompassing all nodes within the network, not solely its immediate neighbors [16].

The protocol employs both periodic and trigger-based update mechanisms to disseminate routing information. However, the inherent nature of periodic updates introduces the potential for routing loops. To address this concern, DSDV introduces the concept of sequence numbers. Each node independently selects its sequence number, ensuring incremental values with each periodic update [17]. Notably, these sequence numbers are always even, a deliberate design choice that simplifies the protocol's operations.

When a node must send an update for a route that has expired to its neighboring nodes, it increases the sequence number of the disconnected node by 1. Receivers of these updates check the sequence number; if it's an odd value, they remove the related entry from the routing table, preventing routing loops.

In the dynamic environment of MANETs, where node mobility can lead to frequent route fluctuations, DSDV incorporates a settling time mechanism. This feature helps dampen the impact of rapid changes, contributing to the stability and reliability of the protocol in the face of evolving network topologies. Overall, DSDV strikes a balance between proactive route maintenance and effective loop prevention, making it a valuable contender in the realm of mobile ad hoc networking protocols [19-21].

The Optimized Link State Routing Protocol (OLSR) is specifically designed for mobile ad hoc networks, functioning as a proactive, table-driven protocol [22, 23]. It consistently exchanges topology information with other nodes in the network. Within OLSR, each node strategically selects a subset of its neighbors as "multipoint relays" (MPRs). These MPRs play a crucial role in forwarding control traffic, efficiently disseminating it throughout the network and minimizing required transmissions. MPR nodes carry a special responsibility in announcing link-state information within the network. OLSR ensures the shortest path routes to all destinations by mandating that MPR nodes declare link-state information for their selected MPRs. Any additional available link-state information can be utilized for redundancy purposes [24].

Nodes designated as MPRs periodically broadcast this status in their control messages, signaling their accessibility to nodes that have designated them as MPRs. In route calculation, MPRs are crucial in establishing routes from a given node to any destination in the network. They also facilitate efficient flooding of control messages across the network [25]. OLSR adopts a cautious approach in MPR selection, picking from one-hop neighbors with bidirectional, symmetric connections. This guarantees that the chosen route through MPRs avoids problems associated with data packet transfer over unidirectional links, such as the absence of link-layer acknowledgments for data packets at each hop, particularly in link-layer implementations utilizing unicast traffic [26].

4. Topologies

Topology in wireless networks refers to the physical or logical structure, organization, and distribution of nodes and connections. The topology defines how devices connect and communicate with each other within a WMN. There are various types of WMN topologies such as random, mesh grid, and Reingold, which we discussed further [27].

Random topology refers to the structural configuration or arrangement of elements within a system or network that lacks a specific pattern or predetermined organization. In different contexts such as network theory, graph theory, or complex systems analysis, a random topology suggests that the connections between components or nodes are formed based on a probabilistic or stochastic process, rather than being systematically arranged or structured according to a defined rule or pattern. For example, in a random network topology, nodes might relate to a certain probability, leading to a heterogeneous and often unpredictable network structure. This contrasts with regular or ordered topologies where connections follow specific rules or patterns, such as in a grid or lattice network. Random topology often exhibits properties such as high variability, robustness, and resilience to certain types of failures or attacks due to its lack of centralized organization [28]. Below, in Figure 1, a random network is constructed and subsequently utilized in the investigation of routing algorithms in Section V.

In wireless mesh networks, the mesh grid topology refers to a structured arrangement where network nodes are organized in a grid-like fashion. Each node typically communicates with its immediate neighbors, forming a dense mesh of interconnected nodes. Mesh grid topologies can be easily scaled by adding more nodes in a systematic grid pattern, allowing for efficient expansion of network coverage. The structured nature of the mesh grid topology enhances network reliability, as multiple redundant paths are available for data transmission. If one path fails, alternative routes can be quickly utilized, minimizing disruptions in communication. Due to the proximity of neighboring nodes, data transmission within a mesh grid network tends to have low latency, making it suitable for applications requiring real-time communication, such as video streaming or online gaming. The predictable arrangement of nodes in a mesh grid topology simplifies network planning and deployment. Nodes can be strategically positioned to optimize coverage and connectivity. Mesh grid topologies ensure uniform coverage across the network area, minimizing dead zones and ensuring consistent signal strength throughout the deployment area. However, mesh grid topologies often require a fixed infrastructure to support the grid layout, such as poles or buildings for node placement.
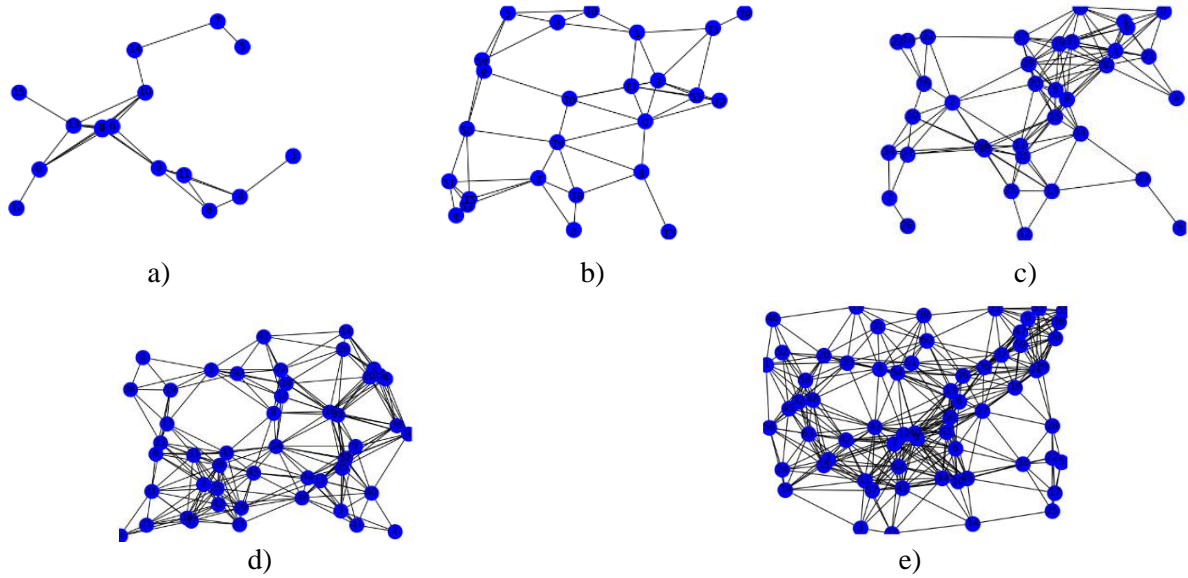
Fig.1. Random topology, where a) 4x4 (16 nodes); b) 5x5 (25 nodes); c) 6x6 (36 nodes); d) 7x7 (49 nodes); e) 8x8 (64 nodes).(1)

This dependency on infrastructure can limit the flexibility of deployment in certain environments. In densely populated areas or environments with high wireless interference, the proximity of nodes in a mesh grid topology may lead to increased interference levels, affecting network performance. Deploying a mesh grid network with many nodes can be costly, both in terms of equipment and installation, especially when compared to more ad-hoc or decentralized topologies [29]. Below, in Figure 2, a mesh grid network is created and then employed in the examination of routing algorithms in Section V.

Fig.2. Mesh grid topology, where a) 4x4 (16 nodes); b) 5x5 (25 nodes); c) 6x6 (36 nodes); d) 7x7 (49 nodes); e) 8x8 (64 nodes). (2)

The "Fruchterman-Reingold" topology, named after its creators, Thomas M. J. Fruchterman and Edward M. Reingold, is a specific type of layout algorithm commonly used in graph visualization. While it is not a typical mesh network topology like random or grid, it can be applied within the context of WMN for

organizing and visualizing node placements. In the Fruchterman-Reingold algorithm, nodes in a network are represented as points in a two-dimensional space, and edges between nodes are represented as lines. The algorithm simulates a physical system where nodes repel each other and edges act as springs, resulting in an equilibrium configuration where nodes are evenly spaced, and edges have minimal overlap. This topology is particularly useful for visualizing and understanding the structure of complex networks, including wireless mesh networks, as it tends to arrange nodes in a way that reveals underlying patterns and relationships. However, in practical implementations of wireless mesh networks, the Fruchterman-Reingold topology may not directly dictate the network's operational layout. Instead, it can serve as a tool for network designers and administrators to visualize and analyze network structures, aiding in optimization, troubleshooting, and planning [30]. In Figure 3 below, a topology is generated using the Fruchterman-Reingold force-directed algorithm and subsequently utilized for examining routing algorithms in Section V.


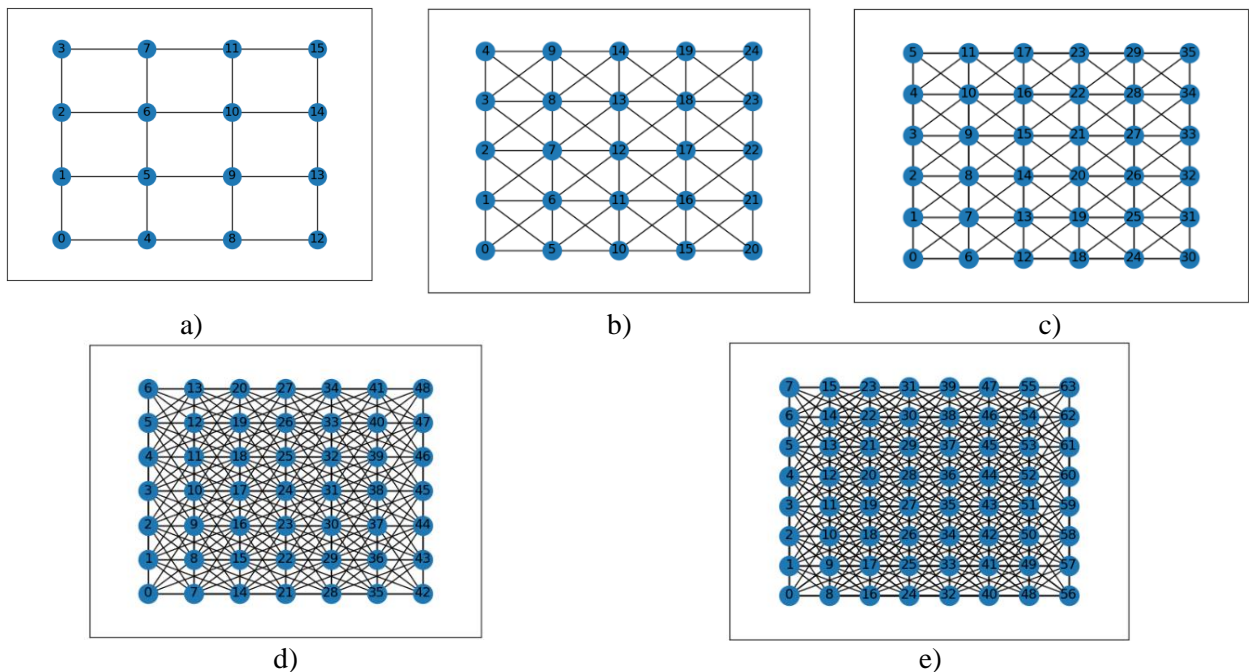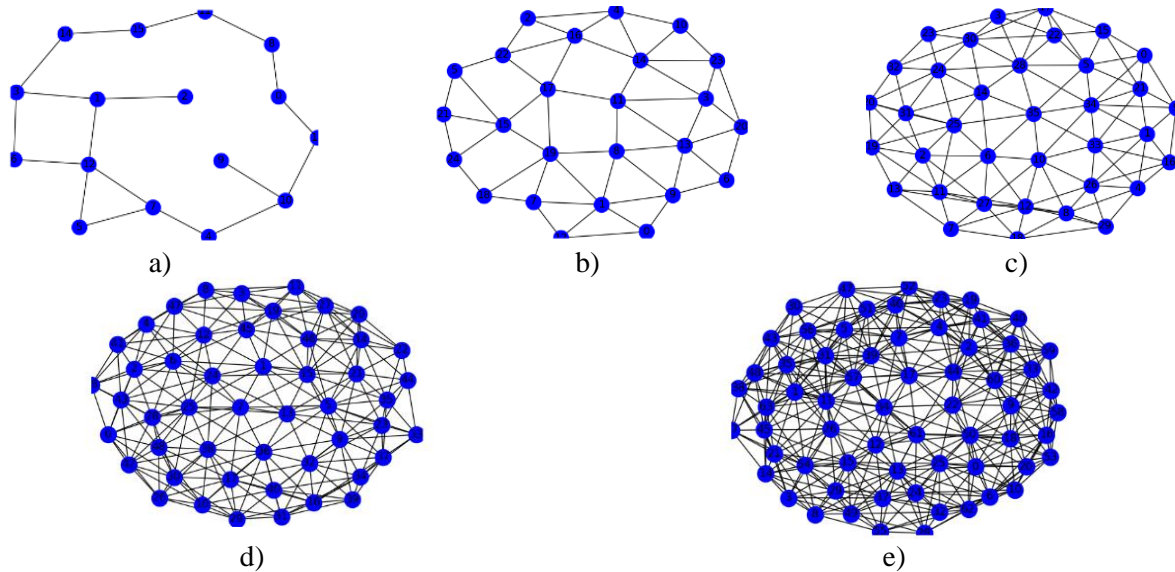**Fig.3.** Fruchterman-Reingold force-directed algorithm topology, where a) 4x4 (16 nodes); b) 5x5 (25 nodes); c) 6x6 (36 nodes); d) 7x7 (49 nodes); e) 8x8 (64 nodes). (3)

In wireless mesh networks, different topologies, such as random, mesh grid, and Fruchterman-Reingold, can be utilized with various routing algorithms to optimize network performance. Each topology offers unique advantages and challenges that can be leveraged with specific algorithms to enhance data transmission, minimize latency, and improve network reliability.

5. Simulation results and discussion

In this section, we will conduct a comparative analysis of the operational effectiveness of the three routing protocols—AODV, DSDV, and OLSR—in diverse wireless mesh network topologies.

In our simulations, we employed the IEEE 802.11p standard and the Two Ray Ground Propagation Loss Model. The IEEE 802.11p is a sanctioned amendment to the IEEE 802.11 standard, designed to facilitate wireless access in vehicular environments (WAVE). The Two Ray Ground Propagation Loss Model takes into account both the direct path and a ground reflection path. The received power at a distance t is determined using equation (1).

$$P_r(d) = \frac{P_t G_t G_r h_t^2 h_r^2}{d^4 L} \qquad (1)$$

where, ht and hr are the heights of the transmit and receive antennas.

Our evaluation of these 4 routing protocols mentioned above will be based on metrics such as throughput, time delay, and packet loss, providing a comprehensive assessment of their performance and suitability for WMNs. To gauge the impact of node quantity on the performance of these routing protocols, simulations were executed using NS-3.40 (ver3.14.1) on the Ubuntu 22.04 LTS platform. The simulation parameters are presented in Table 1.

.

Table 1. Simulation parameters

Network simulator	NS-3.40 (ver3.14.1)
Channel type	Wireless channel
Propagation model	Friis Propagation Loss Model
Network interface type	Phy/Wireless Phy
Mac type	Mac/802.11ac
Interface Queue type	Drop Tail/PriQueue
Link layer type	LL
Antenna Model	Single Antenna
Traffic type	CBR
Transport protocol	UDP
Simulation time	50 s
Packet size	1024
Simulation area	1000m*1000m
Mobility model	Constant
Adhoc protocols	OLSR version Pre-0.9.9, AODVv2, DSDV
Number of nodes in Random, MeshGrid and Fruchterman-Reingold force-directed algorithm topologies	16, 25, 36, 49, 64

A) Throughput

The results of the throughput measurement reflect the amount of data efficiently transmitted over the network over time. The throughput is determined using equation (2).

$$Throughput = (\sum successfully\ receiver\ bits\ /\ Time\ of\ simulation\ \times 1024) \qquad (2)$$

Figure 4 shows the throughput achieved by the AODV routing algorithm in various WMN topologies. The random and Reingold topology configurations demonstrate superior throughput when the optimal number of nodes is 50. These findings underscore their efficacy within the experimental context, suggesting a higher level of efficiency and reliability compared to mesh grid topology. In figure 5 OLSR routing algorithm achieves higher throughput when the optimal number of nodes is 50 in random topology compared to mesh grid and Reingold topologies, highlighting the efficacy of random topology in facilitating higher data transmission.
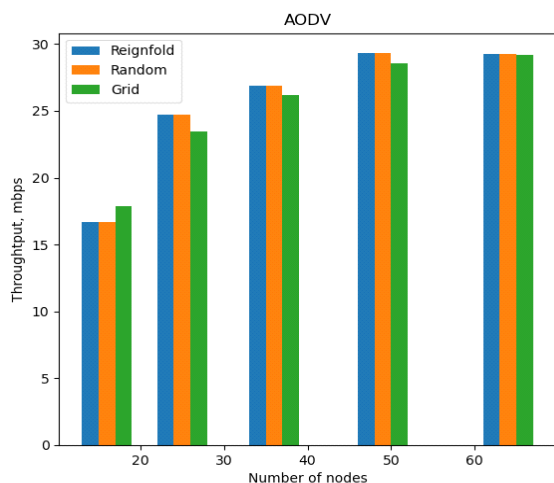
Fig.4. Throughput for AODV routing algorithm (4)
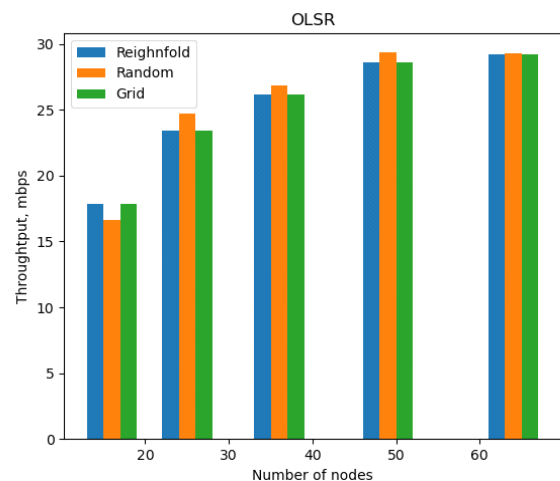
Fig.5. Throughput for OLSR routing algorithm (5)

In the following figure 6 DSDV routing algorithm exhibits superior performance in Reingold and Random topologies when the optimal number of nodes is 50 compared to mesh grid topology, indicating higher throughput speeds.
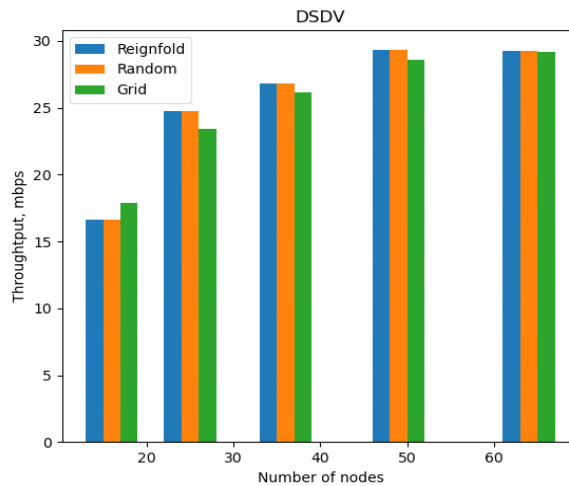
Fig.6. Throughput for DSDV routing algorithm (6)

B) Packet loss. Packet loss represents the proportion of data packets that do not reach their designated destination owing to diverse factors like network congestion or link breakdowns. The Packet loss is determined using equation (3).

$$Packet\ Lost = (\sum Packets\ send\ by\ sources\ -\ \sum Packets\ successfully\ received) \qquad (3)$$

Figure 7 demonstrates the packet loss rates encountered with the AODV routing algorithm for each topology. It was found that packet loss reduction is observed in mesh grid topology when the number of nodes is 50 compared with two other topologies. Figure 8 illustrates the packet loss rates experienced with the OLSR routing algorithm for each topology. It was discovered that there is a decrease in packet loss in the random topology when the optimal number of nodes is 50, compared to the other two topologies.
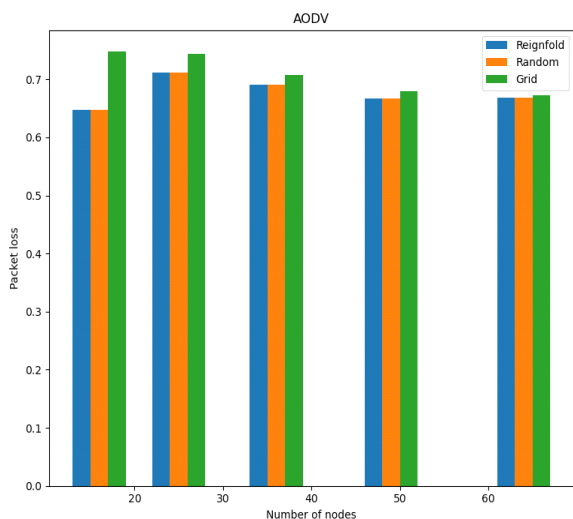
Fig.7. Packet loss for AODV routing algorithm (7)
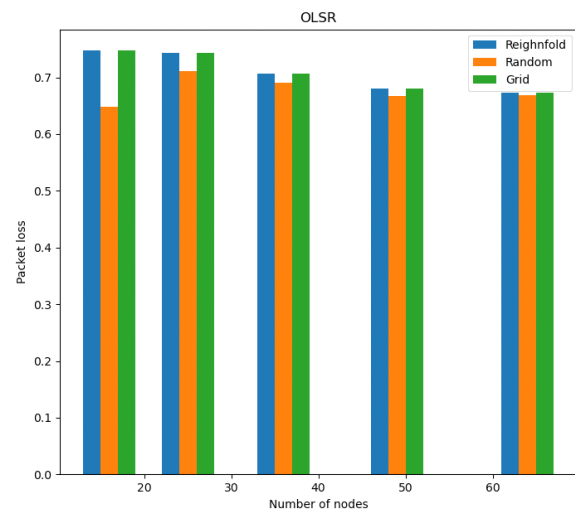
Fig.8. Packet loss for OLSR routing algorithm (8)

Figure 9 illustrates the packet loss rates observed with each topology. It was found that Reingold and random topologies for the DSDV routing algorithm consistently had the lowest packet loss rates across all tested scenarios. The optimal number of nodes at which the lowest packet loss was achieved was 50.
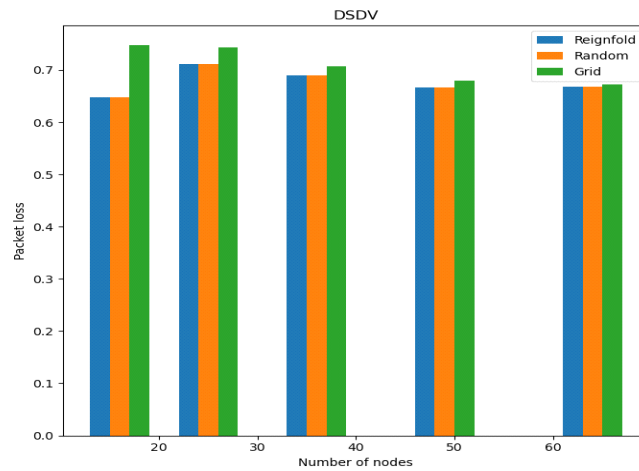
Fig.9. Packet loss for DSDV routing algorithm (9)

C) Time delay. Time delay refers to the time it takes for data packets to move from the sender to the receiver. The Time delay is determined using equation (4).

$$Time\ delay = |EndTime_i - StartTime_i| \qquad (4)$$

where, EndTime$_i$ is the time that packet i was sent by the source, is received successfully by the destination and StartTime$_i$ is the time of starting to send packet i by the source. Figure 10 illustrates the time delay experienced by data packets when using the AODV routing algorithm for various topologies. When the optimal number of nodes is 60, both random and Reingold topologies exhibit the lowest time delay. Figure 11 depicts the time delay encountered by data packets when employing the OLSR routing algorithm across different topologies. In Figure 11, it is observable that with an increasing number of nodes, the time delay diminishes. When the optimal number of nodes is 60, random topologies demonstrate the lowest time delay compared to others.
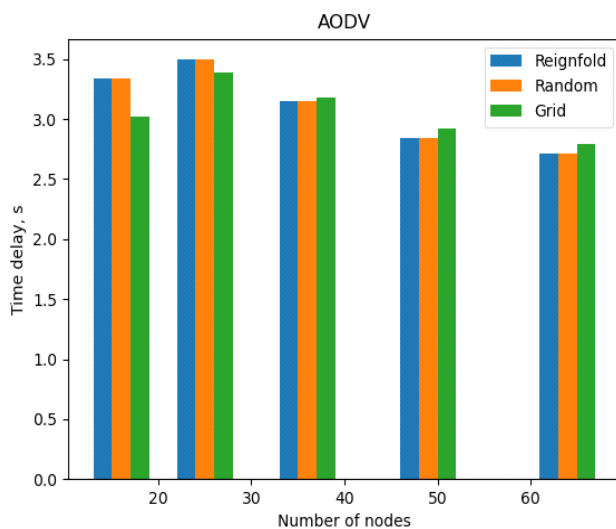
Fig.10. Time delay for AODV routing algorithm (10)
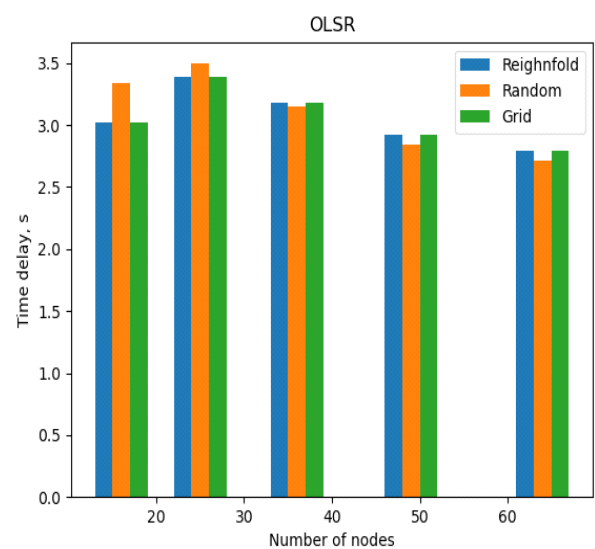
Fig.11. Time delay for OLSR routing algorithm (11)

Figure 12 illustrates the time delay experienced by data packets when utilizing the DSDV routing algorithm across various topologies. It can be observed in Figure 11 that as the number of nodes increases, the time delay decreases. At the optimal number of 60 nodes, random and Reingold topologies exhibit the lowest time delay compared to others.
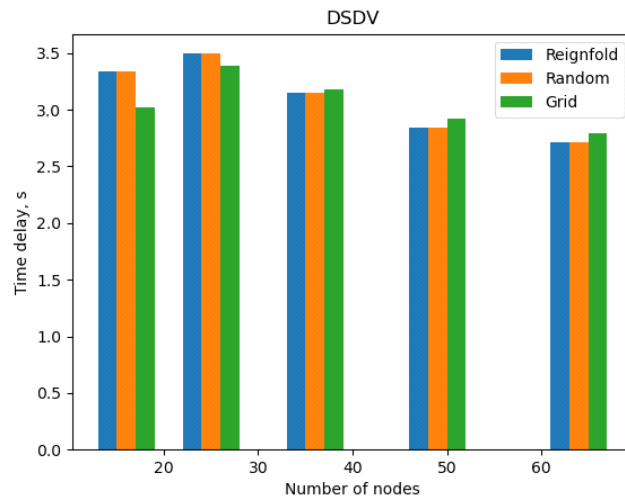
Fig.12. Time delay for DSDV routing algorithm (12)

D) Jitter. Jitter is the variation in the delay of received packets in a network. Jitter can occur due to network congestion, routing changes, or varying packet arrival times. Jitter is determined using equation (5).

$$Jitter = |(D_{i+1} - D_i) - (S_{i+1} - S_i)| \tag{5}$$

where, S_i is the time when packet i was sent from the source, and D_i is the time when it was received by the destination. Figure 13 illustrates the jitter experienced by data packets when utilizing the DSDV routing algorithm across various topologies. In the graph shown in Figure 13, it is noted that as the number of nodes in the network rises, the jitter decreases, indicating more consistent data transmission. This indicates that the mesh grid topology is more efficient when using the AODV routing algorithm compared to other topologies, especially when the optimal number of nodes is 60. Figure 14 depicts the jitter experienced by data packets when using the OLSR routing algorithm across different topologies. In Figure 14, the observed jitter values indicate the advantages of using the OLSR routing algorithm in mesh grid and Reingold topologies compared to random topology.
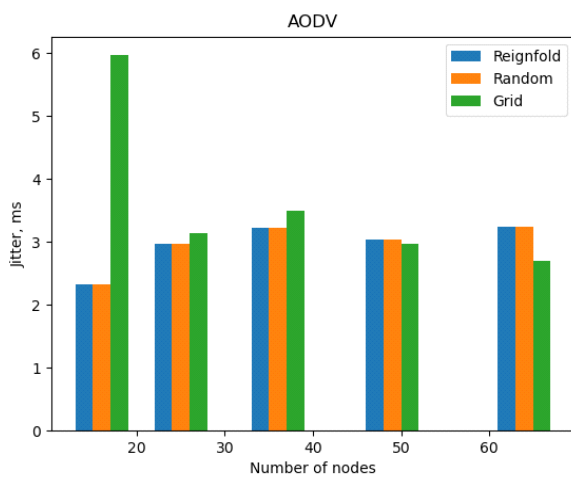
Fig.13. Jitter for AODV routing algorithm (13)
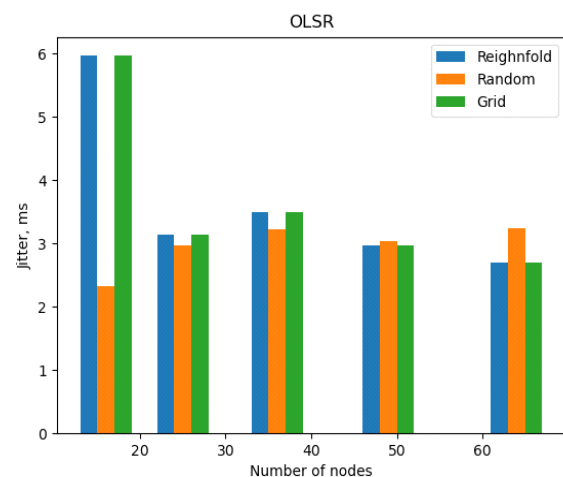
Fig.14. Jitter for OLSR routing algorithm (14)

Figure 15 illustrates the jitter encountered by data packets when employing the DSDV routing algorithm across various topologies. The graph depicted in Figure 15 suggests that for the DSDV routing algorithm, the mesh grid topology is more effective compared to the other two topologies.

.
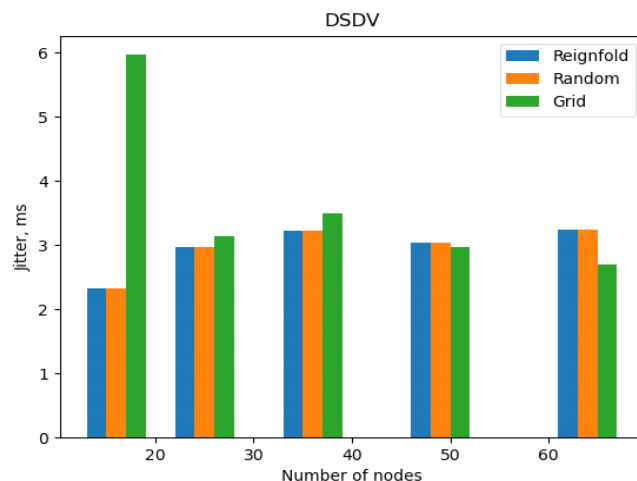
Fig.15. Jitter for DSDV routing algorithm (15)

Based on the analysis of throughput, jitter, time delay, and packet loss across various topologies, the following conclusions can be drawn about the suitability of different routing algorithms. For the AODV routing algorithm, the mesh grid topology appears to be the most suitable, as it offers reduced packet loss and stable data transmission, especially with around 60 nodes. For the OLSR routing algorithm, the random topology performs better in terms of throughput and time delay with around 50 to 60 nodes. For the DSDV routing algorithm, both random and Reingold topologies show promising results across various metrics, particularly with around 50 to 60 nodes.

6. Conclusion

In summary, this study aimed to assess the efficacy of AODV, DSDV, and OLSR routing algorithms across diverse Wireless Mesh Network (WMN) topologies using simulations in the NS-3 environment. Through extensive analysis, valuable insights into the performance of these protocols in different scenarios were gained. Initially, it was noted that the mesh grid topology proves optimal for the AODV routing algorithm, especially with approximately 60 nodes, offering minimized packet loss and stable data transmission, thus ensuring reliable network communication. Additionally, the OLSR routing algorithm exhibited superior performance in random topologies, particularly with around 50 to 60 nodes, demonstrating higher throughput and reduced time delay compared to other configurations. This underscores the effectiveness of random topologies in facilitating efficient data transmission. Lastly, for the DSDV routing algorithm, both random and Reingold topologies showed promising outcomes across various metrics, particularly with approximately 50 to 60 nodes, featuring lower packet loss rates and efficient data transmission, thus making them viable choices for deploying DSDV routing in WMNs.

The study provides valuable insights into the suitability of routing algorithms across different WMN topologies, offering guidance for network designers and administrators in optimizing network performance and reliability. Further research in this area can lead to advancements in routing protocols and network design, ultimately enhancing the functionality and efficiency of Wireless Mesh Networks in diverse applications and environments.

Conflict of interest statement

We want to make it clear that we have absolutely no conflicts of interest that could sway the findings or conclusions presented here. Financially, personally, or in terms of authorship, there's nothing that could interfere with the integrity of our work. It's important to us that our research is seen as unbiased and credible.

CRediT author statement

Turlykozhayeva D.A.: Conceptualization, Supervision, Akhtanov S.N.: Data Curation, Writing - Original Draft, Baigaliyeva A.N.: Writing - Review & Editing, Temesheva S.A.: Writing - Review & Editing, Zaidyn M.: Data Curation, Writing - Original Draft, Ussipov N.M.: Data Curation, Writing - Original Draft. The final manuscript was read and approved by all authors.

Acknowledgments

Funding

References

1   Parvin J. R. (2019) An overview of wireless mesh networks. *Wireless mesh networks- security, architectures and protocols*. DOI:10.5772/intechopen.83414.

2   Taleb S.M., Meraihi Y., Gabis A.B., Mirjalili S., Ramdane-Cherif A. (2022) Nodes placement in wireless mesh networks using optimization approaches: a survey. *Neural Computing and Applications*. 34(7), 5283-5319. DOI:10.1007/s00521-022-06941-y.

3   Bhushan S., Singh A.K., Vij S. (2019) Comparative study and analysis of wireless mesh networks on AODV and DSR. *In 2019 4th International conference on internet of things: smart innovation and usages* (IoT-SIU), 1-6. DOI:10.1109/IoT-SIU.2019.8777466.

4   Kaur J., Singh H. (2023). Several Routing Protocols, Features and Limitations for Wireless Mesh Network (WMN): A Review. In ICDSMLA 2021: *Proceedings of the 3rd International Conference on Data Science, Machine Learning and Applications*, 187-200. DOI:10.1007/978-981-19-5936-3_18.

5   Khairi T.W., Al-Zubidi A.F., Ahmed E.Q. (2021) Modified Multipath Routing Protocol Applied On Ns3 Dcell Network Simulation System. *International Journal of Interactive Mobile Technologies*, 15(10). DOI:10.3991/ijim.v15i10.22703.

6   Taterh S., Meena Y., Paliwal G. (2020) Performance analysis of ad hoc on-demand distance vector routing protocol for mobile ad hoc networks. *Computational Network Application Tools for Performance Management*, 235-245. DOI:10.1007/978-981-32-9585-8_20.

7   Abbas T., Qamar F., Hindia M.N., Hassan R., Ahmed I., Aslam M.I. (2020) Performance analysis of ad hoc on-demand distance vector routing protocol for MANET. *Proceeding of the 2020 IEEE student conference on research and development (SCOReD)*. 194-199. DOI:10.3390/engproc2023032005.

8   Nurlan Z., Zhukabayeva T., Othman M., Adamova, A., Zhakiyev N. (2021) Wireless sensor network as a mesh: Vision and challenges. *IEEE Access*. 10, 46-67. DOI:10.1109/ACCESS.2021.3137341.

9   Chai Y., Zeng X.J. (2020) Delay-and interference-aware routing for wireless mesh network. *IEEE Systems Journal*. 14(3), 4119-4130. DOI: 10.1109/JSYST.2020.2966795.

10   Khudayer B.H., Alzabin L.R., Anbar M., Tawafak R.M., Wan T.C., AlSideiri A., Al-Amiedy T.A. (2023) A Comparative Performance Evaluation of Routing Protocols for Mobile Ad-hoc Networks. *International Journal of Advanced Computer Science and Applications*. 14(4). DOI: 10.14569/IJACSA.2023.0140449.

11   Singh M., Singh M. (2019) Routing protocol for WMNs. *Node-to-Node Approaching in Wireless Mesh Connectivity*. 15-20. DOI: 10.1007/978-981-13-0674-7.

12   Rozy N.F., Ramadhiansya R., Sunarya P.A., Rahardja U. (2019) Performance Comparison Routing Protocol AODV, DSDV, and AOMDV with Video Streaming in Manet. *Proceeding of the 7th international conference on cyber and IT service management (CITSM)*. 1-6. DOI:10.1109/CITSM47753.2019.8965386.

13   Shrivastava P.K., Vishwamitra L.K. (2021) Comparative analysis of proactive and reactive routing protocols in VANET environment. *Measurement: Sensors*. 16, 100051. DOI: 10.1016/j.measen.2021.100051.

14   AL-Hasani B., Waheed B. (2022) Comparative study and performance investigation of MANET routing protocols. *International Journal of Nonlinear Analysis and Applications*. 13(2), 1953-1964.

15   Gupta N., Vaisla K.S., Jain A., Kumar A., Kumar R. (2022) Performance Analysis of AODV Routing for Wireless Sensor Network in FPGA Hardware. *Computer Systems Science & Engineering*, 40(3). DOI:10.32604/csse.2022.019911.

16   Kurniawan A., Kristalina P., Hadi M.Z.S. (2020) Performance analysis of routing protocols AODV, OLSR and DSDV on MANET using NS3. *Proceeding of the international electronics symposium (IES2020)*. 199-206. DOI: 10.1109/IES50839.2020.9231690.

17   Arega K.L., Raga G., Bareto R. (2020) Survey on performance analysis of AODV, DSR and DSDV in MANET *Computer Engineering and Intelligent Systems*. 23-32. DOI: 10.7176/CEIS/11-3-03.

18   Rajeswari A.R. (2020). A mobile ad hoc network routin protocols: A comparative study. *Recent trends in communication networks*. 6(1), 1-24. DOI: 10.5772/intechopen.92550.

19 Singh R., Singh N., Dinker A.G. (2021) Performance analysis of TCP variants using AODV and DSDV routing protocols in MANETs. Recent advances in computer science and communications. *Formerly: Recent Patents on Computer Science*. 14(2), 448-455. DOI: 10.2174/2666255813666190911114130.

20 Singh R., Singh N. (2020) Performance assessment of DSDV and AODV routing protocols in mobile adhoc networks with focus on node density and routing overhead. *Proceeding of the International Conference on Emerging Smart Computing and Informatics (ESCI).* 298-303. DOI: 10.1109/ESCI48226.2020.9167627.

21 Afzal K., Tariq R., Aadil F., Iqbal Z., Ali N., Sajid M. (2021) An optimized and efficient routing protocol application for IoV. *Mathematical Problems in Engineering*. 2021, 1-32. DOI:10.1155/2021/9977252.

22 Arega, K.L., Raga G., Bareto R. (2020) Survey on performance analysis of AODV, DSR and DSDV in MANET. *Computer Engineering and Intelligent Systems,* 11(3), 23-32. DOI: 10.7176/CEIS/11-3-03.

23 Wheeb A.H., Al-Jamali N.A.S. (2022) Performance analysis of OLSR protocol in mobile ad hoc networks. *iJIM*. 16(01), 107. DOI: https://doi.org/10.3991/ijim.v16i01.26663.

24 Hussain T., Ali I., Arif M., Baseer S., Pervez F., Rehman Z.U. (2020) An investigation of the performance optimized link state routing protocol on the basis of mobility models. *Journal of mechanics of continua and mathematical sciences.* 15(9), 306-327. DOI: 10.26782/jmcms.2020.09.00025.

25 Shaban A.M., Kurnaz S., Shantaf A.M. (2020). Evaluation DSDV, AODV and OLSR routing protocols in real live by using SUMO with NS3 simulation in VANET. *Proceeding of the International Congress on Human-Computer Interaction, Optimization and Robotic Applications (HORA)*. 1-5. DOI: 10.30534/ijatcse/2021/591032021.

26 Akhtanov S., Turlykozhayeva D., Ussipov N., Ibraimov M., Zhanabaev Z. (2022) Centre including eccentricity algorithm for complex networks. *Electronics Letters.* 58(7), 283-285. DOI: 10.1049/ell2.12424.

27 Turlykozhayeva D., Akhtanov S., Ussipov N., Akhmetali A., Bolysbay A., Shabdan Y. (2023). Routing Algorithm for Software Defined Network Based on Boxcovering Algorithm. *Proceeding of the 10th International Conference on Wireless Networks and Mobile Communications (WINCOM)*. 1-5. DOI: 10.1109/WINCOM59760.2023.10322960.

28 Turlykozhayeva D., Ussipov N., Baigaliyeva A., Temesheva S., Bolysbay A., Abrakhmatova G., Akhtanov S. (2024). Routing metric and protocol for wireless mesh network based on information entropy theory. *Eurasian phys. tech. j., 20.* 4(46), 90–98. DOI: 10.31489/2023No4/90-98.

29 Zhanabaev Z., Akhtanov S., Turlykozhayeva D., Ussipov N., Ibraimov M. (2022) Cluster pourer based on eccentricity. *Eurasian phys. tech. j.* 19, 3(41), 84–90. DOI: 10.31489/2022No3/84-90.

30 Mathieu Jacomy (2015) Fruchterman Reingold. Retrieved from Online website: https://github.com/gephi/gephi/wiki/Fruchterman-Reingold

_____

AUTHORS' INFORMATION

Turlykozhayeva, Dana Abdikumarovna - PhD student, Researcher, Lecturer, Department of Physics and Technology, al-Farabi Kazakh National University, Kazakhstan; ORCID iD: 0000-0002-7326-9196; turlykozhayeva.dana@kaznu.kz

Akhtanov, Sayat Nusipbekovich - PhD, Researcher, Senior Lecturer, Department of Physics and Technology, al-Farabi Kazakh National University, Kazakhstan; ORCID iD: 0000-0002-9705-8000; ahtanov.saiyat1@kaznu.kz

Baigaliyeva, Aiym Nurlanovna - Master student, Department of Physics and Technology, al-Farabi Kazakh National University, Kazakhstan; aiymbglva@mail.ru

Temesheva, Symbat Aidynkyzy - Master of technical sciences, Department of Physics and Technology, al-Farabi Kazakh National University, Kazakhstan; ORCID iD 0009-0000-2795-9586; symbat.temesheva@gmail.com

Zhexebay, Dauren - PhD, Researcher, Senior Lecturer, Department of Physics and Technology, al-Farabi Kazakh National University, Kazakhstan; ORCID iD: 0009-0006-8505-7277; Dauren.Zheksebay@kaznu.edu.kz

Zaidyn, Marat - Bachelor student, Department of Physics and Technology, al-Farabi Kazakh National University, Kazakhstan; ORCID iD 0009-0006-8505-7277; maratzafden@gmail.com

Ussipov, Nurzhan Musayipuli - PhD student, Researcher, Lecturer, Department of Physics and Technology, al-Farabi Kazakh National University, Kazakhstan; ORCID iD: 0000-0002-2512-3280; ussipov.nurzhan@kaznu.kz

Skabylov, Alisher A. - PhD, Researcher, Senior Lecturer, Department of Physics and Technology, al-Farabi Kazakh National University, Kazakhstan; ORCID iD: 0000-0002-5196-8252; Alisher.Skabylov@kaznu.edu.kz

UDC 534.6.08

MODELING OF NOISE SOURCES LOCALIZATION ON A CONSTRUCTION SITE BASED ON RADIAL MICROPHONE ARRAY AND HIGHEST SIGNAL DIRECTION INTERSECTIONS

Utepov Ye.B.[1], Imanov A.Zh.[1]*, Mukanova B.G.[2], Nazarova A.G.[3], Aniskin A.[4], Akhazhanov S.B.[5]

[1] Department of Civil Engineering, L.N. Gumilyov Eurasian National University, Astana, Kazakhstan
[2] Department of Computational and Data Science, Astana IT University, Astana, Kazakhstan
[3] Department of Physics, Nazarbayev University, Astana, Kazakhstan
[4] Department of Civil Engineering, University North, Varazdin, Croatia
[5] Faculty of Mathematics and Information Technology, Karaganda Buketov University, Karaganda, Kazakhstan
*Corresponding author: glad.alisher@gmail.com

Abstract. *Noise pollution from construction activities affects both workers and nearby residents. This study proposes a new method for localizing noise sources on construction sites. The method uses a radial microphone array and an algorithm based on the highest signal direction intersections. Simulations show this approach can identify noise source locations with relatively decent accuracy. The method localized noise sources within an area of about 180 m² with an average uncertainty of 6 % for single-spot sources. The uncertainties for multiple-spot sources, particularly two-spot sources, were 83.2 % and 6.1 %, depending on the size and number of sources. These results highlight the method's accuracy and its sensitivity to site conditions. Our approach offers lower computational needs compared to existing solutions. Future work will focus on the refinement of the algorithm and integration of IoT technologies for real-time monitoring.*

Keywords: construction noise, sound source localization, radial microphone array, highest signal direction, sound monitoring, acoustic mapping, signal processing.

1. Introduction

The construction process is one of the causes of noise pollution in settlements that to a certain level affect the quality of life of residents [1]. The construction noise may cause stress, mental state discomfort, exhaustion, sleeping disturbance, or insomnia [2]. It has a greater impact on construction workers than on the general population or nearby residents [3]. Hearing problems have become a common occupational disease among construction workers [4]. [5] states that there are four main factors influencing the occurrence of noise pollution in construction sites: use of heavy machinery (excavator, bulldozer, cranes, loaders, and pile drivers); communication in raised tones; construction activities (piling, welding, banging, hammering); and vehicles. The maximum number of employees in the survey conducted by [5] agreed that construction noise pollution is mainly caused by heavy machinery. Each type of work requires different tools and equipment, which leads to the mixing of different types of noise [2], and potential resonances with levels exceeded. Thus,

the permissible sound pressure levels (SPLs) regulated in the CIS should not exceed those given in [6].

Violations related to noise in Kazakhstan are regulated by the Administrative Offences Code, which stipulates that the disturbance of peace from 22:00 to 9:00 on weekdays and from 23:00 to 10:00 on weekends and public holidays, as well as noise unrelated to urgent necessity that disrupts normal rest and peace of individuals, results in fines: 5 monthly calculation indices (MCI) for individuals, 20 for small businesses or non-profit organizations, 30 for medium-sized businesses, and 100 for large businesses (1 MCI = 3692 KZT as of 01.01.2024) [7]. It must be recognized that compliance with noise regulations not only contributes to human health and well-being but also maintains the ecological balance of urban and suburban environments.

Various measures can now be used on construction sites to prevent a breach of silence, including the use of sound-measuring instruments and monitoring systems. Table 1 below provides a comparison of various existing solutions, including commercial and those presented in recent research studies.

Table 1. Comparison of existing sound measuring and monitoring systems.

Features	GM1356 [8]	EM2030P [9]	Cirrus Invictus [10]	AQBot [11]	ASMS [12]	NOMOS [13]	HMAS [14]	CSLF [15]
Type	Instrument	System	System	System	System	System	System	System
Status	Commercial	Commercial	Commercial	Commercial	Prototype	Prototype	Prototype	Prototype
Sensing unit portability	Yes	Yes	Yes	No	Yes	Yes	Yes	Yes
Autonomous operation	No	Yes	Yes	Yes	Yes	Yes	Yes	No
Weather-resistant	Yes	Yes	Yes	Yes	No	No	Yes	No
Realtime monitoring	No	Yes	Yes	Yes	Yes	Yes	Yes	Yes
Remote monitoring	No	Yes	Yes	Yes	Yes	Yes	Yes	No
Threshold alarms	No	No	Yes	Yes	Yes	Yes	Yes	No
Data synchronization	No	Yes	No	Yes	Yes	Yes	Yes	Yes
Fixed sensing position	Yes	Yes	Yes	Yes	Yes	Yes	No	Yes
Noise distraction-free	Yes	Yes	Yes	Yes	Yes	Yes	No	Yes
Integration of IoT	No	No	No	Yes	Yes	Yes	No	No
Reporting capability	No	Yes	No	Yes	Yes	Yes	No	No
Wireless data transmission	No	Yes	No	Yes	Yes	Yes	Yes	No
Microphone array	No	No	No	No	No	No	Yes	Yes
Direction recognition	No	No	No	No	No	No	Yes	No
Single source localization	No	No	No	No	No	No	Yes	Yes
Multisource localization	No	No	No	No	No	No	No	Yes
Spatial noise mapping	No	No	No	No	No	No	No	Yes

The comparison of considered solutions shows that the commercial solutions disable noise source direction recognition, localization, and spatial mapping, for both single and multiple source cases [8–11].

They also do not have a microphone array, which complicates the integration of localization algorithms. The majority of the commercial solutions are not integrated with IoT, which limits simultaneous data synchronization, remote storage, and processing. The latter is partially resolved by [12-13]. However, their prototypes are not weatherable, as well as do not apply any source localization strategies.

The solution namely HMAS by [14] used SEVD-MUSIC and iGSVD-MUSIC localization methods and evaluated their pros and cons. However, its circular visualization tool based on azimuth and elevation angles enables only the recognition of sound source direction by color map, disabling the spatial mapping of both single and multiple sources.

[15] proposed a solution called CSLF that is specialized for construction sites. CSLF does have not as many features as HMAS, but a more comprehensive localization algorithm that enables spatial localization and mapping of multiple noise sources. Its algorithm is a combination of TDOA [16], GCC-PHAT [17], and triangulation. The spatial localization in CSLF was possible due to an array comprising equally distanced microphones connected by cables. However, such an array has limitations in detecting sound sources beyond their canvas. This means that a lot of cables will be needed to cover the entire construction site, and the connection can fail at times if the cables accidentally get crushed by machinery. Moreover, the algorithm makes lots of iterations to get closer to the sources' real locations, which necessitates additional computational power to achieve better approximation accuracy.

It turned out that the solutions discussed above do not cover the needs of effective construction noise monitoring and are not able to spatially localize sources with less computational power. To overcome the shortcomings of existing solutions this study aims to design a radial microphone array (RMA) along with the sound source localization (SSL) algorithm, based on highest signal direction (HSD) intersections. The feasibility of the proposed approaches was studied by simulation and statistically analyzed.

2. Methods
2.1 SSL based on HSD intersections

We assume that the HSD intersections from microphones of the array installed on the corners of a construction site may form polygons delineating potential sources with the centroids representing the next-to-source point, or at least an intersection representing the same. To test this assumption this study proposes a radial array of 7 microphones with the central one in line with the corner bisector of the construction site (Fig. 1).
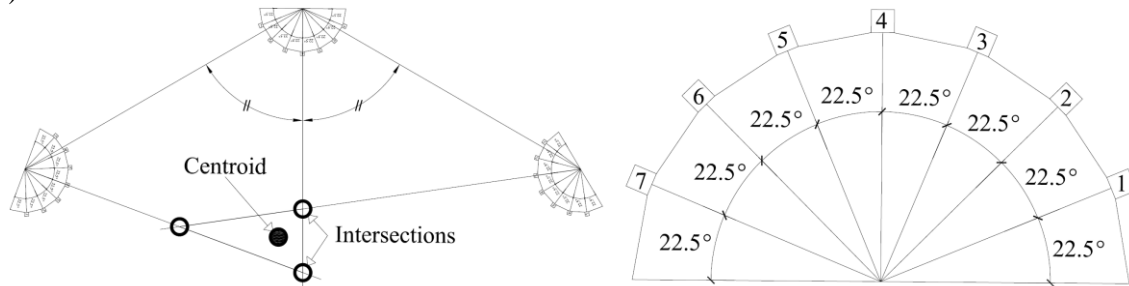
Fig. 1. Array of 7 microphones at the corners of the construction site for SSL

The inter-microphone angles in the proposed array are 22.5°, all comprising a straight angle of 180°. Such a concept helps to cover the construction site's inner corners of any size representing both acute and obtuse angles.

The positions and orientations of microphones in a 2D space help formulate the following linear equation describing the highest signal directions:

$$y_i = k_i \cdot x_i + b_i, \tag{1}$$

where i is an ordinal number of the construction site's corner; y and x are variables equivalent to the SPL and microphone position in the abscissa axis, respectively; k is a slope of the HSD; b is the y-intercept, which is the point where the HSD crosses the y-axis. Determination of k and b are explained in [18].

Each HSD intersection coordinate may be defined by equalizing the expressions obtained by Equation (1) for each corner:

$$y_i = y_{i+1}, \text{or } k_i \cdot x_i + b_i = k_{i+1} \cdot x_{i+1} + b_{i+1}, \tag{2}$$

where $x_i = x_{i+1}$ since they are common for the intersected lines.

The centroid coordinates may be defined as the arithmetic mean of HSD intersection coordinates:

$$x_m = \frac{1}{n}\sum_{i=1}^{n} x_i, \tag{3}$$

$$y_m = \frac{1}{n}\sum_{i=1}^{n} y_i, \tag{4}$$

where n is a number of HSD intersection clusters; m is a number of potential sources.

2.2 Decay-based SPL

In [19] was assumed that in an unobstructed homogeneous medium, the sound decay (D) occurs uniformly, i.e., D is constant. It is also known that point sound propagates spherically around its source if there is no reverberation [20]. Therefore, when the source is located within the construction site, the measured sound values at its corners (L_P) represent the decayed SPLs at different distances (Fig. 2).
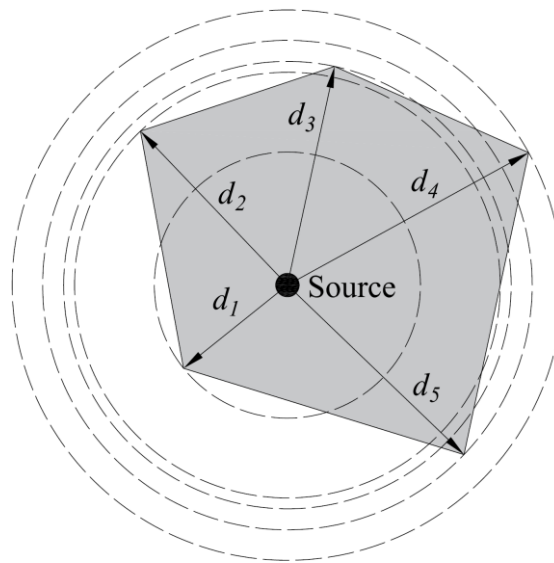
Fig. 2. Scheme of spherical sound propagation on the construction site:
d_1, d_2, d_3, d_4, d_5 – distances from the source to five corners of the construction site

Figure 2 above presents the spherical propagation of the point sound source and the distances from it to the corners of the construction site. The following equation may be used to define the SPL decay, based on the spherical propagation of the sound discussed above:

$$D_m = \frac{L_{P_{i+1}} - L_{P_i}}{d_{i+1} - d_i}, \tag{5}$$

where i is the ordinal number of the measured point (e.g., corner of construction site); d is a distance between source and the microphone array. In other words, SPL measured at different corners of the construction site will be parameters of the sound source at different distances from it. Therefore, the SPL at the sound source L_{P_m} (dB) can be calculated as follows:

$$L_{P_m} = L_{P_i} + D_m \cdot d_i \tag{6}$$

The combination of Equations (5) and (6) gives the following:

$$L_{P_m} = L_{P_i} + \frac{L_{P_{i+1}} - L_{P_i}}{d_{i+1} - d_i} \cdot d_i \tag{7}$$

It is important to note that the proposed equation does not consider environmental constraints.

2.3 Proximity-based SPL

The nature of sound propagation [21] provides an equation for finding the sound value at one point along its path given the sound value at another point:

$$L_{p_{d_2}} = L_{P_{d_1}} - 20 \log_{10} \frac{d_2}{d_1}, \tag{8}$$

where $L_{P_{d_1}}$ is the known SPL at the first point along the sound propagation path (usually measured data or equipment supplier data); $L_{p_{d_2}}$ is the unknown sound pressure value at the second point, farther from the source; d_1 is the distance from the source to the first point; d_2 is the distance from the source to the second point.

We now consider the reverse equation to find SPL at a distance d_1 from the sound source given the SPL at a distance d_2 (farther from the source than d_1). This helps deriving the $L_{P_{d_1}}$:

$$L_{p_{d_1}} = L_{P_{d_2}} + 20\log_{10}\frac{d_2}{d_1} \tag{9}$$

The calculations using Equations (8) and (9) help assuming that if the sound pressure value is 50 dB at a distance of 10 m from the sound source, then the sound pressure value will be 30 dB at a distance of 100 m. Suppose d_1 is very close to the sound source, for example, at a distance of 0.1 m.

The maximum approximate value at the sound source can be found by substituting 0.1 m into Equation (18). However, the calculation yields a negative value, -10 dB, which is inappropriate. Moreover, if d_1 is assumed to be 0.001 m, then the sound pressure value (the assumed value at the source) will be equal to -50 dB, which is also inappropriate on one hand and significantly different from the value of $L_{P_{d_1}}$ at $d_1 =0.1$ m on the other hand. This approach is not suitable for finding the sound pressure at the sound source. However, while logical, it may contribute to finding an optimal solution. For example, by considering the limits of functions as the distance approaches zero ($d_1 \rightarrow 0$).

3. Results and discussion

Figure 3 below shows the results of the simulation for single-spot sound sources to check the feasibility of the proposed SSL algorithm based on HSD intersections. The simulation was performed in Excel.
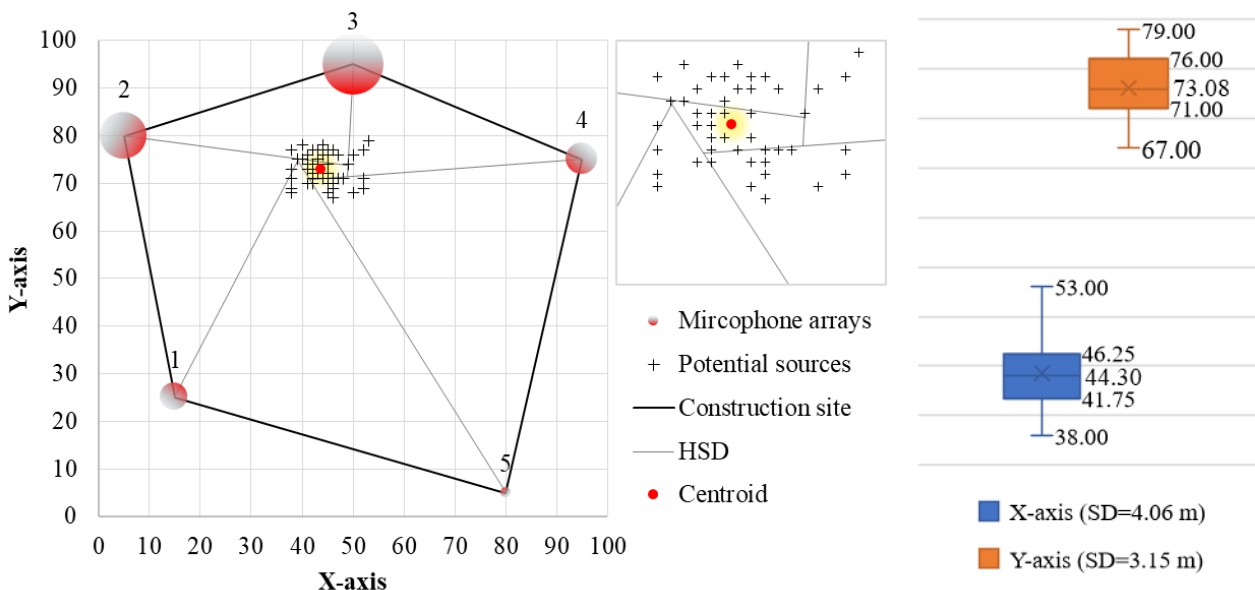
Fig. 3. The single-spot sound source simulation results

From Figure 3 is seen that the construction site (marked with bold line) is arranged on a simulated space referenced to the Cartesian system [18], with dimensions of 100 by 100 m. The microphone arrays (marked with gradient-color circles) were set on their corners. After numerous iterations, a total of 50 potential sources (marked with a plus-sign) were irregularly distributed on a random spot covering about 180 m². Such a scenario was chosen to associate with the real situation on the construction site. Examples include masonry work on a similar spot, where distinctive noises may occur over a short period. These sounds can include the operation of a crane delivering brick blocks, the use of an angle grinder for cutting and sanding bricks, or masonry workers communicating in raised voices.

.

The simulation showed that for the chosen spot the highest signal directions (marked with a grey line) were stable forming an irregular pentagonal polygon. Its centroid (marked with red point) coordinates [43.504; 73.146] were expectedly located in the vicinity of potential sources. The Boxplot diagram in Figure 3 shows that the potential sources were spread in the ranges of 38-53 m and 67-79 m along the X and Y axes, respectively, forming a kind of cluster. The variability of the spread was characterized by the estimation of Standard Deviation (SD) for both X and Y coordinates, which yielded 4.06 and 3.15 m, respectively. The mean coordinates [44.30; 73.08] of the cluster were also depicted in the Boxplot.

Evaluation of the algorithm incorporated such measures of descriptive statistics, as SD, Variance (i.e., Dispersion), and Range. The scatter of values for each of these measures on the X and Y axes was calculated to obtain their coverage areas (Fig. 4).
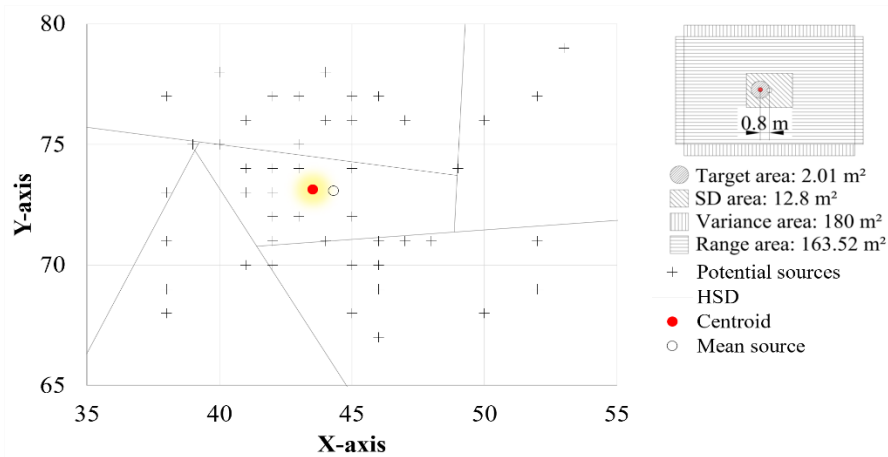
Fig. 4. The scatter analysis

Figure 4 shows the zoomed-in view of the studied spot, where it can be seen that the centroid is close to the mean source, the coordinates of which were estimated as the arithmetic mean of the coordinates of all potential sources. The distance between the centroid and the mean source is 0.8 m. The area of the circle described by this distance (radius) was taken as a target area, which is roughly 2.01 m^2. To assess the uncertainty (%) of the proposed algorithm, the ratios of this target area to the coverage areas derived from the scatter of statistical measures were calculated. The uncertainties amounted to 15.7, 1.1, and 1.2 %, respectively With coverage areas of SD, Variance, and Range being 12.8, 180, and 163.52 m^2. The average uncertainty amounted to 6 %.

Figure 5 shows the results of the simulation for the case of multiple-spot sound sources, in particular, two spots were considered in the same space. Both spots were iteratively filled with 50 potential sources.
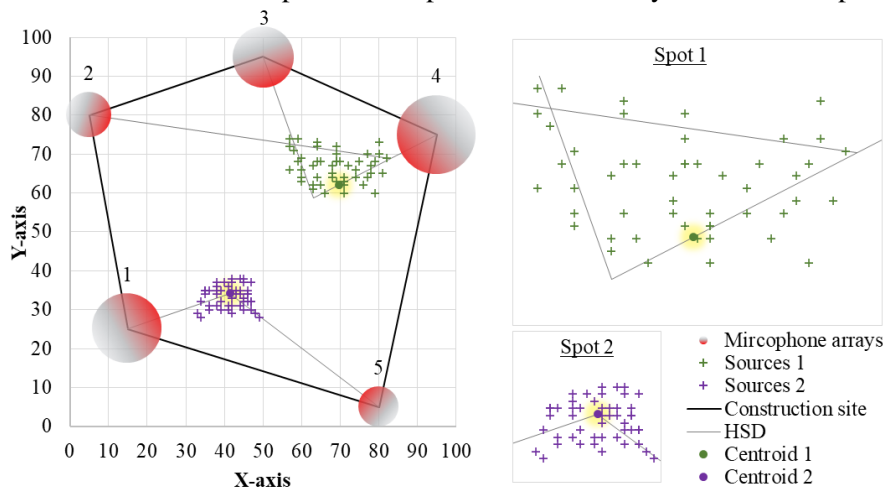
Fig. 5. The two-spot sound sources simulation results

Figure 5 shows that the size of spot 1 is almost twice as wide as spot 2. Such a scenario may often occur in reality when construction works are carried out simultaneously on several spots, and the size of the spots may vary considerably. For the considered case our algorithm consistently produced intersections of HSDs with the 2-4 microphone arrays resulting in a triangle, and a single intersection resulted by 1 and 5 arrays. The coordinates of centroids were [69.657; 62.083] and [41.41; 34.19] for the triangle and intersection, respectively.

Figure 6 presents Boxplots for both considered spots.
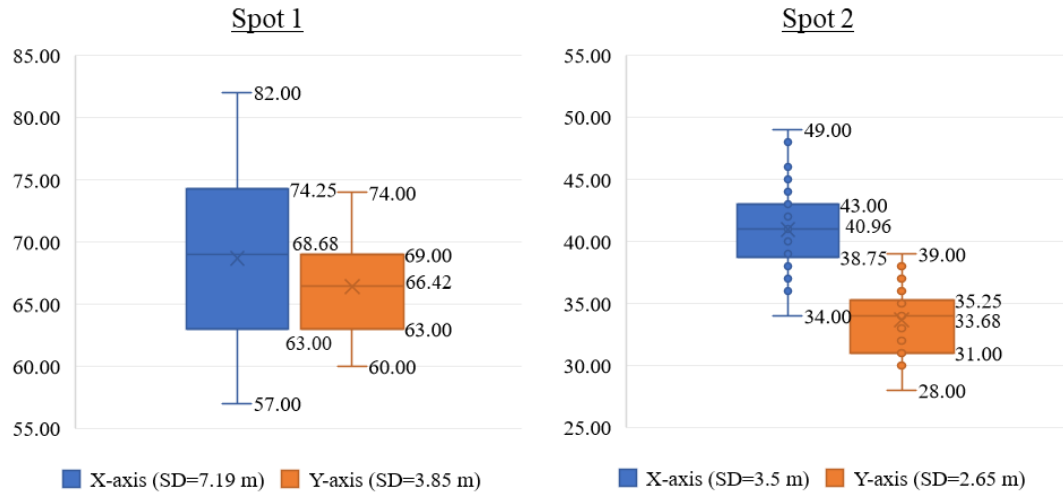
Fig. 6. The boxplots for two spots of sound sources

Boxplots above show the distribution ranges for X and Y coordinates of 57-82 and 60-74 for spot 1, as well as 34-49 and 28-39 for spot 2, respectively. The mean coordinates of the spots are [68.68; 66.42] and [40.96; 33.68], correspondingly. The distance between centroids to the means amounted to 4.45 and 0.68 m, which in turn define the target areas of 62.08 and 1.45 m^2, accordingly. The coverage areas of SD, Variance, and Range amounted to 768.78, 350.00, and 27.73 m^2 for spot 1, and 85.67, 165.00, and 9.26 m^2 for spot 2. The corresponding uncertainties amounted to 8.1, 17.7, and 223.9 % for spot 1, and 1.7, 0.9, and 15.7 % for spot 2. The average uncertainties for the spots amounted to 83.2 and 6.1 %, showing a large difference. Such a difference is rather related to the influence of the area covered by the construction processes. The influence of too many (fifty) simultaneously appearing sound sources should not go unnoticed either. This suggests the importance of considering each case and duration of noise separately.

The proposed SSL method based on RMA and HSD intersections offers significant advancements. Unlike GM1356 [8] and EM2030P [9], our method enables identifying noise source directions. It also supports spatial noise mapping, unlike Cirrus Invictus [10] and AQBot [11]. The use of a radial array reduces cabling needs and enhances detection accuracy compared to CSLF [15]. Additionally, our algorithm requires less computational power than HMAS [14] while maintaining decent accuracy. These improvements make our method more effective for managing noise pollution on construction sites.

4. Conclusion

This study developed an effective method for localizing noise sources on construction sites using a radial microphone array (RMA) and a sound source localization (SSL) algorithm based on the highest signal direction (HSD) intersections. Our simulations demonstrated the feasibility of this approach, forming stable polygons for accurate noise source localization. The potential noise sources were clustered within 180 m², with centroid coordinates [43.504; 73.146] and an average uncertainty of 6% for single-spot sources. The algorithm produced centroids at [69.657; 62.083] and [41.41; 34.19], with uncertainties of 83.2% and 6.1%, respectively For multiple-spot sources. These results highlight the algorithm's effectiveness and the influence of field size and noise source number. The proposed RMA and SSL algorithm significantly improves over existing commercial solutions, offering accurate noise source localization with lower computational power. This can enhance noise management on construction sites, improving health and safety for workers and reducing noise pollution in nearby communities. Future work will aim to refine the algorithm, reduce

uncertainties, and integrate IoT technologies for real-time, remote monitoring, and data synchronization, increasing the system's practical utility and effectiveness.

References

1. Yi Feng C., Md Noh N.I.F., Al Mansob R. (2020) Study on The Factors and Effects of Noise Pollution at Construction Site in Klang Valley. *Journal of Advanced Research in Applied Sciences and Engineering Technology.* 20(1), 18–26. DOI: 10.37934/araset.20.1.1826.

2. Burkhart G., Schulte P.A., Robinson C., Sieber W.K., Vossenas P., Ringen K. (1993) Job tasks, potential exposures, and health risks of laborers employed in the construction industry. *American Journal of Industrial Medicine.* 24 (4), 413–425. DOI: 10.1002/ajim.4700240407.

3. Koushki P.A., Kartam N., Al-Mutairi N. (2004) Workers' perceptions and awareness of noise pollution at construction sites in Kuwait. *Civil Engineering and Environmental Systems.* 21 (2), 127–136. DOI: 10.1080/10286600310001642839.

4. Suter A.H. (2002) Construction Noise: Exposure, Effects, and the Potential for Remediation; A Review and Analysis. *AIHA Journal.* 63 (6), 768–789. DOI: 10.1080/15428110208984768.

5. Shaikh H.H., Zainun N.Y., Khahro S.H. (2023) Impact of Noise Pollution at Construction Sites of Sindh Pakistan. *E3S Web of Conferences.* 437, 02003. DOI: 10.1051/e3sconf/202343702003.

6. GOST 12.1.003-2014 Occupational Safety Standards System. Noise. General Safety Requirements.

7. On Administrative Infractions. The Code of the Republic of Kazakhstan Dated 5 July 2014 No. 235-V. Available at: https://adilet.zan.kz/eng/docs/K1400000235 (May 23, 2024).

8. Sound Level Meter GM1356. Available at: http://www.benetechco.net/en/products/gm1356.html (May 23, 2024).

9. EM2030P Portable Online Noise Monitor. Available at: https://www.noisemeters.com/product/sonitus/em2030p/ (May 23, 2024).

10. Active Environmental Solutions. Invictus Noise Monitoring System. Available at: https://aesolutions.com.au/invictus-noise-monitoring-system (May 23, 2024).

11. AQBot Noise Sensor Monitoring Device for Industries. Available at: https://oizom.com/product/aqbot-noise-monitor/ (May 23, 2024).

12. Arbaiy N., Sapuan S.A., Lah M.S.C., Othman M.H.H., Lin P.C. (2019) The Construction Site Ambient Noise Monitoring System with Internet of Things (IoT). *Computational Research Progress in Applied Science Engineering.* 2019, 5 (4), 118–121.

13. Badruddin M.B., Hamid S.Z.A., Rashid R.A., Hamsani S.N.M. (2020) IoT Based Noise Monitoring System (NOMOS). *IOP Conference Series: Materials Science and Engineering.* 884, 1, 012080. DOI:10.1088/1757-899X/884/1/012080.

14. Hoshiba K., Washizaki K., Wakabayashi M., Ishiki T., Kumon M., Bando Y., Gabriel D., Nakadai K., Okuno H. (2017) Design of UAV-Embedded Microphone Array System for Sound Source Localization in Outdoor Environments. *Sensors.* 17, 11, 2535. DOI: 10.3390/s17112535.

15. Kim I.-C., Kim Y.-J., Chin S.-Y. (2022) Sound Localization Framework for Construction Site Monitoring. *Applied Sciences.* 12 (21), 10783. DOI: 10.3390/app122110783.

16. Kim J.I., Lee J.G., Park C.G. (2008) A mitigation of line-of-sight by TDOA error modeling in wireless communication system. *2008 International Conference on Control, Automation and Systems.* 1601–1605. DOI:10.1109/ICCAS.2008.4694487.

17. Kwon B., Park Y., Park Y.S. (2010) Analysis of the GCC-PHAT technique for multiple sources. *International Conference on Control, Automation and Systems 2010.* 2070–2073.

18. Barnett R.A., Ziegler M.R., Byleen K. (2008) *College mathematics for business, economics, life sciences and social sciences,* 11th ed. Upper Saddle River, N.J.: Pearson/Prentice Hall, 1042 p.

19. Utepov Y., Imanov A. (2022) Conceptual model of noise monitoring system for construction projects in cramped conditions, based on sensors and GIS. *Technobius*. 2 (3), 0025. DOI:10.54355/tbus/2.3.2022.0025.

20. Longhurst R.S.(1967) *Geometrical and physical optics* (2nd ed.). London, Longman, 622 p.

21. Comerford P. (2000) David Howard and James Angus, Acoustics and Psychoacoustics. Focal Press, Oxford, 2000. *Organised Sound.* 2001, Vol. 6, No. 3, pp. 229–232. DOI:10.1017/S1355771801213090.

_____

AUTHORS' INFORMATION

Utepov, Yelbek Bakhitovich – PhD, Professor, Department of Civil Engineering, L.N. Gumilyov Eurasian National University, Astana, Kazakhstan; ORCID ID: 0000-0001-6723-175X; utepov-elbek@mail.ru

Imanov, Alisher Zhanzakovich – PhD Student, Department of Civil Engineering, L.N. Gumilyov Eurasian National University, Astana, Kazakhstan; ORCID ID: 0000-0002-0965-7039; glad.alisher@gmail.com

Mukanova, Balgaisha Gafurovna – Doctor of Physical-Mathematical Sciences, Professor, Department of Computational and Data Science, Astana IT University, Astana, Kazakhstan; ORCID ID: 0000-0002-0823-6451; mbsha01@gmail.com

Nazarova, Aida Gafurkyzy – PhD, Laboratory Assistant, Department of Physics, Nazarbayev University, Astana, Kazakhstan; ORCID ID: 0000-0002-0083-3219; aida.maratova@nu.edu.kz

Aniskin, Aleksej – Candidate of Technical Sciences, Associate Professor, Department of Civil Engineering, University North, Varazdin, Croatia; ORCID ID: 0000-0002-9941-1947; aaniskin@unin.hr

Akhazhanov, Sungat Berkinovich – PhD, Associate Professor, Faculty of Mathematics and Information Technology, Karaganda Buketov University, Karaganda, Kazakhstan; ORCID ID: 0000-0002-0903-3517; stjg@mail.ru

.

FINITE TEMPERATURE EFFECTS WITHIN SCALAR FIELD DARK MATTER MODEL

Suliyeva G.B.[1,2,3], Kurmanov Ye.B.[1,2,4], Konysbayev T.K.[1,2], Boshkayev K.A.[1,2,5], Urazalina A.A.[1,2,5], Luongo O.[2,6,7,8,9]

[1] National Nanotechnology Laboratory of Open Type, Almaty, Kazakhstan
[2] Al-Farabi Kazakh National University, Almaty, Kazakhstan
[3] Fesenkov Astrophysical Institute, Almaty, Kazakhstan
[4] International Engineering Technological University, Almaty, Kazakhstan
[5] Institute of Nuclear Physics, Almaty, Kazakhstan
[6] Università di Camerino, Camerino, Italy
[7] SUNY Polytechnic Institute, New York, USA
[8] INAF – Osservatorio Astronomico di Brera, Milano, Italy
[9] Instituto Nazionale di Fisica Nucleare, Perugia, Italy
*Corresponding author: kurmanov.yergali@kaznu.kz

Abstract. *The distribution of dark matter in four low surface brightness spiral galaxies is studied using two models within the scalar field theory of dark matter, an alternative to the cold dark matter paradigm. The first model is a Bose-Einstein condensate, in which bosons occupy the ground state at zero temperature. The second model includes finite temperature corrections to the scalar field potential, which allows the introduction of excited states. A nonlinear least squares approximation method is used to determine the free parameters of the models, including scale radius, characteristic (central) density and total mass, based on observational data of rotation curves. Quantitative analysis shows the importance of considering finite temperatures at the galactic level. In addition, the two models are compared with results from widely used and accepted phenomenological dark matter profiles such as the isothermal sphere, Navarro-Frank-White and Burkert profiles. The reliability of each model was assessed based on the Bayesian information criterion of completeness. Statistical analysis provides meaningful interpretation of the choice of a particular profile. Ultimately, this study contributes to a better understanding of the distribution of dark matter in low surface brightness spiral galaxies by shedding light on the performance of scalar field models compared to traditional phenomenological profiles.*

Keywords: scalar field, dark matter, Bose-Einstein condensate, galaxy rotation curves.

1. Introduction

The presence of dark matter (DM) in the Universe is firmly confirmed by extensive observational data. Initially, the concept of DM emerged as a solution accounting for the rotation curves of spiral galaxies, the velocity dispersions observed within galaxy clusters, and the measured mass-to-light ratios in individual galaxies as well as in clusters of galaxies [1-3]. Afterwards, its importance became increasingly evident in interpreting a variety of astrophysical and cosmological phenomena, such as gravitational lensing, the

presence of acoustic baryonic oscillations, the power spectrum of galaxies, and0 the formation of cosmic structures in the early Universe [4-5]. The widely known model for DM is the Cold Dark Matter (CDM) paradigm which demonstrated remarkable success in reproduction and explanation of many cosmic phenomena on cosmological scales [6-7]. Nevertheless, it encounters several notable challenges and shortcomings when applied to the galactic and sub-galactic levels [8].

Namely, among them:

– the cusp-core problem, arising as CDM model predicts that DM halos should have a density profile with a central "cusp" (a steep increase in density toward the center), whereas observations of galaxies often suggest a "core" (a relatively flat density profile);

– the redundant presence of substructures as predicted by N-body numerical simulations, which significantly exceed the observed values.

There exist different candidates for DM, but in this work, we will examine the Scalar Field Dark Matter (SFDM) as this model provides a naturally emerging solution to the CDM problems mentioned above. Unlike many other DM models that require the existence of new particles or forces beyond those in the Standard Model of particle physics, SFDM relies on a simple and elegant concept – a scalar field (SF).

The central idea suggesting that dark matter is a spin-0 SF forming Bose-Einstein condensate (BEC) "drops" was first considered in [9] and independently in [10-12]. Indeed, this model may admit various specific properties studied by different authors. In the literature, it is also appeared as fuzzy DM [13], wave DM [14], Bose-Einstein condensate DM [15]. In the framework of SFDM, it is possible to account for temperatures (see Sec. 1). In the present paper, we focus on manifestation of SFDM properties on galactic level. The issue of dark matter distribution in galaxies is primarily concerned with halo regions and is linked to the rotation curves (RC) of galaxies obtained from observations. The aim of this work is to explore the consistency of the two SFDM models by comparing the rotation curves of four representative Low Surface Brightness spiral galaxies without involving the baryonic component and taking into account the internal galaxies' structure. To achieve this, we perform nonlinear fitting procedure and employ a statistical tool - the Bayesian Information Criterion (BIC) to estimate the goodness of the fit.

On the other hand, for comparison we consider well-corroborated phenomenological profiles, which are widely exploited in the literature: Navarro-Frenk-White (NFW), Burkert profiles and Isothermal sphere (ISO). These profiles have been proposed as parametrized functions that can fit numerical simulations and observations fairly well, regardless the underlying theories or theoretical motivation. The model parameters for each of these profiles are the scale radius r_0 and the DM density at galaxy center ρ_0.

The article is organized as follows. In Sec. 2, we describe the features of two specified SFDM models. In Sec. 3, the methods necessary for carrying the fitting procedure are presented. Sec. 4 introduces the major results of the paper. In Sec. 5, conclusion remarks are reported.

2. Dark matter models: fundamental and phenomenological

2.1 Haloes at zero-temperatures

Bosons at zero temperature are studied in many works. Since almost all bosons occupy the ground state at temperatures close to absolute zero, the behavior of the haloes can be effectively described using the principles of Bose-Einstein condensation (BEC). Employing the Bogolyubov approximation [16], which is a method commonly used in the study of quantum systems, allows for a classical mean-field representation of the ground state of the SFDM haloes. This approach simplifies the analysis by neglecting the contribution of excited states, thereby focusing solely on the dominant ground state configurations.

Bohmer and Harko [15] utilized the Thomas-Fermi limit, where the self-interactions of the SF play a prominent role in the SFDM potential. This limit simplifies the analysis by allowing the mass term $\sim \Phi^2$ to be disregarded and the potential is expressed in the form $V(\Phi) \sim \lambda \Phi^4$, where λ is the coupling constant. Using this limit, the authors derived the solution of equation describing the single static BEC:

$$\nabla^2 \rho(r) + k^2 \rho(r) = 0, \qquad (1)$$

where $\rho(r)$ is the DM density distribution, k is the parameter. The solution is:

$$\rho(r) = \rho_0 \frac{\sin(kr)}{kr}, \qquad (2)$$

with $\rho_0 = \rho(0)$ being the central density. The above solution has a condition for a bound halo radius R given by $\rho(R) = 0$ in order to obviate non-physical negative densities. Hence, one gets $k = \pi / R$. The radius of the BEC halo is given by expression:

$$R = \pi \sqrt{\frac{\hbar^2 a}{Gm^3}}, \qquad (3)$$

consisting of fixed values, where $\hbar$ is the reduced Plank's constant, G is the gravitational constant, m is the boson's mass, a is the scattering length. Eq. (3) is linked to the coupling constant via $\lambda = 4\pi\hbar^2 a / m.$

2.2 Finite-temperature haloes

The study [17] introduced a scenario where the scalar field (SF) operates under conditions of finite temperature. The authors considered a self-interacting spin-0 real SF immersed in a thermal bath (i.e. a medium or reservoir of particles that are in thermal equilibrium) at temperature T. The SF potential is written in the following form [18]:

$$V(\Phi) = -\frac{1}{2}m^2\Phi^2 + \frac{1}{4}\lambda\Phi^4 + \frac{1}{8}\lambda\Phi^2 T^2 - \frac{\pi^2}{90}T^4, \qquad (4)$$

in the units where the speed of light $c = 1$, the Boltzmann constant $k_B = 1$ and $\hbar = 1$. The first term corresponds to the mass term, the second term represents the repulsive self-interaction, the third term describes the interaction of the field with the thermal bath, and the last term accounts for the influence of the thermal bath alone.

It was shown that early dark matter (DM) haloes were formed after the growth in SF fluctuations occurring after the spontaneous symmetry breaking (SSB) of the system [19]. The equilibrium temperatures of these haloes vary depending on when each halo forms.

Since galactic halos are well described by Newtonian dynamics, an exact analytic solution for SF can be found in the limit of weak gravitational field regime. Finally, the analytical solution, in the weak field regime, is presented as a linear combination:

$$\rho(r) = \sum_j \rho_0^j \left[\frac{\sin(k_j r)}{k_j r} \right]^2, \qquad (5)$$

where $j = 1, 2, 3, \ldots$ is the number of exited states, required to fit the distribution; $\rho_0^j = \rho^j(0)$ is the central density of a single state, and the scale of the SF configuration is determined due to the condition $\rho^j(R) = 0$, i.e. $k_j R = j\pi$. This density has a naturally occurring core. Consequently, the overall solution allows for a configuration beyond a completely condensed system, and the potential adjusted for finite temperature suggests the presence of separate excitation states j as solutions to the perturbation equation of the SF. This indicates that the bosons are distributed thermally among both ground and excited states at higher energy levels.

2.3 Phenomenological models

Here we review some basic models widely exploited in the literature.

The NFW profile [20] was introduced after stacking numerous halos in order to fit the data of N-body simulations within the CDM model. It is given by

$$\rho(r) = \frac{\rho_0}{(r/r_0)(1 + r/r_0)^2}. \qquad (6)$$

The Burkert profile [21] which firstly was proposed in the attempt to determine the density law that best fit the measured rotation curves of dwarf galaxies, which are known to be dominated by DM, has the following form:

$$\rho(r) = \frac{\rho_0}{(1 + r/r_0)(1 + (r/r_0)^2)}. \qquad (7)$$

The ISO profile [22] has been employed in the context of galactic dynamics, particularly in explaining the flat rotation curves observed in spiral galaxies. It is expressed as:

$$\rho(r) = \frac{\rho_0}{1 + (r/r_0)^2}. \tag{8}$$

These models along with the two SF models will be employed to analyze DM distribution in the LSB galaxies.

3. Methods

The galaxy RC is a measure of how the rotational velocity of objects in a galaxy changes with their distance from the galactic center. Since the Newtonian dynamics is sufficient at the galactic level, rotational velocity $V(r)$ is represented by:

$$V(r) = \sqrt{r\frac{\partial\phi}{\partial r}} = \sqrt{\frac{GM(r)}{r}}, \tag{9}$$

where $\phi(r)$ is the gravitational potential corresponding to the mass distribution $M(r)$. Each profile generates a particular RC and hence yields corresponding DM mass distributions that can be calculated by integration of density:

$$M(r) = 4\pi\int_0^r r'^2\rho(r')dr'. \tag{10}$$

Thereby, taking Eqs. (2) and (5) one obtains the mass profile

$$M(r) = \frac{4\pi\rho_0 r}{k^2}\left(\frac{\sin(kr)}{kr} - \cos(kr)\right), \tag{11}$$

for haloes with zero temperatures, and

$$M(r) = \sum_j M_j = \sum_j \frac{2\pi\rho_0 r}{k_j^2}\left(1 - \frac{\sin(2k_j r)}{2k_j r}\right), \tag{12}$$

for finite temperatures haloes with M_j being the total mass of state j.

It should be noted, that in numerical computations/analyses the mass is expressed in the units of solar mass ($M_\odot$) and the radial distance is in kilo-parsecs (kpc).

After establishing the mass and velocity profiles, the next step is to perform fitting procedure. In this work, we employ the Levenberg-Marquardt nonlinear least squares method [23-24]. The calibration is based on observational data including measurements of radial velocity. After that, an objective function χ^2 representing the squared differences between observed V_l^{obs} and expected $V(r)$ velocities describing each profile is created:

$$\chi^2 = \sum_{l=1}^{N}\left[\frac{V_l^{obs} - V(r)}{\sigma_{V,l}^{obs}}\right]^2, \tag{13}$$

where N is the number of data points, $\sigma_{V,l}^{obs}$ is their corresponding errors. The key to the approach is to minimize this objective function by iteratively modifying the model parameters. This will guarantee the best possible fit, since the process systematically reduces the discrepancies between the model and the observed data, leading to an accurate and reliable representation of the galaxy's RC. The "best fit" in this context means that the model parameters have been chosen such that the divergence between the observed data and the model's predictions is minimized.

In this context, models fitted to the same data set can be compared quantitatively using the Bayesian Information Criterion (BIC):

$$\text{BIC} = \chi^2 + p\ln N, \tag{14}$$

where p is the number of free model parameters. A better trade-off between model fit and simplicity is demonstrated by lower BIC values increasing the benefits of the model.

4. Results

In this section we present the results of fitting procedure for 4 LSB spiral galaxies - NGC 1560, NGC 1003, NGC 3741, NGC 6503, the observational data points of which are taken from the SPARC database (Spitzer Photometry and Accurate Rotation Curves) [25]. In comparison to high surface brightness galaxies, LSB galaxies are thought to contain a higher proportion of DM relative to visible matter. This fact allows one to neglect the baryonic component in the galaxy structure and adopt the total mass M_{tot} approximately equal to the DM mass M_{DM} ($M_{tot} \approx M_{DM}$).

Primarily, we compare two SFDM models, declared by Eqs. (2) and (5), to estimate quantitatively how the influence of finite temperature effects affects the consistency of the models with the observations. In the case of the BEC SFDM profile, fitting analysis provides two free parameters: the halo radius R and the central density ρ_0, imposing the ground state only ($j = 1$). At the same time, for the mSFDM model three free parameters are required: as we take two states, the central density of each state should be ensured (finally, we have R, ρ_0^i, ρ_0^j). It is worth mentioning, that the combination of states (i, j) differs from one galaxy to another and is selected manually until the best correspondence with observations is achieved. The numerical outcomes are presented in Table 1 and in Fig. 1.

Table 1. Fitting parameters for 4 LSB galaxies within the SFDM models.

Profile	i, j	R, kpc	ρ_0^i, $10^{-3}\frac{M_\odot}{pc^3}$	ρ_0^j, $10^{-3}\frac{M_\odot}{pc^3}$	M_{tot}, $10^{10}M_\odot$	$<\rho>$, $10^{-3}\frac{M_\odot}{pc^3}$	BIC	ΔBIC
NGC 1560								
BEC SFDM	1	8.37	23.36	-	0.87	3.52	199.9	80.0
mSFDM	1, 3	12.46	8.86	33.88	1.04	1.28	119.9	-
NGC 1003								
BEC SFDM	1	15.15	16.03	-	7.08	4.87	195.3	124.7
mSFDM	1, 4	42.91	0.79	24.69	8.27	0.25	70.6	-
NGC 3741								
BEC SFDM	1	6.66	16.88	-	0.33	2.69	105.8	60.5
mSFDM	1, 6	8.69	7.97	85.44	0.35	1.27	45.3	-
NGC 6503								
BEC SFDM	1	5.68	15.47	-	7.30	9.53	161.9	45.0
mSFDM	1, 3	13.70	26.74	964.65	7.41	6.87	116.9	-

For both models, the total mass M_{tot} is computed using the last data point of the distance by substituting the fitting parameters into the Eqs. (11) and (12). The average density $<\rho>$ is obtained through the standard density definition, dividing the total mass M_{tot} by the volume enclosed within the corresponding distance. It should be noted, that a third (forth, and so on) exited state might be added to the analysis, however it is not necessary, as the introduction of only two states is enough for the whole procedure.

As mentioned before, the model that has the lowest BIC, say BIC_0, is regarded as the best-suited model. When compared to other models, the difference $\Delta\text{BIC} = \text{BIC} - \text{BIC}_0$ certifies the statistical evidence supporting the reference model as the best-fitting one. In particular, the case $\Delta\text{BIC} \in [0,2]$ shows a weak evidence, the case $\Delta\text{BIC} \in [3,6]$ shows a mild evidence, and the case $\Delta\text{BIC} > 6$ shows a strong evidence.

For all considered galaxies, mSFDM model demonstrates lower values of BIC, indicating that this model is more suitable to represent DM. Moreover, from Fig. 1 one can see that RCs for mSFDM model reveal better concordance with observational data in comparison to BEC SFDM. Notably, for one galaxy (NGC 6503), the best fit is reached with two exited states only ($i = 2$, $j = 7$), while for the rest galaxies (NGC 1560, NGC 1003, NGC 3741) the ground state ($j = 1$) is present. In addition to SFDM models, we

carried out the fitting procedure for phenomenological profiles: NFW, Burkert and ISO to assess the contrast between them and to be convinced whether mSFDM is a reliable alternative for DM representation.
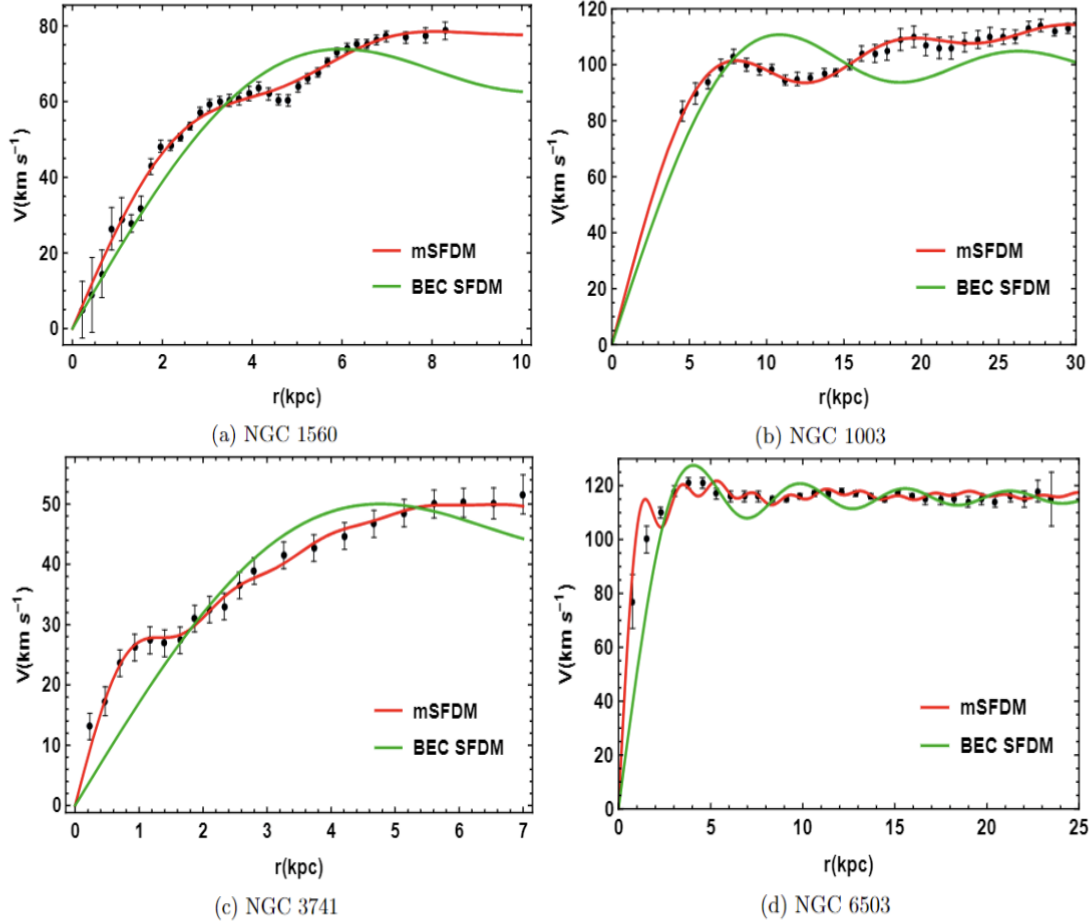
Fig.1. Rotation curves of LSB galaxies for the two SFDM models: black dots represent the observational data with their error bars, the green solid curve corresponds to the BEC SFDM, the red solid curve - to the mSFDM

In Table 2, the fitting parameters (scale radius r_0 and central (characteristic) density ρ_0) are shown. The total mass M_{tot} and the average density $<\rho>$ are calculated in the same way as in the Table 1. Note, that here values of ΔBIC are calculated with respect to mSFDM being the reference model with BIC=BIC$_0$ = [119.9, 70.6, 45.3, 116.9] for NGC 1560, NGC 1003, NGC 3751, NGC 6503 galaxies, correspondingly. When comparing the values of BIC in Tables 2 and 1, it is clearly seen that, in cases of all considered galaxies, they consistently emerge as the lowest for mSFDM model.

Values of ΔBIC demonstrate strong evidence for mSFDM model to be preferable over phenomenological models with two exceptions: for NGC 3741 NFW profile yields ΔBIC=5.7, indicating the mild evidence, and for NGC 6503 ISO profile gives ΔBIC=0.5, implying that it provides fit as well as mSFDM. Meanwhile, for NGC 1560, NGC 1003 and NGC 1560 the phenomenological models display lower BIC values in comparison to BEC SFDM. However, for NGC 6503 the highest BIC shows the Burkert profile. This emphasizes the importance of the choice of DM model to the specific characteristics of each galaxy, as different systems may demand different representations of DM distribution.

Based on graphical representation of fitting results (Fig.2), mSFDM model is able to reproduce the wiggles in observed RCs, in contrast to phenomenological ones. This possibility is crucial for understanding the dynamics of galaxies and provides a significant advantage to mSFDM model.

Table 2. Fitting parameters for 4 LSB galaxies within the phenomenological models.

Profile	r_0, kpc	ρ_0, $10^{-3}\dfrac{M_\odot}{pc^3}$	M_{tot}, $10^{10}M_\odot$	$<\rho>$, $10^{-6}\dfrac{M_\odot}{pc^3}$	BIC	ΔBIC
NGC 1560						
NFW	21.06	2.12	0.12	5.19	151.2	31.3
Burkert	3.23	4.73	0.01	0.59	159.2	39.3
ISO	1.84	4.61	1.63	68.3	150.9	31.0
NGC 1003						
NFW	15.11	4.55	0.13	0.12	151.3	80.7
Burkert	6.58	23.35	0.06	5.52	173.9	103.3
ISO	2.07	57.99	9.41	8.12	145.5	74.9
NGC 3741						
NFW	15.17	1.52	0.04	2.63	51.0	5.7
Burkert	2.29	37.49	0.004	0.29	88.5	43.2
ISO	1.15	43.16	0.51	3.52	83.9	38.6
NGC 6503						
NFW	3.57	95.82	0.04	7.86	145.8	28.9
Burkert	2.09	296.16	0.03	5.33	174.6	57.7
ISO	0.16	98.68	7.56	13.9	117.4	0.5

(a) NGC 1560
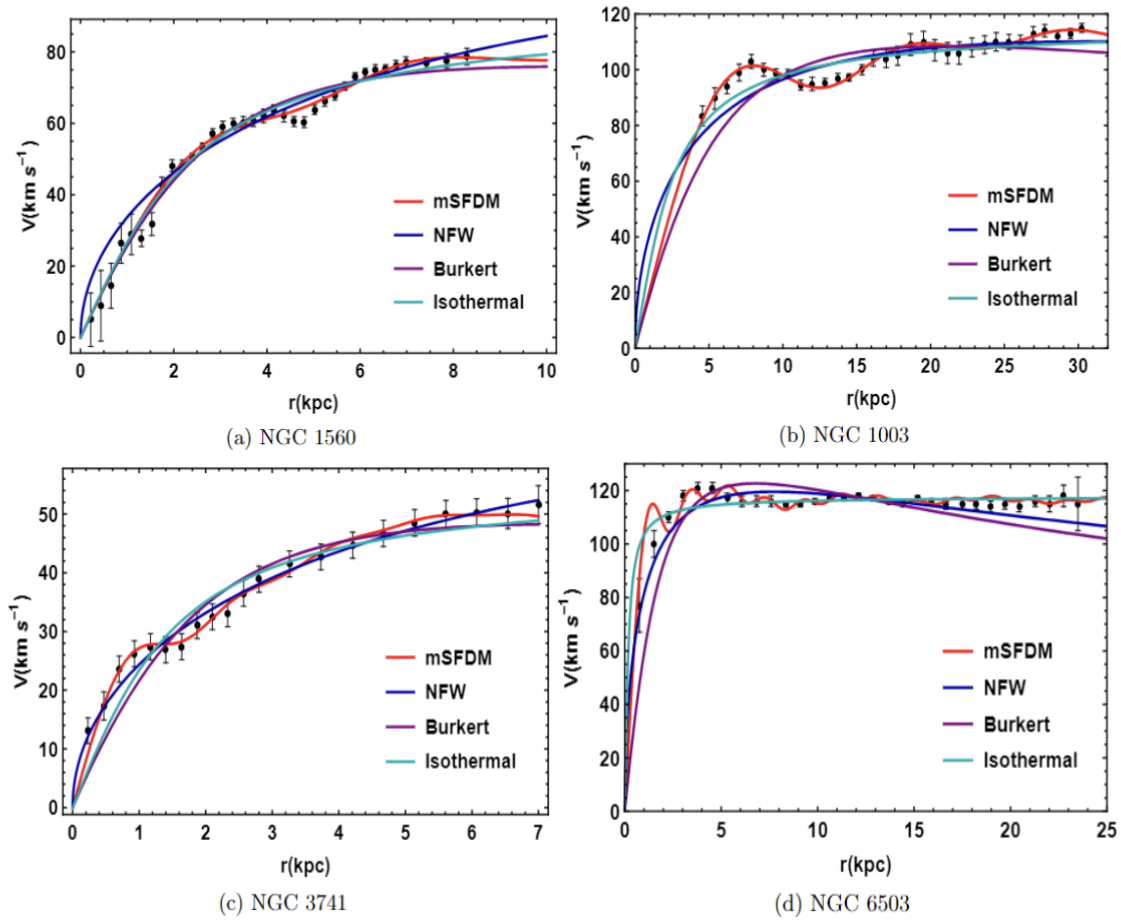
(b) NGC 1003

(c) NGC 3741

(d) NGC 6503

Fig.2. Rotation curves of LSB galaxies for mSFDM and three phenomenological (NFW, Burkert, ISO) models

5. Conclusion

In this work, we have analyzed four LSB spiral galaxies (range of sizes $\sim 7-30$ kpc) within the framework of two SFDM models regardless of the impact of baryonic component and internal structure of galaxies. First one, the so-called BEC SFDM, implies the system of bosons in the ground state and at zero-temperature in the Thomas-Fermi limit. Second one, mSFDM, is the model with finite temperature corrections which lead to taking into consideration exited states of bosons. We performed the fitting procedure to constrain the free models' parameters and to estimate which model is more preferable and consistent with observations. The mSFDM with lower values of BIC for all considered galaxies proved to be better representation model for DM. To further verify the appropriateness of mSFDM model, we compared it with NFW, Burkert and ISO profiles as representative examples of phenomenological framework. For each galaxy, mSFDM provides better results keeping the lowest values of BIC and showing the excellent agreement with observations. The mSFDM model incorporates finite temperature effects and allows for multistate occupation of bosons, which are particularly relevant in scenarios where thermal effects cannot be ignored. This is expected to be the case in certain early-universe conditions or in environments with significant thermal history affecting dark matter distribution.

Within this article, we did not conduct a detailed analysis and comparison between phenomenological models themselves, since related work was done in several papers (see, for example, [26-30]).

Nevertheless, in case of NGC 1560 and NGC 6503 there are some data points not covered even by mSFDM, suggesting the need for further analysis. An additional numerical analysis is required to examine the influence of baryonic matter as well as including into consideration the inner structure of galaxies. Besides, more galaxies should be analyzed, to estimate the degree of applicability mSFDM model within the wide range of galaxies. Moreover, it would be interesting to examine the SFDM models in Milky Way and Andromeda galaxies, following the methodology described in [31-33].

References

1   Zwicky F. (1933) Die rotverschiebung von extragalaktischen nebeln. *Helvetica Physica Acta*. 6, 110-127. Available at: https://ned.ipac.caltech.edu/level5/March17/Zwicky/frames.html

2   Rubin V.C., Ford Jr.W. K., Thonnard N. (1980) Rotational properties of 21 SC galaxies with a large range of luminosities and radii, from NGC 4605/R= 4kpc/to UGC 2885/R= 122 kpc. *Astrophysical Journal*. 238, 471- 487. Available at: https://articles.adsabs.harvard.edu/pdf/1980ApJ...238..471R

3   Rubin V.C. (1983) The rotation of spiral galaxies. *Science*. 220, 4604, 1339-1344, Available at: https://www.science.org/doi/10.1126/science.220.4604.1339

4   Bertone G., Hooper D., Silk J. (2005) Particle dark matter: Evidence, candidates and constraints. *Physics reports*. 405, 5-6, 279-390. DOI:10.1016/j.physrep.2004.08.031.

5   Bennett C.L., Larson D., Weiland J.L., Jarosik N., Hinshaw G., Odegard N., Smith K.M., Hill R.S., Gold B., Halpern M., Komatsu E., Nolta M.R., Page L., Spergel D.N, Wollack E., Dunkley J., Kogut A., Limon M., Meyer S.S., Tucker G.S., Wright E.L. (2013) Nine-year Wilkinson Microwave Anisotropy Probe (WMAP) observations: final maps

and results. *The Astrophysical Journal Supplement Series*. 208, 2, 1-54. Available at: https://iopscience.iop.org/article/10.1088/0067-0049/208/2/20

6   Benson A.J. (2010) Galaxy formation theory. *Physics Reports*. 495, 2-3, 33-86. DOI:10.1016/j.physrep.2010.06.001.

7   Larson D., Dunkley J., Hinshaw G., Komatsu E., Nolta M.R., Bennett C.L., Gold B., Halpern M., Hill R.S., Jarosik N., Kogut A., Limon M., Meyer S.S., Odegard N., Page L., Smith K.M., Spergel D.N., Tucker G.S., Weiland J.L., Wollack E. and Wright E.L. (2011) Seven-year wilkinson microwave anisotropy probe (WMAP*) observations: power spectra and WMAP-derived parameters. *The Astrophysical Journal Supplement Series*. 192(2), 1-19. DOI:10.1088/0067-0049/192/2/16.

8   Weinberg D.H., Bullock J.S., Governato F., Kuzio de Naray R., Peter H.G. (2015) Cold dark matter: controversies on small scales. *Proceedings of the National Academy of Sciences*. 112, 40, 12249-12255. DOI:10.1073/pnas.1308716112.

9   Ji S.U., Sin S.J. (1994) Late-time phase transition and the galactic halo as a Bose liquid. II. The effect of visible matter. *Physical Review D*. 50, 6, 3655-3659. DOI:10.1103/PhysRevD.50.3655.

10   Guzmán F.S., Matos T. (2000) Scalar fields as dark matter in spiral galaxies. *Classical and Quantum Gravity*. 17 (1) L9-L16. DOI:10.1088/0264-9381/17/1/102.

11   Guzman F.S., Matos T., Villegas H.B. (1999) Scalar fields as dark matter in spiral galaxies: comparison with experiments. *Astronomische Nachrichten: News in Astronomy and Astrophysics*. 320, 3, 97-104. DOI:10.1002/1521-3994(199907)320:3<97::AID-ASNA97>3.0.CO;2-M.

12   Lee J., Koh I. (1996) Galactic halos as boson stars. *Physical Review D*. 53, 4, 2236-2239. DOI:10.1103/PhysRevD.53.2236.

13   Hu W., Barkana R., Gruzinov A. (2000) Fuzzy cold dark matter: the wave properties of ultralight particles. *Physical Review Letters*. 85, 6, 1158-1161. DOI:10.1103/PhysRevLett.85.1158.

14   Schive H.Y., Chiueh T., Broadhurst T. (2014) Cosmic structure as the quantum interference of a coherent dark wave. *Nature Physics*. 10, 7, 496-499. DOI:10.1038/nphys2996.

15   Boehmer C.G., Harko T. (2007) Can dark matter be a Bose–Einstein condensate? *Journal of Cosmology and Astroparticle Physics*. 06, 1-27. DOI:10.1088/1475-7516/2007/06/025.

16   Bogoliubov N. (1947) On the theory of superfluidity. *J. Phys*. 11 (1), 23. Available at: https://inspirehep.net/literature/45477

17   Robles V.H., Matos T. (2012) Exact solution to finite temperature SFDM: natural cores without feedback. *The Astrophysical Journal*. 763, 1, 1-8. DOI:10.1088/0004-637X/763/1/19.

18   Kolb E.W., Turner M.S. (1981) The early universe. *Nature*. 294, 5841, 521-526. DOI:10.1038/294521a0.

19   Castellanos E., Matos T. (2013) Klein–Gordon Fields and Bose–Einstein Condensates: Thermal Bath Contributions. *International Journal of Modern Physics B*. 27, 11, p. 1350060. DOI:10.1142/S0217979213500604.

20   Navarro J.F. (1996) The structure of cold dark matter halos. *Symposium-international astronomical union*. 171, 255-258. DOI:10.48550/arXiv.astro-ph/9511016.

21   Burkert A. (1995) The structure of dark matter halos in dwarf galaxies. *The Astrophysical Journal*. 447, 1, L25-L28. DOI:10.1086/309560.

22   Jimenez R., Verde L., Oh S.P. (2003) Dark halo properties from rotation curves. *Monthly Notices of the Royal Astronomical Society*. 339, 1, 243-259. DOI:10.1046/j.1365-8711.2003.06165.x.

23   Levenberg K. (1944) A method for the solution of certain non-linear problems in least squares. *Quarterly of applied mathematics*. 2 (2), 164-168. DOI:10.1090/qam/10666.

24   Marquardt D.W. (1963) An algorithm for least-squares estimation of nonlinear parameters. *Journal of the society for Industrial and Applied Mathematics*. 11, 2, 431-441. Available at: https://www.jstor.org/stable/2098941.

25   Lelli F., McGaugh S.S., Schombert J.M. (2016) SPARC: Mass models for 175 disk galaxies with Spitzer photometry and accurate rotation curves. *The Astronomical Journal*. 152, 6, 1-14. DOI:10.3847/0004-6256/152/6/157.

26   Kurmanov Ye., Boshkayev K., Konysbayev T., Muccino M., Urazalina A., Ikhsan G., Saiyp N., Rabigulova G, Karlinova M., Suliyeva G., Taukenova A. and Beissen N. (2023) Analysis of dark matter profiles in the halos of spiral galaxies. *Physical Sciences and Technology*. 10, 3-4, 4-16. DOI:10.26577/phst.2023.v10.i2.01.

27   Boshkayev K., Konysbayev T., Kurmanov E., Muccino M. (2020) Dark matter properties in galaxy U5750. *News of the National Academy of Sciences of the Republic of Kazakhstan physico-mathematical series*. 6, 81-90. DOI:10.32014/2020.2518-1726.101.

28   Boshkayev K., Konysbayev T., Kurmanov E., Muccino M., Zhumakhanova G. (2020) Physical properties of dark matter in galaxy U11454. *Physical sciences and technology*, 7, 11-20. DOI:10.26577/phst.2020.v7.i2.02.

29   Boshkayev K., Konysbayev T., Kurmanov E., Luongo O., Muccino M. (2020) Imprint of pressure on characteristic dark matter profiles: the case of ESO0140040. *Galaxies*. 2020, 74, 1-13. DOI:10.3390/galaxies8040074.

30   Boshkayev K., Zhumakhanova G., Mutalipova K., Muccino M. (2019) Investigation of different dark matter profiles. *News of the National Academy of Sciences of the Republic of Kazakhstan Physical and Mathematical Series*. 6, 328, 25-33. DOI:10.32014/2019.2518-1726.70.

31   Sofue Y. (2015) Dark halos of M 31 and the Milky Way. *Publications of the Astronomical Society of Japan*. 67, 4, 75-84. DOI:10.1093/pasj/psv042.

32   Salucci P. (2019) The distribution of dark matter in galaxies. *The Astronomy and Astrophysics Review*. 27, 1 – 60. DOI:10.1007/s00159-018-0113-1.

33   Boshkayev K., Konysbayev T., Kurmanov Ye., Luongo O., Muccino M., Quevedo H., Zhumakhanova G. (2024) *Numerical analyses of M31 dark matter profiles*. 33, 03-04. DOI:10.1142/S0218271824500160.

_____

AUTHORS' INFORMATION

Suliyeva, Gulnara – PhD student, al-Farabi Kazakh National University, Almaty, Kazakhstan; Scopus Author ID: 57818572500; ORCID iD: 0000-0001-5072-7898; g_suliyeva@mail.ru

Kurmanov, Yergali – PhD, Acting Associate Professor, al-Farabi Kazakh National University, Leading Research Associate at the National Nanotechnology Open Laboratory (NNLOT), Almaty, Kazakhstan; Scopus Author ID: 57695578100; ORCID iD: 0000-0003-3695-0166; kurmanov.yergali@kaznu.kz

Konysbayev, Talgar – PhD, Senior Researcher, National Nanotechnology Open Laboratory (NNLOT), al-Farabi Kazakh National University, Almaty, Kazakhstan; Scopus Author ID: 5721980000; ORCID iD: 0000-0001-9476-3700; talgar_777@mail.ru

Boshkayev, Kuantay – PhD, Professor, al-Farabi Kazakh National University, Chief Researcher at the National Nanotechnology Open Laboratory (NNLOT), Almaty, Kazakhstan; Scopus Author ID: 54883880400; ORCID iD: 0000-0002-1385-270X; kuantay@mail.ru

Urazalina, Ainur – PhD, Senior Lecturer, al-Farabi Kazakh National University, Leading Research Associate at the National Nanotechnology Open Laboratory (NNLOT), Almaty, Kazakhstan; Scopus Author ID: 57076979300; ORCID iD:0000-0002-4633-9558; y.a.a.707@mail.ru

Luongo, Orlando – PhD, Associate Professor, University of Camerino, Camerino, Italy; Scopus Author ID: 35176257700; ORCID iD: 0000-0001-7909-3577; orlando.luongo@unicam.it

Research Article

INVESTIGATION OF CYCLIC PROPERTIES OF SOLAR AND GEOMAGNETIC ACTIVITIES: IMPLICATION FOR GLOBAL SURFACE TEMPERATURE VARIABILITY

Ibanga E.A.[1], Inyang E.P.[1], Agbo G.A.[2]

[1] Department of Physics, National Open University of Nigeria, Jabi, Abuja-Nigeria
[2] Department of Industrial Physics, Ebonyi State University, Abakaliki, Nigeria
*Corresponding author email: etidophysics@gmail.com

Abstract. *The cyclic properties of solar-geomagnetic activity and global surface temperature have been investigated using trend, frequency and time-frequency analyses. Results reveal that on decadal-to-centennial timescales, low-frequency cycles in the half-century (~49 to 56 years per cycle) and Gleisberg (~99 to 114 years per cycle) range run in the background of the Schwabe (~9 to 11 years per cycle) as the dominant cycle of solar-geomagnetic activity. The only dominant cycle in the global surface temperature series is the half-century cycle and suggests a possible causal link between it and solar-geomagnetic activity phenomena. Evolution of the amplitudes of the cycles is such that the Schwabe and Gleisberg periods have increased in power from the beginning of the series until the mid-20th century after which they declined. The half-century cycle decreased in amplitude after 1800 to the present. For geomagnetic activity, the amplitude of Gleisberg cycle increased from the beginning of the series around 2000 while the amplitudes of Schwabe and half-century cycles declined within the same interval, except the Schwabe cycle which amplitude increased rapidly after 1980 to the present. For the global surface temperature, the amplitudes of Gleisberg and half-century cycles have continuously increased from the beginning of the series while Schwabe cycle oscillates with very low amplitudes until 1980 after which it increased slightly. Evolution of the amplitudes of cycles of solar-gemagnetic activity suggests a recovery from Maunder Minimum and decline into a grand epsode most likely to be a minimum.*

Keywords: geomagnetic activity, solar activity, low-frequency cycle, grand episode, spectral power, global wavelet power.

1. Introduction

It is now known that the time series of solar and geomagnetic activities as well as climate phenomena are inherently characterized by multiple periodicities buried in noise, which may include the effects of interactions and nonlinearities. Detection and estimation of periodic components in forcing signals require the application of techniques that could eliminate or suppress the noisy background. Several techniques have been applied to study the periodic properties of the time series of solar activity, geomagnetic activity and climate change phenomena, using different proxies and on different temporal scales. Among such techniques include filtering to test for the existence of multiple periodicities and reveal trends of varying degrees and resolution of cyclicity of the forcing signals [1,2], frequency analysis based on spectral methods [3], deep learning and predictive models using neural network [4-6] and time-frequency analysis based on wavelet methods [7-9] and so on. Solar activity, characterized by variations in solar irradiance and sunspot numbers, follows an approximately 11-year cycle known as the solar cycle. Geomagnetic activity, influenced by solar wind and coronal mass ejections, is often quantified by indices such as the Ap and Kp indices. Both solar and

geomagnetic activities have been hypothesized to affect Earth's climate, but the extent and mechanisms of this influence remain subjects of ongoing research.

The arguments concerning climate change, and in particular the recent climate warming, are based on observations and predictions in terms of time and frequency of occurrences. For this purpose, wavelet analysis has been extensively explored. For solar and geomagnetic activities, once the dominant cycles have been revealed, their effects on and possible causal relationship to climate time series may become evident.

How and to what extent the evolution of temporal structures of solar-geomagnetic activity and climate interaction have contributed to the recently observed climate warming forms the basis of this study. The essence is to examine the cycles inherent in their temporal variability with a view to revealing the time-frequency patterns in the structures and how they may relate to and help to predict the near-future climate scenarios.

2. Data and Methods of Analysis

(i) Solar activity proxy comprised the annual mean sunspot number (R_Z) (1700-2020), obtained from World Data Centre (WDC), Sunspot Index and Long-term Solar Observations, http://www.sidc.be/silso/datafiles.

(ii) Geomagnetic activity proxy was characterised by antipodal activity (aa) index (1868-2020), obtained from NASA website at https://omniweb.gsfc.nasa.gov/form/dx1.html.

(iii) Global Surface Temperature Anomaly (dT) (HadCRUT5) and HadSST3 (1850-2023) obtained from Met Office Hadley Centre, https://www.metoffice.gov.uk/hadobs/hadcrut5/data/current/download.html

Time-series analyses comprising filtering, smoothing, trending, regression and curve fitting were performed on the relevant time series. The cyclic variabilities inherent in trends of the relevant phenomena were studied.

Spectral analysis derived from Fast Fourier Transforms (FFT) was performed to determine the strength of the cycles and establish the cyclic relationships among the phenomena under consideration.

To reveal the evolution of cycles in time and frequency of solar-geomagnetic activity and global surface temperature, time-frequency analysis using the continuous wavelet transforms was performed. The mother wavelet represents a family of functions [10] and is given as:

$$\psi(t)_{s,\tau} = \frac{1}{\sqrt{s}}\left(\frac{t-\tau}{s}\right) \tag{1}$$

where s, $\tau \epsilon R$; $s \neq 0$; s, τ are scaling (dilation or contraction) and translation (shifting) factors respectively while $\frac{1}{\sqrt{s}}$ is for the normalisation of energy across the different scales.

The computation of continuous wavelet coefficients is based on eqn. 2:

$$W_x(s,\tau) = \left|\frac{s}{\delta t}\right|^{-\frac{1}{2}} \sum_0^{N-1} x(t)\psi^*\left(\left(\frac{t-\tau}{s}\right)\delta t\right) \tag{2}$$

where N is the time series length and $\left|\frac{s}{\delta t}\right|^{-\frac{1}{2}}$ is the normalization parameter of the wavelet function[10] and was obtained by dilating or contracting the wavelet scale, s and translating along localized time position, τ. Wavelet coefficients describe the contribution of the scale s to the time series x(t) at different time position τ.

In this study, the continuous wavelet transformation was performed using Morlet wavelet as the analyzing wavelet [11] and is expressed as:

$$\psi\left(\frac{t-\tau}{s}\right) = \pi^{-\frac{1}{4}}e^{i\omega_0\left(\frac{t-\tau}{s}\right)}e^{-\left(\frac{t-\tau}{s}\right)^2/2} \tag{3}$$

where ω_0 is the wave number and is taken to be 6.0 in this case.

The wavelet spectral power $P(s,\tau)$ is computed as shown in eqn. 4.

$$P(s,\tau) = 2^s\left|W_{j,k}(t)\right|^2 \qquad j,k = 0,1,2,\dots,N-1 \tag{4}$$

where, 2^s is the bias correction factor [12]. The scale s of the Morlet wavelet is related to Fourier frequency f as in eqn. 5:

$$\frac{1}{f} = \frac{4\pi s}{\omega_0 + \sqrt{2+\omega_0^2}} \tag{5}$$

The scale s is approximately equal to the reciprocal of the Fourier frequency, $s \approx \frac{1}{f}$ [13].

3. Results and Discussion

The eleven-year (Schwabe) annual mean cycles are numbered 1 in 1749 to 24 in 2014 Fig.1 (a). The grand episodes are clearly illustrated. The highest peak of the cycles occurred in the International Geophysical Year (1957) with $R = 269.5$. The observed minima $R_1 = 0$ in 1711, $R_2 = 0$ in 1810, $R_3 = 2.4$ and $R_4 = 4.2$ in 2008 give an average cycle length of 98.7 years (Gleissberg period).
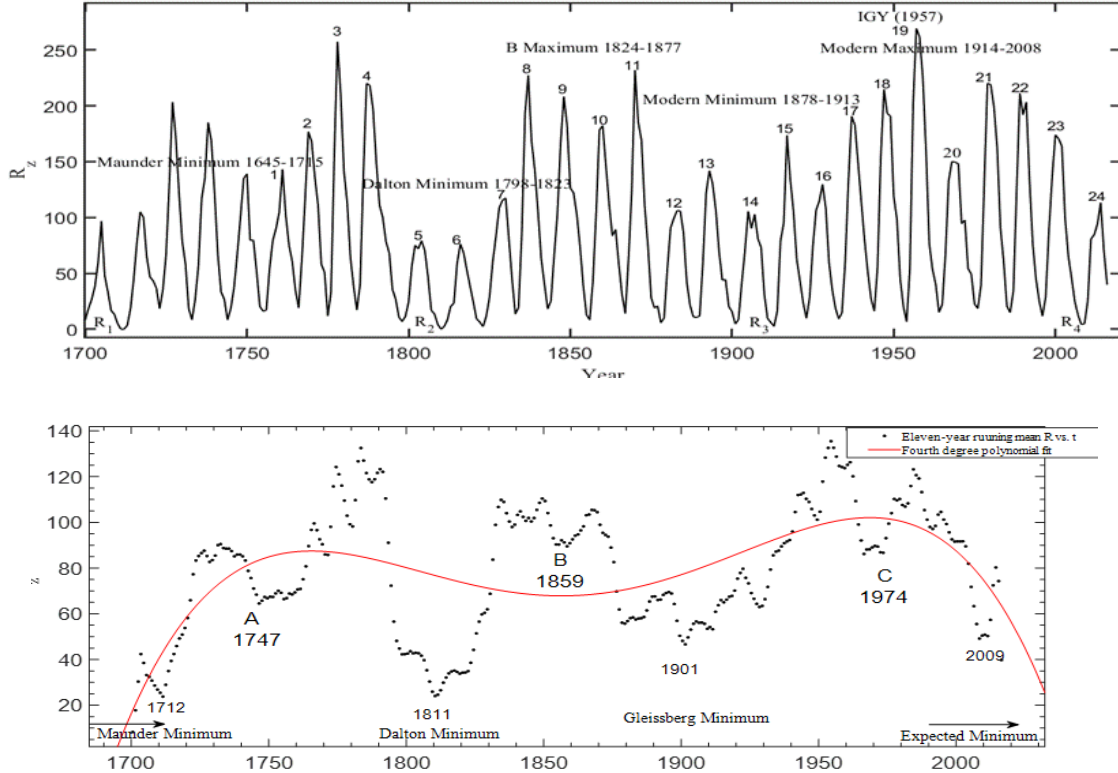

Fig.1. (a) Annual mean sunspot number (b) eleven-year running-mean with fourth-degree regression model

The eleven-year running-mean R_Z also reveals a minimum-to-minimum cycle of length ~99 years (Gleissberg period) Fig.1 (b). The maximum to maximum of the fourth-degree polynomial gives a low-frequency cycle of ~277 years but cycle length taken from the corresponding maxima of the eleven-year running mean is ~179 years. The average of the two values suggests a bi-centennial cycle (BC) of ~227 years. It is clear that subsequent minima after the Maunder Minimum were successively higher, which implies that solar activity has gradually been recovering (increasing in strength) after the grand minimum.

Quasi-grand episodes, laballed A, B, and C are approximately 114 years apart on the average (Gleissberg period range). Further still, the minimum-to-minimum, taking account of the quasi-minima, is approximately 52.4 years on the average. Therefore, sunspot activity of 11-, 52-, 114-year and 227-year periodicities have been identified using our trend analysis. For ease of reference, these cycles are herein labelled as Schwabe cycle (SB), half-century cycle (HC), Gleissberg cycle (GB) and bi-centennial cycle (BC) respectively. These cycles are in agreement with those found using other methods. For instance, Dergachev & Raspopov (2000), using sundry solar activity proxies such as total solar irradiance (TSI), carbon-14 (^{14}C) and Beryllium-ten (^{10}Be) levels and galactic cosmic ray (GCR), identified a 210-year SC.

The correlation of aa with R_Z is shown in Fig.2. The annual mean aa time series shows greater variability than the eleven-year running-mean (Fig. 2a) but are strongly correlated on the eleven-year solar activity cycle time scale (Fig. 2b). The correlation coefficient of the annual mean and eleven-year running mean aa and R_z time series are $r = 0.56$ and 0.87 respectively, within 95% confidence bounds. The relatively low value of r for the annual mean variability of aa is quantitative evidence of the prevalence of transient heliosphysical and interplanetary activities on shorter cycle-time scales, acting as background noise in concert with low frequency solar cycles. It is observed that annual mean aa variation is characterized by multiple peaks, comprising those that occur with peaks and those that occur in the declining phases of the

eleven-year sunspot activity cycles. The trend also reveals a dual peak B and C in SC19 and SC23. The peak A near the beginning of the time series corresponds to 1877 solar activity maximum. The quasi-minima marked a, b, c and d do not exhibit any consistent cycle lengths. The year marked d is not necessarily a minimum but is included to show the downward trend. It is also known that solar activity peaks of 1989 and 2003 were accompanied by severe space weather events. Although the filtering process tends to shift the position of the peaks of trended time series with respect to those of the annual mean variability, it is obvious from Fig. 2a that while the peak of solar activity occurred during the International Geophysical Year (IGY) 1957, the peak of geomagnetic activity occurred four solar cycles after, in 2003, evidently in the declining phase of solar activity low-frequency cycle.

Fig. 3 shows the annual mean global surface temperature represented by two recent time series HadSST3 (sea surface) and HadCRUT4 (land and sea) time series, together with their eleven-year running means and seventh-degree polynomial regression model of HadCRUT5, which closely fits both data and trend.

a)

b)
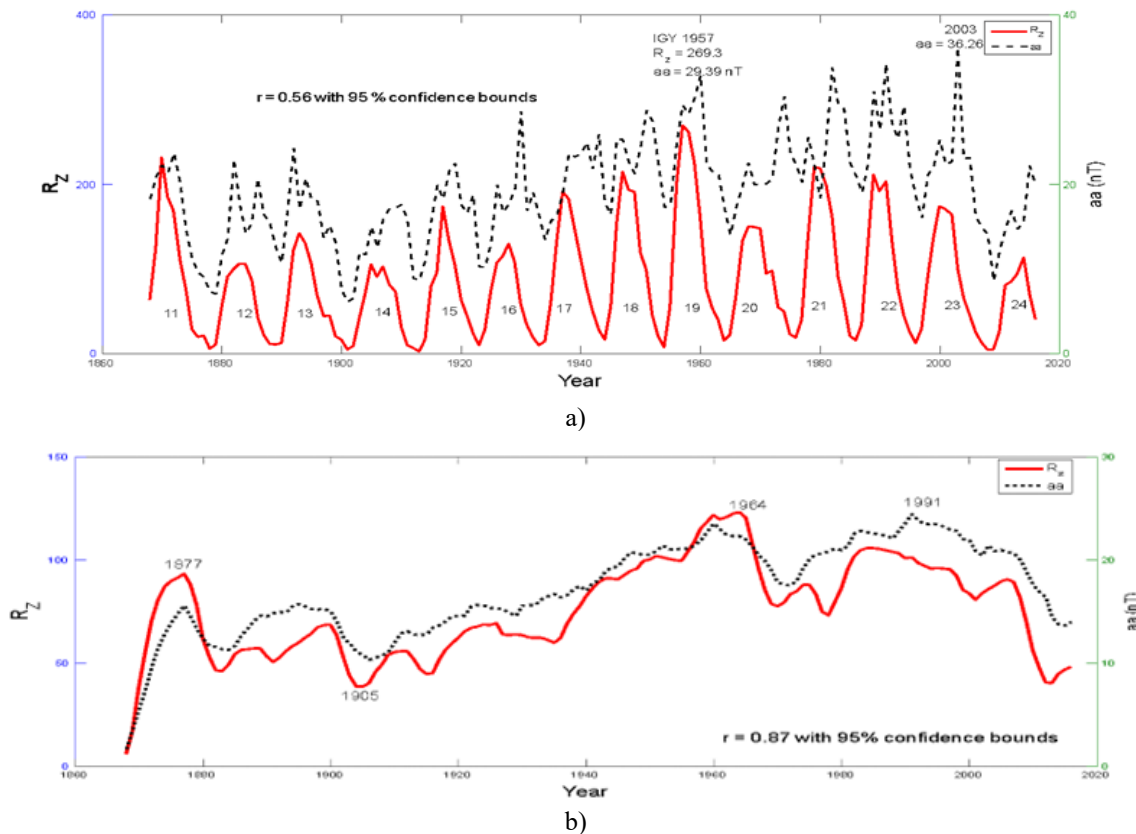
Fig.2. Sunspot number versus geomagnetic activity (a) annual mean (b) eleven-year running mean
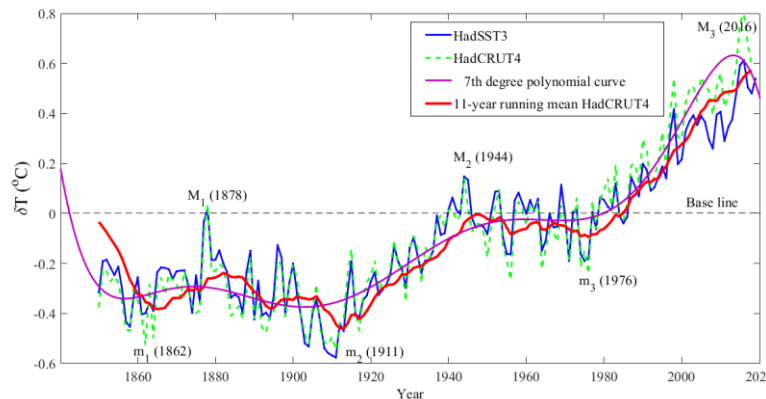
Fig.3: Global Sea surface temperature (HadCRUT5 & HadSST3) with the eleven- year running and the seventh-degree polynomial model

Clearly, the time series began in a descending phase, reached a minimum in 1911, and exhibited two maximum-to-maximum marked $M_1(1878)$ $M_2(1944)$ and $M_3(2016)$ of average cycle length of 64c. It also exhibits two minimum-to-minimum labelled $m_1(1862)$, $m_2(1911)$ and $m_3(1976)$ of average cycle length of 57 years. This suggests a global temperature cycle of an average period of 60 years (which is in the HC range). Identification of this cycle is crucial to the determination of the phenomenon that drives it. The spectral power of sun spot activity, antipodal geomagnetic activity and global surface temperature anomaly series are displayed (Fig. 4).

a)

b)

c)
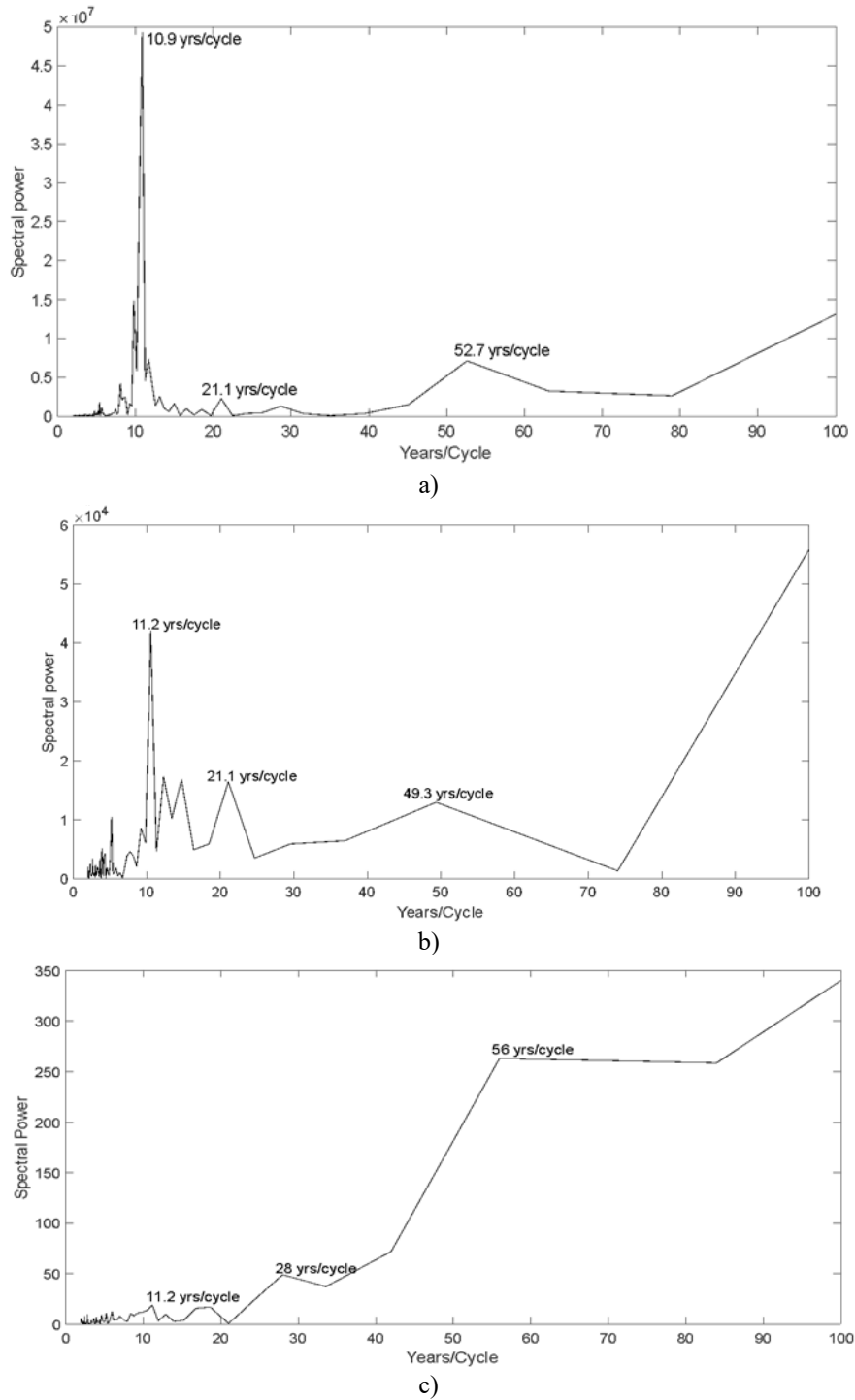
Fig.4. Periodogram of (a) solar activity and (b) geomagnetic activity proxies (c) global surface temperature anomaly

The most prominent cycle of solar and geomagnetic activities is the SBC followed in order of magnitude by the HC (Fig. 4a). The same is the case for geomagnetic activity (Fig. 4b), except that the HC is of slightly lower cycle length (49.3 years/cycle) compared to that of solar activity (52.7 years/cycle). The most prominent cycle of global surface temperature anomaly is the HC, ~56-years (Fig. 4c). Other less prominent cycles are also labelled. The apparent similarity of the spectral powers of solar and geomagnetic activities provides further evidence of the correlation that exists between the two series. Spectral analysis allows us to examine the frequency components of these activities, revealing patterns that might not be immediately obvious in the time domain. By observing that both solar and geomagnetic activities exhibit similar spectral power distributions, we can infer that they are influenced by common factors or mechanisms. This similarity suggests a strong connection, likely driven by the Sun's influence on the Earth's magnetic field. For example, solar phenomena such as sunspots, solar flares, and coronal mass ejections can significantly impact geomagnetic activity, causing variations in the Earth's magnetosphere. The alignment in their spectral powers indicates that changes in solar activity are mirrored by corresponding changes in geomagnetic activity, reinforcing the idea of a dynamic and interdependent relationship between these two series.

By comparison with the spectral powers of solar and geomagnetic activities, it is clear that the spectral power of global surface temperature anomaly (Fig. 4c) follows the same pattern of variability, with some degree of modulation. It implies that global surface temperature variability has components that are attributable to the variability of solar and geomagnetic activities. Fig. 5 (a) shows the continuous wavelet transform of sunspot activity. All the cycles increase in level between 1750 and 2000 except the HC which diminishes after 1850. SB and GB reached maximum levels between 1950 and 2000. The global wavelet power (Fig. 5b) exhibits three peaks corresponding to SB, HC and GB, with SB and GB as the most dominant cycles.

a)

b)
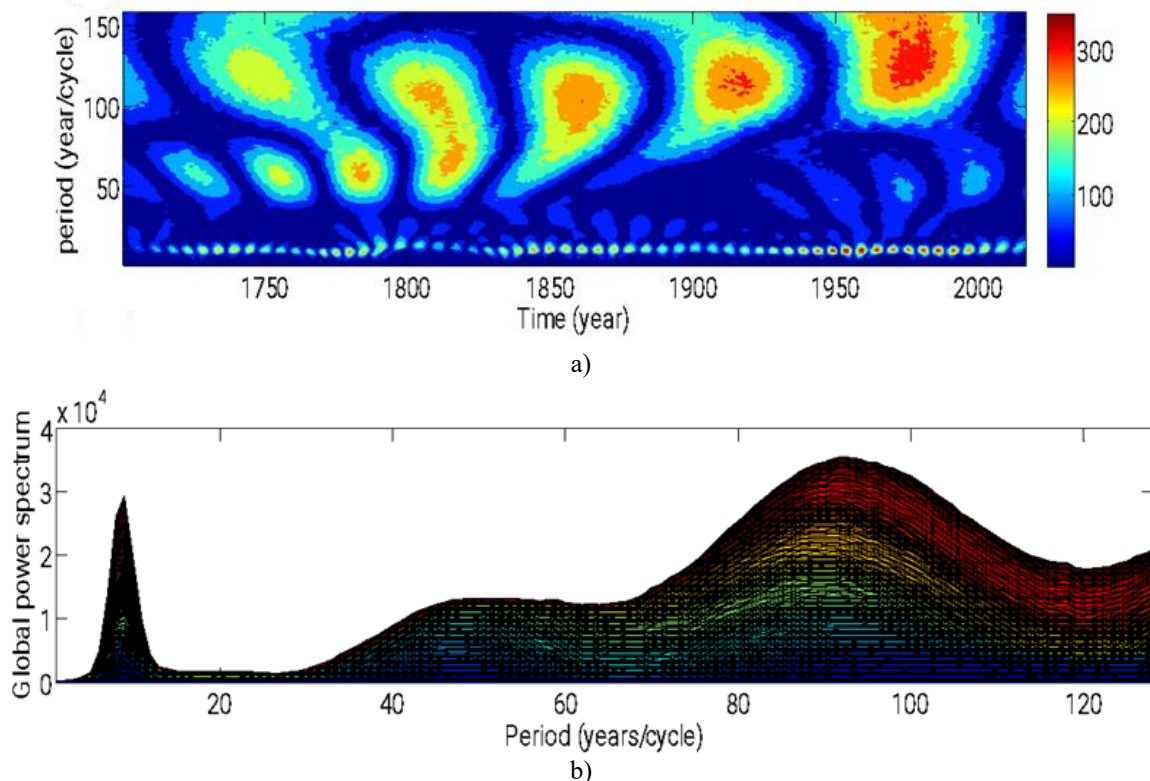
Fig.5. Continuous wavelet transforms and global wavelet power spectrum of sunspot activity.

Fig. 6 displays the plots of continuous wavelet transform and the global power spectrum of geomagnetic activity. GB is the most prominent cycle. It increases in level to a maximum between 1970 and early 2000s. HC also followed the same pattern of variability, although it is less prominent. The SB is less prominent compared to GB and HC. In addition to the three cycles, it is apparent that a lower frequency cycle, possibly of 150-year cycle is present and is localized between 1940 and 2000 (Fig. 6a). The global

power spectrum (Fig. 6b) reveals three peaks corresponding to the SB, HC and GB respectively, and possible existence a lower frequency cycle in the 150-year range. The strongest cycle is the GB followed by the HC.

The continuous wavelet transform and global wavelet power spectrum of the global surface temperature are shown in Fig. 7. Fig. 7a shows that HC increases in strength from the beginning the series to a maximum in. It is noticed that cycles with higher periods (above 150 years/cycle) are localized around 1900 and 2000.

a)

b)
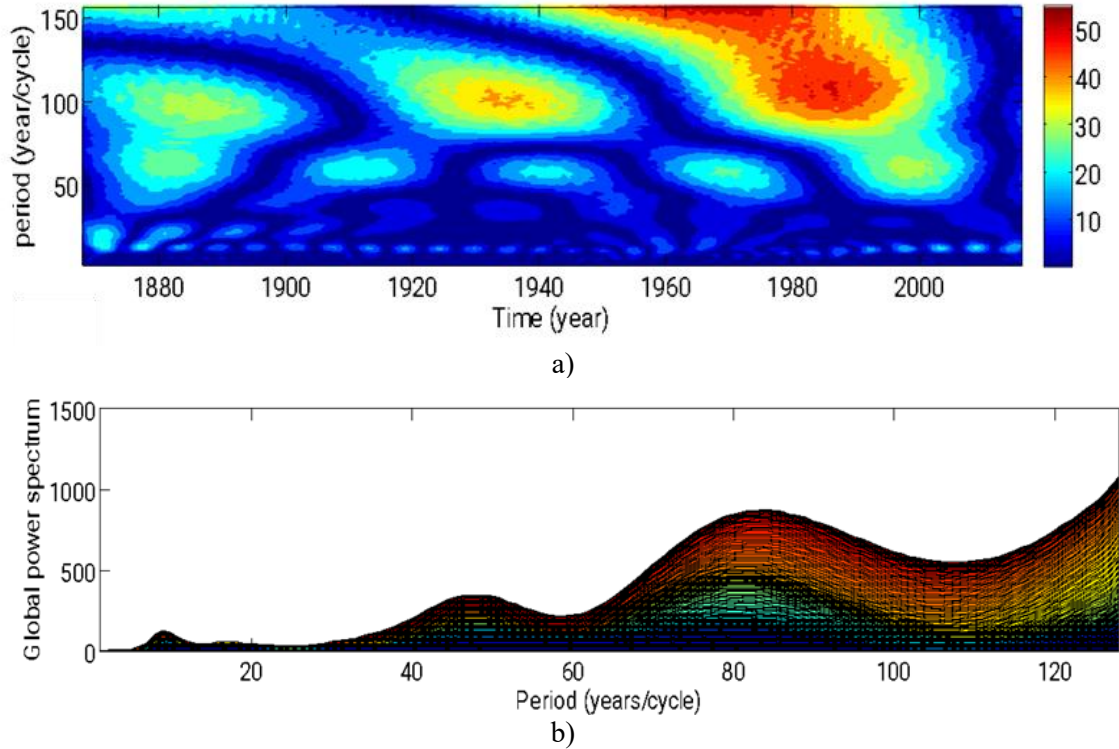
Fig.6. (a) Continuous wavelet transforms coefficients (b) Global wavelet power spectrum of geomagnetic activity

a)

b)
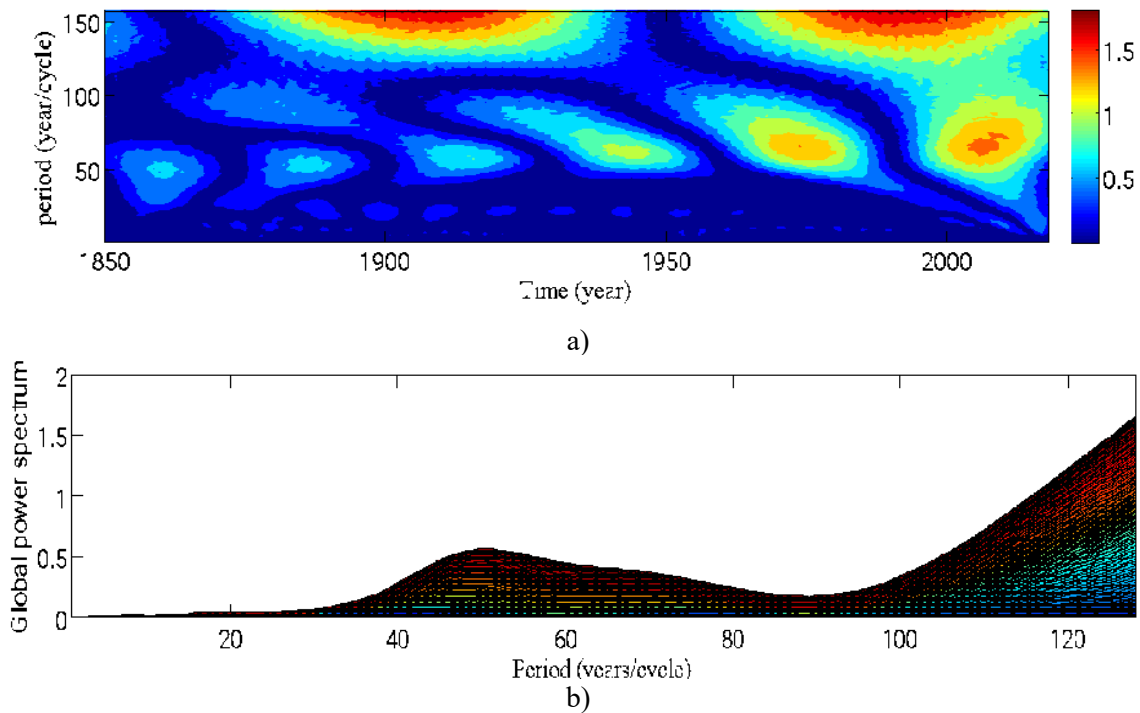
Fig.7. Plots of continuous wavelet transform coefficients and global wavelet power spectrum of global surface temperature

Fig. 7b shows a prominent peak only at 51 years/cycle corresponding to the HC. There appears to be a low-frequency cycle, possibly in the 150 years range. The HC component of cyclicity clearly exists in all the three times series. It is apparent that global surface temperature, solar activity and geomagnetic activity have a possible causal link through the HC and, possibly, lower frequency cycles.

It is clear that the low frequency cycles have continued to increase in level in all the three series. It suggests that the low frequency components of solar and geomagnetic activities possibly contribute to the current climate warming scenario. Fig. 8 shows the trends in the evolution of the amplitudes of the SB, HC and GB of sunspot activity, geomagnetic activity and global surface temperature.

a)

b)

c)
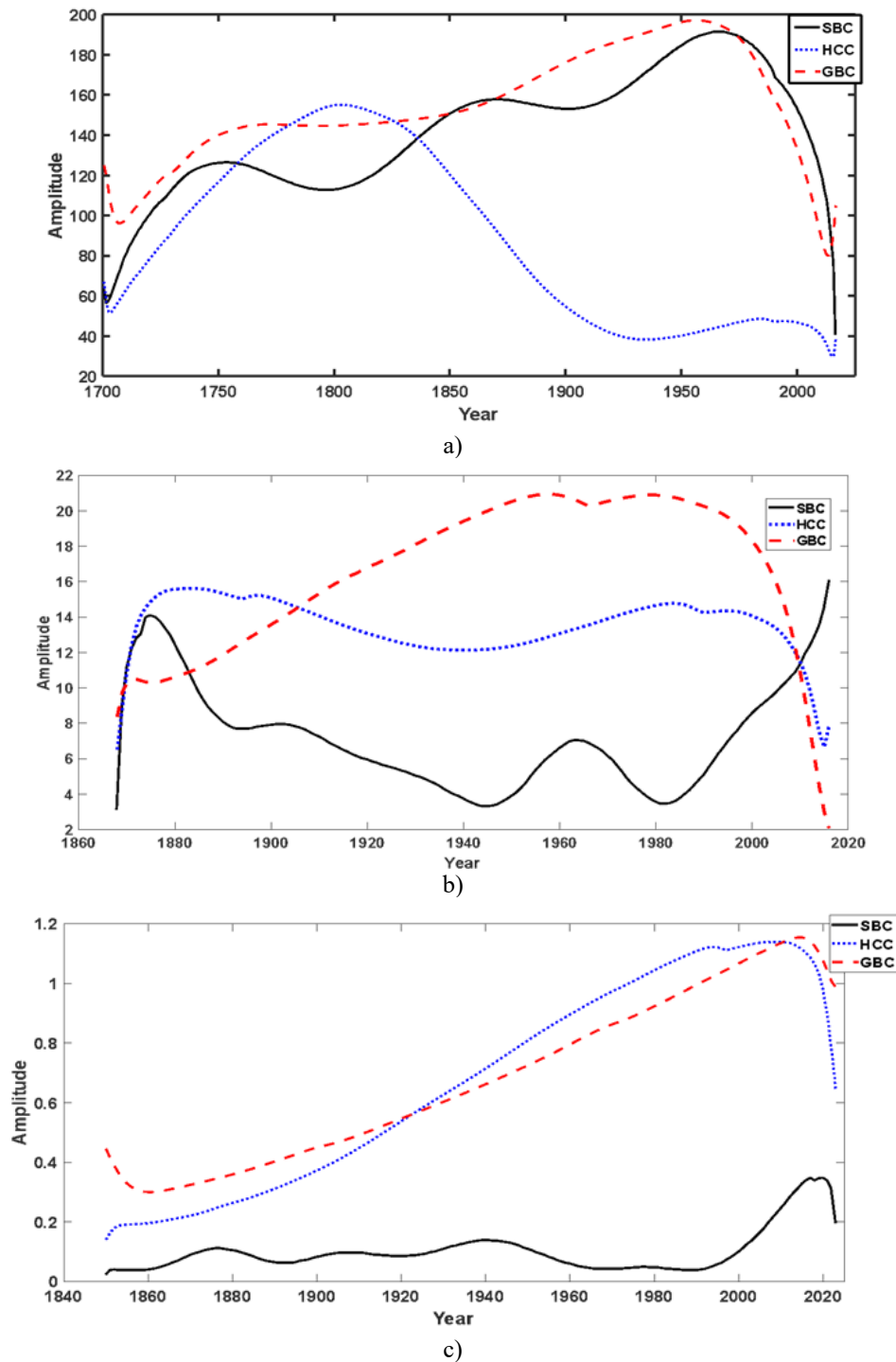
Fig.8. Evolution of the amplitudes (a) (Rz) (b) aa (c) dT

In Fig. 8a, it is found that between 1700 and 1780 the amplitude of GB was higher than those of SB and HC. The amplitude of HC was higher than both the SB and GB from 1781 and 1826, reaching its peak in 1802 and declining thence after. From 1836, the amplitude of HC was lower than those of SB and GB. The SB dominates other cycles from 1974 to the present. Most importantly, it could see that the cycles of sunspot activity are evolving to low magnitudes, suggesting a decline, possibly into a grand minimum.

Fig. 8b illustrates the evolution in amplitude of geomagnetic activity. It shows that the HC increased from the beginning of the time-series to around 1880 and declined to low amplitudes thereafter reaching a minimum in 1940. It dominated over SB and the GB between 1868 and 1909. It rose again in magnitude until its peak was attained in 1997 before a final plunge. The GB, which has increased in magnitude from the beginning of the series, took dominance over the other cycles from 1908 to 2006, reaching its peak value in 1983 before a final plunge. The SB and HC were in the depending phase after about 1875, reaching some minimum values around the early 1940s. This observation appears to be consistent with the decrease in global surface temperature observed from 1944 (Fig. 3). Also, all the cycles reached their maximum amplitudes at different times. The GB reached its maximum level between 1960 and 1980. The HC reached its maximum level between 1980 and 2000. However, the leading cycles (GB and HC) declined rapidly after. It is observed that the SB increased in level after 1980 till the end of the series. Fig. 8c shows the plot of the trends and evolution in time of the magnitudes of the SB, HC and GB of annual mean global surface temperatures. It is found that the GB dominated the other two up to about 1922. The HC then took dominance over the others to the end of the time series. It is noted that the low-frequency HC and GB have continuously increased from the beginning of the series. The SB oscillated with very low amplitudes until after 1980 when it increased sharply. All the three cycles exhibit the tendency to decrease in level toward the end of the series.

4. Summary and Conclusions

In this study, the cyclic properties of sunspot activity, geomagnetic activity and global surface temperature were investigated using trend, spectral and wavelet analyses. These analyses clearly show that low frequency cycles of decadal to centennial timescales run in the background of the eleven-year cycle. The eleven-year running mean showed a trend of cyclicity of sunspot activity in the Gleisberg cycle range (between 99 to 114 years per cycle) and a bi-centennial cycle of approximately 227 years/cycle. Evidence of the bi-centennial cycle had been found in the natural archives as in Ref. [14] which identified a cycle length of 210 years. Spectral analysis revealed three peaks in all three series corresponding to eleven-year Schwabe cycle, the half-century cycle and Gleisberg cycle of slightly varying cycle lengths. The strongest cycle in sunspot and geomagnetic activity series is the Schwabe cycle. Schwabe and Gleisberg cycles are not significant compared to the half-century cycle in the global surface temperature series. It suggests that the half-century cycle of global surface temperature variability may be related to those of solar and geomagnetic activities.

Wavelet analysis reveals three peaks in solar and geomagnetic activities corresponding to the Schwabe, half-century and Gleisberg cycles respectively. However, it reveals only a peak corresponding to the half-century cycle in the global surface temperature series. It suggests a link between the solar and geomagnetic activities with global surface temperature series at a low-frequency cycles. The regression model suggests a recovery of solar activity from the Maunder Minimum and that the expected grand episode after the Modern Maximum will most likely be a minimum. The evolution of the amplitudes of the low-frequency cycles of solar and geomagnetic activities to lower values suggests a possible descent into a new grand episode which is expected to be a minimum. The evolution of the amplitudes of Schwabe, half-century and Gleisberg cycles of global surface temperature also indicate the tendency toward lower values. Thus, the low-frequency cycles of global surface temperature variability responses to the low-frequency components of solar and geomagnetic activity.

References

1   Ibanga E.A., Agbo G. A., Inyang E. P., Ayedun F., Onuora L.O. (2020) Prediction of Solar Cycles: Implication for the Trend of Global Surface Temperature. *Communication in Physical Sciences*. 6(2), 882 – 890. Available at https://journalcps.com/index.php/volumes

2   Petrovay K. (2020) Solar cycle prediction. *Living Rev Sol Phys.* 17, 2-10. DOI:10.1007/s41116-020-0022-z(0123456789.

3   Kim J.H., Chang H.Y. (2014) Spectral Analysis of Geomagnetic Activity Indices and Solar Wind Parameters. *Journal of Astronomy and Space Science*. 31(2), 159 – 167. DOI: 10.5140/JASS.2014.31.2.159.

4   Okoh D.I., Seemala G.K., Rabiu A.B., Uwamahoro J., Habarulema J.B., Aggarwal M. (2018) Hybrid Regression-Neural Network (HR-NN) Method for Forecasting the Solar Activity. *Space Weather.* 16 (9), 1424-1436. DOI:10.1029/2018SW001907.

5   Hanslmeier A., Brajša R. (2010) The chaotic solar cycle I. Analysis of cosmogenic ^{14}C-data. *Astronomy and Astrophysics*. 509, A5. DOI:10.1051/0004-6361/200913095.

6   Peguero J.C., Carrasco V.M.S. (2023) A Critical Comment on "Can Solar Cycle 25 Be a New Dalton Minimum?" *Solar Physics*. 298: 48. DOI:10.1007/s11207-023-02140-7.

7   Kasde S.K; Sondhiya D.K., Gwal A.K. (2016) Analysis of Sunspot Time Series During the Ascending Phase of Solar Cycle 24 Using the Wavelet Transform. *American Journal of Modern Physics.* 5(5): 79 – 86. DOI:10.11648/j.ajmp.20160505.11.

8   Kristof P. (2020) Solar cycle prediction. *Living Reviews in Solar Physics*, 17: 2. DOI:10.1007/s41116-020-0022-z.

9   Muraki Y., Shibata S., Takamaru H., Oshima A. (2023) The 48-Year Data Analysis Collected by Ngoya Muon Telescope – A Detection of Possible (125±45)-Day Periodicity. *Universe.* 9, 372-387. DOI:10.3390/universe9090387.

10   Torrence C., Compo G.P. (1998) A Practical Guide to Wavelet Analysis. *Bulletin of the American Meteorological Society*. 79(1), 61–78. DOI:10.1175/1520-0477(1998)079<0061:APGTWA>2.0.CO;2.

11   Riabova S. (2018) Application of wavelet analysis to the analysis of geomagnetic field variations. *Journal of Physics: Conference Series*. 1141: 012146. DOI:10.1088/1742-6596/1141/1/012146.

12   Liu Y., San Liang X., Weisberg R.H. (2007) Rectification of the Bias in the Wavelet Power Spectrum. *Journal of Atmospheric and Oceanic Technology*. 24, 2093–2102. DOI:10.1175/2007JTECHO511.1.

13   Cazelles B., Chavez M., Berteaux D., Menard F., Vik J.O., Jenouvrier S., Stenseth N.C. (2008) Wavelet analysis of ecological time series. *Oecologia*. 156 (2): 287–304.

14   Mohamed A.E., Eman S., Aly A., Shady E.M. (2010) Spectral Analysis of Solar Variability and their Possible Role on the Global Warming. *Journal of Environmental Protection*. 1, 111-116.

_____

AUTHORS' INFORMATION

Ibanga, Efiong A. - Dr. (Sci.), Professor, Department of Physics, National Open University of Nigeria, Jabi, Abuja-Nigeria Victoria Island, Lagos, Nigeria; ORCID iD 0000-0002-5452-0613; eibanga@noun.edu.ng

Inyang, Etido P. – Dr. (Sci.), Professor, Department of Physics, National Open University of Nigeria, Jabi, Abuja-Nigeria Victoria Island, Lagos, Nigeria; ORCID iD: 0000-0002-5031-3297; etidophysics@gmail.com

Agbo, Godwin A. Professor, Department of Industrial Physics, Ebonyi State University, Abakaliki, Nigeria; profgodwinagbo@gmail.com

SUMMARIES	ТҮСІНІКТЕМЕЛЕР	АННОТАЦИИ

Козловский А.Л., Кабиев М.Б., Шлимас Д.И., Углов В.В.

MgO және Y_2O_5 қосындыларының әсерінен неодим цирконаты негізіндегі екі фазалы керамика түзілуінің сәулелену кезінде беріктік пен термофизикалық параметрлердің тұрақтылығына әсерін зерттеу

Жұмыста MgO және Y_2O_5 қосылған неодим цирконатының ($Nd_2Zr_2O_7$) ядролық отынның бөліну фрагменттерімен салыстырылатын ауыр иондармен сәулеленуден туындаған радиациялық зақымдануға төзімділігін анықтауға арналған зерттеу нәтижелері берілген. Керамиканың бұл түріне қызығушылық цирконий диоксидімен салыстырғанда жоғары жылу өткізгіштікке, сонымен қатар керамиканың сыртқы әсерлерге төзімділігін сипаттайтын жоғары беріктік параметрлеріне байланысты жаңа буын ядролық реакторларының ядросының жұмыс температурасын жоғарылату мүмкіндігімен байланысты. Бұл зерттеудің негізгі нәтижелері магний және иттрий оксидтерін құрамға қосқанда орынбасушы немесе алмастыру фазалардың түзілуінің, $Nd_2Zr_2O_7$ беріктігінің тұрақтылығы мен термофизикалық параметрлерінің тұрақтылығын арттыруға, зақымдалған беткі қабатта радиациялық ақаулардың жинақталуына әсерін анықтау болып табылады. Зерттеулер барысында MgO қосындылары (композицияға қосқанда) түріндегі қоспа фазаларының және $Y_2Zr_2O_7$ түріндегі алмастыру фазаларының (Y_2O_5 қосылғанда) түзілуі тұрақтылығының жоғарылауына әкелетіні анықталды. $Nd_2Zr_2O_7$ керамикасының қаттылығы мен жарыққаққа төзімділігі, бұл жоғары дозалы сәулелену кезінде зақымдалған қабаттың деформациялық сынғыштықты болдырмайтын қосымша фазааралық шекаралардың пайда болуымен байланысты легирлеудің оң әсерін көрсетті. Зерттелетін $Nd_2Zr_2O_7$ керамикасының жылуфизикалық параметрлерін анықтау кезінде легирлеу кезінде фазааралық шекаралардың пайда болуы тек жылу өткізгіштіктің жоғарылауына ғана емес, сонымен қатар $Nd_2Zr_2O_7$ қосылмаған керамикаларымен салыстырғанда екі фазалы керамикалар үшін сәулелену кезінде жылу өткізгіштік коэффициентінің нашарлау тенденцияларының төмендеуіне әкелетіні анықталды.

Кілт сөздері: неодим цирконаты, допирлеу, тұрақтылықтың артуы, радиациялық ақаулар, қатаю, жылуфизикалық параметрлер.

Козловский А.Л., Кабиев М.Б., Шлимас Д.И., Углов В.В.

Исследование влияния формирования двухфазных керамик на основе цирконата неодима за счет допирования MgO и Y_2O_5 на стабильность прочностных и теплофизических параметров при облучении

В работе представлены результаты исследования определения устойчивости цирконата неодима ($Nd_2Zr_2O_7$) допированного MgO и Y_2O_5 к радиационным повреждениям, вызванным облучением тяжелыми ионами, сравнимыми с осколками деления ядерного топлива. Интерес к данному типу керамик обусловлен возможностями повышения рабочих температур активной зоны ядерных реакторов нового поколения, в виду высоких показателей теплопроводности в сравнении с диоксидом циркония, а также более высокими показателями прочностных параметров, характеризующих устойчивость керамик к внешним воздействиям. Основные результаты данного исследования заключаются в определении влияния формирования фаз замещения или внедрения при добавлении в состав оксидов магния и иттрия, на повышение устойчивости прочностных и теплофизических параметров $Nd_2Zr_2O_7$ к накоплению радиационных дефектов в поврежденном приповерхностном слое. В ходе проведенных исследований было установлено, что формирование примесных фаз в виде включений MgO (при его добавлении в состав) и фазы замещения типа $Y_2Zr_2O_7$ (при добавлении Y_2O_5) приводит к повышению устойчивости твердости и трещиностойкости $Nd_2Zr_2O_7$ керамик, что свидетельствует о положительном эффекте допирования, связанного с формированием дополнительных межфазных границ, препятствующих деформационному охрупчиванию поврежденного слоя при высокодозном облучении. При определении теплофизических параметров исследуемых $Nd_2Zr_2O_7$ керамик было установлено, что формирование межфазных границ при допировании приводит не только к увеличению теплопроводности, но и более низким трендам ухудшения коэффициента теплопроводности при облучения для двухфазных керамик в сравнении с недопированными $Nd_2Zr_2O_7$ керамиками.

Ключевые слова: цирконат неодима, допирование, повышение стабильности, радиационные дефекты, упрочнение, теплофизические параметры.

Rahman R.A., Sulistyo, Utomo M.S.K.T.S., Febriansyah I.

Төмен тығыздықты полимер маркасының қатты сұйық жылу аккумуляторы ретінде температуралық ауысуға және балауыздың зарядтау әрекетіне әсері.

Жылу жинағыш материал ретінде парафинді техникалық жақсарту үшін жүктеменің бастапқы бағалауы төмен тығыздықты пластиктер тобымен композициялау арқылы жүзеге асырылады. Бағалау химиялық

спектр мен жылуфизикалық тәртіпті қоса алғанда, қоспаның температуралық ауысуын алуға бағытталған. Қоспада негізгі фазалық ауысудан кейін қосымша өту шыңы бар. Ол 15,26–19,34 °С (балқу) және 11,98–9,45 °С (салқындау) аралығында болады. Химиялық бақылаулар жақсы сәйкестікті көрсетті, себебі композит химиялық реакциясыз түзілуі мүмкін. Сонымен қатар, ыдыраудың сипаттамасы қоспаның бөлек балқитынын көрсетеді. Зарядты бағалау үшін PW/LDPE композиті PW-мен салыстырғанда максималды өсімі шамамен 25% болатын жақсы зарядтау сипаттамаларына ие. Сондай-ақ оның бірегей температура профиліне ие, оның изотермиялық профилін қысқа мерзімде алуға болады. Дегенмен, PW/LLDPE композиті төмен зарядтауға ие, бұл PW-мен салыстырғанда зарядтау уақытының ұзаруына әкеледі. Айырмашылықтарға қарамастан, екі полимердің де HSM үшін тұрақтандырғыш ретінде пайдалану мүмкіндігі айтарлықтай жоғары және жылуды жинау облысы үшін нақты талаптарына сәйкес бейімделуі мүмкін.
Кілт сөздері: ыдырау, спектрлер, көмірсутектер, балқу, қатаю, термиялық.

Rahman R.A., Sulistyo, Utomo M.S.K.T.S., Febriansyah I.
Влияние марки полимера низкой плотности на температурный переход и зарядовое поведение воска как твердожидкого теплоаккумулятора.
Первоначальная оценка загрузки для технического улучшения парафина в качестве теплоаккумулирующего материала проводится путем композитинга с группой пластиков низкой плотности. Оценка направлена на получение температурного перехода смеси, включая химический спектр и теплофизическое поведение. В смеси имеется дополнительный пик перехода после основного фазового перехода. Она колеблется в пределах 15,26–19,34 °С (плавление) и 11,98–9,45 °С (замерзание). Химические наблюдения указывают на хорошее соответствие, поскольку композит может быть образован без химической реакции. Более того, характеристика разложения предполагает, что смесь плавится раздельно. Для оценки заряда композит PW/LDPE имеет лучшие характеристики заряда с максимальным приращением около 25% по сравнению с PW. Он также имеет уникальный температурный профиль, изотермический профиль которого можно получить за короткое время. Однако композит PW/LLDPE имеет низкую зарядку, что приводит к более длительному заряду по сравнению с PW. Несмотря на различия, оба полимера имеют значительные шансы быть использованы в качестве стабилизаторов для HSM и могут быть адаптированы в соответствии с конкретными требованиями для применения в области аккумулирования тепла.
Ключевые слова: разложение, спектры, углеводороды, плавление, затвердевание, термические.

Болегенова С.А., Аскарова А.С., Оспанова Ш.С., Маканова А.Б., Жумагалиева С.А., Нурмуханова А.З., Адильбаев Н.А., Шалкар А.
Әсерлесетін турбулентті ағындағы сұйық отын бүркулерінің қалыптасуы мен таралуын модельдеу.
Мақалада сұйық отынды бүрку және оның тамшыларының турбулентті әсерлесетін ағында таралуы бойынша есептеу тәжірибелері келтірілген. Жану болғандағы екі түрлі сұйық отын (изооктан және додекан) тамшыларының бірінші және екінші ретті бүркілуі үзіліссіздік, импульс, ішкі энергия, әсерлесетін заттардың компоненттерінің концентрацияларының теңдеулерімен және турбулентті ағысты есептеудің қоспараметрлік моделімен сипатталды. Форсунканың бүрку бұрышы өзгергендегі модельдік жану камерасындағы көмірсутекті сұйық отындардың тамшыларының бүрку, дисперсиясы мен жануын зерттеу нәтижелері алынды. Бүрку бұрышының мәндері 2-ден 10 градус аралығында өзгерілді. Есептеу тәжірибесінің негізінде әр түрлі уақыт мезеттеріндегі температура профильдері және жану камерасындағы жану өнімдері мен газдың концентрациялық сипаттамалары алынды. Тамшылардың Саутер орташа диаметрлерінің таралуының сандық есептеулері додекан үшін ұқсас дисперсия қисықтарына ие. Бұл әсерлесетін ағындағы бүркудің қалыптасуы мен таралуының әзірленген кешенді моделінің дәлдігі мен сәйкестігі оның күшті корреляциясымен және модельдеу нәтижелерінің басқа зерттеушілердің эксперименттік деректерімен жақсы келісімімен расталғанын көрсетеді. Мұндай модельдеу әдістері және олардың негізінде алынған есептеу эксперименттерінің нәтижелері дәстүрлі жылуэнергетикасында ғана емес, сонымен қатар жаңа буын қозғалтқыштарының жану камераларындағы технологиялық процестерді зерттеуде, баламалы отындарды жағу және оларды оңтайландыру кезінде кеңінен қолданылады.
Кілт сөздері: қазбалы отын, бүрку, модельдеу, жану, бүрку бұрышы, зиянды қалдықтар.

Болегенова С.А., Аскарова А.С., Оспанова Ш.С., Маканова А.Б., Жумагалиева С.А., Нурмуханова А.З., Адильбаев Н.А., Шалкар А.
Моделирование образования и распределения впрысков жидкого топлива в реагирующем турбулентном потоке.
В статье представлены вычислительные эксперименты по распылению жидкого топлива и распределению его капель в турбулентном реагирующем потоке. Первичное и вторичное распыление капель двух видов жидких топлив (изооктана и додекана) при наличии горения описывалось уравнениями неразрывности, импульса, внутренней энергии, концентрации компонентов реагирующих веществ и двухпараметрической

моделью расчета турбулентного течения. Получены результаты исследования распыления, дисперсии и горения капель углеводородных жидких топлив в модельной камере сгорания при изменении угла впрыска форсунки. Значения угла впрыска варьировались от 2 до 10 градусов. На основе вычислительного эксперимента получены температурные профили и концентрационные характеристики продуктов сгорания и газа в камере сгорания в различные моменты времени. Численные расчеты распределения Саутеровского среднего диаметра капель имеют аналогичные кривые дисперсии для додекана. Это говорит о том, что точность и адекватность разработанной комплексной модели образования и распределения распыла в реагирующем потоке подтверждена ее сильной корреляцией и хорошим согласием результатов моделирования с экспериментальными данными других исследователей. Такого рода методы моделирования и полученные на их основе результаты вычислительных экспериментов широко используются не только в традиционной теплоэнергетике, но и при исследовании технологических процессов в камерах сгорания двигателей нового поколения, при сжигании альтернативных видов топлива и их оптимизации.
Ключевые слова: ископаемое топливо, распыление, моделирование, сжигание, угол впрыска, выбросы.

Тлеубергенова А.Ж., Дюсембаева А.Н., Танашева Н.К., Бахтыбекова А.Р., Кутумова Ж.Б., Мұхамедрахим А.Р.

Құрамалы қалақшаларына ие жел турбинаның жұмыс тиімділігін эксперименттік зерттеу.

Берілген мақалада әртүрлі орап ағу параметрлері кезіндегі жел энергетикалық қондырғысының аэродинамикалық сипаттамалары зерттелген. Осы мақсатта қозғалмайтын қалақшаларға ие айналмалы цилиндрлер түріндегі құрамалы күш элементтері бар қондырғының эксперименттік үлгісі жасалды. Ауа ағынының жылдамдығы 3-тен 12 м/с-қа дейін өзгерді. Жел энергетикалық қондырғының аэродинамикалық күштерінің ағын жылдамдығына тәуелділігі зерттелді. Ауа ағынының жылдамдығынан цилиндрге қатысты қозғалмайтын қалақшаның α бұрышының өзгеруін зерттеу бойынша эксперимент нәтижелеріне талдау жүргізілді. Маңдайлық кедергі күші мен көтергіш күштерінің ағын жылдамдығына тәуелділігі бойынша график құрылды. Қозғалмайтын қалақшаның цилиндрге қатысты α=0° минималды бұрышта көтергіш күш пен маңдайлық кедергі күшінің мәні жоғары екендігі анықталды. Маңдайлық кедергі күші мен көтергіш күшінің коэффициенті Рейнольдс санына тәуелділігінен Re=1·10^5 кезде 0º градус бұрышта көтергіш күші коэффициентінің минималды мәні 0,012 Н және маңдайлық кедергі күші коэффициентінің максималды мәні 10,07 Н екендігі анықталды. Қондырғының жұмыс тиімділігін арттыру үшін көлденең осьті цилиндрлерді айналдыру кезінде қозғалатын қосымша күшті қолдануға болатындығын эксперимент нәтижелері көрсетеді. Алынған нәтижелер желдің төмен жылдамдығында жұмыс істейтін құрамалы қалақшаларға ие жел энергетикалық қондырғыларын әзірлеу және зерттеу кезінде пайдаланылуы мүмкін.
Кілт сөздері: Жел энергетикалық қондырғы, құрамалы қалақшалар, Т-1-М аэродинамикалық құбыр, ағын жылдамдығы, маңдайлық кедергі күші, көтергіш күші, Рейнольдс саны.

Тлеубергенова А.Ж., Дюсембаева А.Н., Танашева Н.К., Бахтыбекова А.Р., Кутумова Ж.Б., Мұхамедрахим А.Р.

Экспериментальные исследования эффективности работы ветротурбины с комбинированными лопастями.

В данной статье изучены аэродинамические характеристики ветроэнергетической установки при различных параметрах обтекания. Для данной цели был изготовлен экспериментальный образец установки с комбинированными силовыми элементами в виде вращающихся цилиндров с неподвижными лопастями. Скорость воздушного потока варьировалась, начиная 3 до 12 м/с. Исследовались зависимости аэродинамических сил ветроэнергетической установки от скорости потока. Проведен анализ результатов эксперимента по изучению изменения угла α расположения неподвижной лопасти относительно цилиндра от скорости воздушного потока. Построен график по зависимости сил лобового сопротивления и подъемной силы от скорости потока. Установлено, что при минимальном угле относительно цилиндра α=0° значение подъемной силы и силы лобового сопротивления неподвижной лопасти выше. Из зависимости коэффициента подъемной силы и силы лобового сопротивления от числа Рейнольдса, установлено, что при угле 0º градусов наблюдается минимальное значение коэффициент подъёмной силы 0,012 Н и максимальное значение коэффициента силы лобового сопротивления 10,07 Н при Re=1·105. Результаты эксперимента показывают, что можно использовать дополнительную силу, возникающим при вращении цилиндров с горизонтальной осью, для увеличения эффективности работы установки. Полученные результаты могут быть использованы при разработке и исследовании ветроэнергетических установок с комбинированными лопастями, работающих при малых скоростях ветра.
Ключевые слова: Ветроэнергетическая установка, комбинированные лопасти, аэродинамическая труба Т-1-М, скорость потока, сила лобового сопротивления, подъемная сила, число Рейнольдса.

Солдатов А.И., Солдатов А.А., Абуэллаиль А.А., Костина М.А.
Термоэлектрлік бақылау кезіндегі бақыланатын үлгідегі электродтардың жанасу кедергісін бақылау.
Мақалада электродтардың жанасу кедергісінің бақылау нәтижесіне әсеріне талдау жүргізілді. Өлшеуіш резисторының шамасы артқан кезде сынақ үлгісімен электродтардың жанасу кедергісінің рұқсат етілген мәні жоғарылайтыны көрсетілген. Жанасу кедергісін басқарудың жанама әдісі ұсынылған, бұл әдіс жоғары жиілікті тұрақты токты жанасу кедергісі арқылы өткізуден және осы кедергідегі кернеуді өлшеуден тұрады. Өлшеуіш резисторындағы салыстырмалы кернеудің контактінің жалпы кедергісіне тәуелділігі тұрғызылды. Жанасу кедергісінің рұқсат етілген мәні есептелген, термоЭҚК-нің өлшенетін мәні ақиқат мәннен 10% - дан аспайды. Ұсынылған әдіс термоЭҚК бақылау процесінде жанасу кедергісін тікелей өлшеуге мүмкіндік береді.
Кілт сөздері: термоЭҚК, ыстық электрод, суық электрод, жанасу кедергісі, ток генераторы, сүзгі, өлшеуіш резисторы.

Солдатов А.И., Солдатов А.А., Абуэллаиль А.А., Костина М.А.
Мониторинг контактного сопротивления электродов с контролируемым образцом при термоэлектрическом контроле.
В статье проведен анализ влияния контактного сопротивления электродов на результат контроля. Показано, что при увеличении величины измерительного резистора увеличивается допустимое значение контактного сопротивления электродов с испытуемым образцом. Предложен косвенный способ контроля контактного сопротивления, заключающийся в пропускании стабильного тока высокой частоты через контактное сопротивление и измерения напряжения на этом сопротивлении. Построена зависимость относительного напряжения на измерительном резисторе от суммарного сопротивления контакта. Рассчитано допустимое значение контактного сопротивления, при котором измеряемое значение термоЭДС будет отличается от истинного не более чем на 10 %. Предложенный способ позволяет проводить измерение контактного сопротивления непосредственно в процессе контроля термоЭДС.
Ключевые слова: термоЭДС, горячий электрод, холодный электрод, контактное сопротивление, генератор тока, фильтр, измерительный резистор.

Качкинова А.К., Туралина Д.Е. , Нурмаханов Н.У.
Алдын ала болжау негізінде уран өнімділігін арттыру әдістерінің тиімділігін зерттеу.
Алдын ала болжау арқылы уран өндірісінің өнімділігін арттыру әдістерінің тиімділігіне зерттеу жүргізілді. Бұл зерттеудің мақсаты қазіргі уақытта өндірістегі технологиялық блокты талдау және оңтайландыру. Блоктың немесе ұяшықтың өнімділігін талдау үшін әртүрлі өнімділік көрсеткіштері пайдаланылады: Tracer cut, Tracer in place, Acid in place. Бірнеше оңтайландыру сценарийлері HYTEC реактивті тасымалдау бағдарламасы және уран өндіру процесін модельдеу арқылы сынақтан өтті. Бұл сценарийлер жаңа ұңғымаларға және ұңғыма өнімділігін арттыратын «химиялық өңдеудің» әсеріне бағытталған. Бұл жұмыс блок өндірісін жақсартуға бағытталған. Үш түрлі сценарий орындалды. Үш сценарийдің ішінде үшіншіден ең көп уран, яғни 154 тонна қордың 133 тоннасы өндірілді. Оңтайландыру кезінде тазалау әрекетінің файлындағы әрбір ұңғыманың соңғы трендінің дұрыс тиімділік мәнін алған дұрыс. Ұңғыманы химиялық өңдеуден кейін pH <1,85 болатын ауданды ұлғайту мүмкін болды. Бұл ұңғымаларды оңтайландыру мен химиялық өңдеудің маңыздылығын көрсетеді.
Кілт сөздері: уран өндіру, жерасты шаймалау, реактивті тасымалдау, hytec, болжам, acid in place, tracer in place, tracer cut, химиялық ұңғымаларды өңдеу.

Качкинова А.К., Туралина Д.Е. , Нурмаханов Н.У.
Исследование эффективности методов повышения продуктивности урана на основе предварительного прогнозирования.
Проведено исследование эффективности методов повышения производительности уранового производства путем предварительного прогнозирования. Целью данного исследования является анализ и оптимизация технологического блока, находящегося в настоящее время на производстве. Для анализа производительности блока или ячейки используются различные показатели производительности: Tracer cut, Tracer in Place, Acid in place. Несколько сценариев оптимизации были протестированы с использованием программы реактивного переноса HYTEC и моделирования процесса добычи урана. Эти сценарии касались новых скважин и влияния «химической обработки скважины», которая увеличивает производительность скважины. В данной работе основное внимание уделялось улучшению добычи блока. Было выполнено три различных сценария. Из трех сценариев третий дал наибольшее количество урана 133 тонны из 154 тонн запасов. При оптимизации лучше получить правильное значение эффективности для последнего тренда каждой скважины в excel-файле

действий по очистке. После химической обработки скважины удалось увеличить область, где pH<1,85. Это говорит о важности оптимизации и химической обработки скважины.

Ключевые слова: добыча урана, внутрипластовое извлечение, реактивный транспорт, hytec, прогноз, кислота на месте, трассер на месте, трассерный разрез, химическая обработка скважины.

Набиев Р. Н., Абдуллаев А.А., Гараев Г.И..

Конвертиплан типті микроұшқышсыз ұшу аппараттарына арналған борттық бақылау-өлшеуіш жүйесі.

Мақалада ұшудың әртүрлі режимдерінде конвертоплан типті микроұшқышсыз ұшқыш аппаратының қозғалтқыштарының негізгі техникалық параметрлерін тіркеуге арналған борттық бақылау-өлшеуіш жүйесі және ол үшін қолданылатын элементтер базасы сипатталған. Борттық бақылау-өлшеуіш жүйесін пайдалануымен стационарлық режимде сынақтар жүргізу әдістемесі әзірленіп, сынақтар жүргізілді. Әзірленген борттық бақылау-өлшеуіш жүйесінің көмегімен қозғалтқыштардың күйлерін диагностикалық тексеру және бағалау жүзеге асырылды, әрбір жеке қозғалтқыштың айналым саны, токтың тұтынуы және температурасы туралы мәліметтер, сондай-ақ осьтердің бағыты және стационарлық режимдегі планер жылдамдығының векторы туралы мәліметтер тіркелді. Тіркелген мәндер негізінде тиісті параметрлердің уақыттық диаграммалары құрылды. Ұшуға дейін және ұшудан кейін микроұшқышсыз ұшу аппараттарының қуат элементтері ретінде қозғалтқыштарды, сондай-ақ ұшу кезінде ауада болуы мүмкін ұшу оқиғаларын жердегі сынақтар мүмкіндігі көрсетілген.

Кілт сөздері: конвертоплан, ұшқышсыз ұшу аппараттары, борттық бақылау-өлшеу жүйесі, акселерометр, гироскоп, диагностика, термометр.

Набиев Р. Н., Абдуллаев А.А., Гараев Г.И..

Бортовая контрольно-измерительная система для микробеспилотных летательных аппаратов типа конвертиплан.

В статье описана бортовая контрольно-измерительная система, предназначенная для регистрации основных технических параметров двигателей микробеспилотного летательного аппарата типа конвертоплан на различных режимах полета, и используемая для этого элементная база. Разработана методика проведения испытаний в стационарном режиме с использованием бортовой контрольно-измерительной системы и проведены испытания. С помощью разработанной бортовой контрольно-измерительной системы осуществлялась диагностическая проверка и оценка состояния двигателей, фиксировались данные о количестве оборотов, токопотреблении и температуре каждого отдельного двигателя, а также данные о направлении осей и векторе скорости планера в стационарном режиме. На основе зарегистрированных значений были построены временные диаграммы соответствующих параметров. Показана возможность наземных испытаний двигателей как силовых элементов микробеспилотных летательных аппаратов до и после полета, а также летных событий, которые могут происходить в воздухе во время полета.

Ключевые слова: конвертоплан, беспилотные летательные аппараты, бортовая контрольно-измерительная система, акселерометр, гироскоп, диагностика, термометр.

Турлыкожаева Д.А., Ахтанов С.Н., Байгалиева А.Н., Темешева С.А., Жексебай Д.М., Зайдын М., Үсіпов Н.М., Скабылов А.А.

NS-3 симуляторын пайдалану арналған сымсыз желілердің түрлі топологияларында бағдарлау алгоритмдерін бағалау

Сымсыз Mesh желілері (WMN) орталықтандырылған инфрақұрылымсыз сенімді қосылымды қамтамасыз ету шешімі ретінде танымал болып келеді. Олар сымсыз түйін қосылымдары арқылы жұмыс істейді, сымды желілер практикалық емес сценарийлер үшін өте ыңғайлы өздігінен реттелетін желілерді құрайды. Түйіндер арасындағы тиімді байланысты қамтамасыз ету үшін WMN желілерінде маршруттау өте маңызды. Дегенмен, WMN топологиялары үшін маршруттау алгоритмдерінің жарамдылығы қосымша зерттеуді қажет етеді. Берілген мақалада NS-3 модельдеуін қолдана отырып, әртүрлі WMN топологияларында AODV, DSDV және OLSR сияқты маршруттау алгоритмдерінің тиімділігін зерттеу ұсынылады. Ол сондай-ақ өткізу қабілеттілігін арттыру және шектеулі аумақта пакеттердің жоғалуын азайту үшін түйіндер мен хаттамалардың оңтайлы санын анықтауға бағытталған. NS-3-ті мұқият модельдеу арқылы зерттеу AODV, DSDV және OLSR кездейсоқ топологияда, торлы топологияда және Фрухтерман-Рейнгольд топологиясында әртүрлі тиімділікті көрсететінін көрсетеді. Бұл нәтижелер WMN үшін маршруттау протоколдарын таңдау және оңтайландыру кезінде топологияға тән факторларды есепке алудың маңыздылығын көрсетеді. Осылайша, сымсыз Mesh желілері орталықтандырылмаған қосылымды ұсынады, бірақ әртүрлі топологиялардағы маршруттау алгоритмдерінің тиімділігі әлі де жақсы түсінілмеген. Бұл зерттеу бұл

олқылықты әртүрлі топологиялардағы маршруттау алгоритмдерін бағалау арқылы жояды, олардың WMN-де жарамдылығы мен өнімділігіне түсіндірме береді.

Кілт сөздері: WMN; AODV; DSDV; OLSR; Проактивті маршруттау хаттамалары; NS-3.

Турлыкожаева Д.А., Ахтанов С.Н., Байгалиева А.Н., Темешева С.А., Жексебай Д.М., Зайдын М., Усипов Н.М., Скабылов А.А.

Оценка алгоритмов маршрутизации в различных топологиях беспроводных сетевых сетей с использованием симулятора NS-3

Беспроводные Mesh-сети (WMN) набирают популярность как решение для обеспечения надежного подключения без централизованной инфраструктуры. Они работают через соединения беспроводных узлов, образуя самонастраивающиеся сети, идеально подходящие для сценариев, где проводные сети непрактичны. Маршрутизация имеет решающее значение в сетях WMN для обеспечения эффективной связи между узлами. Однако пригодность алгоритмов маршрутизации для топологий WMN требует дальнейшего изучения. В статье предлагается исследование эффективности алгоритмов маршрутизации, таких как AODV, DSDV и OLSR, в различных топологиях WMN с использованием моделирования NS-3. Он также направлен на определение оптимального количества узлов и протоколов для максимизации пропускной способности и минимизации потерь пакетов в пределах ограниченной области. С помощью тщательного моделирования NS-3 исследование показывает, что AODV, DSDV и OLSR демонстрируют разную эффективность в случайной топологии, топологии ячеистой сетки и топологии Фрухтермана-Рейнгольда. Эти результаты подчеркивают важность учета факторов, специфичных для топологии, при выборе и оптимизации протоколов маршрутизации для WMN. Таким образом, беспроводные Mesh-сети предлагают децентрализованное соединение, но эффективность алгоритмов маршрутизации в различных топологиях остается недостаточно изученной. Данное исследование устраняет этот пробел путем оценки алгоритмов маршрутизации в различных топологиях, проливая свет на их пригодность и производительность в WMN.

Ключевые слова: WMN; АОДВ; ДСДВ; ОЛСР; Протоколы проактивной маршрутизации; NS-3.

Утепов Е.Б., Иманов А.Ж., Муканова Б.Г., Назарова А.Г., Анискин А., Ахажанов С.Б.

Радиалды микрофондар массиві және ең үлкен сигнал бағыттарының қиылысы негізінде құрылыс алаңында шу көздерін оқшаулауды модельдеу.

Құрылыс жұмыстарының шудың ластануы жұмысшыларға да, жақын маңдағы үйлердің тұрғындарына да әсер етеді. Бұл зерттеу құрылыс алаңдарындағы шу көздерін оқшаулаудың жаңа әдісін ұсынады. Әдіс радиалды микрофон массивін және ең үлкен сигналдардың бағыттарының қиылысына негізделген алгоритмді қолданады. Модельдеу көрсеткендей, бұл тәсіл шу көзінің орнын салыстырмалы түрде жоғары дәлдікпен анықтауға мүмкіндік береді. Жеке көздер үшін әдіс шу көздерін шамамен 180 м² аумаққа локализациялады, орташа қателігі 6 %. Бірнеше көздер үшін, атап айтқанда екі көз үшін, көздердің өлшемі мен санына байланысты қателік 83,2% және 6,1% құрады. Бұл нәтижелер әдістің дәлдігін және оның жер бедерінің жағдайына сезгіштігін көрсетеді. Қолданыстағы шешімдермен салыстырғанда біздің көзқарасымыз аз есептеуді қажет етеді. Болашақ жұмыс алгоритмді жетілдіруге және нақты уақыттағы мониторинг үшін IoT технологияларын біріктіруге бағытталған.

Кілт сөздері: құрылыс шуы, дыбыс көзін оқшаулау, радиалды микрофон массиві, ең үлкен сигналдың бағыты, дыбыстық бақылау, дыбысты картаға түсіру, сигналды өңдеу.

Утепов Е.Б., Иманов А.Ж., Муканова Б.Г., Назарова А.Г., Анискин А., Ахажанов С.Б.

Моделирование локализации источников шума на строительной площадке на основе массива радиальных микрофонов и пересечений направлений наибольшего сигнала.

Шумовое загрязнение от строительных работ влияет как на рабочих, так и на жителей близлежащих домов. В данном исследовании предлагается новый метод локализации источников шума на строительных площадках. Метод использует радиальный микрофонный массив и алгоритм, основанный на пересечении направлений наибольших сигналов. Симуляции показывают, что этот подход позволяет определить местоположение источника шума с относительно высокой точностью. Для одиночных источников метод локализовал источники шума на площади около 180 м² со средней погрешностью 6 %. Для множественных источников, в частности двух источников, погрешность составила 83,2 % и 6,1 % в зависимости от размера и количества источников. Эти результаты подчеркивают точность метода и его чувствительность к условиям местности. По сравнению с существующими решениями наш подход требует меньше вычислений. Будущая работа будет направлена на усовершенствование алгоритма и интеграцию IoT-технологий для мониторинга в реальном времени.

Ключевые слова: строительный шум, локализация источника звука, радиальный микрофонный массив, направление наибольшего сигнала, звуковой мониторинг, картирование звука, обработка сигнала.

Сулиева Г.Б., Курманов Е.Б., Қонысбаев Т.К., Бошкаев К.А., Уразалина А.А., Luongo O.
Скаляр өрісімен ұсынылған қараңғы материя моделіндегі соңғы температураның әсерлері.

Суық қараңғы материя парадигмасына балама болып табылатын скаляр өрісінің қараңғы материя теориясы аясында екі модельді қолдануымен беттік жарықтылығы төмен төрт спиральды галактикалардағы қараңғы материяның таралуы зерттелді. Бірінші модель Бозе-Эйнштейн конденсаты болып табылады, онда бозондар нөлдік температурада негізгі күйде болады. Екінші модель қозған күйлерді енгізуге мүмкіндік беретін скаляр өрісінің потенциалына соңғы температуралық түзетулерді қамтиды. Масштабты радиусты, сипаттық (орталық) тығыздықты және толық массаны қоса алғанда, модельдердің бос параметрлерін анықтау үшін айналу қисықтарын бақылау мәліметтері негізінде ең кіші квадраттарды сызықсыз жуықтау әдісі қолданылды. Мөлшерлік талдау галактикалық деңгейде соңғы температураны ескерудіңі маңыздылығын көрсетеді. Сонымен қатар, екі модель изотермиялық сфера, Наварро-Френк-Уайт және Буркерт профильдері сияқты кеңінен қолданылатын және қараңғы материяның қабылданған феноменологиялық профильдерінің нәтижелерімен салыстырылды. Әрбір модельдің дұрыстығын бағалау Байес толықтығының ақпараттық критерийі негізінде жүргізілді. Статистикалық талдау белгілі бір профильді таңдаудың мазмұнды интерпретациясын қамтамасыз етеді. Нәтижесінде бұл зерттеу дәстүрлі феноменологиялық профильдермен салыстырғанда скаляр өріс модельдерінің тиімділігіне түсіндірме беріп, беттік жарықтылығы төмен спиральды галактикалардағы қараңғы материяның таралуын жақсырақ түсінуге ықпал етеді.

Кілт сөздері: скаляр өрісі, қараңғы зат, Бозе-Эйнштейн конденсаты, галактикалардың айналу қисықтары.

Сулиева Г.Б., Курманов Е.Б., Қонысбаев Т.К., Бошкаев К.А., Уразалина А.А., Luongo O.
Эффекты конечной температуры в модели темной материи, представленной скалярным полем.

Исследовано распределение темной материи в четырех спиральных галактиках с низкой поверхностной яркостью с использованием двух моделей в рамках теории темной материи скалярного поля, альтернативной парадигме холодной темной материи. Первая модель представляет собой конденсат Бозе-Эйнштейна, в котором бозоны занимают основное состояние при нулевой температуре. Вторая модель включает конечные температурные поправки в потенциал скалярного поля, что позволяет ввести возбужденные состояния. Для определения свободных параметров моделей, включая масштабный радиус, характерную (центральную) плотность и полную массу, на основе данных наблюдений кривых вращения применен метод нелинейной аппроксимации наименьших квадратов. Количественный анализ показывает важность учета конечных температур на галактическом уровне. Кроме того, сравниваются две модели с результатами широко используемых и принятых феноменологических профилей темной материи, таких как изотермическая сфера, профили Наварро-Френка-Уайта и Буркерта. Оценка достоверности каждой модели проведена на основе Байесовского информационного критерия полноты. Статистический анализ обеспечивает содержательную интерпретацию выбора конкретного профиля. В конечном итоге, это исследование способствует лучшему пониманию распределения темной материи в спиральных галактиках с низкой поверхностной яркостью, проливая свет на эффективность моделей скалярного поля по сравнению с традиционными феноменологическими профилями.

Ключевые слова: скалярное поле, темная материя, конденсат Бозе-Эйнштейна, кривые вращения галактик.

Ibanga E.A., Inyang E.P., Agbo G.A.
Күн және геомагниттік белсенділіктің циклдік қасиеттерін зерттеу: беткі температураның ғаламдық өзгергіштігінің маңызы.

Күн-геомагниттік белсенділіктің және ғаламдық жер бетіндегі температураның циклдік қасиеттері трендтік, жиіліктік және жиілік-уақыттық талдауды қолдануымен зерттелді. Нәтижелер онжылдықтан ғасырға дейінгі уақыттық масштабтарында жарты ғасырлық (бір цикл үшін~ 49-56 жыл) және Глейсберг (бір цикл үшін 99-114 жыл) диапазонындағы төмен жиілікті циклдер Шваб фонында (бір цикл үшін~ 9-11 жыл) басымдылықты күн-геомагниттік белсенділік циклі ретінде жүретінін көрсетеді. Ғаламдық жер бетіндегі температуралар қатарындағы жалғыз басым циклі - бұл жарты ғасырлық цикл, ол оның және күн-геомагниттік белсенділік құбылыстарының арасындағы ықтимал болатын себеп-салдарлық байланысты болжайды. Цикл амплитудасының эволюциясы Швабе мен Глейсберг кезеңдерінің қуаты серияның басынан 20 ғасырдың ортасына дейін артты, содан кейін ол төмендей бастады. Жарты ғасырлық цикл амплитудасы бойынша 1800 жылдан кейін және қазіргі уақытқа дейін төмендеді. Геомагниттік белсенділікке келетін болсақ, Глейсберг циклінің амплитудасы серияның басынан бастап шамамен 2000 жылға дейін өсті, ал Швабе циклдерінің амплитудасы мен жарты ғасырлық циклдері сол аралықта төмендеді, тек 1980 жылдан кейін амплитудасы тез өскен Швабе циклін қоспағанда. Ғаламдық жер бетіндегі температураға келетін болсақ, Глейсберг циклдері мен жарты ғасырлық циклдердің амплитудасы қатар басталғаннан бері үздіксіз өсті, ал Швабе циклі өте төмен амплитудамен 1980 жылға дейін ауытқиды, содан кейін ол аздап өсті. Күн-геомагниттік белсенділік циклдерінің амплитудасының эволюциясы Маундердің минимумынан қалпына келуді және үлкен эпизодқа құлдырауды, ең алдымен, минимумды қамтиды.

Кілт сөздері: геомагниттік белсенділік, күн белсенділігі, төмен жиілікті цикл, үлкен эпизод, спектрлік қуат, ғаламдық вейвлет-қуаты.

Ibanga E.A., Inyang E.P., Agbo G.A.

Исследование циклических свойств солнечной и геомагнитной активности: значение для глобальной изменчивости температуры поверхности.

Циклические свойства солнечно-геомагнитной активности и глобальной приземной температуры были исследованы с использованием трендового, частотного и частотно-временного анализа. Результаты показывают, что во временных масштабах от десятилетия до столетия низкочастотные циклы в полувековом (~ 49–56 лет за цикл) и Глейсбергском (от 99 до 114 лет за цикл) диапазоне протекают на фоне Швабе (~ от 9 до 11 лет за цикл) как доминирующий цикл солнечно-геомагнитной активности. Единственным доминирующим циклом в ряду глобальных приземных температур является полувековой цикл, который предполагает возможную причинную связь между ним и явлениями солнечно-геомагнитной активности. Эволюция амплитуд циклов такова, что мощность периодов Швабе и Глейсберга увеличивалась с начала серии до середины 20 века, после чего она пошла на убыль. Полувековой цикл уменьшился по амплитуде после 1800 г. и по настоящее время. Что касается геомагнитной активности, то амплитуда цикла Глейсберга увеличилась с начала ряда около 2000 г., в то время как амплитуды циклов Швабе и полувековых циклов снизились в том же интервале, за исключением цикла Швабе, амплитуда которого быстро увеличивалась после 1980 г. по настоящее время. Что касается глобальной приземной температуры, то амплитуды циклов Глейсберга и полувековых циклов постоянно увеличивались с начала ряда, в то время как цикл Швабе колеблется с очень низкими амплитудами до 1980 года, после чего он немного увеличился. Эволюция амплитуд циклов солнечно-гемагнитной активности предполагает восстановление от минимума Маундера и спад в большой эпизод, скорее всего, минимум.

Ключевые слова: геомагнитная активность, солнечная активность, низкочастотный цикл, большой эпизод, спектральная мощность, глобальная вейвлет-мощность.